

The Characterization of Disordered Membrane-Binding Proteins of Myelin

A Biophysical Approach

Arne Raasakka

Thesis for the Degree of Philosophiae Doctor (PhD)
University of Bergen, Norway
2019

UNIVERSITY OF BERGEN



The Characterization of Disordered Membrane-Binding Proteins of Myelin

A Biophysical Approach

Arne Raasakka



Thesis for the Degree of Philosophiae Doctor (PhD)
at the University of Bergen

Date of defence: 12.04.2019

© Copyright Arne Raasakka

The material in this publication is covered by the provisions of the Copyright Act.

Year: 2019

Title: The Characterization of Disordered Membrane-Binding Proteins of Myelin

Name: Arne Raasakka

Print: Skipnes Kommunikasjon / University of Bergen

In loving memory of Raimo, my amazing grandfather.

ABSTRACT

Myelin is a multilayered lipid-rich structure that surrounds selected axonal segments in the central and peripheral nervous systems (CNS and PNS, respectively). Myelin insulates axons, which increases nerve conduction velocity by up to two orders of magnitude. The correct formation and stability of myelin are crucial for the function of the nervous system, as demonstrated in the case of demyelinating diseases. The disruption of myelin and its compact structure can result from an autoimmune response, such as in the case of multiple sclerosis (MS), which affects the CNS. Another mechanism arises from mutations, which compromise myelin protein function and lead to disease. Such disorders include PNS neuropathies. Demyelinating conditions are generally chronic, incurable diseases. Remedies for these remain to be developed due to insufficient understanding of the formation and stability of healthy myelin.

The insulative nature of myelin arises from a specialized plasma membrane that is wrapped dozens of times around the axon, before myelin undergoes compaction that excludes most water content. Stacked lipid membranes are adhered together by myelin-specific proteins with unique structural and functional properties. Such proteins include the intrinsically disordered myelin basic protein (MBP) and the integral membrane protein, myelin protein zero (P0), in the CNS and PNS, respectively. These proteins are only abundantly expressed in myelin and they are highly conserved within vertebrates. Both MBP and P0 have been linked to demyelinating disorders, with the structural details remaining to be elucidated.

In this thesis, a cross-complementary biophysical method ensemble was established and used to characterize the folding, lipid binding, and membrane stacking properties of MBP, uncovering a putative mechanism for MBP-induced formation of compact myelin. The same workflow was used to characterize the cytoplasmic domain of P0 (P0ct), which has been suggested to adhere membranes together in the PNS similarly to MBP in the CNS. Indeed, P0ct behaved similarly to MBP in various lipid

environments. The results provide a model for P0-induced membrane stacking in the PNS.

The effect of ions on the function of MBP and P0ct was studied, unveiling that Ca^{2+} , the most abundant divalent cation in myelin, modulates their activity. The study was expanded to peripheral neuropathy-related mutant variants of P0ct, and a specific gain-of-function mutation may explain the aberrant myelin phenotype in patients.

The biophysical approach described in this thesis enables the characterization of myelin proteins and their disease variants. While well-behaving model lipid conditions were employed here, more physiologically relevant conditions should be studied in the future, possibly by the inclusion additional methods.

SCIENTIFIC ENVIRONMENT

The work outlined in this thesis was carried out at the Department of Biomedicine, University of Bergen, Norway, under the supervision of Professor Petri Kursula (Department of Biomedicine, University of Bergen, Norway; Faculty of Biochemistry and Molecular Medicine, University of Oulu, Finland) with co-supervision from Dr. Anne Baumann (Department of Biomedicine, University of Bergen, Norway; Division of Psychiatry, Haukeland University Hospital, Bergen, Norway). Synchrotron and neutron radiation data collections were performed at the following facilities: ASTRID2, Institute for Storage Ring Facilities in Aarhus (ISA), University of Aarhus, Denmark; German Electron Synchrotron (DESY), Hamburg, Germany; Diamond Light Source, Harwell Science and Innovation Campus, United Kingdom; Institut Laue-Langevin (ILL), Grenoble, France; ISIS Neutron and Muon source, Harwell Science and Innovation Campus, United Kingdom, and Karlsruhe Research Accelerator (KARA, formerly ANKA), Karlsruhe Institute of Technology, Germany. Mass spectrometric measurements were carried out at the Biocenter Oulu Proteomics and protein analysis core facility, Faculty of Biochemistry and Molecular Medicine, University of Oulu, Finland.

The work has been financed by the Faculty of Medicine and Dentistry, and later by the Faculty of Medicine, University of Bergen. Funding received from the Norwegian Research Council (NFR; SYNKNØYT program), the Norwegian Graduate School in Biocatalysis (BioCat), The National Graduate School in Structural Biology (BioStruct), the Norwegian Biochemical Society (NBS), The Norwegian Academy of Science and Letters (DNVA), and the Biophysical Society provided financial aid to participate in synchrotron and neutron data collections, courses, and scientific meetings.

ACKNOWLEDGEMENTS

I met Professor Petri Kursula, my supervisor-to-be, in 2011. I was a young, naïve MSc student at the time, interested in a project. In the end of 2014, Petri asked me if I would like to consider moving to Norway and set up his lab with him. This 4-year journey began in May 2015 and is now nearing completion – the greatest adventure of my life. I can wholeheartedly say that I could not have asked for a better mentor. Petri is my paragon of science and I am thankful for every opportunity he gave me.

Anne Baumann, my co-supervisor, we share a passion to pursuit knowledge, to plan things early, and to do things ‘right from the start’. I knew that we would achieve many things together in the lab. You guided me with your expertise with lipid-based experiments – I helped you with crystallography and scattering methods. Thank you for supervising my work, I thoroughly enjoyed it and I learned many useful skills.

Inari Kursula, I have watched you lead your own group alongside Petri. Your research is as difficult as it is important, which makes me look up to you every single day. Your diplomatic attitude and hospitality are something that I always appreciate.

During the time with Petri, I worked with many great people, most notably Saara Laulumaa, Salla Ruskamo and Matti Myllykoski. Saara, we spent long nights figuring out those bloody reflectometers all by ourselves. There were always problems, but in the end we learned many things about science and each other. Salla, you were my go-to person in Finland when I needed to vent. I am happy about our discussions and scientific achievements together. Matti, you are one of the hardest working and most focused people I know – someone who does rather than talks. You excel in science and I sincerely believe you have a successful road ahead of you.

I am happy for the opportunity to collaborate with many people from the Department and outside of it: Rob and Julia, you have greatly contributed to this work I am about to present. You helped me and Petri answer fundamental questions regarding the functions of our proteins. Anni, Mathias and Jan – I am grateful that you let me and Petri be involved in your projects and that we all could mutually benefit from it.

Jarkko, my dearest friend, we have great memories from our past and there will be many more in times to come. I try to see you as often as I can and I greatly appreciate that you feel the same. Our friendship brings more joy to my life than I could ask for.

Kati, we started together as freshmen studying biochemistry in 2007. You wanted to go to med school, but you found your place in science as we studied together. Now we defend at the same time. If I ever had a twin, it would be you – we are so alike.

Kata and Jaakko, I am happy for your achievements and that you get to do what you most enjoy. I am grateful that you always wanted to travel and hang out with me.

Juha K., Juha V., Erik, Illimar and Kai – you guys absolutely rock. Life is more than science. Sometimes it is a night of pinnekjøtt and a walk of shame the next morning. Sometimes it is brewing hideous beer together. Sometimes it is procrastination at work – a bad, entertaining habit. I am glad to have you as my colleagues and friends.

I would like to thank my colleagues for a great time in the Neurotargeting group, at the Department in general, and outside of it: Huijong, Maryna, EP, Ju, Leila, Andrea, Sasha, Jussi, Kumar, Atta, Isa, Henni, Christine, Devaki, Weisha, Ábris, Bhargav, Péter, Øyvind, Peder, Ann-Kari, Sadaf, Ela, Nibal, Sunil, Hanne, Ingeborg, Marianne, Aurora, Ruth, Marte, Helene, Åge, Kunwar, Oscar, Karina, Maite, Fredrik and Knut. Big thanks to the students I supervised: Oda, Anushik, Helen, Cecilie and Guro.

I am happy that I met Hans Harald, Katrine, Helena, Rebecca, Are, Vanessa, Alva, Anders and Jo. You were some of the first people I ever got to know in Bergen and I have had the time of my life bouldering with you at Bryggeriet! Kom igjen!

Laura, sweetheart, I admire you and your focus. You work hard for you goals and you never give up in the face of obstacles. A great path awaits you in science and I hope that our journey together is as grand – I am so happy we found each other.

Finally, I would like to express my deepest gratitude towards my family. You always supported me, even when I left the life I had in Finland for many unspoken reasons. I know that at times I neglected you and others because of it, but in time I came to see that distance – of all things – brought you closer to me than ever before.

TABLE OF CONTENTS

| | |
|---|----|
| Abbreviations..... | xi |
| List of publications..... | xv |
| 1 Introduction..... | 1 |
| 1.1. Myelin, a nerve insulator..... | 1 |
| 1.1.1. The nervous system..... | 1 |
| 1.1.2. The structure and function of myelin..... | 2 |
| 1.2. The molecular characteristics of myelin..... | 12 |
| 1.2.1. The lipid composition of myelin..... | 12 |
| 1.2.2. Myelin proteins..... | 14 |
| 1.3. The biochemistry of (de)myelination..... | 30 |
| 1.3.1. Myelination..... | 30 |
| 1.3.2. Demyelination..... | 31 |
| 2 Aims of the study..... | 39 |
| 3 Materials and methods..... | 41 |
| 3.1. Recombinant protein preparation..... | 41 |
| 3.2. Lipids and detergents..... | 43 |
| 3.3. General workflow..... | 51 |
| 3.4. Preliminary characterization..... | 52 |
| 3.4.1. Denaturing gel electrophoresis..... | 52 |
| 3.4.2. Mass spectrometry..... | 53 |
| 3.4.3. Monodispersity analysis..... | 54 |
| 3.5. Protein conformation..... | 58 |
| 3.5.1. Synchrotron small-angle X-ray scattering..... | 58 |
| 3.5.2. Synchrotron radiation circular dichroism spectroscopy..... | 60 |
| 3.6. Protein-lipid interactions..... | 64 |
| 3.6.1. Surface plasmon resonance..... | 64 |

| | | |
|--------|---|-----|
| 3.6.2. | Differential scanning calorimetry | 66 |
| 3.6.3. | Lipid vesicle turbidimetry | 66 |
| 3.6.4. | Atomic force microscopy | 68 |
| 3.6.5. | Neutron reflectometry | 69 |
| 3.7. | Experiments performed in collaboration | 70 |
| 3.7.1. | Electron microscopy..... | 70 |
| 3.7.2. | Small-angle neutron scattering | 71 |
| 4 | Overview of results | 73 |
| 4.1. | Article I | 74 |
| 4.2. | Article II | 77 |
| 4.3. | Article III..... | 80 |
| 4.4. | Article IV..... | 84 |
| 5 | Discussion..... | 89 |
| 5.1. | Methodological considerations..... | 89 |
| 5.1.1. | Research material and quality control..... | 89 |
| 5.1.2. | Myelin basic protein, the reference molecule..... | 90 |
| 5.2. | The formation of the major dense line..... | 92 |
| 5.3. | The structure and function of myelin protein zero in peripheral myelin..... | 96 |
| 5.4. | The impact of ionic content on the activity of basic proteins | 98 |
| 5.5. | The effect of peripheral neuropathy mutations on the myelin protein zero C-terminal segment | 100 |
| 5.6. | Future considerations | 105 |
| 6 | Concluding remarks | 109 |
| | References | 111 |

Article I

Article II

Article III

Article IV

ABBREVIATIONS

| | |
|------------|--|
| AFM | atomic force microscopy |
| CD | circular dichroism |
| Cit | citrulline |
| CMT | Charcot-Marie-Tooth disease |
| CNPase | 2',3'-cyclic nucleotide 3'-phosphodiesterase |
| CNS | central nervous system |
| cryo-EM | cryogenic electron microscopy |
| Cx32 | connexin 32 |
| DLS | dynamic light scattering |
| D_{\max} | maximum dimension |
| DM | 1,2-dimyristoyl |
| DMPC | 1,2-dimyristoyl- <i>sn</i> -glycero-3-phosphocholine |
| DMPE | 1,2-dimyristoyl- <i>sn</i> -glycero-3-phosphoethanolamine |
| DMPG | 1,2-dimyristoyl- <i>sn</i> -glycero-3-phospho-(1'- <i>rac</i> -glycerol) |
| DMPS | 1,2-dimyristoyl- <i>sn</i> -glycero-3-phospho-L-serine |
| DO | 1,2-dioleoyl |
| DOPC | 1,2-dioleoyl- <i>sn</i> -glycero-3-phosphocholine |
| DOPG | 1,2-dioleoyl- <i>sn</i> -glycero-3-phospho-(1'- <i>rac</i> -glycerol) |
| DOPS | 1,2-dioleoyl- <i>sn</i> -glycero-3-phospho-L-serine |
| DPC | <i>n</i> -dodecylphosphocholine |
| DSC | differential scanning calorimetry |
| DSS | Dejerine-Sottas syndrome |
| EAE | experimental autoimmune encephalomyelitis |
| EC | epithelial cadherin |
| ER | endoplasmic reticulum |
| ESI | electrospray ionization |
| EOM | ensemble optimization method |
| GISAS | grazing-incidence small-angle scattering |

| | |
|-----------|--|
| Golli | gene in the oligodendrocyte lineage |
| GUV | giant unilamellar vesicle |
| His-MBP | myelin basic protein with a cleavable N-terminal hexahistidine-tag |
| IDP | intrinsically disordered protein |
| I_0 | forward scattering intensity |
| Ig | immunoglobulin |
| IMAC | immobilized metal ion affinity chromatography |
| IPL | intraproduct line |
| LDAO | <i>n</i> -dodecyl- <i>N,N</i> -dimethylamine- <i>N</i> -oxide |
| LUV | large unilamellar vesicle |
| MAG | myelin-associated glycoprotein |
| MALDI-TOF | matrix-assisted laser desorption/ionization time-of-flight |
| MBP | myelin basic protein |
| MBP-His | myelin basic protein with a C-terminal hexahistidine-tag |
| MDL | major dense line |
| MLV | multilamellar vesicle |
| MOBP | myelin/oligodendrocyte basic protein |
| MOG | myelin oligodendrocytic glycoprotein |
| mRNA | messenger ribonucleic acid |
| MS | multiple sclerosis |
| NLS | nuclear localization signal |
| NR | neutron reflectometry |
| OCD | oriented circular dichroism spectroscopy |
| OG | <i>n</i> -octyl β -D-glucopyranoside |
| P/L | protein-to-lipid ratio |
| P0 | myelin protein zero |
| P0ct | myelin protein zero cytoplasmic extension |
| P2 | peripheral myelin protein 2 |
| PA | phosphatidic acid |
| PC | phosphatidylcholine |
| PDB | Protein Data Bank |
| PE | phosphatidylethanolamine |
| PG | phosphatidylglycerol |
| PI | phosphatidylinositol |
| pI | isoelectric point |
| PLP | proteolipid protein |
| PMP22 | peripheral myelin protein 22 |

| | |
|----------|--|
| PNS | peripheral nervous system |
| PRX | periaxin |
| PS | phosphatidylserine |
| PTM | post-translational modification |
| QC | quality control |
| R_g | radius of gyration |
| R_h | radius of hydration |
| RNA | ribonucleic acid |
| S2 | sirtuin-2 |
| SANS | small-angle neutron scattering |
| SAXD | small-angle X-ray diffraction |
| SAXS | small-angle X-ray scattering |
| SEC | size-exclusion chromatography |
| SEC-MALS | size-exclusion chromatography-coupled multi-angle laser light scattering |
| SDS | sodium dodecyl sulphate |
| SDS-PAGE | sodium dodecyl sulphate polyacrylamide gel electrophoresis |
| SLB | supported lipid bilayer |
| SLD | scattering length density |
| SLI | Schmidt-Lanterman incisure |
| SM | sphingomyelin |
| SPR | surface plasmon resonance |
| SRCD | synchrotron radiation circular dichroism spectroscopy |
| SUV | small unilamellar vesicle |
| T_m | lipid tail phase-transition temperature |
| TEM | transmission electron microscopy |
| TFE | 2,2,2-trifluoroethanol |
| TOF | time-of-flight |
| UPR | unfolded protein response |
| UV | ultraviolet |

LIST OF PUBLICATIONS

- I Raasakka A., Ruskamo S., Kowal J., Barker R., Baumann A., Martel A., Tuusa J., Myllykoski M., Bürck J., Ulrich A.S., Stahlberg H. & Kursula P. (2017) **The Membrane Association Landscape of Myelin Basic Protein Portrays Formation of the Myelin Major Dense Line at the Molecular Level.** *Scientific Reports* 7(1):4974. DOI: 10.1038/s41598-017-05364-3.

- II Raasakka A., Ruskamo S., Kowal J., Han H., Baumann A., Myllykoski M., Fasano A., Rossano R., Riccio P., Bürck J., Ulrich A.S., Stahlberg H. & Kursula P. (2019) **Molecular structure and function of myelin protein P0 in membrane stacking.** *Scientific Reports* 9(1):642. DOI: 10.1038/s41598-018-37009-4.

- III Raasakka A., Jones N.C., Hoffmann S.V. & Kursula P. (2019) **Ionic strength and calcium regulate the membrane interactions of myelin basic protein and the cytoplasmic domain of myelin protein zero.** *bioRxiv* 529586. DOI: 10.1101/529586.†

- IV Raasakka A., Ruskamo S., Barker, R., Krokengen O.C., Vatne G.H., Kristiansen C.K., Hallin E.I., Skoda M.W.A., Bergmann U., Wacklin-Knecht H., Jones N.C., Hoffmann S.V. & Kursula P. (2019) **Neuropathy-related mutations alter the membrane binding properties of the human myelin protein P0 cytoplasmic tail.** *bioRxiv* 535013. DOI: 10.1101/535013.†

† Preprint; submitted for peer-review.

RELATED PUBLICATIONS NOT INCLUDED IN THE PHD THESIS

- V Tuusa J., Raasakka A., Ruskamo S. & Kursula P. (2017) **Myelin-derived and putative molecular mimic peptides share structural properties in aqueous and membrane-like environments.** *Multiple Sclerosis and Demyelinating Disorders* **2**:4. DOI: 10.1186/s40893-017-0021-7.
- VI Ruskamo S., Nieminen T., Kristiansen C.K., Vatne G.H., Baumann A., Hallin E.I., Raasakka A., Joensuu P., Bergmann U., Vattulainen I. & Kursula P. (2017) **Molecular mechanisms of Charcot-Marie-Tooth neuropathy linked to mutations in human myelin protein P2.** *Scientific Reports* **7**(1):6510. DOI: 10.1038/s41598-017-06781-0.
- VII Laulumaa S., Nieminen T., Raasakka A., Krokengen O.C., Safaryan A., Hallin E.I., Brysbaert G., Lensink M.F., Ruskamo S., Vattulainen I. & Kursula P. (2018) **Structure and dynamics of a human myelin protein P2 portal region mutant indicate opening of the β barrel in fatty acid binding proteins.** *BMC Structural Biology* **18**(1):8. DOI: 10.1186/s12900-018-0087-2.
- VIII Raasakka A., Linxweiler H., Brophy P.J., Sherman D.L. & Kursula P. (2019) **Direct binding of the flexible C-terminal segment of periaxin to β 4 integrin suggests a molecular basis for CMT4F.** *bioRxiv* 524793. DOI: 10.1101/524793.[†]

[†] Preprint; submitted for peer-review.

1 INTRODUCTION

1.1. MYELIN, A NERVE INSULATOR

1.1.1. THE NERVOUS SYSTEM

Humans and all vertebrates alike enjoy the luxury of a nervous system – the immensely complicated, yet organized biological network that specializes in transmitting, storing, and processing information as nervous impulses originating from internal or external stimuli, or commands from the organism itself. The nervous system is classically divided into two interconnected parts: the central and the peripheral nervous systems (CNS and PNS, respectively). The CNS is comprised of the brain and spinal cord, and functions as a mainframe to process and compile information needed for maintaining normal bodily functions, making decisions, learning and memory. The PNS connects to the CNS, and consists of sensory (afferent) and motor (efferent) nerves that encompass all other nerves in the body. The PNS is subdivided into autonomic and somatic, or voluntary and involuntary nervous systems, respectively, which control information relay between the CNS and peripheral organs, muscles, the skin, and sensory organs. Together with the CNS, the PNS forms a tremendously efficient system that allows the vertebrate to maintain normal everyday existence and respond to stimuli¹.

The most important cell type in both the CNS and the PNS is the neuron. This specialized cell is composed of (1) a soma, where the nucleus resides and the majority of cell respiration and protein synthesis occurs, (2) the axon, the only process used to relay nervous impulses towards synapses, and (3) dendrites, which are processes connecting to other neurons through synapses and act in nerve impulse reception². The axon connects to other neurons or cells of peripheral organs, and relays nerve

impulses, also known as action potentials. In these events, voltage-gated ion channels open on the axonal plasma membrane (axolemma) and cause a rapid influx of Na^+ ions from the extracellular space to the Na^+ -deficient axonal cytoplasm (axoplasm), which results in membrane depolarization and a flow of ions traveling along the axon towards the synapse due to the rapidly formed concentration gradient. The flow of Na^+ consecutively triggers opening of more Na^+ -channels on the way, increasing the amount of cytosolic Na^+ , thus allowing the action potential to propagate. The membrane is repolarized through a flux of intracellular K^+ to the extracellular milieu, followed by active Na^+/K^+ exchange through the membrane, returning the resting potential³.

In addition to neurons, both the CNS and PNS consist of several other cell types, collectively referred to as glial cells. In the CNS, this group includes microglia and astrocytes. Microglia act as immune response cells in the brain and spinal cord, where macrophages and other immune cells cannot normally enter due to the presence of the blood-brain barrier. Astrocytes carry out a myriad of roles in the CNS, including structural and metabolic support to other cell types, such as neurons. Glial cells found in the PNS include satellite cells and enteric glia. Satellite cells carry out supportive roles in sensory, sympathetic and parasympathetic neuronal clusters, whereas enteric glia have similar roles in the digestive system².

Very abundant cell types in both the CNS and PNS are myelinating glia. These cell types have several supportive roles, but most importantly they are responsible for the generation of myelin, which will be introduced in the forthcoming chapter.

1.1.2. THE STRUCTURE AND FUNCTION OF MYELIN

In the nervous system, myelinating glia produce a periodic structure called myelin, which forms a sheath by wrapping around short, adjacent segments of selected axonal regions with the main purpose of insulating them. After the initial discovery of myelin over 160 years ago⁴, the structure and function of myelin has been extensively studied and reviewed^{5, 6}. Myelin is essentially a highly specialized plasma membrane

that is wrapped around an axonal length in the order of 20-200 μm , but can be as long as 1500 μm . Several dozens or even hundreds of membrane layers are formed, which undergo protein-mediated compaction through the tight adhesion of adjacent, apposing membranes. This excludes nearly all solvent content from the cytoplasmic and extracellular compartments of myelin, and makes myelin into an incredibly lipid-rich structure, forming the basis of its insulative function⁷.

Insulation of axons results in an enhancement in action potential velocity. The underlying mechanism is relatively simple: the insulative nature of myelin blocks most of direct ionic contact with the axolemma, which prevents ionic entry and leakage to and from the axoplasm. Between evenly spaced, individual myelin units, short segments of axolemma remains unmyelinated and thus accessible to extracellular ionic content. It is at these segments, called nodes of Ranvier, where massive concentrations of voltage-gated ion channels are present, waiting for an action potential to occur. Upon channel activation, a tremendous ionic influx occurs almost instantaneously towards the axoplasm, generating membrane depolarization and a high, sudden local concentration of Na^+ , which will rapidly dissipate along the axon, until reaching the next node of Ranvier, where the effect re-occurs⁸. This fast mode of nerve impulse conduction, with a velocity of up to two orders of magnitude compared to unmyelinated axons, is called saltatory conduction. It is the product of the combined effect of myelin-mediated insulation, regularly spaced nodes of Ranvier, as well as the local concentration of voltage-gated ion channel at these nodes⁵.

Historically, myelin was thought to be merely involved in axonal insulation, but in more recent times, novel roles for myelin have been suggested and unveiled⁹⁻¹¹. Axons by themselves vary between 0.1 - 20 μm in diameter, and can be even a meter in length^{1, 12}. This makes them inherently fragile, and myelin has been shown to have a supportive role in providing mechanical strength to axons and brain matter itself¹³. Additionally, since membrane polarization in axons is actively maintained by Na^+/K^+ exchangers, axons require substantial amounts of energy in the form of adenosine 5'-triphosphate, which needs to be primarily generated through cell respiration⁹.

Recently, a supportive role of myelin by supplying substrates that can be fed to axonal metabolic pathways has been suggested, allowing axons to gain a more constant stock of chemical energy in their otherwise insulated environment^{9, 10}. This trophic support is not limited to the transfer of small molecules from myelin to the axon, but the transfer of entire proteins and even ribosomes has been documented^{14, 15}.

Myelin in the CNS and PNS carries out the same function(s), and while they structurally resemble each other, there are some notable morphological differences in myelinating glia and myelin itself. These differences will be described in more detail in the forthcoming sections, finally followed by the description of the molecular ultrastructure of myelin.

1.1.2.1. Central nervous system myelin

The myelinating cell of the CNS is the oligodendrocyte – a type of glial cell that develops and matures during embryogenesis and early post-natal life from oligodendrocytic progenitor cells¹⁶. From the oligodendrocytic cell body, several long outgrowths make contacts with axonal segments, which become enclosed in myelin. A single oligodendrocyte often myelinates axons of several neurons and can also produce multiple adjacent or separate myelin units on a single axon (Fig. 1)¹⁷. Most CNS axons that have a diameter of 0.2 μm or more are myelinated by oligodendrocytes, and the myelination is controlled through cell signaling¹⁸. Most axons in the CNS are myelinated, but those few unmyelinated axons that remain are by no means “naked”. These axons are covered in astrocytes, which harbor a maintenance role¹⁹.

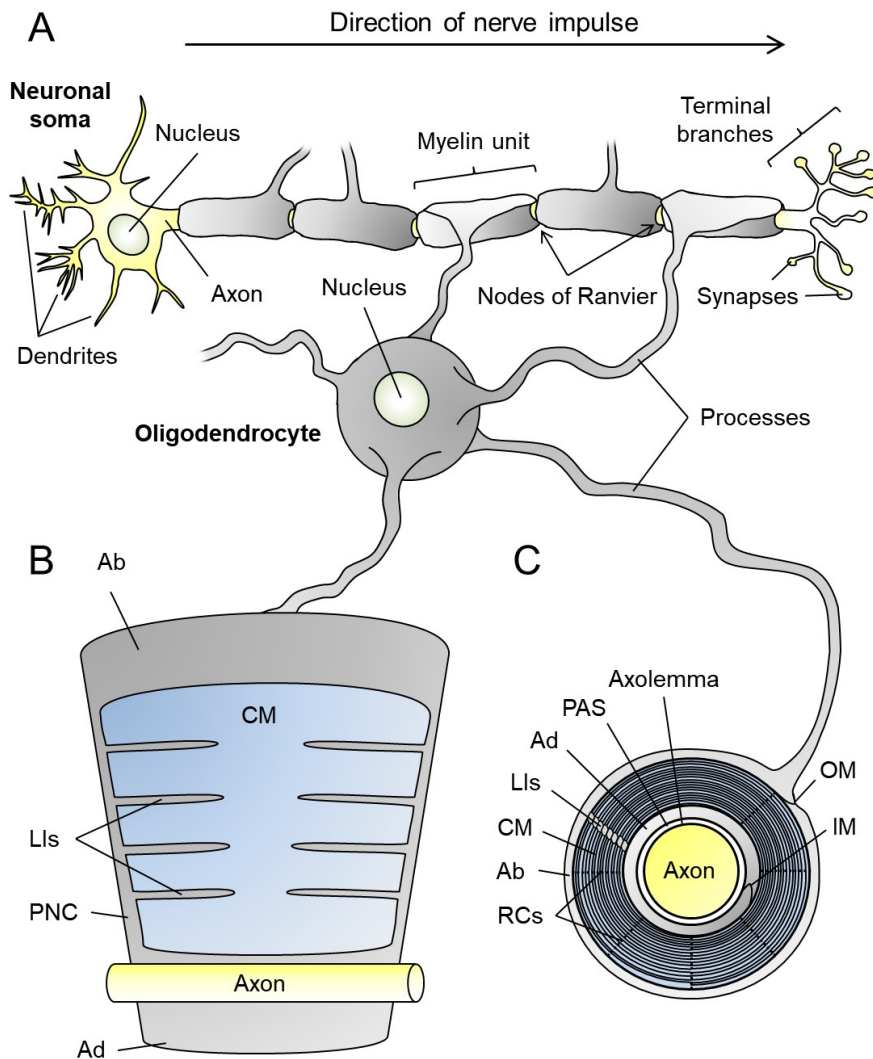


Fig. 1. Oligodendrocytic myelin sheath. (A) Schematic of a CNS neuron with its axon decorated with oligodendrocytic myelin. (B) Unrolled myelin sheath with various compartments indicated. (C) Cross section of an oligodendrocytic myelin-axon unit, with compartments and features indicated. Legend: Ab, abaxonal collar; Ad, adaxonal collar; CM, compact myelin; IM, inner mesaxon; LIs, longitudinal incisures; OM, outer mesaxon; PAS, periaxonal space; PNC, paranodal collar; RCs, radial components. Light blue and gray denote compact and non-compact myelin, respectively.

Even though myelin clearly has its benefits, one might still ask if myelin is absolutely necessary. In practical terms, insulation is the only feasible method to increase nerve impulse conduction in vertebrates, as the amount of axons and neurons that build up nerves can be immensely high. In the absence of myelin, however, it is known that nerve impulse conduction velocity does correlate with axonal diameter²⁰, and a notable example is the squid axon, which lacks a myelin sheath, but ensures efficient nerve impulse conduction by having a diameter of up to 1 mm²¹. The sheer complexity of the vertebrate nervous system seems to have favored the emergence of myelin in evolution so much that it has occurred twice: in the CNS and in the PNS²².

1.1.2.2. Peripheral nervous system myelin

PNS myelin is formed by Schwann cells, named in the honor of Theodor Schwann, who discovered peripheral myelin. The fundamental difference to oligodendrocytic myelin is that each individual Schwann cell forms a single myelin unit and as such is situated very close to the axon itself, with the Schwann cell nucleus residing on the outer edge of the myelin unit. Hundreds of Schwann cells may decorate a single axon, each separated by a node of Ranvier (Fig. 2)²³. Schwann cells are surrounded by a basal lamina – a carbohydrate-rich sheath that smoothly transitions from one myelin unit to another. This basal lamina is a specific structure of unknown function and is not found around oligodendrocytic myelin²⁴. The myelination of PNS axons seems to correlate with axonal diameter, with axons having a diameter below 2 μm being unmyelinated. The fate and amount of ensheathment is governed by the axon through signaling pathways²⁵. Unmyelinated PNS axons are still wrapped by Schwann cells, but as opposed to forming multiple layers of tight water-deficient membrane stacks, the axons only become surrounded by a non-compacted structure called amyelin, where a single Schwann cell can ensheath multiple nearby axons²⁶. However, the general consensus of axonal diameter being the regulator of myelination in the scientific community has been challenged, as axonal signaling with Schwann cells has been shown to be an important regulatory mechanism in the formation of myelin, similarly to CNS myelination²⁷.

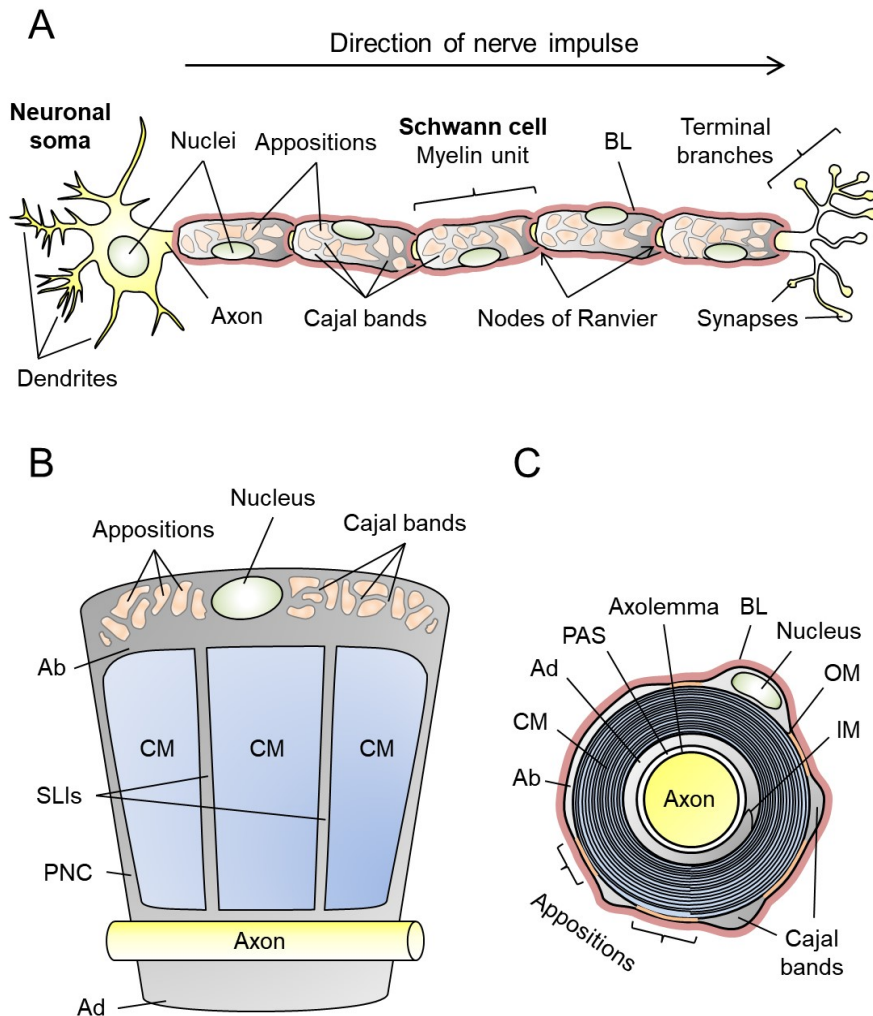


Fig. 2. Schwann cell myelin sheath. (A) Schematic of a peripheral neuron with its axon decorated by Schwann cells. (B) Unrolled Schwann cell with various compartments indicated. (C) Cross section of a Schwann cell-axon unit, with compartments and features indicated. Legend: Ab, abaxonal collar; Ad, adaxonal collar; BL, basal lamina; CM, compact myelin; IM, inner mesaxon; OM, outer mesaxon; PAS, periaxonal space; PNC, paranodal collar; SLIs, Schmidt-Lanterman incisures. Light blue and gray denote compact and non-compact myelin, respectively.

In addition to oligodendrocytes and Schwann cells, it is worth mentioning that these two cell types are often mistakenly considered the only myelinating glia of the nervous system. In fact, Schwann cell-like olfactory ensheathing cells are present both in the CNS and PNS in small numbers, specifically involved in myelinating axons of the olfactory bulb and the olfactory nerve, respectively²⁸. Additionally, a relatively new discovery of myelinating cells termed motor exit point glia seems to also extend over the boundaries of CNS and PNS²⁹. In this thesis, we will focus only on myelin originating from Schwann cells and oligodendrocytes, as those cell types are generally responsible of producing the major fraction of all endogenous myelin.

1.1.2.3. The ultrastructure of myelin

While myelination in the CNS and PNS is organized rather differently in terms of how the myelinating glia actually form myelin, the ultrastructure of a single myelin sheath is quite similar between the two nervous systems in terms of the overall structure and molecular organization. Of the total mass of myelin, less than half is water on average³⁰, and on the molecular level, myelin is mostly composed of lipids, around 70 – 85% of the dry mass, with proteins representing the remaining 15 – 30%³¹. This equals an average protein-to-lipid (P/L) ratio of 0.25, by mass, and is significantly less than in other biological membranes. For comparison, most plasma membranes have a P/L ratio of 0.7 – 1.5 by mass³², and in the mitochondrial inner membrane the P/L ratio can be as high as 3 – 4 by mass^{32, 33}. Additionally, several ionic species are present, most notably the divalent cations Ca^{2+} and Zn^{2+} , at concentrations of 1 mM and 50 μM , respectively^{34, 35}.

As illustrated in Fig. 3, a myelin unit can be longitudinally divided into three principal segments: the internode spans most of the myelin unit, and at the distal ends of the internode, the myelin membrane curves in towards the axon. This curved segment is called the juxtanode, which then transitions into the paranode, mostly consisting of the paranodal loops. The paranodes form the ends of the myelin sheath, which flank the nodes of Ranvier on either side.

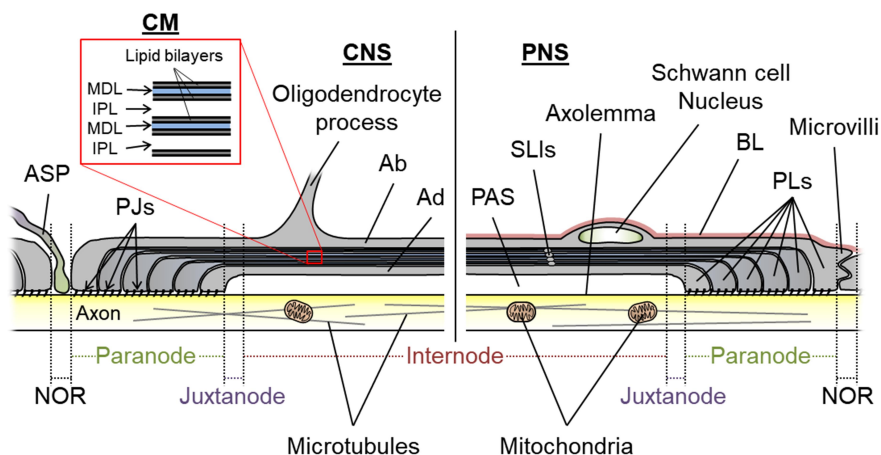


Fig. 3. Myelin ultrastructure. Schematic view of a longitudinal section of myelin in the CNS and PNS with the internode, juxtanodes and paranodes indicated. The cytoplasmic (MDL, major dense line) and extracellular/intramyelinic (IPL, intraperiod line) compartments form the periodicity of compact myelin (CM), as shown in the zoom-in (red inset). Adjacent myelin units cover the nodes of Ranvier (NOR) with microvilli in the PNS. Schwann cells are additionally shrouded by a basal lamina (BL). In the CNS, the nodes of Ranvier are covered with astrocyte processes (ASP). Non-compact myelin is shown in gray. The axoplasm is colored yellow. Most of the indicated morphological features are shared between the CNS and PNS myelin. Legend: Ab, abaxonal layer; Ad, adaxonal layer; PAS, periaxonal space; PJs, paranodal junctions; PLs, paranodal loops; SLIs, Schmidt-Lanterman incisures.

The two major morphological structures in myelin are compact and non-compact myelin, which differ from each other in appearance, function, solvent content, protein content, and subdivisions³⁶. The general architecture of a myelin sheath is fairly simple and has been illustrated in various ways in Fig. 1-3. Starting from inside, after the axolemma resides the periaxonal space – the extracellular compartment between the axon and the innermost myelin membrane known as the adaxonal membrane. Cellular communication between the axon and the myelinating glia takes place through the periaxonal space³⁷. Additionally, the myelin sheath supplies the periaxonal space with lactate and pyruvate, which can be transported to the axon for energy metabolism^{9,38}.

The adaxonal membrane encompasses the adaxonal collar, a single aqueous cytosolic compartment of non-compact myelin, where also the leading edge of the myelinating plasma membrane, the inner mesaxon, resides. This is followed by dozens of tightly stacked myelin membranes that form the bulk content of compact myelin. Moving outwards, compact myelin is followed by the abaxonal collar, another non-compact compartment of high cytosolic content³⁶. Finally, the abaxonal membrane, the outermost plasma membrane, separates the myelin sheath from the extracellular milieu. Here, the non-leading end of the plasma membrane, the outer mesaxon, is present. Additionally, the abaxonal layers in the PNS form villi that shroud the nodes of Ranvier. In the CNS, such villi are not present. Instead, the nodes are covered by astrocyte processes³⁹.

While the overall myelin architecture in the CNS and PNS is similar, the two myelin systems are not identical. There are noteworthy differences present, including the radial component and longitudinal incisures in CNS myelin, and Cajal bands and Schmidt-Lanterman incisures (SLIs) in PNS myelin. Further details about these structures, as well as compact and non-compact myelin in general, will be covered in the next chapters.

1.1.2.4. Compact myelin

Compact myelin forms the major fraction of the entire myelin sheath. As the name implies, this is the main structure containing stacked adhered membranes, which substantially decreases solvent content and provides myelin with its insulative character. Alternating between the stacked membranes of compact myelin is the cytoplasm of the myelinating cell and the enclosed extracellular compartment, also known as the intramyelinic compartment (Fig. 3). These two compartments have differences in protein content as well as their volume. Early electron micrographs already provided evidence of this periodic structure in the myelin sheath, where alternating electron-dense features and separating spaces between them could be resolved⁴⁰⁻⁴². The electron-dense feature, the major dense line (MDL), turned out to be the substantially compacted cytosolic compartment, where the two apposing

membrane bilayers are nearly fused together (Fig. 3), with a mere 3-nm spacing between them. For comparison, a single myelin lipid bilayer is typically around 4.5 nm in thickness. The space between the separate MDLs, the intraperiod line (IPL), was in fact the less compacted extracellular compartment, with a spacing of ~ 5 nm⁴³. The high periodicity of these alternating structures was discovered many decades ago, with a level of organization capable of producing a diffraction pattern, when exposed to X-rays^{44, 45}. In CNS, a unique structure is present in compact myelin, known as the radial component, which is a network of tight junctions between the myelin membranes. The radial component lacks cytosolic content, and is thought to contribute to the stabilization of the multilamellar structure of compact myelin^{46, 47}.

1.1.2.5. Non-compact myelin

Despite being the lesser myelin compartment in terms of volume and dry mass, non-compact myelin carries an essential role in myelin maintenance. In addition to encompassing various cell organelles and metabolic pathways that maintain the homeostasis of the myelin sheath, translation of all compact myelin proteins required for the stability and formation of myelin occur in non-compact myelin.

Within the abaxonal collar, vast amounts of respiration and other cellular metabolism occurs in addition to the transport of extracellular nutrients and exchange of other factors with the cytoplasm³⁸. Various cellular interactions and processes are present in the abaxonal collar and in the extracellular milieu, such as metabolic exchange with astrocytes, linking the metabolic flux towards myelinating glia to the blood stream⁴⁸. An interesting difference can be noted for the abaxonal layer between the CNS and PNS: whereas the abaxonal collar in the CNS is uniformly non-compacted, the abaxonal collar in the PNS contains membrane appositions that exclude substantial amounts of cytosolic volume. Whilst similar to compact myelin, albeit not as tight, these appositions form the morphologically distinct boundaries for non-compact myelin veins known as Cajal bands⁴⁹.

The adaxonal collar acts as a reservoir of cargo that crosses the adaxonal membrane to and from the periaxonal space, as well as factors relevant for compact myelin maintenance^{9, 38}. The paranodal collars connect the abaxonal and adaxonal collars with each other at the ends of the myelin unit. At the end of the myelin unit, the collar arranges in a longitudinal fashion around the axon and forms structures called paranodal loops. These are attached to the axon through tight paranodal junctions, separating the periaxonal space from the extracellular space⁵⁰.

In addition to the paranodal collars, cytoplasmic channels that span through compact myelin are present in myelin. Longitudinal incisures in CNS myelin are arranged along the length of the myelin unit, whereas the equivalent channels found in PNS myelin, the SLIs, are arranged transversely. These channels are filled with cytosolic content, and in wrapped myelin, these channels will stack on each other, creating a gap junction-mediated shortcut through compact myelin from the abaxonal collar to the adaxonal collar^{50, 51}.

1.2. THE MOLECULAR CHARACTERISTICS OF MYELIN

1.2.1. THE LIPID COMPOSITION OF MYELIN

Since myelin is notably rich in lipids, it is necessary to consider the lipid species present. Despite being quite different from other biological membrane arrangements in terms of morphology and total lipid fraction, the lipid species present are, surprisingly, not specific to myelin, but only enriched in certain aspects.

Around 700 different individual lipid species have been identified in myelin, which differ in terms of headgroup and fatty acid complexity⁵². In humans, the CNS myelin lipid content consists of 27.7% cholesterol, 27.5% galactosphingolipids and 43.1% phospholipids by mass. The major fraction of galactosphingolipids exists as cerebroside at 22.7% of total myelin lipid content, accompanied by sulfatides, present at around 3%. The phospholipid pool consists of the neutral phospholipids phosphatidylcholine (PC), phosphatidylethanolamine (PE) and sphingomyelin (SM), as well as the major negatively charged phospholipid phosphatidylserine (PS).

Marginal amounts of cardiolipin, phosphatidic acid (PA), phosphatidylinositols (PI), and phosphatidylglycerol (PG) are also present⁵³. Additionally, a rather large fraction of total myelin lipids is formed of plasmalogens, at around 12.3%, mostly ethanolamineplasmalogens⁵⁴. The length and saturation degree of fatty acids in myelin vary: virtually all fatty acid chains are between 16 and 22 carbons long, with 46% being fully saturated (lacking double bonds; major species are 16, 18, and 20 carbon units in length) and 54% unsaturated (major species are 18 and 22 carbons long with 1 and 3 double bonds present, respectively). The fraction of polyunsaturated fatty acids, with two or more double bonds present, is around 30%, from which around half consists of fatty acids with 22 carbons and 3 double bonds⁵⁵.

The myelin membrane is asymmetric, meaning that the two monolayers that form the bilayer have different lipid profiles. Whilst cholesterol is rather uniformly distributed in the bilayer, the outer membrane monolayer is mostly composed of galactolipids, whereas the inner monolayer is enriched in phospholipids⁵⁶. This essentially makes the outer monolayer surface covered in sugar moieties on the extracellular side, whereas the inner monolayer surface, which faces the cytoplasm, becomes net negatively charged due to the presence of PS, PI, PG, and PA. Past lipid quantifications of marmoset white matter allow us to elaborate further on the composition of the inner myelin monolayer: in healthy marmoset CNS myelin, the dominant lipid species are cholesterol at 31.6%, and the zwitterionic PC and PE at 25.9% and 29.0%, respectively. SM makes up 6.2%, whereas PS, the major negatively charged lipid, is present at 7%^{57, 58}. Given that around 12.3% of total myelin lipids are (ethanolamine)plasmalogens, one can also calculate that as much as 70% of all PE content is in fact present as plasmalogens⁵⁴. Additionally, one should note that the headgroups of phospholipids are significantly larger and more polar compared to the single hydroxyl group of cholesterol. Due to this, as well as its highly hydrophobic tail, cholesterol tends to embed deep into the membrane, causing the membrane surface on the cytoplasmic side to be almost entirely covered by phospholipid headgroups⁵⁹. Therefore, the headgroup fractions can be further calculated to be 38%, 42%, 10%, and 9% for PC, PE, PS, and SM, respectively, with the neutral zwitterionic species making up 89% of all major headgroups in the

cytoplasmic monolayer. Marmoset lipid compositions are described here, instead of human, due to the fact that demyelinating models in marmosets, more specifically experimental autoimmune encephalitis (EAE) models, have been characterized and will be further discussed in Chapter 1.3.2. Very notably, the cholesterol fraction in EAE lipid compositions is increased from 31.6% to 37.4%^{57, 58}, which is an almost 20% increase in total cholesterol amount, and in this disease model, myelin compaction is aberrant. Cholesterol is generally very abundant in myelin. In fact, endogenous free cholesterol is mostly present in myelin membranes, and only minor changes in its abundance can be tolerated, especially when its total lipid fraction is lowered; its availability is considered a rate-limiting step in myelin formation^{60, 61}.

The differences between CNS and PNS myelin in terms of lipid species are rather small. Compared to CNS myelin, the amount of galactolipids is lower in PNS myelin, and SM is present in higher amounts⁵³. This is rather important to note, since SM is known to influence the behaviour of the membrane and its lipid rafts, together with cholesterol⁶². SM has also been shown to interact with some myelin proteins⁶³. In PNS myelin, the distribution of fatty acid lengths and saturation degrees is rather similar to CNS myelin, with the single most abundant type of fatty acid being oleoyl, consisting of 18 carbon units and a single *cis*-double bond in carbon position 9. This type of fatty acid makes up over 30 mol-% of total fatty acid content in PNS myelin⁶⁴.

1.2.2. MYELIN PROTEINS

As opposed to lipids, the myelin proteome is significantly different from any other biological system. Both CNS and PNS myelin harbor only a handful of very abundant and specific proteins that are strictly localized to either non-compact or compact myelin in a manner that is at least partially driven by size exclusion⁶⁵. The proteins in these two compartments carry out various structural and functional roles, which will be only generally outlined in this chapter before focusing more on specific proteins. It is noteworthy that a general trait of myelin proteins is that their functions are rather poorly characterized, if known at all. An overview of myelin proteins and their major localization in the CNS and PNS has been illustrated in Fig. 4.

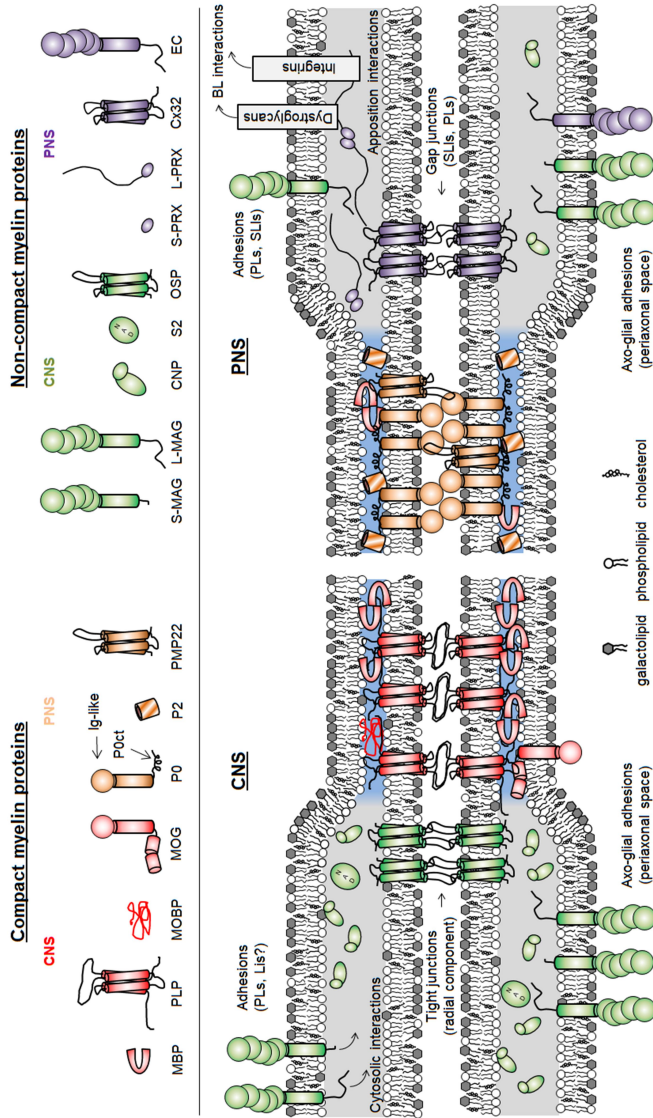


Fig. 4. Localization of myelin-specific proteins. Proteins of compact and non-compact myelin are illustrated in their compartments. Membrane binding and oligomeric states are drawn as accurately as possible. Note that some proteins are shared between both CNS and PNS myelin. Intracellular compartment is colored blue and gray for compact and non-compact myelin, respectively. The extracellular/intramyelinic compartment is white. Note that cytoskeletal elements are not included in the figure. For protein abbreviations refer to Chapters 1.2.2.1 and 1.2.2.2. Legend: BL, basal lamina; LIs, longitudinal incisures; PLs, paranodal loops; SLIs, Schmidt-Lanterman incisures.

1.2.2.1. Compact myelin proteins

As compact myelin needs to remain stable, it is enriched with structural proteins that promote membrane adhesion in both the MDL and IPL. Despite the apparent similarity of CNS and PNS myelin, they in fact contain a different assortment of proteins with little overlap.

In the CNS, the major compact myelin proteins are proteolipid protein (PLP), myelin basic protein (MBP), myelin-associated oligodendrocytic basic protein (MOBP), and myelin/oligodendrocyte glycoprotein (MOG). Of the total myelin protein mass, PLP and MBP solely make up around 50% and 30%, respectively⁶⁶. The function of the highly hydrophobic tetraspan proteins PLP and its minor splice variant 'DM20' are not entirely understood. Both are thought to be involved in oligodendrocyte maturation, and PLP is a required component for the structural integrity of myelin, likely to be involved in the formation of stacked bilayers⁶⁷⁻⁶⁹. MBP is rich in Arg and Lys, making it strongly positively charged and capable of interacting with negatively charged phospholipids. MBP has a key role in the formation and stability of compact myelin as a membrane stacker, and MBP is a key factor involved in multiple sclerosis (MS)⁷⁰. MBP is one of the principal proteins for this thesis, and will be discussed in closer detail in Chapters 1.2.2.3. and 1.3.2.1. MOBP is the third most abundant protein in CNS myelin, and like MBP, is notably abundant in cationic amino acids. Its function, however, is most likely involved in the formation of the radial component rather than MBP-like membrane stacking⁷¹⁻⁷³. MOBP, like MBP, is an antigenic protein in MS^{74, 75}, and sequence analyses have revealed a potential zinc-finger domain⁷⁶, which might have functional implications, given that Zn²⁺ is rather abundant in myelin^{34, 35}. MOG is an exclusively mammalian protein, present only on the outermost surface of oligodendrocytic myelin^{77, 78}. It is further a member of the immunoglobulin (Ig) superfamily, and contains an extracellular, glycosylated Ig-like domain, followed by a transmembrane domain and a membrane-associated cytoplasmic segment⁷⁹. While MOG is known to be involved in MS⁸⁰, its physiological function is unknown⁸¹.

In PNS myelin, the most abundant compact myelin proteins are myelin protein zero (P0), peripheral myelin protein 2 (P2), peripheral myelin protein 22 (PMP22), and MBP. A striking difference to CNS compact myelin is that the abundance of MBP is merely 5 – 18%, while the other three are present at over 50%, 15% and 2 – 5%, respectively⁸².

P0 is a 30-kDa single-pass transmembrane protein and the most abundant protein in PNS compact myelin. It is involved in membrane stacking in the IPL through homophilic interactions involving its Ig-like domain⁸³, and the molecular aspects of P0 will be explained deeper in Chapter 1.2.2.4., as well as its role in peripheral neuropathies in Chapter 1.3.2.2. PMP22 is a 22-kDa transmembrane protein with four membrane-spanning helices and is involved in the formation of cholesterol-rich lipid patches and linking the actin cytoskeleton to the membrane⁸⁴. Whilst none of the tetraspanning membrane proteins of myelin have been characterized structurally, a recent structure of claudin-15 and the subsequent construction of a PMP22 homology model have provided insights into the PMP22 conformation and potential arrangement in the myelin membrane^{85, 86}. Both P0 and PMP22 are glycosylated on the extracellular side of the membrane, and while both are integral membrane proteins confined to the lipid membrane environment, P2 is a folded, soluble protein in the cytoplasm. Discovered already in the early 1970s, P2 carries out a function in MDL membrane stacking, similarly to and in synergy with MBP, although the interesting feature remains that P2 is not ubiquitously expressed between separate PNS myelin units⁸⁷⁻⁹⁰. P2 is structurally well-characterized; crystal structures have been solved numerous times of the wild-type protein as well as mutants⁹¹⁻⁹⁷, and shown to belong to the superfamily of fatty acid-binding proteins. P2 is a 14.5-kDa protein with a β -barrel fold, topped with a helical lid segment, which is known to be involved in membrane binding in the cytoplasm. Crystal structures have supported the function of P2 as a lipid carrier in myelin maintenance. The transportation of cholesterol by P2 has also been suggested^{93, 98}.

1.2.2.2. *Non-compact myelin proteins*

Sequestered from compact myelin are the proteins present in non-compact myelin. Much different from other glia, there are factors that specifically express in these distinct compartments and co-exist with the more canonical cellular elements, often in very high levels. Non-compact myelin is involved in the maintenance of compact myelin and the axon, and includes metabolic functions as well as nutrient transport, and therefore carries a different proteome than compact myelin^{9, 99}. Additionally, some non-compact myelin proteins define the boundaries of major cytoplasmic content and tight membrane adhesions¹⁰⁰⁻¹⁰².

In the CNS, one of the most abundant proteins by far is 2',3'-cyclic nucleotide 3'-phosphodiesterase (CNPase), a member of the 2H phosphodiesterase superfamily and makes up 4% of all myelin proteins^{66, 103}. Part of the pool of CNPase is membrane-associated *via* a fatty acylated cysteine^{104, 105}, and since it interacts with filamentous actin and tubulin, it has been proposed to link the cytoskeleton to the myelin membrane^{106, 107}. This function is important in myelin, as a recent study revealed that it is this specific function that together with MBP regulates the balance between compact and non-compact myelin, which has a fundamental importance not only in insulation, but in establishing cytoplasmic channels essential for myelin maintenance¹⁰². Perhaps the most important function of CNPase is its enzymatic activity in depleting 2',3'-cyclic nucleotides from the cytosol¹⁰⁸⁻¹¹³, many of which are thought to be transported into myelin from the axon¹¹⁴. These compounds damage mitochondria, potentially to an apoptotic degree^{110, 115}, and CNPase therefore has been suggested to be essential in ensuring the long-term survival of the myelinated axon¹¹⁴. Additionally, CNPase has been shown to interact with calmodulin, much like many other myelin proteins, and potentially be involved in ribonucleic acid (RNA) metabolism and trafficking¹¹⁶⁻¹¹⁹.

Non-compact CNS myelin includes several other specific proteins, the most abundant ones including myelin-associated glycoprotein (MAG), sirtuin-2 (S2), and oligodendrocyte-specific protein (OSP, also known as claudin 11)^{66, 103, 120, 121}. MAG is present at relatively moderate levels, at 1% of all myelin proteins, and exhibits a

long (L-MAG) and a short (S-MAG) isoform¹⁰³. L-MAG has a function in establishing physical contact with the axon through the periaxonal space, by the use of its multiple Ig-like domains¹²², and L-MAG and S-MAG both are capable of interacting with several cytosolic factors with distinct selectivity between the two isoforms, as reviewed earlier^{76, 122}. S2 is a nicotinamide adenine dinucleotide-dependent deacetylase, which is involved in the deacetylation of microtubules, for instance¹²⁰. S2 has been shown to be present in myelin, and its transport to myelin is governed by the presence of PLP¹²³. OSP is an integral membrane protein that forms local tight junctions between apposed myelin membranes in the radial component¹²¹.

PNS myelin is rather different from the CNS regarding its proteome. Both MAG and CNPase are present at reduced amounts, at a mere 0.3% and 0.5%, respectively⁸². Unlike in CNS myelin, MAG is present in SLIs, both mesaxons and paranodal loops, in addition to the adaxonal membrane¹²². The most abundant protein in PNS non-compact myelin is periaxin (PRX), present as a short (S-PRX, 16 kDa) and long (L-PRX, 155 kDa) isoform, the latter harboring a nuclear localization signal (NLS) sequence and predicted to be mostly disordered^{124, 125}. S- and L-PRX, which form cytosolic homo- and heterodimers through their N-terminal PDZ domains¹²⁶⁻¹²⁸, are abundant at the abaxonal layer, where L-PRX scaffolds dystrophin-related protein 2 and integrin $\beta 4$, forming membrane appositions through a protein meshwork underneath the myelin membrane itself^{100, 129, 130}. The function of S-PRX is unclear to date, although it might have relevance in sequestering the aforementioned meshwork or blocking the nuclear export of L-PRX^{128, 131}. The exact significance of these appositions that line Cajal bands is not understood, let alone them specifically being present in PNS myelin, but the absence of PRX or dystrophin-related protein 2 abolishes the morphology^{49, 100, 101}.

One noteworthy, less abundant protein is connexin 32 (Cx32), which like other connexins is not exactly specific for myelin, but is important for its development¹³²⁻¹³⁴. This transmembrane protein is present in paranodal loops and SLIs, where it has been hypothesized to form gap junctions with the axonal membrane, contributing to the isolation of the periaxonal space and to provide a direct route for small molecule

flux through compact myelin, as well as between the Schwann cell and the axon^{134, 135}. Finally, epithelial cadherin (EC) is another low-abundance protein, which is involved in the formation of Ca²⁺-dependent homophilic adherens junctions between myelin membranes in SLIs, at the paranode, and at the outer mesaxon¹³⁶⁻¹³⁸.

One might consider myelin as a relatively simple system in terms of the proteins present and the functions they perform, given the overwhelming abundance of a relatively small collection of proteins compared to the entire myelin proteome. However, especially recent research has made it obvious that the few abundant proteins in myelin are not meant for a single task, but rather carry out multifunctional roles. These proteins include, but are not limited to, MBP, CNPase, and P2, which are very abundant in myelin^{66, 70, 76, 82, 125, 139}. Be it membrane adhesion/interaction with the myelin membrane, protein-protein interactions, fatty acid transport, or enzyme activity, it is enticing to speculate that myelin has evolved to accommodate proteins that are capable of simultaneous but functionally different tasks, or at least adapt to carry out such tasks upon need. Due to the spatial confinement of myelin, as well as its requirement to remain under stable equilibrium for prolonged times, the high expression levels of extremely long-lived¹⁴⁰, multifunctional proteins might be advantageous, as opposed to multiple proteins carrying out solely distinct tasks.

In the chapters that follow, we will focus deeper on MBP and P0, two of the most abundant compact myelin proteins in the CNS and PNS, respectively. Most of what is discussed in the current study from now on will particularly involve these two proteins and their variants.

1.2.2.3. Myelin basic protein

MBP is one of the most important and abundant multifunctional proteins in CNS compact myelin. Originally, MBP was named A1 protein after its discovery as an elongated myelin-specific protein¹⁴¹⁻¹⁴⁵. The name ‘myelin basic protein’ is more descriptive in the sense that the protein resides in myelin and has an alkaline nature, ergo, a high positive net charge. However, the name is also misleading; in fact, we

cannot consider MBP to be a single protein, but rather a heterogeneous ensemble of different splice variants that are subject to numerous post-translational modifications (PTM), although a predominant form exists endogenously¹⁴⁶.

In humans, the *Mbp* gene is located in chromosome 18 after the gene in the oligodendrocyte lineage (*Golli*), which are transcribed together into a long 179-kb RNA transcript that gets spliced into several messenger RNAs (mRNAs) encoding for a total of six known MBP protein isoforms (UniProt P02686)¹⁴⁷. Two of them consist of translated content encoded by *Golli* exons, in addition to *Mbp* exons. The remaining four are solely encoded by *Mbp* – these four are often referred to as the ‘classical isoforms’¹⁴⁸. All four undergo N-terminal processing in the form of initial Met removal and subsequent N-terminal acetylation, which are thought to occur co- or post-translationally¹⁴⁹. The Golli-MBP isoforms are less characterized non-classical MBPs, which undergo nuclear localization and bind nuclear factors that regulate gene expression¹⁵⁰. They also have been shown to regulate Ca²⁺ entry in different cell types^{151, 152}. It is probable that more classical isoforms exist in humans, based on studies on other organisms: especially mouse and rat MBPs have been extensively characterized and found to undergo similar splicing and N-terminal processing as the human protein (UniProt P04370; P02688)¹⁵³⁻¹⁵⁹. The major classical mouse MBP isoforms are listed in Table I.

Table I. Details of the major classical mouse MBP isoforms. All data is based on the sequences from UniProt P04370 (MBP_MOUSE). Isoelectric points (pI) were calculated using ProtParam¹⁶⁰.

| Isoform # | Residues* | Mass (kDa)* | pI** | Localization^{161, 162} |
|------------------|------------------|--------------------|-------------|--|
| 4 | 194 | 21.5 | 11.24 | Nucleus, cytosol |
| 5 | 168 | 18.5 | 11.14 | Cytosol |
| 6 | 153 | 17.2 | 11.75 | Nucleus, cytosol |
| 8 | 127 | 14.2 | 11.75 | Cytosol |

*Post-translational initial Met removal and subsequent N-terminal acetylation.

**PTMs are not accounted for.

The predominant isoform of all endogenous MBP in myelin, the ‘18.5-kDa isoform’¹⁴⁶, will be a major focus in this thesis. MBP is not homologous to any other known proteins, yet it is conserved among vertebrates, especially in mammals¹⁶³. As selected examples, the human and chimpanzee 18.5-kDa MBP isoforms are almost 100% identical, mouse and rat proteins both have sequence identities of 94% compared to the human protein, whereas for bovine MBP the same identity is 91%. More distantly related vertebrates, the chicken and the African clawed frog, have sequence identities of only 69% and 59%, respectively. The discussed sequences are aligned in Fig. 5. The most distantly related MBPs have been identified in cartilaginous fish^{163, 164}.

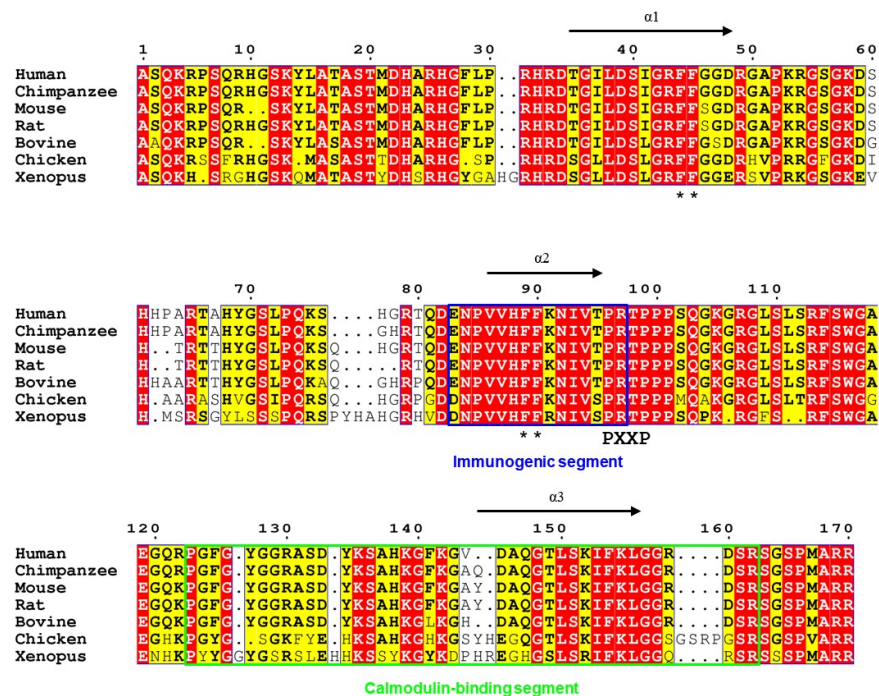


Fig. 5. Sequence alignment of selected vertebrate MBP 18.5-kDa isoforms. Selected sequences have been aligned to highlight the conservation of MBP among vertebrates^{165, 166}. Residue numbering is based on the human protein. The secondary structure labels denote the known α -helical segments of lipid-bound MBP¹⁶⁷. ‘Xenopus’ denotes the African clawed frog (*Xenopus laevis*). All sequences were retrieved from UniProt (P02686, P06906, P04370, P02688, P02687, P15720, P87346). Double Phe-motifs (**), the Src homology 3-binding motif (PXXP), the predicted calmodulin-interaction site (green) and the immunogenic segment (blue) are highlighted.

Fig. 5 displays that MBPs are abundant in Arg and Lys, which increase their isoelectric points (pI; see Table I) and give them an unusually high net charge at physiological pH. Based on the amino acid sequence of N-terminally acetylated mouse 18.5-kDa isoform, this charge is +19, and has a significant impact on the structure and functions of MBP. Free in solution, MBP has been shown to be an intrinsically disordered protein (IDP), lacking substantial secondary and tertiary structure content¹⁶⁸⁻¹⁷¹. MBP is often considered an archetypal IDP, which exists as an ensemble of flexible, dynamically interchanging conformers in solution¹⁷², rather than having defined molecular boundaries like folded proteins do^{173, 174}. The unfolded nature of MBP was already realized quite early^{142, 143} and finally accepted as a consensus when rigorous crystallization attempts for structure determination had failed¹⁷⁵. MBP is present in the stacked membranes of compact myelin (Fig. 6). Upon lipid binding, MBP gains significant amounts of folding as shown by circular dichroism (CD) spectroscopy¹⁷¹. Attempts to determine the detergent- and lipid-bound structures of MBP have been carried out using electron microscopy and modeling techniques¹⁷⁶⁻¹⁷⁸, and to this date, the best experimental structure of lipid-bound MBP is a low resolution C-shaped, folded molecule with a diameter of 5 nm¹⁷⁷, which has also been supported by small-angle X-ray scattering (SAXS) experiments on lipid-bound MBP¹⁶⁹. Modeling studies suggest that the core of this C-shaped conformation is rich in β -sheets (Protein Data Bank (PDB) ID: 1QCL)¹⁷⁸. More recently, some more elaborate experiments on MBP-derived peptides using nuclear magnetic resonance (NMR) and electron paramagnetic resonance spectroscopy been conducted to uncover helical segments and solvent exposed areas of lipid-bound MBP^{170, 179-182}. Three transient α -helical segments within MBP have been discovered in the presence of 30% 2,2,2-trifluoroethanol (TFE), a compound that decreases the dielectric nature of water, favoring spontaneous protein folding. These helices have been shown to be amphipathic when folding in the presence of lipids and detergents^{167, 183, 184}. In the computationally predicted model of MBP, none of these segments adopt a helical fold, but are specifically part of the β -sheet core, indicating that more structural studies are required to understand the conformation of MBP in myelin.

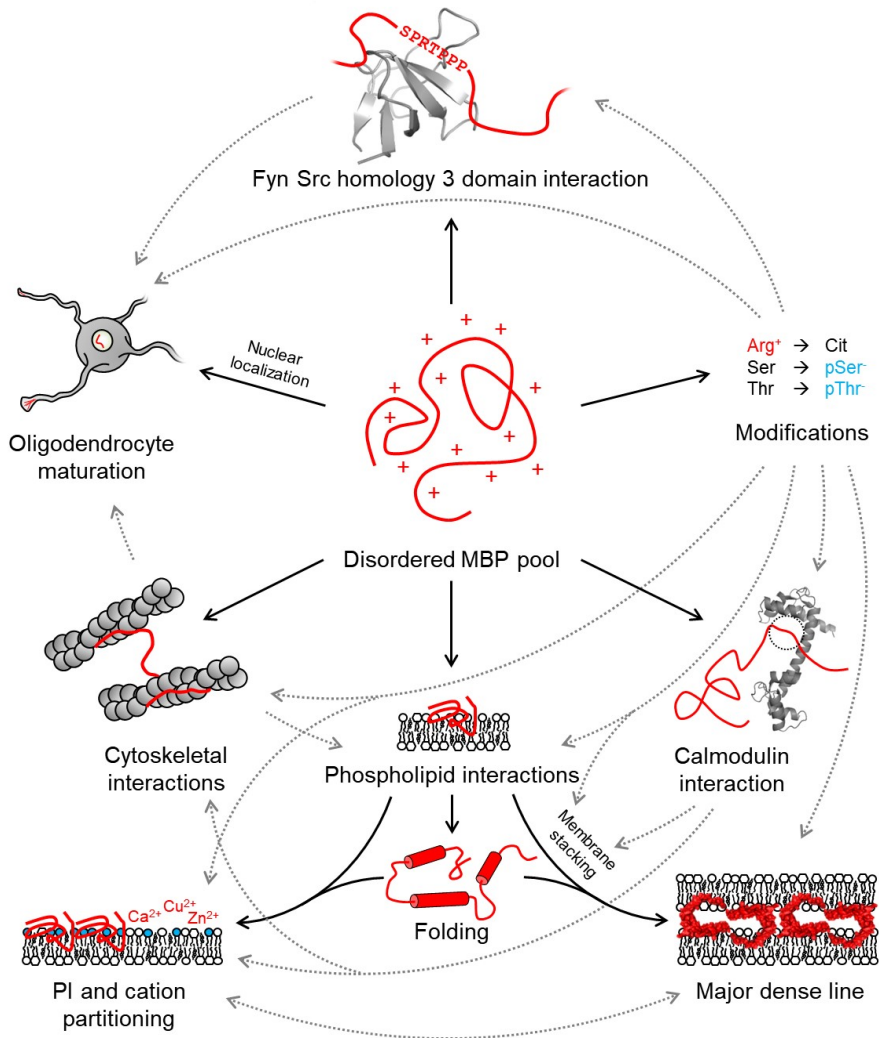


Fig. 6. The structure, functions, and modifications of MBP. MBP is multifunctional, and in its soluble disordered state takes upon many tasks. MBP and cations are drawn in red, whereas other proteins and the oligodendrocyte are drawn in gray. In modifications, Arg is colored red due to its positive charge, whereas the phosphoresidues pSer and pThr are colored blue to denote negative charge. Black arrows represent the functions of MBP, whereas gray dashed arrows represent modulation effects. Legend: PI, phosphatidylinositols. The structures of calmodulin and Fyn Src homology 3 domain are based on PDB IDs ICLL¹⁸⁵ and 4EIK¹⁸⁶, respectively. The C-shaped model for MBP is based on PDB ID IQCL^{177,178}. The figure is not exhaustive in terms of protein-protein interactions.

In addition to membrane stacking, which is the most important function regarding this thesis, MBP is multifunctional. These various functions of MBP have been illustrated in Fig. 6. Amongst many protein-protein interactions, MBP interacts with actin- and tubulin-based cytoskeletal elements, calmodulin, and Fyn kinase^{171, 187-191}. The cytoskeletal interactions affect oligodendrocyte process formation^{191, 192}, and the occurrence of certain MBP isoforms in the nucleus has been linked to oligodendrocyte differentiation, although the nuclear interaction partners of MBP are not known^{162, 193}. Additionally, MBP contains a PXXP polyproline motif (Fig. 5–6), which binds the Src homology 3 domain of Fyn kinase, an important signaling molecule in neuronal differentiation and development^{194, 195}. These functions link MBP to oligodendrocytic myelination that is clearly separate from membrane stacking. The calmodulin interaction has been shown to be Ca²⁺ dependent¹⁸⁷, having an impact on the membrane-stacking function and cytoskeletal interactions of MBP^{171, 183}. A major calmodulin binding site has been identified in the C-terminus of MBP^{188, 189, 196}, but also other sites have been proposed to be present¹⁹⁰.

More recent findings around the membrane-stacking function of MBP has been studied and reviewed extensively. The membrane stacking and involved folding of MBP are spontaneous; however, they are affected by the individual lipid types as demonstrated in several biophysical studies: the essential requirement for the association of MBP with membranes is the presence of net negatively charged lipids, namely PS and PI^{171, 197, 198}. Additionally, cholesterol and PE have been shown to enhance the binding of MBP to lipid vesicles, especially in conditions that disfavor electrostatic binding, indicating either specific molecular interactions between the lipids and the protein, or the involvement of the general biophysical properties of the membrane itself^{197, 198}. Ions, especially divalent cations, have an effect on MBP binding and membrane stack organization, likely impacting myelin formation and pathology^{199, 200}. Indeed, MBP has been shown to sequester PIs in the membrane, PI-phosphates specifically, as well as divalent cations^{201, 202}.

At the molecular level, membranes stacked by MBP in *in vitro* model systems resemble those of endogenous myelin^{89, 90, 94, 203, 204}. Especially recent experiments

have shed light on the molecular details of MBP-mediated membrane stacking: cell culture models expressing MBP have shown that plasma membranes can collapse into a myelin-like stack⁶⁵, and atomic force microscopy (AFM) studies have revealed that MBP adsorbs into net negatively charged membranes *in vitro* and eventually stacks them in a cholesterol-dependent manner^{89, 203}. Characterization of MBP bound to lipid vesicles has also been performed using X-ray and neutron scattering methods. The membrane repeat distance of MBP-adhered vesicles was determined using small-angle X-ray diffraction (SAXD) to be around 80-82 Å, depending on P/L ratio, where an increased amount of protein tightened the membrane stack⁹⁴. Recent studies have allowed a more detailed picture on this, showing that the interlamellar space between the membranes is around 35 Å²⁰⁴, which is expected considering the repeat distances observed for the MDL in endogenous myelin²⁰⁵. Additionally, the impact of temperature and the presence of P2 alter the repeat distance⁹⁰.

The arrangement of MBP within a membrane stack is thought to be very dense, existing as a protein meshwork, which is phase-separated from the surrounding solvent, as was shown through a combined approach of fluorescence microscopy, visible light microscopy, and AFM. More importantly, the arrangement seems to be governed by specific amino acids: two pairs of Phe residues were identified to be essential for the phase separation to occur in MBP charge-neutralizing conditions, as mutagenesis of these amino acids abolished the behaviour²⁰⁶. Still, some key aspects of myelination are open: how does MBP associate with a membrane at the molecular level? What is the conformation of MBP on a single membrane prior to stacking?

Finally, a notable aspect of MBP that separates it from many other proteins is the vast assortment of PTMs it undergoes, especially in higher vertebrates¹⁶⁴. In addition to co-translational N-terminal processing, including N-terminal acetylation, MBP has been found to undergo N-terminal butylation, hexylation, octylation, and decylation^{149, 207}. Other PTMs include adenosine diphosphate ribosylation^{208, 209}, Arg deimination (citrullination)²¹⁰⁻²¹³, Arg N ω -methylation and dimethylation^{214, 215}, Gln deamidation^{212, 216, 217}, Lys acetylation¹⁶⁴, Met oxidation²¹⁸ and Ser/Thr/Tyr phosphorylation^{212, 217, 219-224}. Many of these modifications alter the charge of the

targeted amino acid, and the most abundant ones are the deimination of Arg to citrulline (Cit) and the phosphorylation of Ser and Thr (Fig. 6)^{210, 212}. These modifications are thought to modulate all functions MBP harbours. As an example, Thr98 phosphorylation in the PXXP motif weakens MBP binding to Fyn kinase^{194, 222}.

The effect of citrullination is the most studied aspect of MBP modifications due to the fact that deamination of Arg, which MBP is very abundant in, irreversibly decreases the net charge of the protein. This affects the binding of MBP to phospholipids^{225, 226}, and has been suggested to potentially alter its cation-binding properties, resulting in stacked myelin membrane destabilization¹⁴⁶. The citrullination of MBP is carried out in the myelin cytosol and nucleus by peptidylarginine deiminases 2 and 4²¹³, resulting in eight charge isomers, denoted C1 – C8 with varying amounts of Cit. The C1 charge variant is completely uncitrullinated, and thus the most cationic species of MBP. C8 on the other hand is the most citrullinated and least cationic variant, containing 6 – 7 Cit residues per protein¹⁴⁶. All 18 highly conserved Arg residues of 18.5-kDa MBP (Fig. 5), have been identified as (potential) targets of deimination²¹⁰⁻²¹².

1.2.2.4. Myelin protein zero

P0, along with MBP and P2, was one of the first myelin-specific proteins discovered⁸⁷. P0 is a 30-kDa transmembrane protein of the PNS, localized into the compact myelin of Schwann cells. It has an extracellular, N-terminal Ig-like domain, a single-span transmembrane helix, and a C-terminal cytosolic extension of 69 residues (P0ct). This domain structure, and the domains themselves, are highly conserved in vertebrates (Fig. 7A). The structure of the rat P0 Ig-like domain was solved in 1996 from a soluble, truncated construct²²⁷. In 2012, the human P0 Ig-like domain was solved²²⁸, and both proteins present a typical Ig-like stacked β -sheet fold with high structural conservation. A conserved disulphide between β -strands 2 and 6 was observed and is required for the correct function of the protein in myelin (Fig. 7B)²²⁷⁻²²⁹. In humans, only one P0 isoform is considered predominant, although a stop codon readthrough has been described in mice and rats, producing an L-MPZ isoform of unknown function, which is 63 residues longer than the major isoform^{230, 231}.

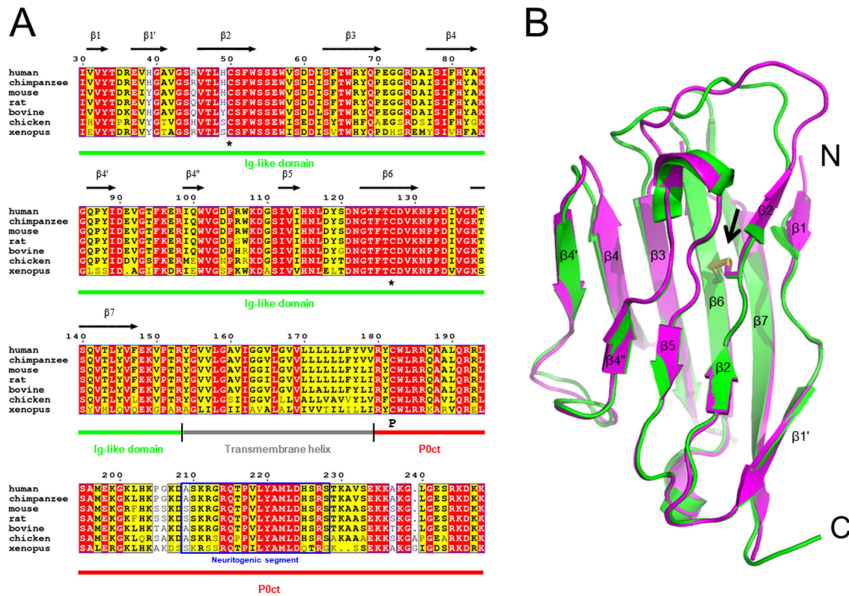


Fig. 7. Sequence alignment of selected vertebrate P0s. (A) Selected sequences have been aligned to highlight the conservation of P0 among vertebrates^{165, 166}. Residue numbering and secondary structure labels are based on the mature human protein. ‘Xenopus’ denotes the African clawed frog (*Xenopus laevis*). All sequences were retrieved from UniProt (P25189, A0A2J8JAV0, P27573, P06907, P10522, P37301, A2VD98). The conserved disulphide-forming Cys residues (*) and the palmitoylation site (P) have been indicated. The colored lines below the alignment mark the boundaries of the Ig-like domain, transmembrane helix and P0ct. The blue box indicates the known neuritogenic segment. (B) Superposition of rat (green; PDB ID 1NEU²²⁷) and human (magenta; PDB ID 3OAI²²⁸) P0 Ig-like domains with N- and C-termini highlighted. The conserved disulphide is indicated with an arrow.

When translated, P0 harbours an N-terminal 29-residue signal sequence that targets the protein to the endoplasmic reticulum (ER)²³². In this thesis, the numbering of P0 will correspond to the precursor sequence, ergo, the first amino acid of mature P0 is residue number 30 (Fig. 7). After membrane insertion and translation, the signal peptide is cleaved off, which results in mature P0. In the ER, the disulphide bond between β -strands 2 and 6 is formed, and Asn122 in the Ig-like domain is glycosylated, before P0 is trafficked to the plasma membrane²³³.

P0 is a membrane stacking protein involved in the compaction of the IPL. The Ig-like domains carry out this function by forming homophilic oligomers⁸³, and the reported PTMs in the Ig-like domain are crucial for its role as a membrane stacker^{229, 234, 235}. The oligomeric state of P0 has puzzled the field for years. Detergent-solubilized P0 has been observed to form dimers and tetramers, but the oligomeric distribution has been noted to be different between P0 from different organisms²³⁶⁻²³⁸. The crystal packing of the rat Ig-like domain provided insights into the potential mechanism of membrane stacking in the IPL, again, hinting a dimeric or tetrameric assembly, resulting in several different suggested arrangements²²⁷. However, the tetramerization of the Ig-like domain in solution was only observed at very high protein concentrations²²⁷. Additionally, the transmembrane domain of P0 has been described as a dimerizing Gly-zipper, which would contribute to the formation of tetrameric P0 assemblies²³⁹, but in the absence of further studies the true oligomerization mode of the apposing Ig-like domains remains obscure. In addition to homophilic adhesion, P0 has been shown to interact with PMP22 in the IPL. This interaction might have additional structural relevance in myelin stability^{240, 241}.

P0ct resides in the cytoplasmic compartment of myelin and is known to be essential for the stacking function of the extracellular domain in the IPL²⁴². Despite lack of homology, P0ct greatly resembles MBP in the sense that it is highly basic, with a pI value of 11.11, due to high abundance of Arg and Lys residues. Similarly to MBP, P0ct is an IDP and binds negatively charged lipids, folding in the process. P0ct has been suggested to function as an MBP-like membrane stacker in the MDL²⁴³⁻²⁴⁶. Especially the presence of cholesterol has been shown to influence the folding of P0ct, and the protein has been suggested to adopt a β -sheet-rich fold in myelin²⁴⁴. Regarding PTMs, P0ct contains a Cys residue close to the end of the transmembrane helix, which is known to be fatty acylated, most often palmitoylated^{247, 248}. The fatty acylation has been shown to be required for the proper membrane stacking function of P0²⁴⁹. P0ct also undergoes phosphorylation at Ser210, Tyr220, Ser226, Ser228, Ser233, Ser237, and Ser243²⁵⁰⁻²⁵³. Mutation of Ser228 and Ser243 blocks phosphorylation and reduces P0-mediated membrane adhesion²⁵⁴. A neuritogenic segment, corresponding to amino acids 209-228, has been identified in P0ct (Fig. 7),

which can be used to induce EAE in rodents²⁵⁵. Within the neuritogenic segment, a conserved YAML-motif, which is required for the trafficking of P0, is present²⁵⁶.

1.3. THE BIOCHEMISTRY OF (DE)MYELINATION

Myelination is the process of myelin formation and is rather poorly understood at the molecular level. The formation of the intricate periodic structure is a carefully regulated event, which requires the coordinated translation and interplay of correctly functioning proteins, as well as the presence of the correct lipids, ions, and other factors^{61, 102, 257, 258}. Successful myelination results in a mature myelin sheath, which needs to be actively maintained. The characterization of myelin at the molecular level is important, as it is the only way to understand demyelination and dysmyelination – the states of myelin destruction and abnormal formation, respectively, both of which lead to incurable diseases. In this chapter, the function of selected myelin proteins in myelination, myelin stability, and disease will be introduced, with emphasis on MBP and P0.

1.3.1. MYELINATION

The cell signaling involved in myelination has been reviewed earlier^{17, 36, 51, 259-261}, but what induces myelin maturation at the biochemical level is still slightly obscure. Nevertheless, progress in this aspect has been made, as a recent study unveiled the central role of actin disassembly in myelin compaction²⁵⁷. This is a logical mechanism, as the MDL is obviously too narrow to accommodate major cytoskeletal structures, but changes in oligodendrocyte process growth requires actin filaments in myelin wrapping²⁶². The regulation of myelin protein expression is carried out by factors like Unc-51-like kinase 4. Hypomorphic mice of this putative kinase developed hypomyelination in the CNS and 40 – 60% lowered transcription and expression levels of the normally very abundant myelin proteins, including CNPase, MAG, MBP, MOBP, MOG, OSP, PLP, S2²⁶³.

The membrane-stacking function of MBP and its regulation in the CNS are pivotal in the formation of compact myelin, as MBP is one of the first proteins to be translated during myelin compaction, even before the most abundant CNS compact myelin protein, PLP²⁶⁴. Clearly MBP orchestrates CNS myelination, but how does MBP exactly stack membranes *in vivo*? It is known that the mRNA of MBP is transported along microtubules to the peripheral processes of oligodendrocytes, and translated in the vicinity of the membrane when compaction occurs²⁶⁵⁻²⁷⁰, which is presumed to be enabled by stimulation by axonal electrical signals²⁷¹. The molecular mechanisms by which MBP actually induce stacking are unclear, although several theories and final stacked arrangements have been proposed based on studies reviewed above^{70, 182, 272, 273}.

The importance of MBP is well demonstrated by its absence, which has an effect on CNS myelination. This is evident from autosomal recessive mouse models, harboring spontaneous MBP-deficiency, termed *shiverer* mice based on their phenotype to ‘shake’ involuntarily. On the cellular level, the phenotype manifests as dysmyelination – the abnormal formation and reduced amounts of myelin – in the CNS, while PNS myelin remains unaffected²⁷⁴. The effect is related to the formation of the MDL, which in MBP-deficient mice does not properly compact^{275, 276}.

The role of P0 in PNS myelination is rather different from MBP. P0 is basally expressed in Schwann cells already before myelination occurs, regardless of whether a Schwann cell is destined to form myelin or amyelin²⁷⁷. Upon myelination, the expression levels of P0 have to be carefully regulated, as overexpression of P0 has been shown to end myelination prematurely²⁷⁸. Nevertheless, the absence of P0 does result in an aberrant myelin phenotype, which cannot be rescued by overexpression of PLP, the most abundant CNS compact myelin protein^{279, 280}.

1.3.2. DEMYELINATION

Loss of myelin mass and/or function can occur through demyelination or dysmyelination. Demyelination is the destruction of the myelin sheath after its

formation, whereas dysmyelination is the abnormal formation of myelin. Both demyelination and dysmyelination can arise from genetic reasons^{281, 282}, but especially demyelination can involve several other factors as well, such as autoimmunogenic events²⁸³, abnormalities in mitochondrial function^{284, 285}, and mechanical disruption such as traumatic brain injury²⁸⁶. Demyelination and dysmyelination not only disturb myelin and its function, but can also contribute to axonal degeneration²⁸⁷. In this chapter, two of the most abundant demyelinating disorders are presented on a general level, followed by discussing the proteins involved in these diseases.

1.3.2.1. Myelin basic protein and multiple sclerosis

MS is a chronic autoinflammatory disease of the CNS, in which nerve impulse conduction velocities decrease substantially due to demyelination, manifesting as a spectrum of neurological problems: numbness, weakness and pain of the limbs, double vision, loss of vision, fatigue, dizziness, tremors, lack of coordination, and speech issues²⁸⁸. Patients suffering from MS might experience several of these symptoms together in a progressive manner, with symptoms becoming worse over time, or a relapsing-remitting manner, with symptoms re-occurring as attacks and disappearing for periods of unpredictable length. At the histological level, demyelination causes lesions, scarring of nerve tissue. MS is the most common neurological disease within the age group of 20 – 40 years, where the disease usually onsets²⁸⁹.

While the possible causes of MS are largely debated, MS patients often display only some of all known symptoms, making the treatment of MS difficult and often personalized. There is no known cure for MS, and patients remain affected for life. The demyelination in MS is at least partially considered to be of autoimmunogenic origin, either caused by T-cells that manage to cross the blood-brain barrier, or by CNS microglia. These immune cells destroy myelin due to myelin factors mistakenly being recognized as threats, decreasing axonal insulation and saltatory conduction^{290, 291}. The recognition occurs by macrophages expressing class II major

histocompatibility molecules that can bind specific myelin proteins and/or peptide segments²⁹².

Numerous myelin-specific proteins have been identified as autoantigens in MS, including CNPase, MAG, MBP, MOBP, MOG and PLP^{74, 75, 211, 293-300}. Several peptide segments of these proteins have been shown to be autoantigenic when injected to animals, causing EAE^{301, 302}, and many EAE animal models have subsequently been used as MS disease models to study the molecular basis of the disease^{57, 302, 303}.

The involvement of MBP in MS has been studied for decades, and multiple aspects of MBP-mediated autoantigenicity have been suggested. In its physiological state, MBP should remain lipid-bound between the myelin membranes, but several factors can cause MBP to 'escape' and become recognized by the immune system^{292, 304}. Indeed, an immunogenic segment within MBP and the critical residues required for antigenicity have been identified and structurally characterized, in which the segment assumes an extended conformation (Fig. 8)³⁰⁵⁻³⁰⁹. These residues are Glu85 – Arg99 in human MBP, and the segment is highly conserved (Fig. 5). Residues 82 – 91 in mouse MBP are likely to be folded as an α -helix when MBP is membrane-bound¹⁸⁴. The roles of citrullination and phosphorylation are rather central, as heavy citrullination reduces the cationic nature of MBP and thus its membrane-binding tendency, potentially allowing dissociation and interaction with the immune system²²⁶. In mouse MBP, Thr92 and Thr95 within the immunodominant segment are known phosphorylation sites that influence membrane binding when phosphorylated³¹⁰. These residues match Thr95 and Thr98 in human MBP, respectively.

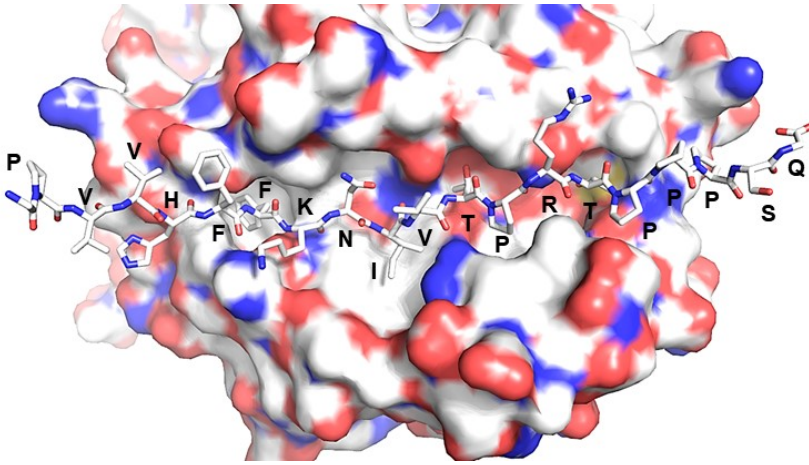


Fig. 8. Molecular recognition of the immunogenic segment of MBP. Crystal structure of major histocompatibility complex class 2 crystallized with the autoantigenic segment of MBP (PDB ID 1FV1³⁰⁸). Residues Pro85 – Gln103 of human MBP have been indicated in the figure from left to right.

Another autoimmunogenic aspect to consider is the proteolytic degradation of myelin proteins, including MBP, resulting in immunogenic peptides. MBP in its unbound state is disordered, and hence an attractive target for proteolysis³¹¹, and MBP has even been reported to undergo autoprolysis³¹². On the other hand, modified MBP-derived peptides have been explored as potential treatment candidates for MS, due to their antagonistic properties in EAE³¹³⁻³¹⁹. The inflammatory peptide recognition of MBP could arise from molecular mimicry, as several immunogenic MBP peptides share sequence and folding similarities to peptides of pathogenic origin, like the human immunodeficiency virus (HIV)³²⁰⁻³²⁴. Recognition of such MBP peptides could therefore trigger inflammation, which normally would occur in the event of a viral infection. This has also been observed in the opposite direction, where HIV patients display MS-like symptoms and produce antibodies against MBP³²⁵.

In EAE/MS models involving MBP, aspects surrounding lipid composition and cellular environment have also been studied: the cytoplasmic lipid composition in EAE-marmosets is altered²⁰⁴, and aberrant phase behaviour of the lipids has been

reported^{55, 57, 204}. Such phase behaviour can be modulated by ionic strength²⁰⁰, and these two factors together could be speculated to drive the progression of MBP release and/or degradation. Understanding how MBP and the other factors mentioned above are involved in MS etiology at the molecular level is necessary for designing novel treatments and remedies.

1.3.2.2. Myelin protein zero and peripheral neuropathies

Charcot-Marie-Tooth disease (CMT) is a peripheral neuropathy and the most common inherited neurological condition, with a prevalence peaking at 1 in 2500. CMT exhibits a broad spectrum of symptoms, including numbness and tingling sensations in limbs, fatigue, weakness, pain, muscle spasms, loss of muscle mass and very commonly arched feet, which is considered a hallmark for the disease. The disease onset varies broadly. Some experience their first symptoms in early childhood, while others reach an age of 40 years before any symptoms surface³²⁶.

CMT occurs due to PNS demyelination and sometimes due to related axonal degeneration. Unlike MS, CMT has a strong genetic component associated to it, and is not an autoimmune disease affecting oligodendrocytes, but a demyelinating condition in which the integrity of Schwann cell myelin decreases and axonal function slows down or fails due to lack of insulation and trophic support³²⁷.

Several subtypes of CMT exist, denoted CMT1, CMT2, CMT4, CMTX, and dominant intermediate CMT, which are further subcategorized with letters (CMT1A, CMT1B, etc.). The various categories enclose differences in the affected proteins, specific mutations (including deletions, duplications and point mutations), and in dominant, recessive or X-linked heritability. These include, but are not limited to, the myelin proteins Cx32, P0, P2, PMP22, PRX, DRP2 and several mitochondrial proteins, implying that mitochondrial dysfunction can also result in CMT in addition to common factors from compact and non-compact myelin^{328, 329}. Mitochondrial dysfunction is also evident in the case of two Pt-containing anti-cancer drugs, carboplatin and *cis-platin*³³⁰, from which the latter is known to bind mitochondrial

DNA and as such could cause a CMT-like peripheral neuropathy as a side effect³³¹. CMT can therefore be induced by defects in structural proteins relevant for myelin structure and by the disruption of myelin and/or axonal maintenance through mitochondrial dysfunction.

One subtype of CMT, Dejerine-Sottas syndrome (DSS; historically CMT3), is characterized as a severely disabling form of CMT that onsets very early in life and causes major muscle degeneration due to lowered nerve conduction velocity. Treatments for CMT and DSS are symptomatic, and the diseases are currently deemed incurable³²⁶.

Specific mutations in P0 account for demyelinating autosomal dominant CMT1B, axonal dominant CMT2I, DSS, and other CMT-like peripheral neuropathies^{332, 333}. Most individual mutations, and the most common ones, occur in CMT1B. These mutations in P0 are mostly localized in the Ig-like domain, but several also exist in P0ct^{251, 332, 334}: T216ER³³⁵, D224Y^{334, 336}, R227S³³², and the deletion of Lys236 (K236del)³³⁷ are connected to CMT1B, K236E³³⁸ occurs in CMT2I, and A221T³³⁹ occurs in DSS together with V42del, which resides in the Ig-like domain. The P0ct mutations have been illustrated in Fig. 9.

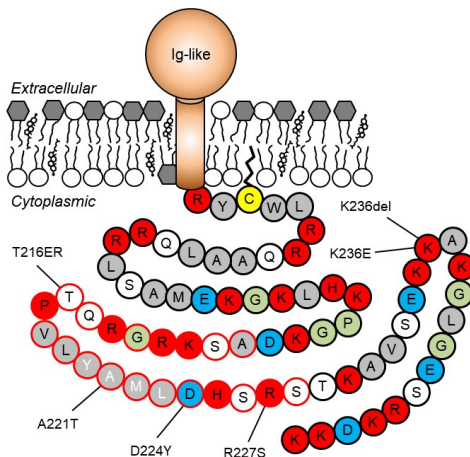


Fig. 9. P0ct mutations. P0 has been drawn in its membrane-bound state with P0ct shown as individual residues. Color coding signifies residue characteristics: red, basic; blue, acidic; gray, non-polar; white, polar; green, Gly and Pro; yellow, Cys. The fatty acyl PTM has been drawn on Cys182. The YAML motif is indicated with white letters and the neuritogenic segment is indicated with a red line color. The Ig-like domain, transmembrane helix and P0ct are not drawn in scale relative to each other.

The effects of many of the mutations in the Ig-like domain or P0ct are not known. The mutations could disturb membrane stacking by affecting the folding of P0, its homophilic adhesion, or its other interactions. Additionally, some mutations have been proposed to induce ER stress and the unfolded protein response (UPR)³⁴⁰. Interestingly, one specific mutation in the Ig-like domain has been shown to introduce a new glycosylation site³⁴¹. Most of the mutations mentioned above are involved in demyelinating phenotypes, but D224Y is a clear outlier as it has been connected to a hypermyelinating CMT1B phenotype, with unusually thick compact myelin³³⁶. The molecular details of mutation-induced myelin malformation are not understood, which also hinders the development of general remedies for peripheral neuropathies.

2 AIMS OF THE STUDY

The study of myelin-related proteins in solution and in native-like environments can be challenging due to the involved physical attributes: hydrophobicity, highly positively charged proteins, low water content, high content of certain ionic species, and intrinsic protein disorder⁷⁶. As MBP and P0 are highly abundant CM proteins in CNS and PNS myelin, respectively, their thorough characterization in lipid-rich conditions is necessary. While numerous past studies have amassed data for MBP regarding its various functions^{70, 342}, the same cannot be stated for P0ct, for which only a few studies have been published²⁴³⁻²⁴⁵. To understand the biochemical foundation of myelin in health and disease, further studies are required for both proteins.

The primary object of this project was to establish a collection of biophysical, cross-complementary methods, suitable for the study of recombinantly produced MBP, P0ct, and other proteins alike. The reasoning behind the chosen methods was to obtain quantitative data for several sample aspects, which allow the description of protein interaction mechanisms, affinities and rates with lipid structures of various compositions, as well as the involved effects on protein folding, dispersity, and potential membrane stacking. A key component of the study was to involve methods that remain independent of using tags, antibodies, or other modifications on the studied proteins and lipids, but rather follow intrinsic biophysical attributes of the analytes. MBP, a protein already characterized earlier, was to be used as a reference protein to test and optimize the methods at hand, and P0ct was chosen as a novel protein, which had been characterized before only to a lesser extent.

The secondary object of this project was to subsequently use the established method workflow to study the role of MBP and P0ct in myelin stability, formation, and disease. Both proteins were to be characterized in different lipid compositions and ionic contents, to gain an insight into which molecular determinants can affect their functions, and to what extent. Additionally, since P0ct is known to be a fundamental player in the disease etiology of peripheral neuropathies, mutant variants of P0ct were to be studied using the same workflow, once one had been established for the wild-type protein.

The expected outcome of the project was to efficiently take advantage of strong cross-complementation of various methods, with the possibility to apply the obtained characterization strategy in future studies involving the same proteins, or physically/functionally similar ones. The application would require only minimal working habit adjustments in screening through different conditions, for instance. Additionally, the project was expected to provide novel information on the molecular structures and functions MBP and P0ct, thereby providing novel structural aspects of myelin stability and formation in general.

3 MATERIALS AND METHODS

In this chapter, experimental procedures used to obtain all relevant data for this thesis are presented, with a focus on background principle, usage, sample requirements, and data analysis. Protein, peptide and lipid preparations are also outlined briefly – more detailed information on all experiments can be found in **Articles I – IV**. Only the relevant experiments that were performed by the author of this thesis are presented in high detail, together with some relevant collaborative studies, which were crucial for the outcome of the study (Chapter 3.7).

3.1. RECOMBINANT PROTEIN PREPARATION

The proteins used in the study were produced using recombinant methods. Bacterial expression plasmids prepared in Gateway vectors (Invitrogen) were available prior to the start of this study. These plasmids encoded for an MBP construct corresponding to the mouse 18.5-kDa isoform (UniProt ID: P04370-5) with a cleavable N-terminal hexahistidine-tag from the pTH27 vector³⁴³ (His-MBP) used in **Articles I** and **III**, and a P0ct construct corresponding to the 69 C-terminal amino acids of human P0 (UniProt ID: P25189-1) with a cleavable N-terminal His-tagged maltose-binding protein (pHMGWA vector^{343, 344}), used in **Articles II, III** and **IV**. Additionally, a plasmid from earlier studies^{171, 345}, encoding for an MBP construct with an uncleavable C-terminal Leu-Glu linker and His-tag (MBP-His) in a pET22b(+) vector (Novagen) was used in **Article I** for nanogold labeling of transmission electron microscopy (TEM) samples.

Detailed expression and purification procedures are described in **Article I** for His-MBP and MBP-His, and in **Article II** for P0ct. In short, the expression of all proteins was carried out in LB medium at 37 °C using 0.4 – 1.0 mM isopropyl β -D-1-thiogalactopyranoside induction for 2-3 h with constant shaking. After expression, the cells were collected by centrifugation and re-suspended in suitable lysis buffers, followed by purification or storage by freezing. The purification of His-MBP was carried out using immobilized metal ion affinity chromatography (IMAC) in denaturing conditions, followed by His-tag removal using selective proteolysis³⁴⁶ and a second IMAC step, and finally by a size-exclusion chromatography (SEC) step in a non-denaturing buffer to ensure monodispersity and removal of soluble aggregates. MBP-His was expressed and purified in a similar manner using IMAC, with the exception of omitting subsequent His-tag removal, and instead dialyzing the protein into a non-denaturing buffer prior to SEC. The reasoning behind the initial denaturing purification steps was the fact that both His-MBP and MBP-His were expressed in an insoluble state. The denaturing buffer allowed solubilization of the proteins and the final purity of the proteins was enhanced due to the lower presence of degradation products and contaminating proteins.

In the case of P0ct, all purification steps were performed in non-denaturing conditions. After the initial IMAC step and proteolytic affinity tag cleavage, the protein mixture was either subjected to sequential SEC runs, or the His-tagged maltose-binding protein was removed using an amylose resin affinity step, prior to SEC. A second IMAC step was deemed impossible since cleaved P0ct was found to have strong affinity for the resin even without an affinity tag (data not shown).

After purification, the obtained cleaved recombinant MBP composed of 170 amino acids (ProtParam¹⁶⁰: 18544.7 Da; pI = 11.14), corresponding to the full 169-amino acid sequence of mouse 18.5-kDa MBP isoform, with an additional N-terminal Gly residue remaining from the tag cleavage. The obtained MBP-His behaved similarly to His-MBP in IMAC purification and SEC, and as such would be composed of 177 amino acids (ProtParam¹⁶⁰: 19552.8 Da; pI = 11.00), but had undergone N-terminal

initial Met removal³⁴⁵, which resulted in a 176-residue protein with an experimentally determined molecular weight of 19421.6 Da.

The obtained P0ct, on the other hand, contained 70 amino acids (ProtParam¹⁶⁰: 7990.3 Da; pI = 11.11), corresponding to residues 180-248 of the human P0 precursor, again with an additional N-terminal Gly. P0 is known to undergo palmitoylation at Cys182^{247, 248}, which would be unlikely to occur in bacteria during expression. Therefore, this residue in P0ct had been deliberately mutated into a Leu, which is a bulky hydrophobic residue that partially mimics a fatty acid moiety and increases the local hydrophobicity in the protein chain. Additionally, the mutation deletes a chemically reactive residue, which could otherwise result in unwanted disulphide-mediated dimers or other oxidized molecular species, as IDPs are known to easily form dimer artifacts that can influence downstream experiments³⁴⁷.

Related to the neuritogenic segment within P0ct²⁵⁵, a synthetic peptide corresponding to the sequence (P0ct_{pept}; NH₂-ASKRGRQTPVLYAMLDHSRS-COOH) was ordered from GenScript and used in **Article II** for folding studies.

In **Article IV**, a total of six CMT and DSS mutations^{332, 334-339} were generated directly in the P0ct expression construct using site-directed mutagenesis, and the six mutant protein variants were expressed and purified in an identical manner to wild-type P0ct. The introduced mutations resulted in the following single amino acid changes: T216ER, A221T, D224Y, R227S, K236E and K236del.

3.2. LIPIDS AND DETERGENTS

The experiments presented later in this study involved the use of various lipids and detergents. Synthetic chemicals were used as opposed to natural extracts whenever possible to gain strict molecular control over different experimental conditions. This allowed testing of specific molecular attributes when determining the functional nuances of the proteins.

To study protein binding to lipids, membrane stacking and protein folding, several chemical aspects were compared: lipid headgroup charge, lipid tail saturation, and the presence of selected lipid species known to be present in myelin. Mixtures of mostly PC, PG and PS headgroups were used to assess the effect of electrostatic forces on the studied proteins and their functions, and additionally, two different lipid tail settings were chosen for checking the effect of fatty acid saturation: 1,2-dimyristoyls (DM) and 1,2-dioleoyls (DO). The following lipids formed the basis of the experimental material: 1,2-dimyristoyl-*sn*-glycero-3-phosphocholine (DMPC), 1,2-dimyristoyl-*sn*-glycero-3-phospho-(1'-*rac*-glycerol) (DMPG), 1,2-dimyristoyl-*sn*-glycero-3-phospho-L-serine (DMPS), 1,2-dioleoyl-*sn*-glycero-3-phosphocholine (DOPC), 1,2-dioleoyl-*sn*-glycero-3-phospho-(1'-*rac*-glycerol) (DOPG), 1,2-dioleoyl-*sn*-glycero-3-phospho-L-serine (DOPS) (Fig. 10A). To compare lipid tail saturation, the DM- and DO-based lipids were chosen for two reasons. Firstly, DO-based lipids, which are abundant in myelin, have their gel-fluid transition temperature (T_m) below 0 °C, and they will always remain in the liquid disordered phase at ambient temperatures. The chosen DM lipid mixtures in most cases can also be brought to the same phase at reasonable temperatures around 25–30 °C, as opposed to 1,2-dipalmitoyl- or 1,2-distearoyl-based lipids that have very high T_m values. Secondly, since DO-based lipids have a *cis*-double bond in carbon position 9, they will be kinked in the middle, essentially reducing the thickness of the bilayer. Bilayers of DOPC and DMPC are roughly the same thickness in the liquid disordered phase at 30 °C, which rules out artifacts in protein function arising from bilayer thickness itself^{348, 349}. In addition to these general lipids and their mixtures, we chose to include other lipids as well, most notably 1,2-dimyristoyl-*sn*-glycero-3-phosphoethanolamine (DMPE), a mixture of SMs, and cholesterol (Fig. 10A-B). PEs, SMs, and cholesterol are all abundant lipids in myelin, and the two latter are known interaction partners of one another and of myelin proteins^{62, 63}. They are also known modulators of membrane phase behaviour^{62, 350, 351}.

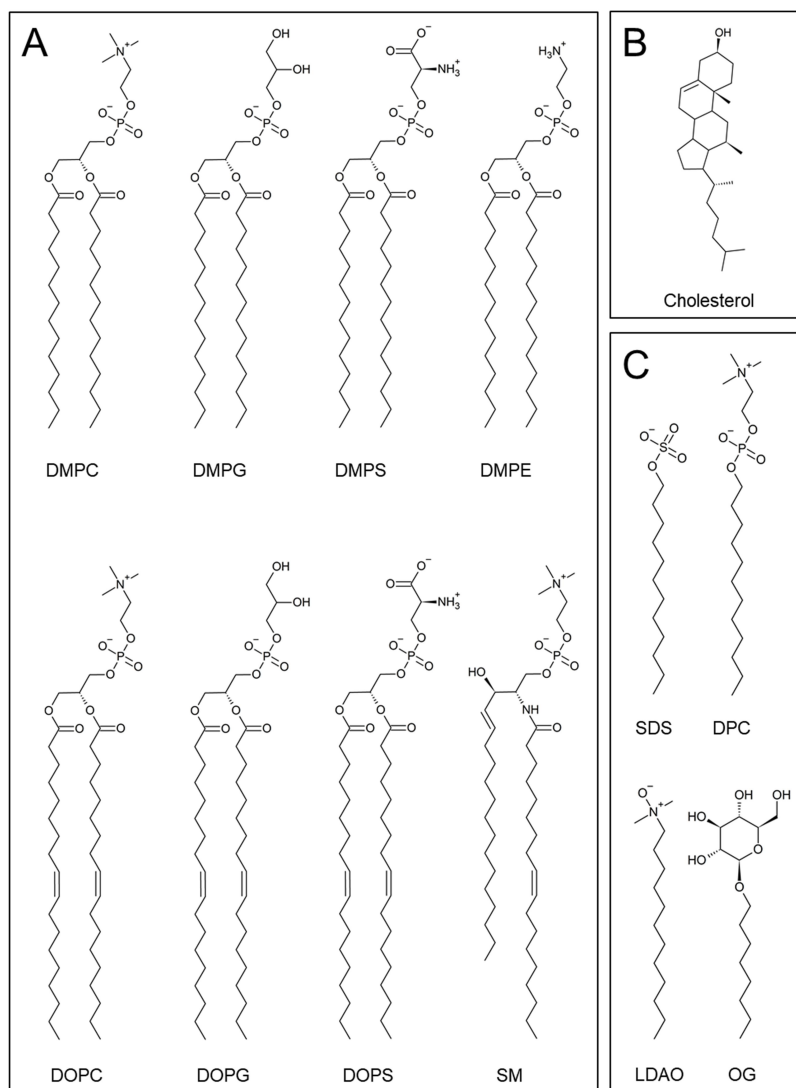


Fig. 10. Detergents and lipids. (A) The phospholipids used in this study varied with respect to their headgroup complexity and charge (PC, PS, PG and PE), as well as lipid tail saturation (DM and DO). The structure of SM is representative with regard to its fatty acyl chain (here drawn as an oleoyl group), as the used SM was a natural extract containing a mixture of several molecular species. (B) Cholesterol was the only sterol used in this study, being the major sterol compound present in myelin membranes. (C) The used detergents were mostly different in headgroup complexity, although OG also had a shorter hydrocarbon tail compared to SDS, DPC and LDAO. For simplicity and when applicable, all lipids and detergents have been drawn without their counter ions they were purchased in.

With the intention of eventually expanding into more physiologically relevant materials, well-behaving model lipid mixtures were initially used. DOPC:DOPS (1:1) was chosen as a base lipid composition, as DO-based lipids are abundant in myelin, and an equimolar amount of PC and PS typically can be used to form small and large vesicle structures that repel each other and do not fuse into larger structures rapidly. To compare the saturation degree, we chose DMPC:DMPG (1:1) for three reasons: (1) this lipid mixture, whilst PG is not as physiologically relevant as PS, is net negatively charged, and forms small vesicles that remain stable in size. (2) DMPC and DMPG both have a T_m around 23 – 24 °C, as opposed to DMPS ($T_m = 35$ °C)³⁵², meaning that their phase behaviour is similar and the transition between the gel phase and fluid phase can be performed at near-ambient temperatures, ensuring protein stability over long periods of time. Finally, (3) as mentioned above, DMPC and DOPC in their fluid phases have very similar lipid bilayer thicknesses^{348, 349}. In this case, the fluid phase has to be considered rather than the gel phase, as DOs remained always in the fluid phase due to all experiments being performed above their T_m . With these points at hand, protein activity in the two lipid mixtures would be mostly governed by fatty acid saturation degree, although the chemical difference between PS vs. PG headgroups could influence binding as well. For the latter, given the equimolar ratio in the mixtures, the specific headgroup complexity was expected to play a minor role in contrast to the total net charge of the chosen lipids. In vesicle aggregation studies, DOPG was initially used instead of DOPS, to gain a better comparison.

It is noteworthy that myelin contains more PE than PC⁵³, both of which have a net neutral charge. Again, PCs were chosen as the major lipid species instead of PEs for two reasons: (1) PEs are mostly present as plasmalogens⁵⁴, and the tail complexity adds another variable to the lipid mixture. We simplified the system to contain only one type of hydrocarbon tail per lipid mixture, with the exception of SM, which could only be obtained as a natural extract, being of heterogeneous composition. (2) In the case of DMPC vs. DMPE, if we consider the T_m values of PC, PE and PS, PE has a significantly higher T_m value (~50 °C)³⁵² as opposed to the other two that melt close

to ambient temperature. With these arguments at hand, PCs were chosen as the net neutral lipid species.

In the current study, both vesicles and supported lipid bilayers (SLB) were used as model systems. Vesicles can essentially be divided into multilamellar vesicles (MLV) and unilamellar vesicles, of which the latter can be further divided into small (diameter <100 nm; SUV), large (diameter 100 – 200 nm, LUV), and giant unilamellar vesicles (diameter >1 μm ; GUV)³⁵³, based on their average size. In this study, GUVs were avoided as they are complicated to prepare in large scale for biophysical studies. The true power of GUVs lies more in methods capable of observing them directly, such as fluorescence and light microscopy³⁵⁴.

To ensure proper lipid mixing, and a subsequent homogeneous lipid composition in the generated vesicles, lipids are typically dissolved and mixed in chosen molar or mass ratios using organic solvents, such as chloroform, methanol, or mixtures thereof. After a desired lipid composition has been obtained, the organic solvent is evaporated using a nitrogen stream, followed by freeze-drying for several hours under vacuum. In the current study, lipid mixing was always performed in glass vessels to avoid plastic contamination in the obtained dry lipid films. After drying, vesicle formation can be induced by swelling the dry lipid film in water or in a chosen buffer, by gentle inversion over time at a temperature above the T_m . Vortex mixing the suspensions breaks down large structures, which can be further subjected to freeze-thaw cycles by immersing to a liquid N_2 bath and a warm water bath, with a temperature above the T_m . Here, the largest lipid structures burst, but the suspension remains heterogeneous in terms of vesicle size and the amount of enclosed lamellae³⁵⁵. MLVs, however, can be useful in some methods: if a method like differential scanning calorimetry (DSC) is used to probe for changes in the behaviour of lipids, due to the fact that MLVs are multilamellar, and thus not completely accessible to the used proteins, they can contain an 'internal standard' of intact bilayers for comparative reasons. On the other hand, in such cases, it is imperative to assess several independently prepared lipid batches in the chosen experiment to avoid artifacts that arise from batch heterogeneity, as MLVs generally are very heterogeneous.

Unilamellar vesicles can be prepared in several manners, all of which have their advantages and drawbacks. In this study, we generated LUVs of an average 100-nm diameter using syringe extrusion through polycarbonate filter membranes. SUVs, on the other hand, were formed using either strong water bath sonication or tip sonication, while avoiding excessive heating, forming vesicles with a diameter below 100 nm on average³⁵⁶.

SUVs were used in most experiments due to their easy preparation procedure, also maximizing total accessible surface area for proteins and retaining accurate sample lipid concentration. LUVs, on the other hand, were only used in surface plasmon resonance (SPR) measurements, since extrusion through the membrane filters any solid particles out from the suspension. The drawback of extrusion is a decrease in the lipid concentration in the suspension. This is not a major issue in SPR, as the accurate concentration of immobilized lipids on the sensor chip is not very important, as long as surface saturation is reached. Regarding SUVs, their concentration remains known after the procedure, assuming that the lipids do not undergo degradation due to elevated temperature, and that the lipids do not oxidize due to introduction of dissolved O₂ in the solvent. Additionally, when using SUVs, it is important that the method of interest does not suffer from a slightly wider vesicle size distribution, as opposed to using LUVs.

After vesicle formation, the vesicles were stored unfrozen for a maximum of 1 week for DO-based lipids and 2 weeks for DM-based lipids, to avoid any artifacts induced by lipid oxidation or degradation. In practice, vesicles were used as fresh as possible in each experiment, and 'base level' samples were measured in most cases, especially during CD measurements, to ensure that the lipids and proteins work as intended. These base level samples, in all cases, were MBP and P0ct in the presence and absence of DMPC:DMPG (1:1) or DOPC:DOPS (1:1).

Several approaches in SLB generation exist as well. SLBs can be formed by spontaneously bursting vesicles on a solid surface (also known as a 'substrate'), often in the presence of Ca²⁺ and salt – a useful approach for AFM, as AFM can distinguish between single and stacked membranes, as well as membrane-free areas, therefore

overcoming the inherent heterogeneous limitations arising from this SLB generation method⁸⁹. Another approach is to dry vesicles on a solid surface and slowly rehydrate them in an atmosphere of high relative humidity, often in the presence of saturated K_2SO_4 at 30 °C. This way, depending on lipid amount, multistacked membranes arise, which can be advantageous for spectroscopy, albeit the structures in a macroscopic scale are heterogeneous³⁵⁷.

Preparation of a single continuous bilayer is also possible, and the gold standard as a preparation method is Langmuir-Schaefer dipping. In this method, lipids in organic solvents are gently dispersed on a wave-free aqueous reservoir. When the solvent evaporates, the lipids orient themselves on the air-water interface, with lipid headgroups pointing down against the solvent and tails pointing up in the air. The area, where the lipids are dispersed, can then be compressed using barriers that prevent the surface lipids from escaping, which essentially increases the molecular surface pressure. At the so-called collapse point, the lipids will form a stable monolayer, and if a suitable substrate is pulled in a vertical geometry through this monolayer from underneath, while maintaining constant surface pressure, a lipid monolayer can deposit on the surface of the substrate³⁵⁸. This process is referred to as Langmuir deposition. After this, the coated substrate can be rotated into a horizontal orientation, where the deposited lipid monolayer inversely faces the monolayer on the reservoir surface, and a Schaefer dipping procedure can be performed: the coated substrate is gently lowered through the surface of the reservoir, and the two lipid monolayers will come together and form a continuous lipid bilayer³⁵⁹.

In this study, Langmuir-Schaefer dipping was used for neutron reflectometry (NR), where the obtained bilayer-coated SiO_2 substrate was assembled into a fluid cell, which retains the aqueous solvent within, and can be further used for sample injections into the cell³⁶⁰.

In addition to lipids, the effects of several detergents on the proteins were studied (Fig. 10C). Above critical micelle concentrations, detergents self-assemble into micelle structures in aqueous solutions. Thus, they lack the complexity of the numerous lipid phases, which are discussed later in more detail. However, detergents

can be useful in their simplicity: while they mimic strong membrane curvature and headgroups that resemble those of certain lipid species, the fact that they retain their size and shape can be useful when proteins tend to disturb lipid phases naturally. Detergents are enough lipid-like to bind proteins and induce conformational changes that would occur during lipid binding, which makes detergents very useful as control substances in probing certain, simplified conditions. Micelles are useful in probing the effect on proteins induced by micellar size, which is also related to surface curvature, as well as the polarity, charge, and complexity of the detergent headgroup³⁶¹.

Detergents used in this study include sodium dodecyl sulphate (SDS), *n*-dodecylphosphocholine (DPC) and *n*-dodecyl-*N,N*-dimethylamine-*N*-oxide (LDAO), which all share the same fully saturated 12-carbon dodecyl tail, but differ from one another in either headgroup complexity and net charge. SDS is negatively charged in aqueous solutions, whereas DPC and LDAO are zwitterionic. In DPC, the oppositely charged phosphate and choline moieties are fairly separated from one another, whereas in LDAO, the two charges are adjacent, essentially neutralizing their electrostatic effects. Additionally, *n*-octyl β -D-glucopyranoside (OG), which has a bulky, polar headgroup that is uncharged in solution and a slightly shorter 8-carbon tail, was included in the study (Fig. 10C). The ultimate goal was to exploit the detergents in probing for changes in protein conformation in the presence of the different headgroup chemistry, without inducing the formation of complex lipid structures that have been reported earlier for MBP, for instance²⁰⁴.

3.3. GENERAL WORKFLOW

In order to reach the aims of this study, a plan for a general experimental workflow was established, illustrated in Fig. 11. Optimization experiments prior to this work had been performed for the relevant proteins, which allowed direct advancement to protein expression and purification to obtain enough research material. After initial protein purification was completed, series of experiments were performed to learn about the general stability and quality of the produced proteins. This initial characterization contained methods that ensured quality control (QC) over subsequent purifications, which was not only important to achieve unbiased data, but to also retain reproducibility between different protein purification batches.

After this, the experimental focus was shifted to more elaborate methods, which were used to study (1) the conformation, (2) the lipid binding and membrane insertion, (3) the putative membrane stacking properties of the chosen proteins, using synthetic model lipid mixtures and detergents.

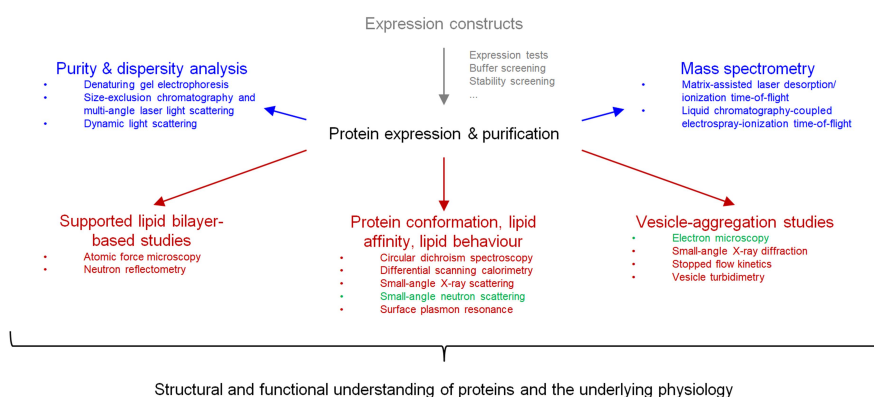


Fig. 11. Outline of general workflow. Protein constructs, expression, purification and optimization thereof had been performed prior to this study (gray). Preliminary characterization (blue) was a QC step used to verify the identity and proper stability of the purified proteins. Various functional and structural characterization experiments (dark red) were carried out afterwards, providing the vast majority of the relevant experimental data. Some experiments for this work were carried out through collaborations (green).

3.4. PRELIMINARY CHARACTERIZATION

Preliminary characterization of proteins was performed to describe their stability, purity and monodispersity in solution, prior to more sophisticated experiments. In order to gain unbiased data in the main experiments, the purified recombinant proteins were subjected to QC to learn about their behaviour in general or at the moment after completion of purification. Several of the methods introduced here are essentially cross-complementary with each other, as well as with more advanced methods described later.

3.4.1. DENATURING GEL ELECTROPHORESIS

Gel electrophoresis of proteins under denaturing conditions is commonly performed towards the positive anode using a polyacrylamide stationary phase and a mobile phase containing high amounts of dissolved glycine, SDS and a slightly alkaline buffer. The method is commonly known as SDS-polyacrylamide gel electrophoresis (SDS-PAGE)³⁶². The method is by far one of the most globally used ones to check protein purity during recombinant protein purification, but it is also useful for other purposes. Virtually any sample that contains one or more proteins can be analyzed using SDS-PAGE, and in this thesis, it was mostly used to verify the adequate purity (>95%) of recombinant proteins for downstream experiments. While SDS-PAGE most often cannot be used to analyze monodispersity, except in rare cases of SDS-resistant oligomers, it does provide an accurate image about the quantitative distribution of *e.g.* a protein and its degradation products, as well as any other contaminants. Additionally, after electrophoresis and band visualization, the separated protein bands can be isolated, and used further to identify the proteins within a single band using mass spectrometry, as explained in Chapter 3.4.2.1.

When performed correctly, denatured SDS-bound proteins will travel a distance through the stationary phase, which is inversely related to the \log_{10} of their molecular weight, and by comparing to a standard sample of proteins with known masses, it is easy to estimate the molecular weight of each well-separated protein band.

3.4.2. MASS SPECTROMETRY

3.4.2.1. Peptide fingerprinting

The identity of unknown proteins can be analyzed using peptide fingerprinting: a denatured protein is treated with the protease trypsin, which has a very defined proteolytic specificity only cutting after Arg and Lys residues that do not border a C-terminal Pro. A trypsinated protein forms a mixture of ‘tryptic peptides’ with defined amino acid compositions. The peptide mixtures can be dried on a solid substrate with a suitable matrix compound, like α -cyano-4-hydroxycinnamic acid. The peptides in this sample are then ionized and their masses and relative abundances determined using matrix-assisted laser desorption/ionization time-of-flight (MALDI-TOF) mass spectrometry. The obtained mass spectrum is a ‘tryptic fingerprint’ of the protein, and based on the protein sequence, the relative abundance and mass of each tryptic peptide can be theoretically calculated and compared to the measured mass spectrum to identify the protein of interest. An unknown protein can also be identified, if a sequence database, *e.g.* the Mascot Server³⁶³, is used for comparison.

A typical sample for peptide fingerprinting is an SDS-PAGE polyacrylamide gel piece with a stained protein band. Due to the sensitivity of mass spectrometers, only marginal amounts of proteins are needed for the analysis. The proteins in the gel piece can be destained using an organic solvent and reduced with mercaptans. Subsequent Cys alkylation using α -iodoacetamide irreversibly prevents spontaneous Cys oxidation. The gel piece is then dried using organic solvents and incubated in a trypsin solution that digests the protein. Tryptic peptides can be extracted from the gel piece under acidic conditions and directly analyzed using MALDI-TOF mass spectrometry.

In this thesis, the identities of purified MBP (**Article I**), P0ct (**Article II**) and the P0ct mutants (**Article IV**) were verified from SDS-PAGE gel pieces.

3.4.2.2. *Protein mass determination*

A common misconception is that the entire mass of a single protein can be determined from a tryptic peptide fingerprint. This is untrue, but luckily, mass spectrometry is not only limited to peptides – it can be used to determine the masses of undigested proteins. This is particularly useful when one is interested in oxidation, degradation, or other covalent modifications. Electrospray ionization (ESI)-coupled time-of-flight (TOF) mass spectrometry is useful in this sense: ESI is a rather gentle ionization method that does not fragment ions as they are brought to the vacuum phase for TOF analysis. ESI, however, does ionize proteins with multiple charges per chain, and therefore, the TOF analysis will not provide a single mass per charge ratio signal, but several of them, which can be back-calculated to reveal the true mass of each mass species. Additionally, since ESI essentially depletes solvent content from around the analyte proteins, it is of high likelihood that protein molecules present themselves as ion adducts from residual salt in the sample solution. This can be avoided by including a desalting step prior to ionization. However, if the resolution of the mass analyzer is high enough, this might not present a problem, as proteins with ion adducts can be resolved from the ion-free proteins.

In this thesis, ESI-TOF was used to check the integrities and expected masses of MBP, P0ct and the P0ct mutants in **Articles I, II** and **IV**. ESI-TOF was performed after a high-performance liquid chromatography-coupled desalting step, from which the output was directly injected to the mass analyzer. Sample requirements for the analysis were generally very small, only around nanomolar protein concentrations in analysis volumes ranging between 1 – 5 μ l, before the chromatography step.

3.4.3. MONODISPERSITY ANALYSIS

3.4.3.1. *Size-exclusion chromatography*

SEC is a chromatography method that separates particles based on their hydrodynamic radius (R_h). A sample of dissolved particles is pushed through a gel bed matrix using an isocratic flow. This gel bed is most often composed of

carbohydrate-based beads that contain a porous matrix of defined size. Small molecules may enter the matrix, which retains them longer in the gel bed, as opposed to large particles that cannot enter the beads and simply bypass them. Hence, particles become sorted based on their size in the gel bed, large particles eluting faster than small ones³⁶⁴.

SEC is useful for a number of different applications. Firstly, it can fractionate a complex sample, separating different oligomers of a protein from one another, or a protein from its degradation products or other contaminating proteins. Secondly, soluble aggregates, which are immensely large compared to individual protein particles, will exit the column material first in the so-called void volume, the volume that is completely excluded from the bead pores. Therefore, removal of soluble aggregates from the protein of interest is very efficient using SEC. Thirdly, SEC can be used to exchange the protein buffer solution quantitatively, either for downstream applications or for improved stability. During protein purification, SEC is the ideal last step after other chromatographic stages for all three reasons described above³⁶⁴. Finally, since SEC separates based on R_h (which, for globular proteins, is strongly related to molecular weight), analytical SEC can be used to estimate the mass and oligomeric state of a protein in solution, if a series of standard proteins are analyzed as well. Disordered proteins behave slightly differently in SEC, as their R_h is larger than those of globular proteins, appearing larger in a SEC run. Additionally, SEC can be useful in studying protein-protein or protein-nucleic acid interactions, or in quantifying the relative abundance of molecular species in solution, for example.

SEC was used in all protein purifications throughout the thesis work to gain monodisperse protein samples. Additionally, and more importantly, SEC was used in an analytical setting to display the monodisperse nature of MBP and P0ct in **Articles I and II**, prior to subsequent experiments, as well as for comparing P0ct mutant variants to the wild-type protein in **Article IV**.

3.4.3.2. *Multi-angle laser light scattering*

If a protein sample is effectively fractionated using SEC, the observed protein peaks will momentarily be monodisperse, given high protein purity within the sample. SEC can be coupled with multi-angle laser light scattering (SEC-MALS), which introduces an analytical method that records the time-averaged scattering of monochromatic laser light at different angles. The magnitude of the scattered signal scales with the mass of the particle and can be normalized by concentration, which allows the determination of the absolute molecular weight of the particle. The concentration of the eluted protein at a given time can be determined by measuring ultraviolet (UV) absorbance or the refractive index of the solution³⁶⁵.

SEC-MALS is very useful in determining the oligomeric state of a protein in solution, and to complement SAXS data. This is particularly true for more complex mixtures with interchanging oligomeric states. Additionally, if several concentration determination sources are used, for instance UV spectroscopy and refractometry, conjugation analyses for detergent-bound membrane proteins or protein-nucleic acid complexes can be performed. With these methods, the mass fractions of each molecular species within a monodisperse peak can be obtained³⁶⁶. As opposed to regular SEC, SEC-MALS is not limited by protein conformation, and the masses of disordered proteins can be accurately determined.

An important sample requirement is a pure protein sample in solution, or at least a sample that will fractionate into separate peaks within the used SEC material. Additionally, a matching background buffer needs to be chosen as the mobile phase, which has to be extensively degassed to remove dissolved air, especially if refractive index measurements are used as a concentration source. These requirements are used to ensure a flat baseline in the chromatograms. The required protein amount per sample varies with molecular weight, large proteins scattering more light than small ones. For P0ct, a protein expected to be ~8 kDa in mass if monomeric, 250 µg of total protein was used in **Article II** in a single SEC-MALS run to gain a light scattering signal providing reliable molecular weight determination.

3.4.3.3. *Dynamic light scattering*

Dynamic light scattering (DLS; also known as quasi-elastic light scattering) is a method that measures scattered monochromatic laser light by particles that diffuse in solution due to Brownian motion. The scattered light, depending on the positions of the diffusing particles over time, can undergo either constructive or destructive interference, which manifests as time-dependent intensity fluctuations of the scattered light. These fluctuations can be described as an autocorrelation function, which can be used to solve the diffusion coefficient of the particle. The rate of diffusion of a particle depends on the size of the particle, solvent viscosity, and temperature. Therefore, given that the latter two parameters are known, the size of the particle, more importantly the R_h , can be solved based on the diffusion coefficient, using the Stokes-Einstein equation³⁶⁷.

DLS is complementary to SEC(-MALS) in determining the monodispersity of protein samples, especially the presence of aggregation. Additionally, DLS can complement SAXS data (see Chapter 3.5.1.), as R_h and the radius of gyration (R_g) obtained using SAXS are related. The R_g/R_h ratio can be used to predict if a protein deviates from globularity: a ratio of 0.77 is ideal for a globular particle, whereas an increased ratio over 1.00 suggests significant elongation or a disordered chain³⁶⁸.

A typical DLS sample is a protein solution with a concentration close to 1 mg/ml, and depending on the used cuvette, 10 – 50 μ l sample volume is required. Due to the sensitivity of DLS to the presence of large particles (*e.g.* dust), samples should be either centrifuged or filtered prior to measurements.

In this thesis, DLS was used to determine protein R_h and monodispersity, particularly the absence of aggregates, in MBP and P0ct samples (**Articles I and IV**).

3.5. PROTEIN CONFORMATION

The conformation of proteins can be considered on several distinct levels: the primary structure refers to the sequence of the covalent amino acid chain. Secondary structures denote local changes induced by intramolecular hydrogen bonding, such as changes in dihedral angles of protein chains seen in helical structures, β -sheets, and random coil. Tertiary structure describes the overall fold of a protein chain, regardless of secondary structure, at its energy minimum: This most often involves collapsing into a globular conformation. Finally, quaternary structure is the homo- or heterogenic association of one or more proteins, respectively, which together form a physiologically functional unit.

In this thesis, the tertiary and secondary structures of proteins were examined using SAXS and synchrotron radiation circular dichroism spectroscopy (SRCD), respectively.

3.5.1. SYNCHROTRON SMALL-ANGLE X-RAY SCATTERING

SAXS is the measurement of the total X-ray scattering of a sample on an area detector, usually from an incident beam with a monochromatic wavelength (λ). In these measurements, the scattering intensity is recorded at small scattering angles (θ) with regard to the incident beam, hence the name small-angle scattering. Radial averaging of this data will produce a scattering curve, which is defined as recorded intensity on the Y-axis as a function the momentum transfer vector (s) on the X-axis, which has a unit of \AA^{-1} or nm^{-1} :

$$s = \frac{4\pi \sin \theta}{\lambda}$$

This also means that the recorded scattering is inversely related to resolution, and since scattering data at small θ angles are collected, SAXS essentially is a low-resolution method³⁶⁹.

In the case of a monodisperse protein sample, total sample scattering can be recorded, and the scattering fraction of a matching buffer reference can be subtracted, resulting

in the isolated scattering profile of the protein itself. Since X-ray scattering from proteins is fairly low in intensity compared to the solvent, high concentrations of proteins (2 – 5 mg/ml) need to be used to record scattering data with high accuracy. This is especially true for small proteins, as the scattering of X-rays scales with molecular weight. Thus, the presence of aggregates is a major issue in SAXS measurements, as their molecular weight compared to the particle of interest is generally very large³⁷⁰.

Since synchrotron SAXS involves an intense hard X-ray beam, eventual radiation damage to the sample is expected, which can change its scattering properties. Therefore, several frames of short illumination periods of the sample are collected, compared and averaged. In case of frames showing scattering artifacts from radiation damage, the affected frames are discarded from the averaging. In case of a radiation damage-resistant sample, low sample concentration can be compensated by acquiring more frames for averaging, resulting in better scattering statistics.

Many choose to use SAXS to measure and analyze the tertiary and quaternary structures of proteins in isotropic solutions, which can greatly complement crystal structures, CD spectroscopy, NMR spectroscopy and EM^{369, 371, 372}. Since the measurements are done in solution, the obtained data often represent the true individual oligomeric and conformational states of the monodisperse scattering particle, being independent of artificial states induced by *e.g.* crystal packing. The obtained scattering curve can be subjected to Guinier analysis, which provides useful parameters, such as the forward scattering intensity, I_0 , directly related to particle molecular weight in solution, and the radius of gyration, R_g , which is the average distance of all scattering entities within a single particle from its mass center. Thus, R_g is a measure of particle size and shape in solution³⁷³. Kratky analysis is useful for proteins in particular, as the shape of the rearranged scattering curve, the Kratky plot, easily reveals the major conformational states of the protein. Kratky analysis can be used to describe whether a protein is folded or extended³⁷⁴.

The shape of the original scattering curve can be used to extract a size distribution of the scattering particle, which can reveal the presence of ordered domains as well as

the maximum dimension (D_{\max}) of the particle³⁷⁵. As SAXS is often used to complement other structural methods, several modeling approaches exist for modeling globular particles from measured SAXS data, some of which use D_{\max} as a starting parameter^{376, 377}. However, as SAXS measures the average scattering from the entire sample over time, it can be also used to study the distribution of different conformationally interchanging particles in solution. This is useful for disordered proteins, since using advanced ensemble optimization modeling (EOM) approaches, the distribution of sizes in a conformational ensemble can be estimated, and compared in different conditions and between different proteins^{347, 378, 379}.

In this thesis, SAXS was used as a control method to characterize MBP, P0ct, and P0ct mutants in **Articles I, II** and **IV**, to compare their size, oligomeric state and conformation in solution. EOM was used to analyze and model conformational flexibility in the samples, in addition to more classical *ab initio* modeling approaches^{379, 380}.

3.5.2. SYNCHROTRON RADIATION CIRCULAR DICHROISM SPECTROSCOPY

3.5.2.1. *Isotropic samples*

Chiral molecules exhibit different absorption properties between left- and right-handed circularly polarized light, compared to achiral molecules or racemic mixtures of chiral molecules. The measured absorption difference between the two polarizations is called circular dichroism (CD), which can be determined for a sample using CD spectroscopy. This is useful for studying proteins, for which most amino acids are chiral and absorb left- and right-handed circularly polarized light differently, depending on their dihedral angles. The total contribution of these angles, which also make up regular secondary structures, affect the differential absorption spectrum for a given wavelength range, which is usually between 170 and 280 nm for far-UV CD measurements.

CD is semi-quantitative, albeit exploiting the method of SRCD, not suffering from diminished light flux at shorter wavelengths, allows to reach nearly quantitative

levels^{381, 382}. Generally, CD and SRCD are considered methods to check for the overall presence of protein folding, but their power lies in probing the folding differences between different sample conditions. This is especially useful for proteins that present a notable gain in regular secondary structure content upon binding to lipids or other molecules that induce folding³⁸³.

The drawback of CD is that the applied light tends to get absorbed by high concentration of different ions and compounds. Certain compounds are considered CD-compatible, and the most commonly used ones are inorganic phosphate as a buffer, and F^- as an anion to increase ionic strength, typically obtained by including KF or NaF in the solution³⁸⁴. Lipids can be troublesome as well, not to mention protein-induced lipid aggregation, which generally decreases protein CD signals³⁸³. Some lipids, like cholesterol, even have a strong intrinsic signal in CD³⁸⁵. Similarly to SAXS measurements, a CD spectrum of a single sample is often acquired as several scans to check for sample stability over the CD measurement, as some proteins are sensitive to temperature- or UV light-induced aggregation, denaturation or degradation. In case the scans overlay with each other, they are averaged to reduce overall noise in the spectrum.

A background CD spectrum is measured and subtracted from the sample spectrum to correct for the background CD contribution as well as instrumental contributions. The obtained CD units, expressed in millidegrees, are converted to a more suitable unit by taking into account protein concentration, the molecular weight, and the number of amino acid residues. Additionally, the pathlength of the cuvette is taken into account. One of the commonly used units is $\Delta\epsilon$, expressed in $M^{-1} \text{ cm}^{-1}$, which can be directly derived from the Lambert-Beer law. $\Delta\epsilon$ describes the difference in the molar absorption coefficients per residue for left and right handed circularly polarized light at a given wavelength. Software tools have been developed to streamline this analysis^{386, 387}.

The shape of the far-UV CD spectrum contains information about the regular secondary structure elements in the studied protein, most notably between random coil, α -helices and β -sheets. For detailed information refer to a review by

Greenfield³⁸⁴, but briefly put, random coil exhibits a strong negative signal peaking at 198 nm, whereas α -helical structures generate a strong positive peak at 192 nm and two negative peaks of similar magnitude at 208 and 222 nm. β -sheet structures generally produce a signal strength lower than that of the two other secondary structures, and they present a single positive peak at 196 nm and a single negative peak at 216 nm. Mixed secondary structure content blends features from all of the above features, and it is important to note that the largest difference between random coil and folded secondary structures occurs around 185 – 210 nm, making this area of the spectrum very sensitive to changes in secondary structure content. These wavelengths are very short, and thus susceptible to noise arising from sample/background absorption or low photon flux. Here, the use of short cuvette pathlengths and synchrotron light is highly advantageous.

In this thesis, SRCD was applied in **Articles I – IV** to study the structural composition of proteins in the presence and absence of lipids, detergents, and ionic species at various concentrations. Additionally, TFE, a molecule decreasing the dielectric environment when it comprises a major solvent fraction of the sample, was used to test for any intrinsic folding tendency of the proteins. To avoid buffer-induced folding artifacts, namely from the binding of inorganic phosphate to proteins, thereby reducing protein-phospholipid interactions, the proteins were studied at dilute concentrations (0.1 – 0.5 mg/ml) under unbuffered conditions. A typical sample volume was 25 – 40 μ l in 100- μ m cuvettes (0.3 – 0.5 mg/ml) or 250 μ l in 0.5 – 1.0-mm cuvettes (0.1 mg/ml).

3.5.2.2. *Oriented samples*

CD measurements performed for proteins in solution are essentially measured in an isotropic setting. Oriented circular dichroism (OCD) spectroscopy is a method that can be used to study the orientations of proteins and peptides, and a commonly employed system is the use of SLBs with membrane-interacting peptides that adopt defined orientations³⁵⁷. When a helical structure is illuminated with circularly polarized light in an isotropic sample, a negative minimum at 208 nm is observed.

However, an anisotropic sample containing oriented lipid bilayers is illuminated with a beam perpendicular to the bilayers. When a membrane-bound helix approaches a perpendicular orientation in the membrane, the minimum at 208 nm is lost. This allows the screening of peptides and/or membrane compositions to qualitatively estimate the tilt angles of peptides in a membrane³⁸⁸. While useful for peptides, the method is less useful for proteins that typically contain several secondary structure elements in various orientations with respect to each other and the incident beam, masking out the anisotropic effect.

OCD samples are prepared on quartz or CaF₂ plates by drying a peptide-lipid mixture, typically containing around 10 µg of peptide per sample. The dried film is slowly rehydrated at high relative humidity (>97%) to spontaneously form oriented membranes. The quartz plate is then mounted perpendicular to the incident beam and measured at several rotational angles, which are averaged in the end to correct for linear dichroism artifacts. OCD was used in **Article II** to study the orientation and folding of P0ct_{pept} in oriented SLBs.

3.5.2.3. *Stopped-flow kinetics*

Due to folded and unfolded proteins producing different CD spectra, monitoring the process of (un)folding is technically possible as a function of time, by choosing a wavelength, at which a major change in CD signal occurs between the two folded states. Such experiments are often performed to follow thermal unfolding, which allows the determination of the melting temperature of the protein.

Monitoring protein (un)folding to uncover kinetic details is also possible, although the formation of secondary structures occurs in sub-second time scales. Stopped-flow kinetics enable the measurement of such events: the contents of two containers, usually syringes, are simultaneously loaded into a mixing chamber, and changes in the resulting sample are monitored, in this case the CD signal. The entire loading process occurs in a matter of milliseconds³⁸⁹. Possible samples include the mixing of

a folded protein with a denaturant, resulting in unfolding, or the mixing of a denatured protein with a renaturant, resulting in folding.

In this work, stopped-flow SRCD measurements were carried out in **Article III** to monitor the folding of MBP and P0ct when interacting with lipids. Unfortunately, the folding kinetics were too rapid to be accurately monitored (See Chapter 4.3. and 5.4.), but a secondary effect that arose from vesicle aggregation was observed: the CD signal decreased strongly upon the nucleation and formation of larger lipid aggregates. Fitting of the obtained kinetic data was performed with two-state decay functions, from which two kinetic constants could be obtained, describing slow and fast processes occurring simultaneously. Therefore, stopped-flow SRCD measurements were used to determine the effects of ionic strength and Ca^{2+} on MBP- and P0ct-induced vesicle aggregation kinetics.

3.6. PROTEIN-LIPID INTERACTIONS

In myelin, several proteins bridge apposing lipid bilayers, which forms the basis of compact myelin stability. Such interactions and their strength can be studied in controlled systems using various biophysical methods, uncovering the involved binding affinities, thermodynamics and molecular distances.

3.6.1. SURFACE PLASMON RESONANCE

SPR is a method that is popular not only in determining binding constants of different interacting molecules, but especially in gaining information about association and dissociation mechanisms and rates. A thin gold surface exhibits a surface plasmon effect when it encounters light in the infrared-visible wavelength range. The presence of the effect is very sensitive to material being deposited on the surface, which changes the refractive index of the interface and thus the reflection angle of the incident light that travels through a prism. Measuring the change in angle of the reflected light essentially measures the amount of material deposited on the surface,

and this can be performed as a function of time to monitor association and dissociation events.

SPR is usually carried out in a fluidics system with several channels that can be monitored simultaneously, usually on a chip³⁹⁰. Various chips exist, in which the gold surfaces are functionalized against the mobile phase with different structures or compounds that suit the needs of the experiment. An analyte sample with a known concentration is injected with a chosen flow rate and contact time, allowing it to associate with the chip and dissociate once the analyte injection ends and a continuous flow of the medium is applied. The association and dissociation patterns can provide kinetic constants (k_a and k_d , respectively), which in turn can be used to calculate the equilibrium dissociation constant:

$$K_d = \frac{k_d}{k_a}.$$

Lipid vesicles can be captured to form a lipid-rich surface on an SPR instrument sensor chip. The chip is coated with lipophilic compounds attached to a carboxymethylated dextran matrix, and it is capable of incorporating lipids with high affinity and very slow dissociation kinetics³⁹¹. By choosing a parallel channel on the chip without lipids and by using a suitable blocking procedure, the specific association of protein samples onto the lipids can be studied. The sensorgrams from the lipid-free channel are subtracted from the lipid channel to cancel out unspecific binding. In the case of ambiguous kinetics or irreversible binding, the steady-state response levels, where no more protein associates to the surface and the sensorgram appears flat, can be recorded. These levels can be plotted against analyte concentration to obtain a binding curve, and one of various fits can be performed, which can provide K_d .

In this work, K_d values for different proteins binding to lipid structures were obtained using SPR in **Articles I, II and IV**. It should be noted that in the case of irreversible binding, the term ‘dissociation constant’ is misleading, as dissociation phases of MBP and P0ct from lipids could not be measured directly. Therefore, an ‘apparent dissociation constant’ is discussed in relation to this work.

3.6.2. DIFFERENTIAL SCANNING CALORIMETRY

Calorimetry measures the absorption or release of energy in the form of heat by a sample that undergoes a physical or chemical transition. DSC is used to scan a temperature range and record exothermal or endothermal events that occur in the sample cell as opposed to a reference cell. The measured events are expressed as gain or loss in heat capacity. DSC is a useful method to analyze the T_m values of lipids that undergo phase transition events, in which they most often either bind or release energy when transiting between phases³⁹². Lipids present a fairly strong endothermic signal in DSC when heated past their T_m , which allows monitoring of changes in phase behaviour induced by proteins. DSC is quite sensitive for lipid-induced heat events, and as little as 160 – 320 μ M lipid is usable per sample, which corresponds to 0.1 – 0.2 mg/ml DMPC:DMPG (1:1), for instance.

In this thesis, DSC was used to probe for any protein-induced changes in T_m or the melting landscape of DM-lipids in **Articles I, II** and **IV**. A typical sample consists of MLVs or LUVs of lipids with added protein at a certain P/L ratio, in this work normally between 1:100 – 1:1000. At these P/L values, protein concentrations are very low, and any protein denaturation or aggregation events remain undetectable by DSC, allowing specific monitoring of the lipids.

3.6.3. LIPID VESICLE TURBIDIMETRY

Mixing MBP with negatively charged lipids results in vesicle aggregation due to MBP bridging the vesicle surfaces together¹⁹⁷. This process can be followed with methods like turbidimetry or X-ray diffraction in a P/L-dependent manner.

3.6.3.1. *Visible-light turbidimetry*

Much like absorption spectroscopy, turbidity, or measurement of optical density, measures the amount of transmitted monochromatic light through a sample. The presence of particles larger than the wavelength of the used light induces light scattering, resulting in lowered transmission and a higher optical density. These larger

particles can, for instance, be aggregating vesicles, when a protein or an ion is added. While events like aggregation or increase in vesicle size cannot be distinguished from each other with this method, it is possible to establish relationships between the amount of induced turbidity and the P/L ratio, for instance. Additionally, kinetic studies can be performed on samples that display reactions within a timescale of minutes to hours.

In this study, MBP, P0ct, and mutants of P0ct were examined with regard to their vesicle aggregation or fusion properties using visible-light turbidimetry in **Articles I – IV**, similarly to what has been reported before^{94, 96, 197, 243}. Care was taken with proper sample mixing, as well as to measure all samples in a manner, in which they appeared uniformly homogeneous, ensuring independence from the presence of substantially large aggregates that accumulate on the bottom of the sample chamber.

3.6.3.2. *Synchrotron small-angle X-ray diffraction*

Protein-induced vesicle aggregation and fusion can be studied using SAXD. Like SAXS, SAXD measures the position of scattered X-rays on a 2D detector, and the recorded images are converted into scattering curves with s as the X-dimension. The presence of repetitive structures within the sample, such as a protein bridging lipid membranes together, or a protein forming a lattice, results in either constructive or destructive interference of the scattered X-rays. In case of high order, these waves sum together accordingly to the Fourier transform and produce diffraction rings in the scattering image, which result in Bragg peaks in the scattering curve. This is true for a uniform sample where the repetitive structure is isotropically present, as opposed to a crystal that has a certain orientation, along with the contents of its unit cell, in the incident beam. The position of the observed diffraction peaks in s are related to the molecular distance d , as described by Bragg's law, $n\lambda = 2d \sin \theta$, which can be reduced to $d = 2\pi/s$, since s is described as above. The mean repeat distance d corresponds to a repetitive structure in the sample, such as two apposing membranes bridged together by a protein. Diffraction can also result from other repetitive

structures, such as proteins forming periodic macrostructures or the lipids themselves existing in periodic structural phases^{204, 393, 394}.

In this thesis, SAXD was used in **Articles I, II** and **IV** to probe for diffraction peaks arising from periodic mean repeat distances in vesicle-aggregated samples, as has been performed for MBP and P2 earlier⁹⁴.

3.6.4. ATOMIC FORCE MICROSCOPY

AFM is a high-resolution scanning probe method employed in the study of sample surface topology and mechanical properties. Unlike light microscopy, AFM is independent of the wavelength of light, and examines a surface based on mechanical properties using a cantilever, which is either physically in continuous contact with the surface or oscillates at a known frequency, tapping the surface. A piezoelectric system is used to adjust the position of the sample and the cantilever in a feedback loop. A laser is reflected from the back of the cantilever onto a position-sensitive photodetector. The deflection signal is used to measure the position of the cantilever in the height dimension, as well as the sample interaction itself³⁹⁵.

AFM can be performed in aqueous conditions to image flat surfaces with SLBs or proteins. It is sensitive to height differences and mechanical differences between bilayer edges and the underlying substrate, for instance. Therefore, even if a protein binding to an SLB would not influence the thickness of the bilayer, changes in the stiffness of the surface can be revealed. AFM can complement other methods that provide information about layered systems, such as NR, especially since AFM scans an area and is, for example, capable of distinguishing lateral inhomogeneity or holes in an SLB^{89, 395}.

AFM was used in **Articles I** and **II** to investigate the effect of MBP and P0ct on the thickness, mechanical properties and stacking of SLBs.

3.6.5. NEUTRON REFLECTOMETRY

Neutron radiation with a suitable wavelength (range) can be scattered by matter, but unlike X-ray scattering from electron clouds, neutrons are scattered by atomic nuclei. Scattering length density (SLD) is the propensity of matter to scatter radiation when exposed to an incident beam. In the case of X-rays, SLD scales with the amount of electrons and is therefore linear as a function of atomic number. Nuclear scattering is peculiar in the sense that neutron SLD does not scale in a mathematical pattern. A very noteworthy example is hydrogen, as its isotope deuterium has drastically different neutron scattering properties. In biology, dominated by aqueous solutions, neutron methodology obviously presents a great tool due to the SLD difference between water (H_2O) and heavy water – deuterium oxide (D_2O)³⁹⁶. H_2O and D_2O can be mixed at different volume ratios, resulting in a linear continuum in solvent scattering length density. As atomic nuclei present specific SLDs, the atomic composition of a molecule, or part of it, defines the SLD of that scattering entity. Generally, neutron methods excel compared to X-rays in ‘contrast matching’ – the ability to tune the SLD of a given parameter, such as the solvent, with another parameter one wants to distinguish from another. In practice, proteins, nucleic acids, lipids and detergents all have specific SLDs, and the solvent SLD can be matched with these, meaning that the matched parameter will scatter identically to the chosen solvent composition. Given the appropriate background and parallel samples, individual molecular species and structures can be distinguished from a complex system by the use of contrast matching^{397, 398}.

NR is relatively simple in physical terms, as it is a method that merely records the specular scattering of neutrons from a planar, layered sample, as a function of the scattering vector q_z , expressed as s in SAXS/SAXD. Not only are neutrons excellent in distinguishing the interfaces resulting from SLD differences within a layered system, but they are highly penetrative and transfer little to no ionizing energy to the sample. In general terms, neutrons probe deep into the system without resulting radiation damage, which is advantageous considering the long measurement times neutron methods generally require^{360, 399}. This is highly useful in case of SLBs and bound proteins when the sample is laterally consistent and sample preparation is

highly reproducible. Therefore, it is advantageous to prepare SLBs using Langmuir-Schaefer deposition to ensure lateral integrity.

NR was used in **Articles I** and **IV** to determine the layer thickness and coverage of membranes and bilayer-adhered MBP and P0ct phases. Different solvent contrasts were used in order to distinguish interfaces and the related thickness differences accurately.

3.7. EXPERIMENTS PERFORMED IN COLLABORATION

Whilst the characterization of the proteins described in this thesis could be performed in-house or at synchrotron/neutron sources, some experiments were carried out in collaboration. This involved the use of TEM in imaging lipid structure behaviour in the presence of MBP and P0ct in **Articles I, II and IV**, as well as cryogenic electron microscopy (cryo-EM) to investigate the fine structure of protein-membrane adhesions in **Articles I and II**. Additionally, small-angle neutron scattering (SANS) was used to study the detergent-bound structure of MBP, to complement detergent-free experiments carried out using SAXS in **Article I**.

3.7.1. ELECTRON MICROSCOPY

TEM is a method capable of direct imaging of a sample using electrons, providing information about the density and structure of the sample. A spray of electrons is generated and focused on the sample, and the amount of electrons that are transmitted through the sample are measured using an area detector. Negative staining, which stains the surroundings of the sample structures of interest, can be used to improve the contrast within the sample, as less electrons pass through the negative stain than through unstained parts of the sample⁴⁰⁰. TEM can be used to directly visualize the size and morphology of lipid vesicles and other lipid structures. It can also be used to image supramolecular complexes, and it can be useful in the case of smaller proteins in determining the monodispersity of the sample⁴⁰¹.

In this thesis, TEM experiments were carried out through collaboration in **Articles I, II and IV**, to observe how MBP, P0ct, and the P0ct mutants aggregate or otherwise influence the size and morphology of lipid vesicles. TEM data acquisition was carried by Dr. Salla Ruskamo at the Biocenter Oulu Electron Microscopy Core Facility, Biocenter Oulu, University of Oulu (Oulu, Finland) and Dr. Julia Kowal at the Center for Cellular Imaging and NanoAnalytics, Biozentrum, University of Basel (Basel, Switzerland).

Cryo-EM is a method used to obtain high-resolution electron micrographs from unstained samples in vitrified ice, usually obtained through sample immersion into liquid ethane. By the use of cryogenic temperatures, molecular movement and tumbling in samples are slowed down substantially, enabling detailed imaging and structural characterization of proteins and other nanoscale structures. The development of advanced area detectors with very low noise has allowed the accurate detection of transmitted electrons, pushing the resolution limit of TEM even further and essentially removed the need for contrast-enhancing agents in sample preparation⁴⁰².

In this thesis, cryo-EM experiments were performed on lipid-bound MBP and lipid-reconstituted full-length P0 in **Articles I and II**. The experiments were carried out by Dr. Salla Ruskamo and Dr. Julia Kowal at the Center for Cellular Imaging and NanoAnalytics, Biozentrum, University of Basel (Basel, Switzerland). Full-length P0 isolated from bovine nerves was obtained from Prof. Paolo Riccio, University of Basilicata (Potenza, Italy).

3.7.2. SMALL-ANGLE NEUTRON SCATTERING

Like in SAXS, SANS records the intensity of scattered radiation by particles in solution at small θ angles, expressed as a function of momentum transfer, s (or q). Neutrons are scattered by atomic nuclei, where the same scattering rules apply as in NR. Therefore, SANS measurements can be used to distinguish between the protomers or substructures of a complex sample using contrast matching, for instance

in determining the conformation of a detergent-bound protein⁴⁰³. By mixing H₂O and D₂O, solvent scattering can be matched to the scattering of the detergent, allowing the scattering of the protein to be separated from the detergent scattering. By subtracting a background scattering curve, the protein scattering alone can be extracted, and subsequently analyzed and used for modeling, similarly to SAXS data.

In **Article I**, SANS measurements were carried out for MBP in the presence of DPC. The SANS experiment was carried out by Dr. Salla Ruskamo and Dr. Anne Martel at Institut Laue-Langevin (Grenoble, France). The obtained scattering curve was used to estimate the size distribution of DPC-bound MBP using EOM³⁷⁹.

4 OVERVIEW OF RESULTS

ARTICLE I

The Membrane Association Landscape of Myelin Basic Protein Portrays Formation of the Myelin Major Dense Line at the Molecular Level

Raasakka A., Ruskamo S., Kowal J., Barker R., Baumann A., Martel A., Tuusa J., Myllykoski M., Bürck J., Ulrich A.S., Stahlberg H. & Kursula P.

Scientific Reports 7(1):4974, 2017. DOI:10.1038/s41598-017-05364-3.

ARTICLE II

Molecular structure and function of myelin protein P0 in membrane stacking

Raasakka A., Ruskamo S., Kowal J., Han H., Baumann A., Myllykoski M., Fasano A., Rossano R., Riccio P., Bürck J., Ulrich A.S., Stahlberg H. & Kursula P.

Scientific Reports 9(1)642, 2019. DOI: 10.1038/s41598-018-37009-4.

ARTICLE III

Ionic strength and calcium regulate the membrane interactions of myelin basic protein and the cytoplasmic domain of myelin protein zero

Raasakka A., Jones N.C., Hoffmann S.V. & Kursula P.

bioRxiv 529586, 2019. DOI: 10.1101/529586.

ARTICLE IV

Neuropathy-related mutations alter the membrane binding properties of the human myelin protein P0 cytoplasmic tail

Raasakka A., Ruskamo S., Barker R., Krokengen O.C., Vatne G.H., Kristiansen C.K., Hallin, E.I., Skoda M.W.A., Bergmann U., Wacklin-Knecht H., Jones N.C., Hoffmann S.V. & Kursula P.

bioRxiv 535013, 2019. DOI: 10.1101/535013.

4.1. ARTICLE I

The study outlined in **Article I** was undertaken to apply a vast selection of biophysical methodology to study MBP and MBP-like proteins. The objective was to establish these methods to be used as tools in the characterization of MBP and other similar proteins, and to gain a deeper insight into the function of MBP in the stability and formation of the MDL and compact myelin, particularly in the CNS.

An intact MBP construct corresponding to the mouse 18.5-kDa isoform was successfully expressed and purified. The construct lacked an affinity tag after the final purification steps, as confirmed using mass spectrometry. The initial characterization and QC using SDS-PAGE, SEC, DLS, SAXS and SRCD indicated that MBP was pure, monomeric, monodisperse and conformationally extended in solution, while presenting very low levels of regular secondary structure content (**Article I, Fig. 1a-c, Supplementary Fig. S1**). Further SRCD experiments showed that MBP folded in the presence of DPC, SDS and TFE, but not with OG or LDAO, indicating a tendency to gain structure when introduced to certain dielectric environments (**Article I, Supplementary Fig. S1d**). EOM analysis of the SAXS data showed that the scattering of MBP in solution was best described by a wide ensemble of conformational states, rather than a fully elongated random coil (**Article I, Fig. 1c, Supplementary Table 1**). SANS experiments revealed that DPC-bound MBP collapsed into a clearly more compact state, but it still remained fairly elongated (**Article I, Fig. 1d-f**).

To gain an insight into the membrane interaction and subsequent folding of MBP, SRCD spectra were measured of MBP mixed with SUVs of various lipid compositions. The negative surface net charge of selected lipid compositions, such as equimolar mixtures of DMPC:DMPG and DOPC:DOPS, induced folding, whereas the net neutral lipids DOPC and DMPC did not, confirming that the membrane association is driven by electrostatics. The folding of MBP was slightly favored by DM-lipids compared to DO (**Article I, Fig. 2a**).

As compact myelin is rich in cholesterol, SM and PE, we studied an equimolar DMPC:DMPG mixture with separately supplemented cholesterol, SM and DMPE,

but none of the introduced additives affected folding significantly (**Article I, Fig. 2b**). To determine the effect of MBP on the behaviour of lipids themselves, DSC measurements were carried out using MLVs of DMPC:DMPG mixtures at 1:1, 4:1 and 1:0 molar ratios. The presence of MBP affected the phase transition behaviour of DM hydrocarbons as a function of temperature, without significantly altering the T_m itself. The effect was increased with higher protein concentrations, as well as with more negatively charged lipids, and absent in net neutral headgroups (**Article I, Fig. 2d**). SRCD temperature scans around the T_m of DMs showed no effect on the conformation of MBP, indicating folding independence from the lipid phase itself (**Article I, Fig. 2c**).

The interaction of MBP with immobilized LUVs of DMPC:DMPG and DOPC:DOPS was studied using SPR. MBP irreversibly bound to both lipid compositions. The headgroup net charge is the same for both compositions, and similar apparent K_d values were obtained in both lipid mixtures. Interestingly, DM-lipids could accommodate more bound MBP than DO-lipids, indicating an effect by lipid hydrocarbon saturation in the quantity of bound protein (**Article I, Fig. 2e, Table 1**). Noteworthy was that the association phases of binding could not be fitted confidently into simple mathematical models, suggesting several surface processes being present during binding (**Article I, Supplementary Fig. S3**).

As MBP is known to be a classical membrane stacking protein⁷⁰, its stacking function was investigated by imaging MBP-treated DOPC:DOPS SLBs using AFM. The data showed that MBP needs to associate with net negatively charged membranes above a certain concentration to produce *de novo* membrane stacks of physiologically relevant thickness. Cholesterol was not essentially required for this function⁸⁹, but including it enhanced the stacking effect notably, without influencing the required critical MBP concentration (**Article I, Fig. 3a**). To look into this effect further, turbidity measurements were performed using DMPC:DMPG and DOPC:DOPG vesicles with and without added cholesterol. The level of SUV aggregation was not significantly different between the choice of lipid saturation degree or cholesterol content (**Article I, Fig. 3b**).

SAXD data was collected from MBP-aggregated DMPC:DMPG SUVs. A Bragg peak at P/L 1:100 (**Article I, Fig. 3a**), corresponding to a repeat distance of 80 Å, was observed. The value is in corroboration with earlier diffraction studies as well as dimensions observed cryo-EM micrographs of endogenous myelin^{42, 45, 94}.

Since AFM and SAXD studies allowed the formation of myelin-like membrane stacks using SLBs and SUVs, TEM and cryo-EM imaging were carried out for SUVs mixed with MBP. The lipid compositions were chosen to be net negatively charged, and aggregated vesicles could be imaged successfully (**Article I, Fig. 4a, Supplementary Fig. S4**). Using MBP-His, the protein could be labeled with nanogold and localized between adhered SUV interfaces (**Article I, Fig. 4a**). Cryo-EM imaging illustrated that MBP formed a continuous 2.5-nm protein phase between two apposed membranes, rather than well-defined, globular protein particles – this phase separation had been suggested earlier²⁰⁶. The measured stack thickness was similar to that of myelin (**Article I, Fig. 4b-c**)⁴².

Interested in the membrane association mode of MBP, NR studies were carried out on an MBP-treated SLB. MBP associated and inserted into a depth of 3 nm within the membrane, but formed an additional ~7–8-nm protein layer over the membrane surface (**Article I, Fig. 5a, Table 2, Supplementary Table 3**). The size of DPC-bound MBP in SANS was similar to this (**Article I, Fig. 1f**). Time-resolved NR measurement series were performed with a similar sample setup, where the association of MBP with a membrane, subsequent folding, and finally insertion could be observed (**Article I, Fig. 5b**).

In conclusion, a biophysical workflow was established to study MBP and proteins of similar function in membrane-adhesion and stacking. The study revealed the MBP-driven molecular landscape of MDL formation: the irreversible lipid association, charge neutralization, and folding of MBP into a pre-stack conformation on a single membrane leaflet, before further MBP accumulation induced membrane stacking.

4.2. ARTICLE II

In **Article II**, the established methodology from **Article I** was implemented in the characterization of P0ct as a potential membrane stacker at the MDL. The folding of the neurotogenic peptide segment of P0ct in membrane-like environments was investigated. Additionally, experiments on full-length P0, purified from bovine nerves, were conducted to understand its oligomeric state and molecular architecture between adhered membranes in the IPL.

A P0ct construct that was straightforward to express and purify was generated. The protein appeared as a single band in SDS-PAGE. While mass spectrometry confirmed the size of P0ct to have the expected mass of 8 kDa, the protein migrated ambiguously in SDS-PAGE. Further QC revealed that P0ct was aggregation-free and monomeric in solution as shown by SEC-MALS (**Article II, Supplementary Fig. S1a**).

SAXS and SRCD measurements demonstrated that P0ct was highly extended, lacking major regular secondary structure content like MBP in **Article I**, and behaved like an ensemble of disordered chains as suggested by EOM analysis (**Article II, Fig. 1, Supplementary Fig. S1a-b, Supplementary Table 1**). Further SRCD studies revealed that increasing TFE content as well as the presence of SDS and DPC induced folding, whereas LDAO and OG did not, essentially demonstrating very similar behaviour to MBP (**Article II, Supplementary Fig. S1b**).

Very similarly to MBP in **Article I**, P0ct bound irreversibly to negatively charged lipid structures with similar affinity as MBP and folded in the process, as shown by SPR and SRCD, respectively (**Article II, Fig. 2a-b,d, Table 1, Supplementary Fig. S2, Supplementary Table 2**). The folding of P0ct was influenced by the presence of SM and cholesterol, unlike in the case of MBP, suggesting that these lipid types, or their phase behaviour, can influence the folding of P0ct (**Article II, Fig. 2b**).

P0ct had previously been suggested to form β -sheet-rich structures in myelin²⁴⁴, and to investigate this, we studied the folding of P0ct in the presence of native myelin- and EAE-like lipid compositions. Neither lipid composition presented the formation

of β -sheet-rich structures, but a mixed secondary structure content was observed. The folding of P0ct was notably different between the two lipid compositions. Importantly, the native-like myelin composition produced a similar SRCD spectrum to the ones observed in model lipid compositions, validating the simplified approach to study P0ct (**Article II, Fig. 2b**).

In DSC, P0ct behaved differently compared to MBP. Addition of P0ct to MLVs produced a separate population of lipids that presented a T_m value 1.5 – 2.0 °C lower than expected for DMs, depending on P/L ratio. This indicated that P0ct strongly interacts with lipids and segregates them in thermodynamic behaviour (**Article II, Fig. 2e**).

To study the potential membrane stacking function of P0ct, vesicle aggregation studies using visible light turbidimetry, SAXD, AFM and TEM were performed. P0ct was able to induce turbidification of DOPC:DOPG and DMPC:DMPG vesicles with and without 10% cholesterol (**Article II, Fig. 3a**), but as opposed to MBP (**Article I**), cholesterol seemed to increase the observed level of turbidity.

SAXD produced two intensive diffraction peaks (peak 1 and 2) when P0ct was mixed with DMPC:DMPG SUVs. The diffraction peaks moved as a function of P/L ratio, and increasing protein concentration tightened the observed repeat distance. The distances varied between 75 – 81 Å, based on peak 1, and peak 2 behaved like a harmonic of peak 1 (**Article II, Fig. 3b-c**). This suggested the presence of multilamellar systems, but surprisingly, multilamellar structures could not be detected in AFM or TEM (**Article II, Fig. 3d, Fig. 4**).

In AFM, P0ct was able to accumulate on the imaged SLBs and increase their thickness by up to 2 nm. P0ct also changed the mechanical properties of the membrane in thickened patches (**Article II, Fig. 3d**). In the TEM experiments, SUVs treated with P0ct seemed to form larger lipid bodies, indicating that P0ct could induce vesicle fusion (**Article II, Fig. 4a-f**). These lipid bodies sometimes formed loose aggregates, but myelin-like multilamellae were not observed unless the P/L ratio was 1:25 or 1:50, where the protein fractions were an order of magnitude higher than the

endogenous protein fraction of P0ct. With these observations at hand, P0ct can putatively act as a membrane bridging protein, although it does not spontaneously form repetitive stacks that were observed with MBP in **Article I**.

Interested in the structure of the neuritogenic region in P0ct, the folding of the segment was studied through SRCD measurements and molecular modeling of the 20-residue peptide P0ct_{pept} (**Article II, Fig. 5**). The peptide was disordered in water, but gained helical structure in the presence of TFE, SDS, and DPC (**Article II, Fig. 5b**). Interestingly, SDS was able to fold P0ct_{pept} more than 70% TFE, indicating a great contribution of charge neutralization in the folding process. Negatively charged lipid SUVs induced folding of P0ct_{pept}, whereas net neutral lipid SUVs did not (**Article II, Fig. 5a**).

The orientation of P0ct_{pept} in SLBs was studied using OCD: P0ct_{pept} adopted a nearly perpendicular orientation in the SLBs when negatively charged lipids were present (**Article II, Fig. 5c**). Modeling of P0ct_{pept} resulted with the first eight N-terminal residues modelled as a flexible chain, followed by a Pro residue, another eight residues that were modelled as an α -helix. The remaining three C-terminal residues remained flexible. The N-terminal flexible part was rich in Arg and Lys, and given the correct electrostatic environment, such as negatively charged phospholipid headgroups, this part may also adopt a helical conformation and reside in the headgroup region of a membrane (**Article II, Fig. 5d-e**).

Experiments on the oligomeric state and stacking-architecture of full-length bovine P0 were performed (**Article II, Fig. 6**). SEC-MALS experiments uncovered the existence of P0 as dimers and tetramers as reported previously²³⁶⁻²³⁸. The oligomerization depended on the chosen detergent, with DPC inducing tetramerization (**Article II, Fig. 5b-c, Supplementary Fig. S3**). DPC is noteworthy as P0ct also gained secondary structure content in the presence of this detergent. P0 was able to form membrane stacks regardless of the chosen lipid species, and cryo-EM experiments unraveled an intermembrane zipper composed of Ig-like domains, which were either opposite to each other or slightly offset from one another – an

arrangement suitable for an earlier proposed homophilic dimerization mechanism based on crystal packing²²⁷ (**Article II, Fig. 5d-f**).

To conclude, P0ct is hereby described as a potential structural factor in myelin, which might as such contribute to intermembrane stacking. P0ct might form an ordered system within membranes and detergents, contributing to the formation of the physiologically relevant oligomeric state of P0 in the IPL. Investigations on P0ct_{pept} revealed the folded nature of this segment when bound to lipids, which might have relevance in anchoring P0ct tightly to the membrane. The study opens up new approaches in the functional characterization of P0 mutations that ultimately cause CMT or DSS.

4.3. ARTICLE III

The effect of ionic content and divalent cations has been shown to influence the function of MBP^{197, 200, 201}, and similar effects could potentially be extrapolated to P0ct. Hence, in **Article III**, vesicle aggregation and CD studies were employed in the characterization of MBP and P0ct in the presence of various salt and Ca²⁺ concentrations.

The studies performed in **Articles I and II** were complemented by performing MBP- and P0ct-induced turbidimetry of DMPC:DMPG 1:1, 4:1 and 9:1 SUVs, with emphasis on assessing the effects of different concentrations of NaCl, NaF and CaCl₂. In addition to NaCl, NaF was chosen as a salt due to its compatibility with CD, which was carried out later in the study. CaCl₂ was included due to the fact that compared to other biological compartments, myelin is abundant in Ca²⁺,³⁵ which is involved in signaling⁴⁰⁴⁻⁴⁰⁶ but also likely binds phospholipids due to the crowdedness of headgroups in the water-deficient MDL.

CaCl₂ at the used concentrations (0.5, 1.0 and 1.5 mM) was able to induce turbidity in lipid samples without proteins, with more CaCl₂ being required for turbidity when the net charge of vesicles became more negative. Neither NaCl nor NaF induced notable

vesicle turbidity at the chosen concentrations of 75, 150 and 300 mM (**Article III, Fig. 1a-c**).

MBP generally induced higher levels of turbidity than P0ct, especially in the presence of NaCl and NaF. The measured P0ct-induced turbidity levels were much less boosted by NaCl and NaF compared to salt-free conditions. While the levels observed in NaCl and NaF samples were not fully identical, the concentration-dependent trends in NaCl and NaF samples were the same (**Article III, Fig. 1a-c**). In DMPC:DMPG (9:1), a turbidity boost was only observed in 75 mM salt concentration, whereas anything above that plummeted to a level comparable to control samples without protein. Additionally, in the absence of salt, P0ct was more efficient in turbidification than MBP in this lipid composition (**Article III, Fig. 1c**).

The concentration of CaCl₂ in the experiments was only a fraction of the other salts, but still induced vesicle turbidity compared to salt-free conditions. Significant turbidification was present in protein-free samples as well, and the levels of turbidity varied between CaCl₂ concentration and vesicle net charge (**Article III, Fig. 1a-c**). 1.5 mM CaCl₂ was required for aggregating DMPC:DMPG (1:1) SUVs, whereas (4:1) SUVs were aggregated efficiently at 1.0 and 1.5 mM CaCl₂ and (9:1) SUVs only aggregated at 0.5 mM CaCl₂. The level of aggregation in the latter case was much lower than for the other two lipid compositions (**Article III, Fig. 1c**).

The turbidity induced by CaCl₂ was inhibited by the presence of proteins – and the other way around. An almost comparable level of protein-induced turbidity was observed in DMPC:DMPG (1:1) regardless of the tested CaCl₂ concentrations, and in this lipid composition, the turbidity levels were lower than those observed in 1.0 and 1.5 mM CaCl₂ in the absence of protein (**Article III, Fig. 1a**). In DMPC:DMPG (4:1), protein-induced turbidity dropped sharply at 1.5 mM CaCl₂ (**Article III, Fig. 1b**), and in DMPC:DMPG (9:1), only low turbidity levels were detected, the highest at 0.5 mM CaCl₂, which was already significantly lower than in salt-free conditions (**Article III, Fig. 1c**).

SRCD experiments were performed to investigate the folding of MBP and P0ct in the presence of salt and Ca^{2+} . Since similar turbidity levels were observed with NaCl and NaF, 150 mM NaF was chosen as the salt to increase ionic strength, as NaCl is incompatible with CD. While the CD spectra of MBP and P0ct were unaffected by the presence of salt or calcium in the absence of lipids or in the presence of 0.5% SDS (**Article III, Supplementary Fig. S1**), the spectral magnitudes in the presence of lipids decreased with the additives (**Article III, Fig. 2a-c**). The positions of the peaks indicated that the folding of the proteins were similar in the different ionic conditions within the same lipid compositions, with the exception of DMPC:DMPG (9:1), in which the proteins appeared much less folded with salt and Ca^{2+} (**Article III, Fig. 2c**).

Initially, SRCD-coupled stopped-flow experiments were undertaken to study the folding kinetics of MBP and P0ct when encountering SUVs of different DMPC:DMPG ratios in the presence of 150 mM NaF or 1 mM CaCl_2 . Unfortunately, these kinetics were too rapid to follow in practice, as the folding was completed within the dead time of the used instrument (data not shown). An unexpected kinetic behaviour was observed in conditions containing NaF or CaCl_2 – a strong decay in the CD signal within 5 – 10 s, which in most cases could be fitted into one- or two-step exponential functions (**Article III, Fig. 3, Supplementary Table 1**). This was speculated to be initial vesicle nucleation, as the measurement wavelength of 195 nm was in a similar range to the size of LUVs or small SUV aggregates, and the effect occurred with CaCl_2 in the absence of proteins as well.

DMPC:DMPG (1:1) SUVs aggregated slower in the presence of 1 mM CaCl_2 than DMPC:DMPG 4:1 and 9:1 SUVs, owing to the underlying electrostatics (**Article III, Supplementary Fig. S2, Supplementary Table 1**). In the presence of proteins, the fast turbidification process of DMPC:DMPG (1:1) stands out from the other two lipid compositions, as the effects of NaF and CaCl_2 on k_1 increase with the fraction of DMPG. In the case of MBP, the ratio of the two obtained rate constants increases in a fashion that is nearly linear in all lipid compositions, except DMPC:DMPG (4:1)

(**Article III, Fig. 3b**). Here, the highest ratio arises from the low k_2 value (**Article III, Supplementary Table 1**).

In DMPC:DMPG (9:1), the obtained rate constants were almost equal for samples with CaCl_2 regardless of the presence of proteins, suggesting a dominant behaviour from the cation itself (**Article III, Supplementary Fig. S2, Supplementary Table 1**). MBP and P0ct were only able to aggregate vesicles in the absence of any salts, and these observations correlate with the steady states observed in turbidimetric experiments (**Article III, Fig. 1c, 3b**). In the other lipid compositions, protein-induced aggregation was practically absent when compared to background samples (**Article III, Fig. 3b-c**).

In conclusion, the effect of ionic strength and Ca^{2+} on MBP and P0ct mediated vesicle turbidification and the involved kinetics was studied. It became evident that the presence of a monovalent salt enhances the observed turbidification, but only to the extent to which protein-lipid charge neutralization can occur to produce protein-mediated lipid bridging. As apparent from the chosen concentrations, Ca^{2+} interacts much more specifically with the lipids, as concentrations around 1 mM can influence the activity of proteins. Similarly, the effect of calcium as a lipid turbidifier is influenced by MBP and P0ct.

A novel SRCD-based method was described in following rapidly forming vesicle bodies that cause sample turbidity. While our kinetic data correlates with steady states from turbidimetry, what kinds of processes specifically are described by k_1 and k_2 is still uncertain. A notable observation was that k_1 changed most between different sample setups, whereas k_2 remained unchanged. Therefore, k_1 values were mostly compared (**Article III, Fig. 3b, Supplementary Table 1**).

4.4. ARTICLE IV

The study undertaken in **Article IV** was to broaden the existing knowledge stemming from **Article II** to include the known disease point mutations within P0ct, essentially to uncover any molecular effects that arise from these mutations and how these possibly result in peripheral neuropathies. More specifically, these mutations were the six known mutations in P0ct, all related to CMT and DSS^{332, 334-339}: T216ER, A221T, D224Y, R227S, K236E, and K236del (**Article IV, Fig. 1a**).

Mutations were individually generated using the P0ct construct from **Article II** via site-directed mutagenesis, producing six disease mutant variants. The presence of the mutations was verified by DNA sequencing and subsequent mass spectrometric characterization after successful protein purification (**Article IV, Table 1**). All mutants but one behaved very similarly to the wild-type protein in terms of expression and purification. The outlier, D224Y, had significantly lower expression levels and yields (**Article IV, Table 1, Supplementary Fig. S1**), and appeared to undergo minor degradation during expression. More interestingly, the mutant could not be subjected to SEC in the standard buffer used for the chromatography of P0ct, but instead, a buffer with a higher salt concentration and increased pH was required, which influenced the retention time of the mutant variant (**Article IV, Fig. 1b**).

Similar QC as described in **Articles I** and **II** was performed using SEC, SAXS, DLS and SRCD, and freely in solution the mutants were monomeric, monodisperse, and disordered, just as the wild-type (**Article IV, Fig. 1b-c, Fig. 2, Fig. 3a, Supplementary Fig. S2, Supplementary Tables 1-2**). SRCD experiments with TFE and various detergents demonstrated that all proteins folded in an identical manner to the wild-type, with the exception of K236del, which seemed to gain more secondary structure content than the other variants in the presence of SDS (**Article IV, Fig. 3b-c, Supplementary Fig. S2**).

We characterized the folding of P0ct wild-type and mutants using SRCD, similarly as in **Article II**. In water, all variants presented an identical level of folding, and in DMPC, none of the variants gained secondary structure content. D224Y deviated slightly from the other variants, seemingly becoming slightly more disordered in

DMPC (**Article IV, Fig. 3a, Supplementary Fig. S2g**). Notable differences were present in lipids with different ratios of DMPC and DMPG. In DMPC:DMPG (1:1), the spectra of P0ct wild-type and K236E were slightly more intensive in magnitude than the others, but generally all variants had the observed peak minima and maxima close to the same wavelength values. D224Y deviated from the other variants producing the two minima observed at 208 and 222 nm at almost equal magnitude, whereas in the other variants the minimum at 208 was significantly more pronounced (**Article IV, Fig. 3d**). The folding of all variants were more comparable in DMPC:DMPG (4:1). Here, the folding of all variants was seemingly the same, with D224Y deviating more obviously from the others, presenting a slightly higher degree of secondary structure content (**Article IV, Fig. 3e**). In DMPC:DMPG (9:1), the spectral magnitudes varied drastically from one another, with the wild-type and K236E again showing the most intensive spectra. The magnitude variation was from the inevitable aggregation within samples, resulting in loss of signal due to light scattering. This led us to interpret the data cautiously. From the two minima, it seemed that D224Y deviated most from the other variants, with T216ER, A221T and K236del producing marginally shifted peak minima compared to wild-type, R227S and K236E (**Article IV, Supplementary Fig. S2h**).

SPR experiments were carried out using DMPC:DMPG (1:1) LUVs, similarly to **Article II**. The obtained K_d values for all variants were in a similar range, but a notable difference to the wild-type and other mutants was D224Y, which could accumulate in higher amounts to the immobilized lipids (**Article IV, Fig. 3f, Table 2**).

We continued the characterization by performing DSC measurements similarly to our past studies. We increased the amount of lipids in the experiment to gain a better baseline level and to reduce noise. The trends seen for the P0ct variants were reproducible, and a separate lipid population with a T_m formed as in **Article II**. The mutants had minor effects on this behaviour: K236E and K236del reduced the T_m marginally more than the wild-type, T216ER, A221T and R227S. D224Y was again

different from the others, producing a wider, less symmetric transition, which might be a product of several smaller overlapping peaks (**Article IV, Fig. 4a**).

Vesicle turbidimetry was carried out to quantify the lipid aggregating/fusing effects of the variants. Statistical analysis revealed that at 1:100 P/L, D224Y, R227S and K236E produced significantly reduced turbidity ($P < 0.001$) and the effect with K236del was slightly reduced ($P < 0.05$). At 1:50 P/L ratio, the only mutant with strongly reduced turbidity was still D224Y. K236E also produced a weak but statistically significant turbidity reduction (**Article IV, Fig. 4b, Supplementary Fig. S3**).

To understand the impact of mutations on molecular order in lipid-bound P0ct, SAXD measurements were performed similarly to **Articles I and II**. While all variants presented a similar trend of molecular distances as a function of P/L ratio, some subtle differences in either the increment rate or distances themselves were observed. Most notable ones were D224Y, which presented distances systematically 5 – 8 Å shorter compared to wild-type. R227S, K236E, and K236del, on the other hand, displayed increased distances, indicating looser packing. K236E generally produced the most loosened distances across the used P/L range (**Article IV, Fig. 4c**).

To directly observe the effect of P0ct variants on vesicles, TEM studies were performed. For all variants except D224Y, we observed large lipid bodies that formed from SUVs, some of which were loosely attached or aggregated to one another. In the presence of D224Y, dense multilamellar structures formed, which resembled those of stacked bilayers in compact myelin (**Article IV, Fig. 5**). These lamellae appeared more ordered and denser at increasing lipid fraction, although the measured repeat distances evolved oppositely in SAXD (**Article IV, Supplementary Fig. S4**).

As in **Article III**, stopped-flow SRCD kinetics were performed in the presence of 150 mM NaF for DMPC:DMPG SUVs with P0ct variants at 1:200 P/L (**Article IV, Fig. 6a**). The obtained kinetic constants from all experiments were in a similar range for all variants, with K236E and K236del presenting k_1 values and thus k_1/k_2 values around 20% lower compared to wild-type, suggesting slightly slower kinetics for the

fast process. D224Y produced a k_1 value about 10% higher compared to wild-type (**Article IV, Fig. 6b, Table 3**). Due to an unclear effect, the kinetic starting level of K236del was notably higher compared to the other variants, and reproducibly remained as such for ~ 0.3 s. The end level of all variants was identical after the 5 s measurement period ended (**Article IV, Fig. 6a**).

To investigate the membrane-binding mode of P0ct on a single SLB, NR measurements were performed similarly to MBP in **Article I (Article IV, Fig. 7a)**. P0ct was observed embed almost entirely in to the membrane, producing only a marginal exposed protein layer, unlike MBP. The thickness, roughness, and water content of the membrane increased in the presence of P0ct (**Article IV, Fig. 7b-c, Table 4**). The SLB thickened by 2 nm, which corresponded to what was measured in AFM (**Article II, Fig. 3d**). Furthermore, NR data was collected for D224Y, but no observable difference to wild-type was present after binding (**Article IV, Supplementary Fig. S5**).

To conclude, a fully embedded membrane association mode of P0ct has been observed, and that the mutations at hand do not seem to affect this. Most mutants characterized here behaved much like the wild-type protein, especially T216ER and A221T, which suggests their disease mechanisms are not directly related to their function in mature compact myelin or its formation.

Based on this characterization, the functionally most unique mutant, D224Y, is capable of forming membrane multilayers efficiently, thus resembling MBP in its mode of action rather than P0ct wild-type.

While the effect of R227S, K236E and K236del were much less dramatic than D224Y, we identified Arg227 and Lys236 as potentially important amino acids in the function of P0ct. Mutating Lys236 decreased the amount of vesicle turbidity and the rate of vesicle aggregation, as well as loosened the molecular order as shown by SAXD, with the charge-inverting K236E pronouncing the effect more than the deletion of Lys236.

5 DISCUSSION

Compact myelin is novel from a biological perspective. Immensely rich in lipids, the unique proteome within and the absence of water make it stand out from other systems. The formation and stability of compact myelin needs to be considered if one wants to understand demyelinating conditions. MBP is a central protein in the formation of the MDL in the CNS, and one of the most abundant myelin proteins in general⁶⁶. In the PNS, P0 makes up the major fractions of all proteins⁸², and its importance in myelin stability is reflected by numerous disease mutations^{332, 333, 335, 336}. In the current study, MBP and P0ct were studied using a biophysical approach to unravel their function and folding in myelin compaction, as well as the effect of ionic factors that influence these. Additionally, point mutant variants of P0ct were characterized to unravel any determinants in the molecular etiology of CMT. Since a strictly biophysical approach was used, the involved methods and samples will be discussed, before moving on to more biologically relevant aspects.

5.1. METHODOLOGICAL CONSIDERATIONS

5.1.1. RESEARCH MATERIAL AND QUALITY CONTROL

This study focused on the detailed biophysical characterization of biomolecules centrally involved in the formation and maintenance of the vertebrate myelin sheath. A variety of biophysical techniques were used, and simplified, controlled conditions were employed in the experiments. This essentially involved the use of synthetic lipids and recombinant proteins, which could be obtained in high amounts.

The proteins were designed to be label- and tag-free to avoid any artifacts arising from these modifications. Especially His-tags can introduce positive charges under

certain conditions, which might influence electrostatic binding to phospholipids and introduce unwanted metal cation coordination. On the other hand, given the small size of P0ct, a His-tag composed of six His residues would increase the length of the 70-residue construct by almost 10%, which in turn can influence its physical behaviour.

Solid protein QC throughout the project enabled robust reproducibility of downstream experiments. Achieving proper protein integrity, purity, monodispersity, and stability was crucial, as the goal was to obtain data that specifically represent the functional and structural behaviour of MBP and P0 under controlled conditions. Effects arising from aggregation, degradation, or oxidation were minimized. The chosen QC methods complement each other in the data they provide: the use of mass spectrometry, SDS-PAGE, and SEC(-MALS) supported each other by providing the mass and purity of the proteins at different levels of accuracy. Another example is the use of DLS, SAXS, and SEC-MALS, which not only provide useful parameters, like molecular weight, R_g , and R_h , but they are all especially sensitive in probing aggregation within the samples. Therefore, at times when only some of the methods were available, other methods were used to gain complementary information

5.1.2. MYELIN BASIC PROTEIN, THE REFERENCE MOLECULE

The goal of this study was to study the biologically relevant structure-function relationships of abundant myelin proteins. This was achieved using a biophysical setup that allowed thorough characterization of the lipid binding and membrane stacking properties of basic proteins. Decades of work has been devoted to the characterization of MBP before the conception of this study, providing a substantial amount of reference data, as extensively reviewed before^{70, 168, 342, 407, 408}.

Based on earlier literature, the tag-free recombinant MBP construct behaved (**Article I**) as expected in AFM⁸⁹, CD¹⁷¹, turbidimetry^{197, 210}, SAXD⁹⁴, and SAXS^{171, 172}. This increased the confidence in the recombinant protein material and simplified lipid compositions, allowing the development of a workflow for the characterization of MBP. DSC experiments had been carried out before with MBP for phospholipids and

gangliosides⁴⁰⁹⁻⁴¹¹, but the impact of MBP on mixtures consisting of net neutral and negatively charged lipid species had not been performed. NR had been used to study MBP before, but as opposed to the DMPC:DMPG (1:1) SLBs used here, DMPA membranes were used⁴¹², and no membrane insertion of the protein was observed. This may be an artifact of the heavily acidic lipid headgroups – the lipid compositions chosen for **Article I** reflected the expected physiological function of MBP and unveiled a substantial insertion of MBP to the SLB.

In this study, all experiments were performed without protein labeling. This is of major importance considering the function and natural environment of myelin proteins. The cytoplasmic compartment of compact myelin is very narrow, which excludes large tags, such as GFP⁶⁵. The methods used in the current work follow the intrinsic molecular attributes of the proteins and lipids, abolishing the need of tags that can interfere with the experiments.

On the downside, there are certain aspects that can decrease the attractiveness of the described methods. One factor is the required protein purity and monodispersity. These are absolutely needed if one wants to follow a single attribute in a meaningful way, as several methods are based on absorbance, which does not distinguish between oligomeric states, and scattering, which is sensitive to molecular size and order. Considering the size of the proteins, reasonably high concentrations of purified proteins are required for the characterizations at hand – this can be practically difficult, especially if the study of PTM variants is desired, most often omitting bacterial expression systems. Finally, some methods required fairly concentrated samples. SAXS and SANS are notable examples, as the quality of the measured scattering pattern improves directly with concentration. The concentrations used in experiments may not be physiologically relevant, and this might translate into observations that show more compacted protein folds than present *in vivo*, since molecular crowding can affect the folding behaviour of individual proteins^{413, 414}.

The limiting factor of biophysical studies is often either the stability of the studied protein, or its yield per purification. QC was established to rule out sample stability issues, leaving purification yield the determining factor of streamlined experiments.

Many of the used methods are rather sensitive, allowing characterization of a single protein batch using several approaches and controls. For example, with SRCD, the purified proteins were always tested for expected folding, usually in water, in the presence of a detergent, and with a standard lipid composition. Individual protein batches behaved well with respect to each other; more variation was observed between lipid batches. Therefore, control experiments were carried out always when lipids were used, most notably in CD, in which the observed spectral magnitudes are very sensitive to aggregation-induced light scattering⁴¹⁵. Such experiments were needed to gain high reproducibility, as evident from the small standard deviations in **Articles I – IV**.

One notable limitation within the study was the employment of PG and PS lipids in a mixed fashion. Both lipids are negatively charged at physiological pH, but present different headgroup structure. This adds another variable to the sample material. The optimal solution would be to employ only PS or PG in all samples, but as explained and justified in Chapter 3.2., we included both headgroups as DOPS or DMPG as the major negative lipids, partially due to their physiological significance, but also based on their physical characteristics.

5.2. THE FORMATION OF THE MAJOR DENSE LINE

The experiments carried out in **Article I** allowed to uncover new aspects of MDL formation and the pivotal role of MBP therein. Most notably, the involved molecular interactions, the role of cholesterol, the conformation of MBP on a single membrane, and the MBP concentration dependency in membrane stacking were studied.

The disordered MBP irreversibly bound negatively charged lipids and folded in the process.^{142, 143, 168-171}. In the absence of negative charge components, folding was not induced, indicating the absence of binding. This was verified using NR, underlining the importance of electrostatic interactions in the activity of MBP. Comparison of lipid saturation degree had minimal role in the lipid binding and structure of MBP. In myelin, the major fraction of lipids is composed of unsaturated fatty acids, with DOs

dominating as the single most abundant fatty acid group⁵⁵. In saturated lipid compositions, however, more MBP could associate with the lipids as shown by SPR. DSC revealed an effect on the lipid phase transition behaviour, which indicated that MBP could influence the (thermo)dynamic behaviour of the lipid tails, as shown before^{90, 416, 417}, possibly through membrane insertion.

The formed lipid aggregates displayed a repeat distance that corresponded to the width of the MDL, around 3 nm⁴³, between bilayers, and this was confirmed using AFM where multilayered membranes formed after a sufficient surface-bound MBP concentration was reached. The real amount of bound MBP on the membranes is difficult to estimate in our experiments, hence, it is difficult to draw conclusions on how the surface bound MBP concentration and stacking induction are related in terms of the apparent K_d determined using SPR.

The presence of cholesterol was earlier postulated to be essential for the formation of stacked membranes⁸⁹, but the current study contradicts this, as stacked membranes formed in cholesterol-free SLBs as well. However, the past study is not fully comparable with the current one since the lipid composition was different, especially considering the fraction of negatively charged lipid species⁸⁹. In the current study, the presence of cholesterol did, however, visibly enhance membrane stacking, most likely due to altering the fluidity of the membranes. In turbidimetry, inclusion of cholesterol did not display a significant effect, suggesting that the enhanced effect of cholesterol arises from elsewhere than intermembrane bridging by the protein. In turbidimetry, vesicles tumble freely in solution, which means that given enough time, MBP-decorated membranes will meet due to Brownian motion and become adhered to each other. In SLB systems, like in AFM, SLBs were treated with MBP and no excess lipids were added after this, which means that any stacks need to form from the pre-existing SLBs. Thus, a likely explanation for the observed cholesterol-enabled effect could be that the fluidity of the SLBs change, allowing MBP to stack lipids easier when cholesterol is present. During myelination, cholesterol-modulated membrane fluidity might affect the function or segregation of relevant proteins, including

MBP^{60, 61, 350}, as cholesterol abundance is crucial for the development of oligodendrocytic myelin⁶⁰.

Using NR and SANS, a novel conformation of MBP was observed. When MBP binds to a single membrane, it partially inserts into a depth of 3 nm and assumes an elongated 7–8-nm pre-stacking conformation on top of the membrane. In cryo-EM, a dense protein phase in between stacked membranes was observed, rather than individual folded MBP particles, which supports the presence of the earlier proposed protein meshwork²⁰⁶. During membrane binding, MBP undergoes charge neutralization, folding, and insertion to a membrane, but stacking of two membranes occurs only when a sufficient concentration of membrane-bound MBP is reached. A model outlining the MBP-driven formation of the MDL is proposed (**Article I, Fig. 6**), which features the steps described above.

The proposed model is logical if one considers the translation of MBP, which occurs in the vicinity of the membrane during myelin compaction⁴¹⁸. As free MBP needs binds to the membrane for the entire cascade to proceed spontaneously, the amount of MBP is a determining factor in the process. Therefore, the translation of MBP needs to be controlled during myelination, and other proteins, most notably the cytoskeleton and CNPase, are likely to be involved^{191, 257, 419, 420}. These factors are known to be important in the formation of correct myelin morphology¹⁰². The proposed model can be used to speculate on the development of MS as well, as changes in the translation levels, affinity, or folding of MBP will likely affect its association with the membranes. The extended MBP conformation in the pre-stack state could leave MBP susceptible to proteolysis^{311, 421}, producing peptide fragments displaying antigenic properties through molecular mimicry (Fig. 12). The model provides a good starting point for further experiments involving citrullination variants of MBP, as well as changes in lipid and ionic compositions known to be involved in MS^{200, 204}.

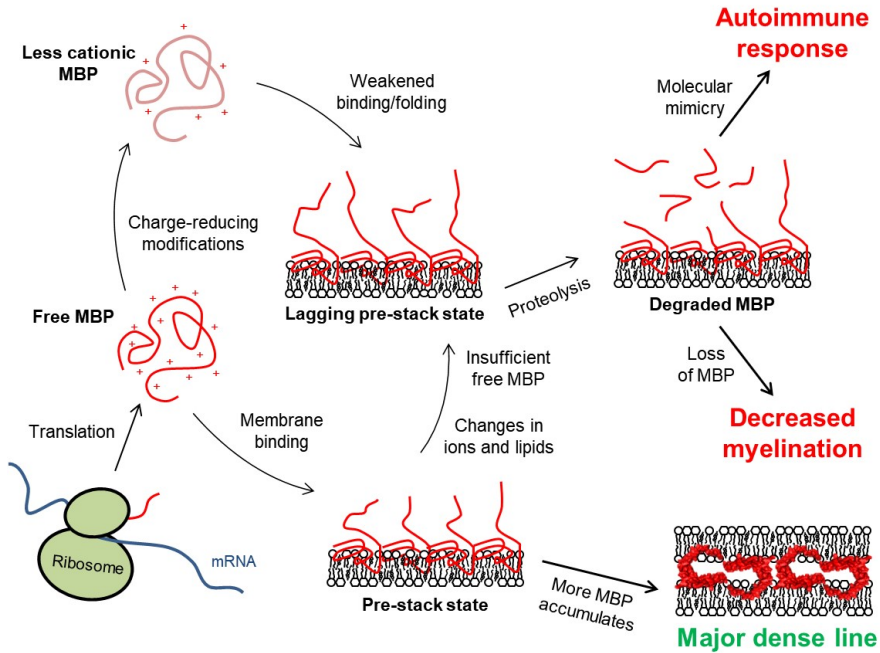


Fig. 12. The role of MBP in the formation of membrane stacks and disease. The translation levels of MBP (red) govern the fate of MDL formation. The destabilization of compact myelin and the formation of an autoimmune response can be speculated to arise from a lagging pre-stack state, which does not form stable membrane stacks rapidly enough. The effect could stem from lowered MBP translation, from PTMs that reduce the net charge of MBP and from changes in ionic and lipid content²⁰¹, affecting the abundance of active membrane-bound MBP. Subsequent proteolysis of exposed MBP could form autoantigenic peptides, promoting the formation of an autoimmune response. The related loss-of-MBP could additionally decrease the stability of myelin and the rate of myelin formation.

5.3. THE STRUCTURE AND FUNCTION OF MYELIN PROTEIN ZERO IN PERIPHERAL MYELIN

The characterization of MBP in **Article I** is a starting point for expansion to other proteins. P0ct was a logical follow-up candidate, since it had been studied in a similar fashion by others²⁴³⁻²⁴⁵, and it might stack myelin membranes similarly to MBP.

An identical characterization was performed for P0ct as for MBP, which essentially revealed similarities between the two proteins: P0ct was disordered in solution, irreversibly bound negatively charged lipid compositions and various detergents, and displayed significant folding in the process. The affinity towards lipids was very similar to that of MBP. In DSC, however, P0ct produced a new population of lipids with a destabilized gel phase, which was a clear difference to MBP. This hints that P0ct can affect the thermodynamics of the lipids it associates with, which might have relevance in the partitioning of P0 into lipid rafts⁴²².

Cholesterol and SM affected the folding of P0ct, which was not observed for MBP. This is notable, as some myelin proteins, like PMP22 that is known to interact with P0, are dependent of the presence of SM when forming myelin-like membrane adhesion structures^{63, 240, 423}, suggesting that the fluidity of the membrane has an impact on P0ct. Therefore, P0ct and lipids most likely affect each other in the membrane more than in the case of MBP. Very importantly, the folding of P0ct in native myelin-like lipids was similar to the used simplified model lipid compositions, suggesting that P0ct does not present a β -sheet-rich fold *in vivo*²⁴⁴.

The level of order P0ct induced when bound to vesicles was higher than that of MBP, as suggested by the diffraction peaks in SAXD. The membrane-stacking activity of P0ct remains slightly obscure, as adding P0ct to SLBs in AFM never induced stacking, only association and membrane thickening. In these experiments, the protein concentrations were an order of magnitude higher than what was performed in similar experiments involving MBP. In EM, P0ct caused SUVs to become larger lipid bodies, which appeared to loosely associate with each other. This is likely the effect observed in turbidity experiments, and while it is tempting to label P0ct as a membrane stacker, its stack formation mode differs to that of MBP in **Article I**, full

length P0 in **Article II**, and P2⁹⁶. More experiments are required to study this aspect: microscopy experiments with full length P0 lacking P0ct should be conducted using vesicle samples as well as nerve cross-sections from knock out animals. Additionally, studying the fine architecture of P0ct-decorated membranes using cryo-EM might be advantageous, as TEM using negative staining cannot reach sufficient magnification to reveal the interface between P0ct-treated vesicles. While P0ct is small, the putative membrane stack it forms is in the same size range as those measured for MBP in **Article I**, which indicates that visualization of P0ct as phase separation or individual particles between the membranes should be possible. Given the small size of P0ct, its structure elucidation might also be possible through NMR spectroscopy or crystallization using lipidic mesophases. To determine whether the observed diffraction emerges from P0ct-bridged bilayers or from within a P0ct-embedded bilayer itself, grazing-incidence small-angle scattering (GISAS) experiments should be performed using a single SLB with bound P0ct.

P0ct contains a conserved neuritogenic segment which has been previously used as a peptide to induce EAE in animals²⁵⁵. This segment was found to fold in net negatively charged lipids, similarly to many other peptides that originate from myelin proteins³²⁴. Differences in folding correlated with the saturation degree of the lipids, and the importance of electrostatic neutralization was obvious. OCD showed that in the peptide assumes a perpendicular orientation in the membrane. This distinguishes P0ct from MBP, for which the known helical segments are thought to insert in a horizontal orientation to the myelin membrane, based on their amphipathic character observed using helical wheel projections^{342, 424, 425}. The neuritogenic segment might function as an important anchor for P0ct in its membrane-bound state, and likely does not become exposed to other factors, such as the immune system, in intact, healthy myelin.

Cryo-EM displayed periodic homophilic adhesion between Ig-like domains, which was independent of the chosen lipids (**Article II, Fig. 2d-f**). The spacing between the adhered apposing membranes was 5 nm – a physiologically relevant value for the IPL – and the adhesions appeared as directly apposing or slightly offset dimers of Ig-like

domains in a zipper-like arrangement. The crystal packing of the rat P0 Ig-like domain (PDB ID 1NEU²²⁷) revealed a possible dimerization mode, in which two β -strands form a short intermolecular β -sheet (**Article II, Fig. 7**). In this arrangement, the C-terminus of each Ig-like domain points towards the membrane, and the C-terminus is followed by the transmembrane domain in full length P0. SEC-MALS revealed dimers and tetramers of P0, as reported earlier^{236, 237}. The oligomeric state depended on the chosen detergent: strikingly, tetrameric P0 was present only in DPC, which also induced folding of P0ct, raising an important point: the folding of P0ct might affect the oligomerization of P0.

The model proposed for the organization of P0 in membrane stacks is realistic, based on the measured distances, which match those of endogenous myelin^{42, 43}, and the packing of the crystal structure²²⁷. Since the folding of P0ct seems to be coupled to the oligomeric state of P0 itself, the measured distances from SAXD data could also represent lateral assemblies of P0ct molecules, rather than bilayer bridging, although distinguishing between the two is not possible from the measured data. One might speculate that an ordered P0ct assembly locks P0 in place, forcing the Ig-like domains to adopt an orientation in the IPL that results in productive homophilic adhesion and the observed protein zipper. Nevertheless, P0 must harbor a role in MDL compaction as well, as mice lacking both MBP and P2 develop normal myelin in the PNS⁹⁸, and the absence of P0 extensively disrupts myelin formation and morphology²⁷⁹.

5.4. THE IMPACT OF IONIC CONTENT ON THE ACTIVITY OF BASIC PROTEINS

In the studies carried out in **Articles I and II**, the effect of ion concentration remained unconsidered. In **Article III**, the effects of salt and Ca^{2+} on the function of MBP and P0ct were studied.

Turbidimetric studies demonstrated the effect of salt concentration of protein-induced vesicle aggregation. While only minor turbidification was observed without salt, increasing ionic strength boosted vesicle turbidity and the involved kinetics. The net charge of the lipid vesicles influenced the salt concentration where highest turbidity

was recorded, with vesicles with less negative net charge being more susceptible to salt concentration competing with the proteins. MBP generally produced higher turbidity levels than P0ct.

The effect of Ca^{2+} seems more specific than that of monovalent ions, as suggested by the magnitude of differences and the concentrations used of Ca^{2+} that were substantially lower than NaCl or NaF. Ca^{2+} could induce vesicle turbidity by itself, but in the presence of MBP or P0ct, the turbidity levels fluctuated rather little between the three Ca^{2+} concentrations, although Ca^{2+} generally lowered turbidity levels. In each lipid composition, a certain level of Ca^{2+} became high enough to block protein-induced turbidity. Thus, an optimal level of Ca^{2+} is expected to carry out its function in myelin, at least when it comes to membrane-bridging²⁵⁸, as changes in ionic conditions or lipid composition might drive the system towards demyelination, as already speculated in Fig. 12.

The kinetics of vesicle aggregation were studied using SRCD, as following protein folding was not possible. Such an approach has not been described before. While it is unclear what the two obtained kinetic constants actually represent, comparing the k_1 constant for MBP and P0ct revealed that P0ct generally performs its activity slightly faster than MBP. This could be due to the smaller size of P0ct, allowing it to interact with phospholipids faster than MBP due to Brownian motion. Additionally, since proteins bound on the surface of vesicles change the net charge of the surface, MBP due to its larger size and higher positive charge could experience electrostatic repulsion, as more protein continues to bind the lipids.

In the end, the study provides new insights into the roles of ionic strength and divalent cations in myelin formation and the molecular amounts involved, and provide a solid foundation for further studies focusing on the protein affinity and involved kinetics of myelin bilayer bridging. Ca^{2+} is an important ion in myelin at a concentration of 1 mM ³⁵, being involved in signaling and myelin development^{201, 404-406}. While too high Ca^{2+} amounts can be detrimental for myelin stability^{199, 201}, the concentration of Ca^{2+} in myelination needs to be maintained to promote the formation of healthy myelin²⁵⁸. Ca^{2+} likely modulates the binding of proteins to membranes by

direct interaction with both players. Ca^{2+} is known to bind MBP⁴²⁶, and this study highlights the importance of the correct ionic conditions in the activity of MBP and P0ct.

5.5. THE EFFECT OF PERIPHERAL NEUROPATHY MUTATIONS ON THE MYELIN PROTEIN ZERO C-TERMINAL SEGMENT

A follow-up study including the known CMT and DSS mutations of P0ct was conceived. As in the structural enzymology of CNPase earlier^{113, 139, 427, 428}, the established method ensemble was used to study protein variants displaying single-amino-acid changes compared to the wild-type protein. Many quality control experiments produced nearly identical outcomes for the six P0ct mutant variants. The lipid binding characterizations produced meaningful differences between the mutants and P0ct wild-type. An overview of these is listed in Table II.

Table II. P0ct mutant comparison to wild-type. Various experiment were employed to determine the effect of the six chosen point mutations on the function and folding of P0ct. An increased or enhanced effect is indicated as one or more plus signs (+), decreases are oppositely indicated with minus (-) signs. No change is indicated with a zero (0). Control experiments are not included in the table.

| Method | T216ER | A221T | D224Y | R227S | K236E | K236del |
|---------------------|--------|-------|-------|-------|-------|---------|
| SRCD, SDS | 0 | 0 | 0 | 0 | 0 | + |
| SRCD, DMPC | 0 | 0 | - | 0 | 0 | 0 |
| SRCD, DMPC:DMPG 4:1 | 0 | 0 | + | 0 | 0 | 0 |
| SPR, K_d^* | + | 0 | + | + | + | 0 |
| SPR, R_{hi}^{**} | 0 | 0 | ++ | 0 | 0 | 0 |
| DSC, T_m | 0 | 0 | *** | 0 | + | + |
| Turbidimetry | 0 | 0 | --- | -- | -- | - |
| SAXD, d_1 | 0 | 0 | - | + | ++ | + |
| EM | 0 | 0 | +++ | 0 | 0 | 0 |
| Stopped flow, k_1 | 0 | 0 | + | 0 | - | - |
| Yield per l | + | + | - | + | + | + |

*Generally very subtle differences.

**Maximum response level from fitting.

***Calorimetric landscape changed.

Characterization of the mutant variants identified a mutation distinct from all the others: D224Y. While other mutants were similar or almost identical to wild-type P0ct in terms of folding, lipid binding affinity, effect on lipid T_m , and vesicle aggregation, D224Y stood out with subtle, but meaningful differences. As opposed to P0ct and the other mutants, EM imaging revealed that D224Y induced heavy membrane stacking, similarly to MBP. This is an important result, as D224Y manifests as an abnormal CMT phenotype, displaying abnormally thickened compact myelin³³⁶. Nearly all studied parameters were changed: turbidimetry displayed a decreased level of optical density, most likely due to tighter lipid aggregates. In DSC, a wider, multimodal distribution in the thermodynamic landscape of DMPC:DMPG (1:1) was observed. In SAXD, molecular repeat distances collapsed by nearly 1 nm. The affinity of D224Y was only marginally decreased compared to wild-type P0ct, but more D224Y accumulated onto the immobilized lipids, as revealed by the increased response levels in SPR. All of these observations were present in DMPC:DMPG (1:1), where the folding of D224Y was not notably different from the other variants, although in DMPC:DMPG (4:1) it displayed slightly more folding. The single amino acid change from Asp to Tyr at this specific position allows P0ct to become a hyperactive stacker, capable of inducing multilayer formation and leaning towards the known physiological phenotype³³⁶. The endogenous effect of D224Y is so substantial that P0ct as a part of P0 becomes a determining factor in disease etiology.

The difference to wild-type P0ct displayed by D224Y was substantial, but even though some mutants displayed milder effects, functionally important amino acids could be identified: Arg227 and Lys236. The changes in these amino acids introduced mild, but meaningful effects in lipid-bound P0ct. Lys236 gradually presented differences when proceeding from the wild-type to a deletion of Lys236, and finally to a charge-inverting mutant, K236E. Vesicle aggregation was most notably affected, indicating that Lys236 could be important for a potential vesicle fusion or stacking function. The mutation of Arg227 into a Ser deletes a positive charge, indicating that Arg227 could carry a role in charge neutralization and subsequent folding, as R227S underperformed in turbidity experiments and produced slightly loosened repeat

distances in SAXD. The impact of R227S might be independent of UPR activation, as R227S has been shown to undergo normal trafficking from the ER to the plasma membrane and the disease phenotype arises only when myelin is properly matured⁴²⁹. Arg227 and Lys236 could thus be speculated to be involved in forming ionic interactions with phospholipid headgroups, driving the charge neutralization, folding and membrane insertion of P0ct.

To elucidate the membrane insertion mechanism of P0ct, NR was performed. A striking difference to MBP was the complete insertion of P0ct into the SLB, without displaying a major non-inserted protein segment that could participate in intermembrane adhesion. Additionally, the binding of P0ct increased the roughness of the entire system, indicating notable mobility of the membrane (Fig. 13). This might be an effect arising from altered fluidity, which could be linked to the destabilized lipid population observed in DSC.

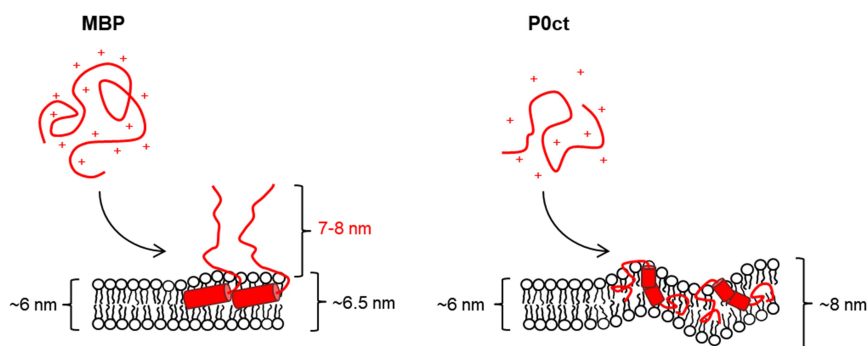


Fig. 13. The membrane insertion differences of MBP and P0ct. Based on NR data, the membrane association of MBP results in partial protein insertion to the bilayer, slightly increasing membrane thickness. A notably thick protein layer forms over the membrane. P0ct undergoes nearly complete membrane insertion, also increasing the membrane thickness, but as opposed to MBP, only a small portion of P0ct remains on the membrane surface. The roughness of the membrane changes drastically, indicating increased lipid fluidity and/or membrane undulation.

Since P0ct was found to participate in membrane-bridging (**Article II**), and the MDL in the PNS is known to form correctly in the absence of MBP and P2⁹⁸, P0ct is left with two options for achievable membrane stacking: either P0ct inserts into a membrane and bridges two membranes together across the MDL by interacting with another P0ct molecule, or P0ct interacts with or fully inserts into an apposing membrane across the MDL, whilst the transmembrane domain remains on the other side of the MDL (Fig. 14). At this point, it remains difficult to answer which mechanism is correct; logically thinking the latter should be impossible, given that P0ct is attracted to a phospholipid membrane directly after translation. Additionally, P0ct becomes fatty acylated at Cys182^{247, 248}, which anchors into a membrane. Given that P0ct is translated together with full length P0, its membrane-bound state is destined before it reaches the stacked compact myelin, as will be described below. As shown by NR, D224Y and P0ct wild-type appeared identical on a single SLB, which indicates that the mutation does not influence the insertion of P0ct into a single membrane directly, but it is likely to enable specific interactions that result in tightly stacked membranes. These interactions remain to be further elucidated.

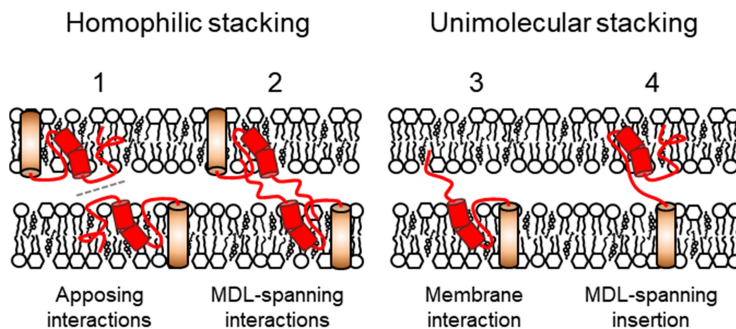


Fig. 14. Possible membrane stacking modes of P0ct. The P0ct-mediated bridging of two apposing membranes together in MDL formation/stability can be speculated to occur through several different arrangements. Homophilic stacking involves either P0ct being fully present in one membrane and weakly interacting with an apposing P0ct molecule (1) or spanning the MDL, forming an oligomer with an apposing P0ct molecule (2). Another possibility is unimolecular stacking, which lacks the formation of oligomeric states. These could occur through P0ct directly interacting with the apposing membrane (3) or by fully inserting into the apposing membrane (4). P0ct is shown in red and the transmembrane helix of P0 is shown in copper. For clarity, the Ig-like domain has not been drawn.

Compared to wild-type P0ct, the results appear mild for all other mutants except D224Y. It should be acknowledged that the characterization in this study is limited, as the samples involve only the cytoplasmic ‘soluble’ part of P0 instead of the full-length protein. The transmembrane segment that could largely influence the conformation and/or depth of P0ct in the membrane is absent. Obviously, P0ct is not translated alone *in vivo*, but as a part of P0 that needs to be inserted into the ER membrane before undergoing PTMs and trafficking to the plasma membrane *via* the Golgi apparatus^{256, 430}.

Model lipid compositions were employed in this study, which work well with the chosen methods but might influence the behaviour of the proteins. In a native myelin lipid composition, differences between the mutant variants may be larger. Additionally, the membrane lipid composition changes when transiting from the ER to the Golgi apparatus and finally to the plasma membrane⁴³¹. The lipid composition of the ER should be included in the study of these particular mutants, as many of them have been reported to induce UPR³⁴⁰. Misfolded P0ct in the ER membrane might cause the aggregation and/or unfolding of P0, resulting in ER stress. Disease mechanisms possibly arising from P0 trafficking, such as directly removing or modifying the YAMM-motif as in the case of A221T²⁵⁶, are not covered in this study, nor is the activation of the unfolded protein response. These remain possible scenarios in CMT disease etiology involving the mutants at hand. This being stated, future studies should involve animal and cell culture studies that allow the pinpointing of P0 and P0ct in mutant models⁴³², combined with structural studies from nerve sections.

5.6. FUTURE CONSIDERATIONS

The ensemble of methods described in this thesis is useful for probing the conformation and lipid-binding properties of basic proteins, assuming adequate QC. This biophysical approach would benefit from the inclusion of several other methods as well as complementation using cell culture studies and experiments on natural myelin extracts. Nevertheless, the study paves way for the characterization of other proteins, domains, and peptides that harbour similar molecular characteristics as MBP and P0ct, as well as the expansion of the study on these two proteins.

As the methodology is now established, it will be straightforward to include more lipid compositions. The use of PEs as phospholipids or plasmalogens would make the lipid composition more physiologically relevant. As shown by the SRCD experiments on P0ct in **Article II**, myelin- and EAE-like phospholipid compositions can be included. It is worth mentioning that similar compositions were also used for MBP, but the data were deemed unusable due to the strong CD signal of cholesterol and light scattering arising from vesicle aggregation (data not shown). Studies with more physiologically relevant lipid compositions are required, and notable progress has been made recently^{200, 204}. More complex sample compositions will not only change the ratios of lipids in vesicles or SLBs, but are also likely to introduce various phase domains to the system *via* lipid segregation and internal interactions in the lipid structures^{62, 350, 351}. In such cases, AFM could prove to be useful, as it is capable of distinguishing rafts and patches of different lipid phases in a membrane sample³⁹⁵.

An addition that could complement AFM studies in distinguishing the time-resolved formation of lipid domains or changes in a membrane structure is Brewster angle microscopy⁴³³. The method is often used together with NR, as NR is unable to distinguish lateral heterogeneity in the sample⁴³⁴. The use of a quartz crystal microbalance with dissipation, which complements SPR by providing association and dissociation data of proteins binding to supported lipid structures, can provide additional information about the stiffness and thickness of the studied system⁴³⁵. GISAS using neutrons and X-rays could help in uncovering lateral organization in a protein-SLB system⁴³⁶. These point-collimated methods would be greatly

complemented by methods providing a picture of lateral surface structures, like AFM and the above-mentioned Brewster angle microscopy. Additionally, infrared spectroscopy could allow *in situ* spectroscopic characterization of protein-lipid systems in SLB samples simultaneously to NR or GISAS measurements^{437, 438}, and solid-state NMR spectroscopy⁴³⁹ could prove extremely useful for uncovering the molecular determinants in protein-lipid samples described in this thesis. While NMR spectroscopy is not a new method in the characterization of MBP⁷⁰, P0ct has not been studied with NMR, and its small size would definitely enable such experiments.

Hydrogen-deuterium exchange of lipid-bound MBP and P0ct might provide useful information about solvent-exposed surfaces⁴⁴⁰ and intein-mediated coupling of protein segments could be used to produce partially labeled full-length proteins⁴⁴¹, introducing contrast variation in methods like NR. Single-residue labeling in proteins and peptide fragments might enable the probing of orientational parameters of specific protein segments. Such experiments have been performed for integral membrane proteins and amphipathic peptides using ¹⁹F labels and solid-state NMR spectroscopy^{442, 443}. Similar SLB experiments as described here using NR should be pursued to uncover which peptide segment(s) of MBP initially insert into the membrane to produce the pre-stack state³⁴².

A logical step further would be to screen different ionic conditions and their impact on the activity of MBP and P0ct. K⁺ is an abundant ion in myelin³⁵. The results of **Article III** suggest that the choice of monovalent anion, in this case Cl⁻ vs. F⁻, has negligible impact on protein function, but similar comparative experiments remain to be performed for monovalent cations. An attractive choice of divalent cation to include in follow-up studies is Zn²⁺, the most abundant trace element in myelin³⁴. Zn²⁺ has relevance in demyelinating conditions^{444, 445} and has been shown to interact with MBP^{171, 446-450}. In compact myelin, Zn²⁺ is likely to interact with phospholipid headgroups within the tight cytoplasmic compartment^{451, 452}.

As already discussed above, the inclusion of more relevant lipid compositions should be done eventually – especially the presence of cholesterol is highly desired^{60, 61, 197, 198, 453}. The unique lipid composition of the cytoplasmic myelin monolayer, and the

related changes in lipid proportions in disease^{57, 58}, presents a putative disease-inducing mechanism, especially when combined with amino acid changes in myelin proteins, such as mutations or PTMs. The impact on protein binding by individual lipid components, such as PE, has been demonstrated by others^{197, 198}.

Protein modifications involved in demyelinating conditions^{212, 407} should also be characterized. While a substantial amount of literature is available regarding the impact of citrullination on MBP and its function^{210, 211, 225, 407, 454, 455}, membrane-binding characterizations involving phosphorylated variants or phosphomimicking mutants is lacking. Phosphorylation has a similar impact on the net charge of MBP as citrullination, but the reversibility of phosphorylation allows natural regulatory mechanisms to exist. When disturbed, however, similar consequences that stem from heavy citrullination could be speculated to surface in the form of demyelination, especially since MBP-phosphorylation levels are known to be age-dependent and altered in MS^{212, 456}.

Proteins involved in myelination, myelin maintenance, and demyelination are all attractive characterization targets, MOBP being a very notable candidate. The true function of MOBP in myelin is not known, but it MOBP is likely to be partially unfolded, since it possesses similar amino acid content as MBP⁷³. MOBP has a putative FYVE-domain⁷⁶, implying Zn²⁺ binding and interactions with PIs⁴⁵⁷, thus possibly harboring a segregation role for lipids and Zn²⁺.

The study of isolated peptide segments is also of interest, including the intracellular loops of the tetraspan protein PLP³²⁴, as well as smaller other segments of PLP or PMP22. Both proteins are among some of the most hydrophobic proteins in humans^{458, 459}, which is a reason why high resolution structural data remains unavailable⁸⁶, not to mention the structural relationship to the (putative) function of these integral transmembrane proteins.

Multiprotein systems should be pursued to uncover any synergistic and competitive systems. MBP and P2 have been demonstrated to work together⁸⁹, and the involvement of PLP, PMP22 and P0 should be studied as well, since interactions

between these proteins are known to exist²⁴⁰. To conclude, it cannot be stressed enough that basic research involving biophysical approaches is required to understand disease conditions, especially arising from a biological environment of such a unique molecular composition as that found in myelin.

6 CONCLUDING REMARKS

A biophysical characterization of MBP, P0ct, and its disease mutants has been performed in this thesis. Through an *in vitro* characterization, the structure-function relationships of MBP and P0ct in the MDL are starting to unravel. MBP, a classical membrane-stacker in compact myelin cytoplasm, appears to be heavily dependent on its translation and modification levels, as a pre-stack state, which might be a key factor in the molecular etiology of demyelination, precedes the formation of the MDL. This pre-stack state is likely to be influenced by the ionic content and lipid composition present at a given time, as changes in these two parameters have been shown to be altered in MS-like conditions. Indeed, the characterization described here raises an important factor in MBP-mediated membrane stacking outside of PTMs: the charge-balance arising from general ionic content, the presence of divalent cations, and phospholipid net charge.

P0ct is the short cytoplasmic domain of P0 – a poorly characterized segment that shares many similarities to MBP in terms of folding and function. The importance of P0ct might very well be in MDL formation, especially since MBP, which is very abundant in the CNS, is not as prominent in the PNS and is not required for MDL formation *in vivo*⁹⁸. The true membrane-bridging mode of P0ct remains to be determined, but putative models have been proposed for achieving the stable MDL ultrastructure in the PNS, where P0 dominates over all other proteins in terms of quantity. These proteins include P2, which does harbour membrane stacking properties but appears to be redundant in mice when the formation of peripheral myelin is followed⁹⁸. The current study shows that some mutations in P0ct have relevance in CMT pathology outside of UPR induction, most notably explaining the hypermyelinating activity of the mutant D224Y, which presents a unique phenotype

on the cellular level³³⁶. Key amino acids relevant for the folding and membrane stacking function of P0ct have also been identified.

To conclude, the current study evokes new directions in the study of myelin proteins. Biophysical studies are a necessity to understand the structure-function relationships of proteins on the biomolecular level, especially in a biologically unique, lipid-rich environment such as myelin. The approach described here enables strict control over the studied proteins and conditions, and robust, established systems can be further expanded to more physiologically relevant conditions that allow the dissection of molecular fundamentals of myelin formation and stability in health and disease. Incurable demyelinating diseases remain as such until novel remedies are developed, and such developments cannot be performed without adequate basic characterizations of the affected biological systems.

REFERENCES

1. Leppäluoto, J. *et al.* in *Anatomia ja fysiologia - Rakenteesta toimintaan* 392-422 (WSOY, Helsinki, 2007).
2. Purves, D. *et al.* *Neuroscience*. **3**, 773 (2004).
3. Bean, B. P. The action potential in mammalian central neurons. *Nat. Rev. Neurosci.* **8**, 451-465 (2007).
4. Virchow, R. Über das ausgebreitete Vorkommen einer dem Nervenmark analogen Substanz in den tierischen Geweben. *Virchows Arch. Pathol. Anat.* **6**, 562-572 (1854).
5. Hartline, D. K. What is myelin? *Neuron Glia. Biol.* **4**, 153-163 (2008).
6. Stassart, R. M., Möbius, W., Nave, K. & Edgar, J. M. The Axon-Myelin Unit in Development and Degenerative Disease. *Front. Neurosci.* **12**, 467 (2018).
7. Snaidero, N. & Simons, M. Myelination at a glance. *J. Cell. Sci.* **127**, 2999-3004 (2014).
8. Debanne, D., Campanac, E., Bialowas, A., Carlier, E. & Alcaraz, G. Axon Physiology. *Physiol. Rev.* **91**, 555-602 (2011).
9. Nave, K. Myelination and the trophic support of long axons. *Nat. Rev. Neurosci.* **11**, 275-283 (2010).
10. Lee, Y. *et al.* Oligodendroglia metabolically support axons and contribute to neurodegeneration. *Nature* **487**, 443-U1502 (2012).
11. Morrison, B. M., Lee, Y. & Rothstein, J. D. Oligodendroglia: metabolic supporters of axons. *Trends Cell. Biol.* **23**, 644-651 (2013).
12. Wang, S. S. H. *et al.* Shaping of white matter composition by biophysical scaling constraints. *J. Neurosci.* **28**, 4047-4056 (2008).
13. Weickenmeier, J., de Rooij, R., Budday, S., Ovaert, T. C. & Kuhl, E. The mechanical importance of myelination in the central nervous system. *J. Mech. Behav. Biomed. Mater.* **76**, 119-124 (2017).

14. Duncan, A., Ibrahim, M., Berry, M. & Butt, A. Transfer of horseradish peroxidase from oligodendrocyte to axon in the myelinating neonatal rat optic nerve: Artefact or transcellular exchange? *Glia* **17**, 349-355 (1996).
15. Court, F. A., Hendriks, W. T. J., MacGillavry, H. D., Alvarez, J. & Van Minnen, J. Schwann Cell to Axon Transfer of Ribosomes: Toward a Novel Understanding of the Role of Glia in the Nervous System. *J. Neurosci.* **28**, 11024-11029 (2008).
16. Bradl, M. & Lassmann, H. Oligodendrocytes: biology and pathology. *Acta Neuropathol.* **119**, 37-53 (2010).
17. Salzer, J. L. & Zalc, B. Myelination. *Curr. Biol.* **26**, R971-R975 (2016).
18. Lundgaard, I. *et al.* Neuregulin and BDNF Induce a Switch to NMDA Receptor-Dependent Myelination by Oligodendrocytes. *PLoS Biol.* **11**, e1001743 (2013).
19. Bélanger, M. & Magistretti, P. J. The role of astroglia in neuroprotection. *Dialogues in clinical neuroscience* **11**, 281-295 (2009).
20. Cragg, B. & Thomas, P. The Relationships between Conduction Velocity and the Diameter and Internodal Length of Peripheral Nerve Fibres. *J. Physiol.* **136**, 606-614 (1957).
21. Young, J. Z. The functioning of the giant nerve fibres of the squid. *Jour. Exp. Biol.* **15**, 170-185 (1938).
22. Zalc, B., Goujet, D. & Colman, D. The origin of the myelination program in vertebrates. *Curr. Biol.* **18**, R511-R512 (2008).
23. Kidd, G. J., Ohno, N. & Trapp, B. D. Biology of Schwann cells. *Handb. Clin. Neurol.* **115**, 55-79 (2013).
24. Court, F. A., Wrabetz, L. & Feltri, M. L. Basal lamina: Schwann cells wrap to the rhythm of space-time. *Curr. Opin. Neurobiol.* **16**, 501-507 (2006).
25. Salzer, J. L. Schwann Cell Myelination. *Cold Spring Harbor Perspect. Biol.* **7**, a020529 (2015).
26. Trapp, B. D., Kidd, G. J., Pfeiffer, S. E. & Anitei, M. in *Myelin Biology and Disorders* (ed Lazzarini, R. A. *et al.*) 29-55 (Academic Press, 2004).
27. Taveggia, C. *et al.* Neuregulin-1 type III determines the ensheathment fate of axons. *Neuron* **47**, 681-694 (2005).
28. Su, Z. & He, C. Olfactory ensheathing cells Biology in neural development and regeneration. *Prog. Neurobiol.* **92**, 517-532 (2010).
29. Fontenas, L. & Kucenas, S. Motor Exit Point (MEP) Glia: Novel Myelinating Glia That Bridge CNS and PNS Myelin. *Front. Cell. Neurosci.* **12**, 333 (2018).
30. Lopachin, R., Castiglia, C. & Saubermann, A. Elemental Composition and Water-Content of Myelinated Axons and Glial-Cells in Rat Central-Nervous-System. *Brain Res.* **549**, 253-259 (1991).

31. Boggs, J. & Moscarello, M. Structural Organization of Human Myelin Membrane. *Biochim. Biophys. Acta* **515**, 1-21 (1978).
32. Guidotti, G. Membrane Proteins. *Annu. Rev. Biochem.* **41**, 731-752 (1972).
33. Hallermayer, G. & Neupert, W. Lipid-Composition of Mitochondrial Outer and Inner Membranes of Neurospora-Crassa. *Hoppe-Seylers Z. Physiol. Chem.* **355**, 279-288 (1974).
34. Bourre, J. M. *et al.* Occurrence of manganese, copper and zinc in myelin. Alterations in the peripheral nervous system of dysmyelinating trembler mutant are at variance with brain mutants (quaking and shiverer). *Neurochem. Int.* **10**, 281-286 (1987).
35. Stys, P. K., Lehning, E., Saubermann, A. J. & LoPachin, R. M. Intracellular Concentrations of Major Ions in Rat Myelinated Axons and Glia: Calculations Based on Electron Probe X-Ray Microanalyses. *J. Neurochem.* **68**, 1920-1928 (1997).
36. Pereira, J. A., Lebrun-Julien, F. & Suter, U. Molecular mechanisms regulating myelination in the peripheral nervous system. *Trends. Neurosci.* **35**, 123-134 (2012).
37. Micu, I., Plemel, J. R., Caprariello, A. V., Nave, K. & stys, P. K. Axo-myelinic neurotransmission: a novel mode of cell signalling in the central nervous system. *Nat. Rev. Neurosci.* **19**, 49-57 (2018).
38. Fünfschilling, U. *et al.* Glycolytic oligodendrocytes maintain myelin and long-term axonal integrity. *Nature* **485**, 517-523 (2012).
39. Poliak, S. & Peles, E. The local differentiation of myelinated axons at nodes of Ranvier. *Nat. Rev. Neurosci.* **4**, 968-980 (2003).
40. Robertson, J. D. in *Molecular Biology. Elementary Processes of Nerve Conduction and Muscle Contraction* (ed Nachmansohn, D.) 87-151 (Academic Press, New York, 1960).
41. Robertson, J. D. The Early Days of Electron-Microscopy of Nerve-Tissue and Membranes. *Int. Rev. Cytol.* **100**, 129-201 (1987).
42. Meller, K. Cryoelectron Microscopy of Vitriified Nerve Myelin. *Cell Tissue Res.* **262**, 59-66 (1990).
43. Avila, R. *et al.* Structure and stability of internodal myelin in mouse models of hereditary neuropathy. *J. Neuropathol. Exp. Neurol.* **64**, 976-990 (2005).
44. Schmitt, F.,O, Bear, R.,S & Clark, G.,L. The Role of Lipoids in the X-Ray Diffraction Patterns of Nerve. *Science* **82(2115)**, 44-45 (1935).
45. Schmitt, F. O., Bear, R. S. & Palmer, K. J. X-ray diffraction studies on the structure of the nerve myelin sheath. *J. Cell. Physiol.* **18**, 31-42 (1941).
46. Peters, A. Radial Component of Central Myelin Sheaths. *J. Biophys. Biochem. Cytol.* **11**, 733-& (1961).

47. Kosaras, B. & Kirschner, D. Radial Component of Cns Myelin - Junctional Subunit Structure and Supramolecular Assembly. *J. Neurocytol.* **19**, 187-199 (1990).
48. Simons, M. & Nave, K. Oligodendrocytes: Myelination and Axonal Support. *Cold Spring Harbor Perspect. Biol.* **8**, a020479 (2016).
49. Ushiki, T. & Ide, C. Scanning Electron-Microscopic Studies of the Myelinated Nerve-Fibers of the Mouse Sciatic-Nerve with Special Reference to the Schwann-Cell Cytoplasmic Network External to the Myelin Sheath. *J. Neurocytol.* **16**, 737-747 (1987).
50. Salzer, J. Polarized domains of myelinated axons. *Neuron* **40**, 297-318 (2003).
51. Aggarwal, S., Yurlova, L. & Simons, M. Central nervous system myelin: structure, synthesis and assembly. *Trends Cell Biol.* **21**, 585-593 (2011).
52. Gopalakrishnan, G. *et al.* Lipidome and proteome map of myelin membranes. *J. Neurosci. Res.* **91**, 321-334 (2013).
53. Morell, P. & Quarles, R. H. in *Basic Neurochemistry: Molecular, Cellular and Medical Aspects* (eds Siegel, G. J., Agranoff, B. W., Albers, R. W., Fisher, S. K. & Uhler, M. D.) (Lippincott-Raven, Philadelphia, 1999).
54. Farooqui, A. & Horrocks, L. Plasmalogens: Workhorse lipids of membranes in normal and injured neurons and glia. *Neuroscientist* **7**, 232-245 (2001).
55. Chia, L., Thompson, J. & Moscarello, M. Alteration of Lipid-Phase Behavior in Multiple-Sclerosis Myelin Revealed by Wide-Angle X-Ray-Diffraction. *Proc. Natl. Acad. Sci. U. S. A.* **81**, 1871-1874 (1984).
56. Kiessling, V., Wan, C. & Tamm, L. K. Domain coupling in asymmetric lipid bilayers. *Biochim. Biophys. Acta-Biomembr.* **1788**, 64-71 (2009).
57. Ohler, B. *et al.* Role of lipid interactions in autoimmune demyelination. *Biochim. Biochem. Acta-Mol. Basis Dis.* **1688**, 10-17 (2004).
58. Min, Y. *et al.* Interaction forces and adhesion of supported myelin lipid bilayers modulated by myelin basic protein. *Proc. Natl. Acad. Sci. U. S. A.* **106**, 3154-3159 (2009).
59. de Meyer, F. & Smit, B. Effect of cholesterol on the structure of a phospholipid bilayer. *Proc. Natl. Acad. Sci. U. S. A.* **106**, 3654-3658 (2009).
60. Saher, G. *et al.* High cholesterol level is essential for myelin membrane growth. *Nat. Neurosci.* **8**, 468-475 (2005).
61. Saher, G., Quintes, S. & Nave, K. Cholesterol: a novel regulatory role in myelin formation. *Neuroscientist* **17**, 79-93 (2011).
62. García-Arribas, A. B., Alonso, A. & Goñi, F. M. Cholesterol interactions with ceramide and sphingomyelin. *Chem. Phys. Lipids.* **199**, 26-34 (2016).
63. Mittendorf, K. F. *et al.* Peripheral myelin protein 22 alters membrane architecture. *Sci. Adv.* **3**, e1700220 (2017).

64. Chrast, R., Saher, G., Nave, K. & Verheijen, M. H. G. Lipid metabolism in myelinating glial cells: lessons from human inherited disorders and mouse models. *J. Lipid Res.* **52**, 419-434 (2011).
65. Aggarwal, S. *et al.* A Size Barrier Limits Protein Diffusion at the Cell Surface to Generate Lipid-Rich Myelin-Membrane Sheets. *Dev. Cell* **21**, 445-456 (2011).
66. de Monasterio-Schrader, P. *et al.* Systematic approaches to central nervous system myelin. *Cell. Mol. Life Sci.* **69**, 2879-2894 (2012).
67. Rosenbluth, J., Stoffel, W. & Schiff, R. Myelin structure in proteolipid protein (PLP)-null mouse spinal cord. *J. Comp. Neurol.* **371**, 336-344 (1996).
68. Palaniyar, N., Semotok, J., Wood, D., Moscarello, M. & Harauz, G. Human proteolipid protein (PLP) mediates winding and adhesion of phospholipid membranes but prevents their fusion. *Biochim. Biophys. Acta-Biomembr.* **1415**, 85-100 (1998).
69. Rosenbluth, J., Nave, K., Mierzwa, A. & Schiff, R. Subtle myelin defects in PLP-null mice. *Glia* **54**, 172-182 (2006).
70. Vassall, K. A., Bamm, V. V. & Harauz, G. MyelStones: the executive roles of myelin basic protein in myelin assembly and destabilization in multiple sclerosis. *Biochem. J.* **472**, 17-32 (2015).
71. Yamamoto, Y. *et al.* Myelin-associated oligodendrocytic basic protein is essential for normal arrangement of the radial component in central nervous system myelin. *Eur. J. Neurosci.* **11**, 847-855 (1999).
72. Yoshikawa, H. Myelin-associated oligodendrocytic basic protein modulates the arrangement of radial growth of the axon and the radial component of myelin. *Medical Electron Microscopy* **34**, 160-164 (2001).
73. Montague, P., McCallion, A., Davies, R. & Griffith, I. Myelin-Associated Oligodendrocytic Basic Protein: A Family of Abundant CNS Myelin Proteins in Search of a Function. *Dev. Neurosci.* **28**, 479-487 (2006).
74. Holz, A., Bielekova, B., Martin, R. & Oldstone, M. Myelin-associated oligodendrocytic basic protein: Identification of an encephalitogenic epitope and association with multiple sclerosis. *J. Immunol.* **164**, 1103-1109 (2000).
75. de Rosbo, N. *et al.* The myelin-associated oligodendrocytic basic protein region MOBP15-36 encompasses the immunodominant major encephalitogenic epitope(s) for SJL/J mice and predicted epitope(s) for multiple sclerosis-associated HLA-DRB1*1501. *J. Immunol.* **173**, 1426-1435 (2004).
76. Kursula, P. Structural properties of proteins specific to the myelin sheath. *Amino Acids* **34**, 175-185 (2008).
77. Brunner, C., Lassmann, H., Waehneltd, T., Matthieu, J. & Linigton, C. Differential Ultrastructural-Localization of Myelin Basic-Protein, Myelin

- Oligodendroglial Glycoprotein, and 2',3'-Cyclic Nucleotide 3'-Phosphodiesterase in the Cns of Adult-Rats. *J. Neurochem.* **52**, 296-304 (1989).
78. Delarasse, C. *et al.* Complex alternative splicing of the myelin oligodendrocyte glycoprotein gene is unique to human and non-human primates. *J. Neurochem.* **98**, 1707-1717 (2006).
 79. Boyle, L. H., Traherne, J. A., Plotnek, G., Ward, R. & Trowsdale, J. Splice variation in the cytoplasmic domains of myelin oligodendrocyte glycoprotein affects its cellular localisation and transport. *J. Neurochem.* **102**, 1853-1862 (2007).
 80. Reindl, M. & Rostasy, K. MOG antibody-associated diseases. *Neurol. - Neuroimmunol. Neuroinflammation* **2**, e60 (2015).
 81. Delarasse, C. *et al.* Myelin/oligodendrocyte glycoprotein-deficient (MOG-deficient) mice reveal lack of immune tolerance to MOG in wild-type mice. *J. Clin. Invest.* **112**, 544-553 (2003).
 82. Patzig, J. *et al.* Quantitative and Integrative Proteome Analysis of Peripheral Nerve Myelin Identifies Novel Myelin Proteins and Candidate Neuropathy Loci. *J. Neurosci.* **31**, 16369-16386 (2011).
 83. Filbin, M., Walsh, F., Trapp, B., Pizzey, J. & Tennekoon, G. Role of Myelin Po Protein as a Homophilic Adhesion Molecule. *Nature* **344**, 871-872 (1990).
 84. Lee, S. *et al.* PMP22 Is Critical for Actin-Mediated Cellular Functions and for Establishing Lipid Rafts. *J. Neurosci.* **34**, 16140-16152 (2014).
 85. Suzuki, H. *et al.* Crystal Structure of a Claudin Provides Insight into the Architecture of Tight Junctions. *Science* **344**, 304-307 (2014).
 86. Mittendorf, K. F., Kroncke, B. M., Meiler, J. & Sanders, C. R. The Homology Model of PMP22 Suggests Mutations Resulting in Peripheral Neuropathy Disrupt Transmembrane Helix Packing. *Biochemistry (N. Y.)* **53**, 6139-6141 (2014).
 87. Greenfield, S., Brostoff, S., Eylar, E. H. & Morell, P. Protein composition of myelin of the peripheral nervous system. *J. Neurochem.* **20**, 1207-1216 (1973).
 88. Trapp, B., McIntyre, L., Quarles, R., Sternberger, N. & Webster, H. Immunocytochemical Localization of Rat Peripheral Nervous-System Myelin Proteins - P2-Protein is Not a Component of all Peripheral Nervous-System Myelin Sheaths. *Proc. Natl. Acad. Sci. U. S. A.* **76**, 3552-3556 (1979).
 89. Suresh, S., Wang, C., Nanekar, R., Kursula, P. & Edwardson, J. M. Myelin basic protein and myelin protein 2 act synergistically to cause stacking of lipid bilayers. *Biochemistry* **49**, 3456-3463 (2010).
 90. Knoll, W. *et al.* Structural and dynamical properties of reconstituted myelin sheaths in the presence of myelin proteins MBP and P2 studied by neutron scattering. *Soft Matter* **10**, 519-529 (2014).

91. Cowan, S., Newcomer, M. & Jones, T. Crystallographic Studies on a Family of Cellular Lipophilic Transport Proteins - Refinement of P2 Myelin Protein and the Structure Determination and Refinement of Cellular Retinol-Binding Protein in Complex with All-Trans-Retinol. *J. Mol. Biol.* **230**, 1225-1246 (1993).
92. Hunter, D. *et al.* Structure of myelin P2 protein from equine spinal cord. *Acta Cryst.* **D61**, 1067-1071 (2005).
93. Majava, V. *et al.* Structural and Functional Characterization of Human Peripheral Nervous System Myelin Protein P2. *PLoS One* **5**, e10300 (2010).
94. Ruskamo, S. *et al.* Atomic resolution view into the structure-function relationships of the human myelin peripheral membrane protein P2. *Acta Cryst.* **D70**, 165-176 (2014).
95. Laulumaa, S. *et al.* Dynamics of the peripheral membrane protein P2 from human myelin measured by neutron scattering—A comparison between wild-type protein and a hinge mutant. *PLoS One* **10**, e0128954 (2015).
96. Ruskamo, S. *et al.* Molecular mechanisms of Charcot-Marie-Tooth neuropathy linked to mutations in human myelin protein P2. *Sci. Rep.* **7**, 6510 (2017).
97. Laulumaa, S. *et al.* Structure and dynamics of a human myelin protein P2 portal region mutant indicate opening of the beta barrel in fatty acid binding proteins. *BMC Struct. Biol.* **18**, 8 (2018).
98. Zenker, J. *et al.* A role of peripheral myelin protein 2 in lipid homeostasis of myelinating Schwann cells. *Glia* **62**, 1502-1512 (2014).
99. Baumann, N. & Pham-Dinh, D. Biology of oligodendrocyte and myelin in the mammalian central nervous system. *Physiol. Rev.* **81**, 871-927 (2001).
100. Sherman, D. L., Wu, L. M. N., Grove, M., Gillespie, C. S. & Brophy, P. J. Drp2 and Periaxin Form Cajal Bands with Dystroglycan But Have Distinct Roles in Schwann Cell Growth. *J. Neurosci.* **32**, 9419-9428 (2012).
101. Brennan, K. M. *et al.* Absence of Dystrophin Related Protein-2 disrupts Cajal bands in a patient with Charcot-Marie-Tooth disease. *Neuromusc. Disord.* **25**, 786-793 (2015).
102. Snaidero, N. *et al.* Antagonistic functions of MBP and CNP establish cytosolic channels in CNS myelin. *Cell Rep.* **18**, 314-323 (2017).
103. Jahn, O., Tenzer, S. & Werner, H. B. Myelin Proteomics: Molecular Anatomy of an Insulating Sheath. *Mol. Neurobiol.* **40**, 55-72 (2009).
104. Agrawal, H. C., Sprinkle, T. J. & Agrawal, D. 2',3'-Cyclic Nucleotide-3'-Phosphodiesterase in the Central-Nervous-System is Fatty-Acylated by Thioester Linkage. *J. Biol. Chem.* **265**, 11849-11853 (1990).
105. DeAngelis, D. A. & Braun, P. E. Isoprenylation of Brain 2',3'-Cyclic Nucleotide 3'-Phosphodiesterase Modulates Cell Morphology. *J. Neurosci. Res.* **39**, 386-397 (1994).

106. Lee, J., Gravel, M., Zhang, R., Thibault, P. & Braun, P. Process outgrowth in oligodendrocytes is mediated by CNP, a novel microtubule assembly myelin protein. *J. Cell Biol.* **170**, 661-673 (2005).
107. De Angelis, D. A. & Braun, P. E. 2',3'-Cyclic Nucleotide 3'-Phosphodiesterase Binds to Actin-Based Cytoskeletal Elements in an Isoprenylation-Independent Manner. *J. Neurochem.* **67**, 943-951 (1996).
108. Verrier, J. D. *et al.* Expression of the 2',3'-cAMP-adenosine pathway in astrocytes and microglia. *J. Neurochem.* **118**, 979-987 (2011).
109. Verrier, J., Jackson, T., Bansal, R., Kochanek, P. M. & Jackson, E. Oligodendrocyte 2',3'-Cyclic Nucleotide 3'-Phosphodiesterase Participates in Localized Adenosine Production: Possible Role in Traumatic Brain Injury. *J. Neurotrauma* **29**, A168-A169 (2012).
110. Verrier, J. D. *et al.* The brain in vivo expresses the 2',3'-cAMP-adenosine pathway. *J. Neurochem.* **122**, 115-125 (2012).
111. Drummond, G. & Perrott-Yee, S. Enzymatic Hydrolysis of Adenosine 3',5'-Phosphoric Acid. *J. Biol. Chem.* **236**, 1126-1129 (1961).
112. Drummond, G. I., Iyer, N. T. & Keith, J. Hydrolysis of ribonucleoside 2',3'-cyclic phosphates by a diesterase from brain. *J. Biol. Chem.* **237**, 3535-3539 (1962).
113. Raasakka, A. *et al.* Determinants of ligand binding and catalytic activity in the myelin enzyme 2',3'-cyclic nucleotide 3'-phosphodiesterase. *Sci. Rep.* **5**, 16520 (2015).
114. Verrier, J. D. *et al.* Role of CNPase in the oligodendrocytic extracellular 2',3'-cAMP-adenosine pathway. *Glia* **61**, 1595-1606 (2013).
115. Azarashvili, T. *et al.* Ca²⁺-dependent permeability transition regulation in rat brain mitochondria by 2',3'-cyclic nucleotides and 2',3'-cyclic nucleotide 3'-phosphodiesterase. *Am. J. Physiol. Cell Physiol.* **296**, C1428-C1439 (2009).
116. Bifulco, M., Laezza, C., Stingo, S. & Wolff, J. 2',3'-Cyclic nucleotide 3'-phosphodiesterase: A membrane-bound, microtubule-associated protein and membrane anchor for tubulin. *Proc. Natl. Acad. Sci. U. S. A.* **99** (2002).
117. Berggard, T. *et al.* 140 Mouse brain proteins identified by Ca²⁺-calmodulin affinity chromatography and tandem mass spectrometry. *J. Proteome Res.* **5**, 669-687 (2006).
118. Gravel, M. *et al.* 2',3'-Cyclic Nucleotide 3'-Phosphodiesterase: A Novel RNA-Binding Protein That Inhibits Protein Synthesis. *J. Neurosci. Res.* **87**, 1069-1079 (2009).
119. Myllykoski, M. *et al.* The N-terminal domain of the myelin enzyme 2',3'-cyclic nucleotide 3'-phosphodiesterase: Direct molecular interaction with the calcium sensor calmodulin. *J. Neurochem.* **123**, 515-524 (2012).

-
120. Maxwell, M. M. *et al.* The Sirtuin 2 microtubule deacetylase is an abundant neuronal protein that accumulates in the aging CNS. *Hum. Mol. Genet.* **20**, 3986-3996 (2011).
 121. Denninger, A. R. *et al.* Claudin-11 Tight Junctions in Myelin Are a Barrier to Diffusion and Lack Strong Adhesive Properties. *Biophys. J.* **109**, 1387-1397 (2015).
 122. Quarles, R. H. Myelin-associated glycoprotein (MAG): past, present and beyond. *J. Neurochem.* **100**, 1431-1448 (2007).
 123. Werner, H. B. *et al.* Proteolipid protein is required for transport of sirtuin 2 into CNS myelin. *J. Neurosci.* **27**, 7717-7730 (2007).
 124. Sherman, D. & Brophy, P. A tripartite nuclear localization signal in the PDZ-domain protein L-periaxin. *J. Biol. Chem.* **275**, 4537-4540 (2000).
 125. Han, H., Myllykoski, M., Ruskamo, S., Wang, C. & Kursula, P. Myelin-specific proteins: A structurally diverse group of membrane-interacting molecules. *Biofactors* **39**, 233-241 (2013).
 126. Dytrych, L., Sherman, D., Gillespie, C. & Brophy, P. Two PDZ domain proteins encoded by the murine periaxin gene are the result of alternative intron retention and are differentially targeted in Schwann cells. *J. Biol. Chem.* **273**, 5794-5800 (1998).
 127. Han, H. & Kursula, P. Periaxin and AHNAC Nucleoprotein 2 Form Intertwined Homodimers through Domain Swapping. *J. Biol. Chem.* **289**, 14121-14131 (2014).
 128. Yang, Y. & Shi, Y. L-periaxin interacts with S-periaxin through its PDZ domain. *Neurosci. Lett.* **609**, 23-29 (2015).
 129. Poitelon, Y. *et al.* A dual role for Integrin $\alpha 6\beta 4$ in modulating hereditary neuropathy with liability to pressure palsies. *J. Neurochem.* **145**, 245-257 (2018).
 130. Raasakka, A., Linxweiler, H., Brophy, P. J., Sherman, D. L. & Kursula, P. Direct binding of the flexible C-terminal segment of periaxin to $\beta 4$ integrin suggests a molecular basis for CMT4F. *bioRxiv* 524793 (2019).
 131. Yang, Y., Liang, M. & Shi, Y. Self-association of L-periaxin occurs via its acidic domain and NLS2/NLS3, and affects its trafficking in RSC96 cells. *RSC Adv.* **7**, 44112-44123 (2017).
 132. Scherer, S. *et al.* Connexin32 is a myelin-related protein in the PNS and CNS. *J. Neurosci.* **15**, 8281-8294 (1995).
 133. Kumar, N. & Gilula, N. The gap junction communication channel. *Cell* **84**, 381-388 (1996).
 134. Menichella, D., Goodenough, D., Sirkowski, E., Scherer, S. & Paul, D. Connexins are critical for normal myelination in the CNS. *J. Neurosci.* **23**, 5963-5973 (2003).

135. Kamasawa, N. *et al.* Connexin-47 and connexin-32 in gap junctions of oligodendrocyte somata, myelin sheaths, paranodal loops and Schmidt-Lanterman incisures: Implications for ionic homeostasis and potassium siphoning. *Neuroscience* **136**, 65-86 (2005).
136. Menichella, D. *et al.* Protein zero is necessary for E-cadherin-mediated adherens junction formation in Schwann cells. *Mol. Cell. Neurosci.* **18**, 606-618 (2001).
137. Young, P. *et al.* E-cadherin is required for the correct formation of autotypic adherens junctions of the outer mesaxon but not for the integrity of myelinated fibers of peripheral nerves. *Mol. Cell. Neurosci.* **21**, 341-351 (2002).
138. Tricaud, N., Perrin-Tricaud, C., Juan, J. & Rutishauser, U. Adherens junctions in myelinating Schwann cells stabilize Schmidt-Lanterman incisures via recruitment of p120 catenin to E-cadherin. *J. Neurosci.* **25**, 3259-3269 (2005).
139. Raasakka, A. & Kursula, P. The myelin membrane-associated enzyme 2',3'-cyclic nucleotide 3'-phosphodiesterase: on a highway to structure and function. *Neurosci. Bull.* **30**, 956-966 (2014).
140. Toyama, B. *et al.* Identification of Long-Lived Proteins Reveals Exceptional Stability of Essential Cellular Structures. *Cell* **154**, 971-982 (2013).
141. Einstein, E., Robertson, D., Moore, W. & DiCaprio, J. Isolation from Bovine Spinal Cord of a Homogeneous Protein with Encephalitogenic. *J. Neurochem.* **9**, 353-361 (1962).
142. Eylar, E. & Hashim, G. Allergic Encephalomyelitis - Structure of Encephalitogenic Determinant. *Proc. Natl. Acad. Sci. U. S. A.* **61**, 644-650 (1968).
143. Hashim, G. & Eylar, E. Structure of Terminal Regions of Encephalitogenic Basic Protein from Bovine Myelin. *Arch. Biochem. Biophys.* **135**, 324-333 (1969).
144. Palmer, F. B. & Dawson, R. M. C. The isolation and properties of experimental allergic encephalitogenic protein. *Biochem. J.* **111**, 629-636 (1969).
145. Eylar, E., Brostoff, S., Hashim, G., Caccam, J. & Burnett, P. Basic A1 Protein of Myelin Membrane - Complete Amino Acid Sequence. *J. Biol. Chem.* **246**, 5770-5784 (1971).
146. Moscarello, M. A. in *Cell Biology and Pathology of Myelin* (ed Juurlink, B. H. J. *et al.*) 13-22 (Plenum Press, New York, 1997).
147. Pribyl, T. *et al.* The Human Myelin Basic-Protein Gene is Included within a 179-Kilobase Transcription Unit - Expression in the Immune and Central Nervous Systems. *Proc. Natl. Acad. Sci. U. S. A.* **90**, 10695-10699 (1993).
148. Mendz, G., Barden, J. & Marteson, R. Conformation of a Tetradecapeptide Epitope of Myelin Basic-Protein. *Eur. J. Biochem.* **231**, 659-666 (1995).

-
149. Moscarello, M., Pang, H., Paceasciak, C. & Wood, D. The N Terminus of Human Myelin Basic-Protein Consists of C2, C4, C6, and C8 Alkyl Carboxylic-Acids. *J. Biol. Chem.* **267**, 9779-9782 (1992).
 150. Fernandes, A. *et al.* Identification of a protein that interacts with the Golli-Myelin basic protein and with nuclear-LIM interactor in the nervous system. *J. Neurosci. Res.* **75**, 461-471 (2004).
 151. Feng, J. *et al.* Golli protein negatively regulates store depletion-induced calcium influx in T cells. *Immunity* **24**, 717-727 (2006).
 152. Smith, G. S. *et al.* Classical 18.5-and 21.5-kDa isoforms of myelin basic protein inhibit calcium influx into oligodendroglial cells, in contrast to golli isoforms. *J. Neurosci. Res.* **89**, 467-480 (2011).
 153. Barbarese, E., Braun, P. E. & Carson, J. H. Identification of prelarge and presmall basic proteins in mouse myelin and their structural relationship to large and small basic proteins. *Proc. Natl. Acad. Sci. U. S. A.* **74**, 3360-3364 (1977).
 154. Roach, A., Boylan, K., Horvath, S., Prusiner, S. & Hood, L. Characterization of Cloned Cdna Representing Rat Myelin Basic-Protein - Absence of Expression in Brain of Shiverer Mutant Mice. *Cell* **34**, 799-806 (1983).
 155. Schaich, M., Budzinski, R. & Stoffel, W. Cloned Proteolipid Protein and Myelin Basic-Protein Cdna - Transcription of the 2 Genes during Myelination. *Biol. Chem. Hoppe-Seyler* **367**, 825-834 (1986).
 156. Newman, S., Kitamura, K. & Campagnoni, A. Identification of a Cdna Coding for a 5th Form of Myelin Basic-Protein in Mouse. *Proc. Natl. Acad. Sci. U. S. A.* **84**, 886-890 (1987).
 157. Campagnoni, A. *et al.* Structure and Developmental Regulation of Golli-Mbp, a 105-Kilobase Gene that Encompasses the Myelin Basic-Protein Gene and is Expressed in Cells in the Oligodendrocyte Lineage in the Brain. *J. Biol. Chem.* **268**, 4930-4938 (1993).
 158. Akiyama, K., Ichinose, S., Omori, A., Sakurai, Y. & Asou, H. Study of expression of myelin basic proteins (MBPs) in developing rat brain using a novel antibody reacting with four major isoforms of MBP. *J. Neurosci. Res.* **68**, 19-28 (2002).
 159. Matheus, L. & Blair, G. Identification and characterisation of a cDNA encoding a 17-kDa isoform of rat myelin basic protein. *Biochim. Biophys. Acta-Gene Struct. Expression* **1630**, 47-53 (2003).
 160. Gasteiger, E. *et al.* in *The Proteomics Protocols Handbook* (ed Walker, J.) 571-607 (Humana Press, New Jersey, USA, 2005).
 161. Pedraza, L. Nuclear transport of myelin basic protein. *J. Neurosci. Res.* **50**, 258-264 (1997).

162. Smith, G. S. T., Seymour, L. V., Boggs, J. M. & Harauz, G. The 21.5-kDa isoform of myelin basic protein has a non-traditional PY-nuclear-localization signal. *Biochem. Biophys. Res. Commun.* **422**, 670-675 (2012).
163. Nawaz, S., Schweitzer, J., Jahn, O. & Werner, H. B. Molecular evolution of myelin basic protein, an abundant structural myelin component. *Glia* **61**, 1364-1377 (2013).
164. Zhang, C. *et al.* Myelin Basic Protein Undergoes a Broader Range of Modifications in Mammals than in Lower Vertebrates. *J. Proteome Res.* **11**, 4791-4802 (2012).
165. Edgar, R. MUSCLE: multiple sequence alignment with high accuracy and high throughput. *Nucleic Acids Res.* **32**, 1792-1797 (2004).
166. Robert, X. & Gouet, P. Deciphering key features in protein structures with the new ENDscript server. *Nucleic Acids Res.* **42**, W320-W324 (2014).
167. Libich, D. S. & Harauz, G. Backbone dynamics of the 18.5 kDa isoform of myelin basic protein reveals transient alpha-helices and a calmodulin-binding site. *Biophys. J.* **94**, 4847-4866 (2008).
168. Harauz, G. *et al.* Myelin basic protein - diverse conformational states of an intrinsically unstructured protein and its roles in myelin assembly and multiple sclerosis. *Micron* **35**, 503-542 (2004).
169. Haas, H. *et al.* Small angle x-ray scattering from lipid-bound myelin basic protein in solution. *Biophys. J.* **86**, 455-460 (2004).
170. Libich, D. S. & Harauz, G. Solution NMR and CD spectroscopy of an intrinsically disordered, peripheral membrane protein: evaluation of aqueous and membrane-mimetic solvent conditions for studying the conformational adaptability of the 18.5 kDa isoform of myelin basic protein (MBP). *Eur. Biophys. J.* **37**, 1015-1029 (2008).
171. Wang, C. *et al.* Charge isomers of myelin basic protein: Structure and interactions with membranes, nucleotide analogues, and calmodulin. *PLoS One* **6**, e19915 (2011).
172. Stadler, A. M. *et al.* Internal nanosecond dynamics in the intrinsically disordered myelin basic protein. *J. Am. Chem. Soc.* **136**, 6987-6994 (2014).
173. Bernado, P. & Svergun, D. I. Structural analysis of intrinsically disordered proteins by small-angle X-ray scattering. *Mol. Biosyst.* **8**, 151-167 (2012).
174. Showalter, S., Sahu, D., Bastidas, M. & Lawrence, C. Assessing Intrinsically Disordered Protein Structure and Function through Carbon Detected NMR. *FASEB J.* **29** (2015).
175. Sedzik, J. & Kirschner, D. A. Is myelin basic protein crystallizable? *Neurochem Res.* **17**, 157-166 (1992).
176. Mendz, G. *et al.* Characterization of Dodecylphosphocholine Myelin Basic-Protein Complexes. *Biochemistry (N. Y.)* **27**, 379-386 (1988).

-
177. Beniac, D. *et al.* Three-dimensional structure of myelin basic protein .1. Reconstruction via angular reconstitution of randomly oriented single particles. *J. Biol. Chem.* **272**, 4261-4268 (1997).
 178. Ridsdale, R., Beniac, D., Tompkins, T., Moscarello, M. & Harauz, G. Three-dimensional structure of myelin basic protein .2. Molecular modeling and considerations of predicted structures in multiple sclerosis. *J. Biol. Chem.* **272**, 4269-4275 (1997).
 179. Zhong, L., Bamm, V. V., Ahmed, M. A. M., Harauz, G. & Ladizhansky, V. Solid-state NMR spectroscopy of 18.5 kDa myelin basic protein reconstituted with lipid vesicles: Spectroscopic characterisation and spectral assignments of solvent-exposed protein fragments. *Biochim. Biophys. Acta-Biomembr.* **1768**, 3193-3205 (2007).
 180. Ahmed, M. A. M., Bamm, V. V., Harauz, G. & Ladizhansky, V. Solid-State NMR Spectroscopy of Membrane-Associated Myelin Basic Protein-Conformation and Dynamics of an Immunodominant Epitope. *Biophys. J.* **99**, 1247-1255 (2010).
 181. Libich, D. S. *et al.* Fuzzy complexes of myelin basic protein: NMR spectroscopic investigations of a polymorphic organizational linker of the central nervous system. *Biochem. Cell. Biol.* **88**, 143-155 (2010).
 182. Kattinig, D. R., Bund, T., Boggs, J. M., Harauz, G. & Hinderberger, D. Lateral self-assembly of 18.5-kDa myelin basic protein (MBP) charge component-C1 on membranes. *Biochim. Biophys. Acta.* **1818**, 2636-2647 (2012).
 183. Bamm, V. V., De Avila, M., Smith, G. S. T., Ahmed, M. A. M. & Harauz, G. Structured Functional Domains of Myelin Basic Protein: Cross Talk between Actin Polymerization and Ca²⁺-Dependent Calmodulin Interaction. *Biophys. J.* **101**, 1248-1256 (2011).
 184. Ahmed, M. A. M. *et al.* Solution nuclear magnetic resonance structure and molecular dynamics simulations of a murine 18.5 kDa myelin basic protein segment (S72-S107) in association with dodecylphosphocholine micelles. *Biochemistry* **51**, 7475-7487 (2012).
 185. Chattopadhyaya, R., Meador, W., Means, A. & Quijcho, F. Calmodulin Structure Refined at 1.7 Angstrom Resolution. *J. Mol. Biol.* **228**, 1177-1192 (1992).
 186. Chen, Q. & Georgiadis, M. Crystallization of and selenomethionine phasing strategy for a SETMAR-DNA complex. *Acta Cryst.* **F72**, 713-719 (2016).
 187. Robb, N. D. & Chen, W. H. Myelin Basic Protein Interaction with Calmodulin and Gangliosides. *J. Neurosci. Res.* **25**, 535-544 (1990).
 188. Harauz, G., Ishiyama, N. & Bates, I. Analogous standard motifs in myelin basic protein and in MARCKS. *Mol. Cell. Biochem.* **209**, 155-163 (2000).
 189. Yap, K. L. *et al.* Calmodulin target database. *J. Struct. Funct. Genomics* **1**, 8-14 (2000).

190. Libich, D., Hill, C., Haines, J. & Harauz, G. Myelin basic protein has multiple calmodulin-binding sites. *Biochem. Biophys. Res. Commun.* **308**, 313-319 (2003).
191. Smith, G. S. T., Homchaudhuri, L., Boggs, J. M. & Harauz, G. Classic 18.5- and 21.5-kDa myelin basic protein isoforms associate with cytoskeletal and SH3-domain proteins in the immortalized N19-oligodendroglial cell line stimulated by phorbol ester and IGF-1. *Neurochem. Res.* **37**, 1277-1295 (2012).
192. Boggs, J. M. *et al.* Interaction of myelin basic protein with cytoskeletal and signaling proteins in cultured primary oligodendrocytes and N19 oligodendroglial cells. *BMC Res. Notes* **7**, 387 (2014).
193. Smith, G. S. T. *et al.* Nucleus-localized 21.5-kDa myelin basic protein promotes oligodendrocyte proliferation and enhances neurite outgrowth in coculture, unlike the plasma membrane-associated 18.5-kDa isoform. *J. Neurosci. Res.* **91**, 349-362 (2013).
194. Smith, G. S. T. *et al.* Proline substitutions and threonine pseudophosphorylation of the SH3 ligand of 18.5-kDa myelin basic protein decrease its affinity for the Fyn-SH3 domain and alter process development and protein localization in oligodendrocytes. *J. Neurosci. Res.* **90**, 28-47 (2012).
195. De Avila, M., Vassall, K. A., Smith, G. S. T., Bamm, V. V. & Harauz, G. The proline-rich region of 18.5 kDa myelin basic protein binds to the SH3-domain of Fyn tyrosine kinase with the aid of an upstream segment to form a dynamic complex in vitro. *Biosci. Rep.* **34**, 775-788 (2014).
196. Majava, V. *et al.* Interaction between the C-terminal region of human myelin basic protein and calmodulin: analysis of complex formation and solution structure. *BMC Struct. Biol.* **8**, 10 (2008).
197. Jo, E. & Boggs, J. Aggregation of Acidic Lipid Vesicles by Myelin Basic-Protein - Dependence on Potassium Concentration. *Biochemistry (N. Y.)* **34**, 13705-13716 (1995).
198. Widder, K., Träger, J., Kerth, A., Harauz, G. & Hinderberger, D. Interaction of Myelin Basic Protein with Myelin-like Lipid Monolayers at Air-Water Interface. *Langmuir* **34**, 6095-6108 (2018).
199. Weil, M. *et al.* Loss of Myelin Basic Protein Function Triggers Myelin Breakdown in Models of Demyelinating Diseases. *Cell Rep.* **16**, 314-322 (2016).
200. Shaharabani, R., Ram-On, M., Talmon, Y. & Beck, R. Pathological transitions in myelin membranes driven by environmental and multiple sclerosis conditions. *Proc. Natl. Acad. Sci. U. S. A.* **115**, 11156-11161 (2018).
201. Nawaz, S. *et al.* Phosphatidylinositol 4,5-Bisphosphate-Dependent Interaction of Myelin Basic Protein with the Plasma Membrane in Oligodendroglial Cells and Its Rapid Perturbation by Elevated Calcium. *J. Neurosci.* **29**, 4794-4807 (2009).

-
202. Musse, A. A., Gao, W., Rangaraj, G., Boggs, J. M. & Harauz, G. Myelin basic protein co-distributes with other PI(4,5)P-2-sequestering proteins in Triton X-100 detergent-resistant membrane microdomains. *Neurosci. Lett.* **450**, 32-36 (2009).
 203. Hu, Y. *et al.* Synergistic interactions of lipids and myelin basic protein. *Proc. Natl. Acad. Sci. U. S. A.* **101**, 13466-13471 (2004).
 204. Shaharabani, R. *et al.* Structural transition in myelin membrane as initiator of multiple sclerosis. *J. Am. Chem. Soc.* **138**, 12159-12165 (2016).
 205. Denninger, A. R. *et al.* Neutron scattering from myelin revisited: bilayer asymmetry and water-exchange kinetics. *Acta Cryst.* **D70**, 3198-3211 (2014).
 206. Aggarwal, S. *et al.* Myelin membrane assembly is driven by a phase transition of myelin basic proteins into a cohesive protein meshwork. *PLoS Biol.* **11**, e1001577 (2013).
 207. Costenino, M., Pritzker, L., Boulias, C. & Moscarello, M. Acylation of Myelin Basic-Protein Peptide-1-21 with Alkyl Carboxylates 2-10 Carbons Long Affects Secondary Structure and Posttranslational Modification. *Biochemistry (N. Y.)* **33**, 4155-4162 (1994).
 208. Boulias, C. & Moscarello, M. A. ADP-ribosylation of myelin basic proteins isolated from normal and mutant mouse brains. *Neuroreport* **1**, 221-224 (1990).
 209. Yamamori, C., Terashima, M., Ishino, H. & Shimoyama, M. ADP-ribosylation of myelin basic protein and inhibition of phospholipid vesicle aggregation. *Enzyme Protein* **48**, 202-212 (1995).
 210. Wood, D. & Moscarello, M. The Isolation, Characterization, and Lipid-Aggregating Properties of a Citrulline Containing Myelin Basic-Protein. *J. Biol. Chem.* **264**, 5121-5127 (1989).
 211. Wood, D., Bilbao, J., O'Connors, P. & Moscarello, M. Acute multiple sclerosis (Marburg type) is associated with developmentally immature myelin basic protein. *Ann. Neurol.* **40**, 18-24 (1996).
 212. Kim, J. *et al.* Multiple sclerosis - An important role for post-translational modifications of myelin basic protein in pathogenesis. *Mol. Cell. Proteomics* **2**, 453-462 (2003).
 213. Wood, D. D. *et al.* Myelin localization of peptidylarginine deiminases 2 and 4: comparison of PAD2 and PAD4 activities. *Lab. Invest.* **88**, 354-364 (2008).
 214. Baldwin, G. & Carnegie, P. Isolation and Partial Characterization of Methylated Arginines from Encephalitogenic Basic Protein of Myelin. *Biochem. J.* **123**, 69-& (1971).
 215. Brostoff, S. & Eylar, E. Localization of Methylated Arginine in A1 Protein from Myelin. *Proc. Natl. Acad. Sci. U. S. A.* **68**, 765-& (1971).
 216. Chou, P. C. H. Basis of Micro Heterogeneity of Myelin Basic Protein. *J. Biol. Chem.* **251**, 2671-2679 (1976).

217. Zand, R., Li, M., Jin, X. & Lubman, D. Determination of the sites of posttranslational modifications in the charge isomers of bovine myelin basic protein by capillary electrophoresis mass spectroscopy. *Biochemistry (N. Y.)* **37**, 2441-2449 (1998).
218. Cheifetz, S., Moscarello, M. & Deber, C. Nmr Investigation of the Charge Isomers of Bovine Myelin Basic-Protein. *Arch. Biochem. Biophys.* **233**, 151-160 (1984).
219. Turner, R., Chou, C., Mazzei, G., Dembure, P. & Kuo, J. Phospholipid-Sensitive Ca-2+-Dependent Protein-Kinase Preferentially Phosphorylates Serine-115 of Bovine Myelin Basic-Protein. *J. Neurochem.* **43**, 1257-1264 (1984).
220. Kishimoto, A. *et al.* Studies on the Phosphorylation of Myelin Basic-Protein by Protein-Kinase C and Adenosine 3'-5'-Monophosphate-Dependent Protein-Kinase. *J. Biol. Chem.* **260**, 2492-2499 (1985).
221. Schulz, P., Cruz, T. & Moscarello, M. Endogenous Phosphorylation of Basic-Protein in Myelin of Varying Degrees of Compaction. *Biochemistry (N. Y.)* **27**, 7793-7799 (1988).
222. Erickson, A. *et al.* Identification by Mass-Spectrometry of Threonine-97 in Bovine Myelin Basic-Protein as a Specific Phosphorylation Site for Mitogen-Activated Protein-Kinase. *J. Biol. Chem.* **265**, 19728-19735 (1990).
223. Ramwani, J. & Moscarello, M. Phosphorylation of Charge Isomers (Components) of Human Myelin Basic-Protein - Identification of Phosphorylated Sites. *J. Neurochem.* **55**, 1703-1710 (1990).
224. Wang, Q. M., Smith, J. B., Harrison, M. L. & Geahlen, R. L. Identification of Tyrosine-67 in Bovine Brain Myelin Basic-Protein as a Specific Phosphorylation Site for Thymus-P56lck. *Biochem. Biophys. Res. Commun.* **178**, 1393-1399 (1991).
225. Boggs, J. *et al.* Effect of arginine loss in myelin basic protein, as occurs in its deiminated charge isoform, on mediation of actin polymerization and actin binding to a lipid membrane in vitro. *Biochemistry* **44**, 3524-3534 (2005).
226. Musse, A., Boggs, J. & Harauz, G. Deimination of membrane-bound myelin basic protein in multiple sclerosis exposes an immunodominant epitope. *Proc. Natl. Acad. Sci. U. S. A.* **103**, 4422-4427 (2006).
227. Shapiro, L., Doyle, J., Hensley, P., Colman, D. & Hendrickson, W. Crystal structure of the extracellular domain from P-0, the major structural protein of peripheral nerve myelin. *Neuron* **17**, 435-449 (1996).
228. Liu, Z. *et al.* Crystal structure of the extracellular domain of human myelin protein zero. *Proteins* **80**, 307-313 (2012).
229. Zhang, K. & Filbin, M. Formation of a Disulfide Bond in the Immunoglobulin Domain of the Myelin P-0 Protein is Essential for its Adhesion. *J. Neurochem.* **63**, 367-370 (1994).

-
230. Yamaguchi, Y. *et al.* L-MPZ, a Novel Isoform of Myelin P0, Is Produced by Stop Codon Readthrough. *J. Biol. Chem.* **287**, 17765-17776 (2012).
 231. Yamaguchi, Y. & Baba, H. Phylogenetically Conserved Sequences Around Myelin P0 Stop Codon are Essential for Translational Readthrough to Produce L-MPZ. *Neurochem. Res.* **43**, 227-237 (2018).
 232. Lemke, G. & Axel, R. Isolation and sequence of a cDNA encoding the major structural protein of peripheral myelin. *Cell* **40**, 501-508 (1985).
 233. Eichberg, J. Myelin P-0: New knowledge and new roles. *Neurochem. Res.* **27**, 1331-1340 (2002).
 234. Filbin, M. & Tennekoon, G. The Role of Complex Carbohydrates in Adhesion of the Myelin Protein, Po. *Neuron* **7**, 845-855 (1991).
 235. Filbin, M. & Tennekoon, G. Homophilic Adhesion of the Myelin Po Protein Requires Glycosylation of both Molecules in the Homophilic Pair. *J. Cell Biol.* **122**, 451-459 (1993).
 236. Inouye, H., Tsuruta, H., Sedzik, J., Uyemura, K. & Kirschner, D. A. Tetrameric Assembly of Full-Sequence Protein Zero Myelin Glycoprotein by Synchrotron X-Ray Scattering. *Biophys. J.* **76**, 423-437 (1999).
 237. Thompson, A. J., Cronin, M. S. & Kirschner, D. A. Myelin protein zero exists as dimers and tetramers in native membranes of *Xenopus laevis* peripheral nerve. *J. Neurosci. Res.* **67**, 766-771 (2002).
 238. Favereaux, A. *et al.* Serum IgG antibodies to P0 dimer and 35 kDa P0 related protein in neuropathy associated with monoclonal gammopathy. *J. Neurol. Neurosurg. Psychiatry* **74**, 1262-1266 (2003).
 239. Plotkowski, M. L. *et al.* Transmembrane domain of myelin protein zero can form dimers: Possible implications for myelin construction. *Biochemistry (N. Y.)* **46**, 12164-12173 (2007).
 240. D'Urso, D., Ehrhardt, P. & Müller, H. W. Peripheral myelin protein 22 and protein zero: a novel association in peripheral nervous system myelin. *J. Neurosci.* **19**, 3396-3403 (1999).
 241. Hasse, B., Bosse, F., Hanenberg, H. & Müller, H. W. Peripheral myelin protein 22 kDa and protein zero: domain specific trans-interactions. *Mol. Cell. Neurosci.* **27**, 370-378 (2004).
 242. Wong, M. & Filbin, M. The Cytoplasmic Domain of the Myelin Po Protein Influences the Adhesive Interactions of its Extracellular Domain. *J. Cell Biol.* **126**, 1089-1097 (1994).
 243. Ding, Y. & Brunden, K. The Cytoplasmic Domain of Myelin Glycoprotein P0 Interacts with Negatively Charged Phospholipid-Bilayers. *J. Biol. Chem.* **269**, 10764-10770 (1994).
 244. Luo, X. *et al.* Cytoplasmic domain of human myelin protein zero likely folded as beta-structure in compact myelin. *Biophys. J.* **92**, 1585-1597 (2007).

245. Luo, X. *et al.* Cytoplasmic domain of zebrafish myelin protein zero: Adhesive role depends on beta-conformation. *Biophys. J.* **93**, 3515-3528 (2007).
246. Myllykoski, M., Baumgartel, P. & Kursula, P. Conformations of peptides derived from myelin-specific proteins in membrane-mimetic conditions probed by synchrotron radiation CD spectroscopy. *Amino Acids* **42**, 1467-1474 (2012).
247. Bizzozero, O., Fridal, K. & Pastuszyn, A. Identification of the Palmitoylation Site in Rat Myelin P-0 Glycoprotein. *J. Neurochem.* **62**, 1163-1171 (1994).
248. Bharadwaj, M. & Bizzozero, O. Myelin P-0 Glycoprotein and a Synthetic Peptide-Containing the Palmitoylation Site are both Autoacylated. *J. Neurochem.* **65**, 1805-1815 (1995).
249. Gao, Y., Li, W. & Filbin, M. Acylation of myelin Po protein is required for adhesion. *J. Neurosci. Res.* **60**, 704-713 (2000).
250. Suzuki, M. *et al.* Phosphorylation of P0 Glycoprotein in Peripheral-Nerve Myelin. *J. Neurochem.* **55**, 1966-1971 (1990).
251. Xu, W. *et al.* Mutations in the cytoplasmic domain of P0 reveal a role for PKC-mediated phosphorylation in adhesion and myelination. *J. Cell Biol.* **155**, 439-445 (2001).
252. Xu, M., Zhao, R., Sui, X., Xu, F. & Zhao, Z. Tyrosine phosphorylation of myelin P-0 and its implication in signal transduction. *Biochem. Biophys. Res. Commun.* **267**, 820-825 (2000).
253. Hilmi, S., Fournier, M., Valeins, H., Gandar, J. & Bonnet, J. Myelin P-0 Glycoprotein - Identification of the Site Phosphorylated In-Vitro and In-Vivo by Endogenous Protein-Kinases. *J. Neurochem.* **64**, 902-907 (1995).
254. Gaboreanu, A. *et al.* Myelin protein zero/P0 phosphorylation and function require an adaptor protein linking it to RACK1 and PKC alpha. *J. Cell Biol.* **177**, 707-716 (2007).
255. de Seze, J. *et al.* Chronic inflammatory demyelinating polyradiculoneuropathy: A new animal model for new therapeutic targets. *Rev. Neurol.* **172**, 767-769 (2016).
256. Kidd, G. J. *et al.* A dual tyrosine-leucine motif mediates myelin protein P-0 targeting in MDCK cells. *Glia* **54**, 135-145 (2006).
257. Zuchero, J. B. *et al.* CNS myelin wrapping is driven by actin disassembly. *Dev. Cell* **34**, 152-167 (2015).
258. Miller, R. H. Calcium control of myelin sheath growth. *Nat. Neurosci.* **21**, 2-3 (2018).
259. Bercury, K. K. & Macklin, W. B. Dynamics and Mechanisms of CNS Myelination. *Dev. Cell* **32**, 447-458 (2015).
260. Sherman, D. & Brophy, P. Mechanisms of axon ensheathment and myelin growth. *Nat. Rev. Neurosci.* **6**, 683-690 (2005).

-
261. Nave, K. A. & Werner, H. B. Myelination of the nervous system: mechanisms and functions. *Annu Rev Cell Dev Biol* **30**, 503-533 (2014).
 262. Nawaz, S. *et al.* Actin Filament Turnover Drives Leading Edge Growth during Myelin Sheath Formation in the Central Nervous System. *Dev. Cell* **34**, 139-151 (2015).
 263. Liu, M. *et al.* Ulk4 deficiency leads to hypomyelination in mice. *Glia* **66**, 175-190 (2018).
 264. Colman, D., Kreibich, G., Frey, A. & Sabatini, D. Synthesis and Incorporation of Myelin Polypeptides into Cns Myelin. *J. Cell Biol.* **95**, 598-608 (1982).
 265. Trapp, B. D. *et al.* Spatial segregation of mRNA encoding myelin-specific proteins. *Proc. Natl. Acad. Sci. U. S. A.* **84**, 7773-7777 (1987).
 266. Ainger, K. *et al.* Transport and Localization of Exogenous Myelin Basic-Protein Messenger-Rna Microinjected into Oligodendrocytes. *J. Cell Biol.* **123**, 431-441 (1993).
 267. Carson, J., Worboys, K., Ainger, K. & Barbarese, E. Translocation of myelin basic protein mRNA in oligodendrocytes requires microtubules and kinesin. *Cell Motil. Cytoskeleton* **38**, 318-328 (1997).
 268. Li, Z., Zhang, Y., Li, D. & Feng, Y. Destabilization and mislocalization of myelin basic protein mRNAs in quaking dysmyelination lacking the QKI RNA-binding proteins. *J. Neurosci.* **20**, 4944-4953 (2000).
 269. Fitzner, D. *et al.* Myelin basic protein-dependent plasma membrane reorganization in the formation of myelin. *EMBO J.* **25**, 5037-5048 (2006).
 270. Torvund-Jensen, J., Steengaard, J., Reimer, L., Fihl, L. B. & Laursen, L. S. Transport and translation of MBP mRNA is regulated differently by distinct hnRNP proteins. *J. Cell. Sci.* **127**, 1550-1564 (2014).
 271. Wake, H., Lee, P. R. & Fields, R. D. Control of Local Protein Synthesis and Initial Events in Myelination by Action Potentials. *Science* **333**, 1647-1651 (2011).
 272. Lee, D. W. *et al.* Lipid domains control myelin basic protein adsorption and membrane interactions between model myelin lipid bilayers. *Proc. Natl. Acad. Sci. U. S. A.* **111**, E768-E775 (2014).
 273. Lee, D. W. *et al.* Adsorption mechanism of myelin basic protein on model substrates and its bridging interaction between the two surfaces. *Langmuir* **31**, 3159-3166 (2015).
 274. Readhead, C. & Hood, L. The Dysmyelinating Mouse Mutations Shiverer (Shi) and Myelin Deficient (Shimld). *Behav. Genet.* **20**, 213-234 (1990).
 275. Privat, A., Jacque, C., Bourre, J., Dupouey, P. & Baumann, N. Absence of the major dense line in myelin of the mutant mouse shiverer. *Neurosci. Lett.* **12**, 107-112 (1979).

276. Dupouey, P. *et al.* Immunochemical studies of myelin basic protein in shiverer mouse devoid of major dense line of myelin. *Neurosci. Lett.* **12**, 113-118 (1979).
277. Lee, M. *et al.* P-0 is constitutively expressed in the rat neural crest and embryonic nerves and is negatively and positively regulated by axons to generate non-myelin-forming and myelin-forming Schwann cells, respectively. *Mol. Cell. Neurosci.* **8**, 336-350 (1997).
278. Yin, X. *et al.* Schwann cell myelination requires timely and precise targeting of P-0 protein. *J. Cell Biol.* **148**, 1009-1020 (2000).
279. Xu, W. *et al.* Absence of P0 leads to the dysregulation of myelin gene expression and myelin morphogenesis. *J. Neurosci. Res.* **60**, 714-724 (2000).
280. Yin, X. *et al.* Proteolipid Protein Cannot Replace P-0 Protein as the Major Structural Protein of Peripheral Nervous System Myelin. *Glia* **63**, 66-77 (2015).
281. Seitelberger, F. Neuropathology and Genetics of Pelizaeus-Merzbacher Disease. *Brain Pathol.* **5**, 267-273 (1995).
282. Oksenberg, J., Seboun, E. & Hauser, S. Genetics of demyelinating diseases. *Brain Pathol.* **6**, 289-302 (1996).
283. Compston, A. & Coles, A. Multiple sclerosis. *Lancet* **372**, 1502-1517 (2008).
284. Carvalho, K. S. Mitochondrial Dysfunction in Demyelinating Diseases. *Semin. Pediatr. Neurol.* **20**, 194-201 (2013).
285. Sadeghian, M. *et al.* Mitochondrial dysfunction is an important cause of neurological deficits in an inflammatory model of multiple sclerosis. *Sci. Rep.* **6**, 33249 (2016).
286. Taib, T. *et al.* Neuroinflammation, myelin and behavior: Temporal patterns following mild traumatic brain injury in mice. *PLoS One* **12**, e0184811 (2017).
287. Stadelmann, C., Wegner, C. & Brueck, W. Inflammation, demyelination, and degeneration - Recent insights from MS pathology. *Biochim. Biophys. Acta-Mol. Basis Dis.* **1812**, 275-282 (2011).
288. Dobson, R. & Giovannoni, G. Multiple sclerosis - a review. *Eur. J. Neurol.* **26**, 27-40 (2019).
289. Ewing, C. & Bernard, C. Insights into the aetiology and pathogenesis of multiple sclerosis. *Immunol. Cell Biol.* **76**, 47-54 (1998).
290. Fletcher, J. M., Lalor, S. J., Sweeney, C. M., Tubridy, N. & Mills, K. H. G. T cells in multiple sclerosis and experimental autoimmune encephalomyelitis. *Clin. Exp. Immunol.* **162**, 1-11 (2010).
291. Luo, C. *et al.* The role of microglia in multiple sclerosis. *Neuropsychiatr. Dis. Treat.* **13**, 1661-1667 (2017).

-
292. Fritz, R., Skeen, M., Chou, C., Garcia, M. & Egorov, I. Major Histocompatibility Complex-Linked Control of the Murine Immune-Response to Myelin Basic-Protein. *J. Immunol.* **134**, 2328-2332 (1985).
293. Kondo, T. *et al.* TCR repertoire to proteolipid protein (PLP) in multiple sclerosis (MS): Homologies between PLP-specific T cells and MS-associated T cells in TCR junctional sequences. *Int. Immunol.* **8**, 123-130 (1996).
294. Rösener, M. *et al.* 2',3'-cyclic nucleotide 3'-phosphodiesterase: A novel candidate autoantigen in demyelinating diseases. *J. Neuroimmunol.* **75**, 28-34 (1997).
295. Andersson, M. *et al.* Multiple MAG peptides are recognized by circulating T and B lymphocytes in polyneuropathy and multiple sclerosis. *Eur. J. Neurol.* **9**, 243-251 (2002).
296. Muraro, P., Kalbus, M., Afshar, G., McFarland, H. & Martin, R. T cell response to 2',3'-cyclic nucleotide 3'-phosphodiesterase (CNPase) in multiple sclerosis patients. *J. Neuroimmunol.* **130**, 233-242 (2002).
297. Clements, C. S. *et al.* The crystal structure of myelin oligodendrocyte glycoprotein, a key autoantigen in multiple sclerosis. *Proc. Natl. Acad. Sci. U. S. A.* **100**, 11059-11064 (2003).
298. Lovato, L. *et al.* Transketolase and 2',3'-Cyclic-nucleotide 3'-Phosphodiesterase Type I Isoforms Are Specifically Recognized by IgG Autoantibodies in Multiple Sclerosis Patients. *Mol. Cell. Proteomics* **7**, 2337-2349 (2008).
299. Kaushansky, N., Eisenstein, M., Zilkha-Falb, R. & Ben-Nun, A. The myelin-associated oligodendrocytic basic protein (MOBP) as a relevant primary target autoantigen in multiple sclerosis. *Autoimmun. Rev.* **9**, 233-236 (2010).
300. Mirshafiey, A. & Kianiaslani, M. Autoantigens and Autoantibodies in Multiple Sclerosis. *Iran. J. Allergy Asthma. Immunol.* **12**, 292-303 (2013).
301. McCarthy, D. P., Richards, M. H. & Miller, S. D. Mouse models of multiple sclerosis: experimental autoimmune encephalomyelitis and Theiler's virus-induced demyelinating disease. *Methods Mol. Biol.* **900**, 381-401 (2012).
302. Perera, C. J. *et al.* Effects of active immunisation with myelin basic protein and myelin-derived altered peptide ligand on pain hypersensitivity and neuroinflammation. *J. Neuroimmunol.* **286**, 59-70 (2015).
303. Constantinescu, C. S., Farooqi, N., O'Brien, K. & Gran, B. Experimental autoimmune encephalomyelitis (EAE) as a model for multiple sclerosis (MS). *Br. J. Pharmacol.* **164**, 1079-1106 (2011).
304. Stapulionis, R. *et al.* Structural insight into the function of myelin basic protein as a ligand for integrin alpha(M)beta(2). *J. Immunol.* **180**, 3946-3956 (2008).

305. Wucherpfennig, K. *et al.* Structural Requirements for Binding of an Immunodominant Myelin Basic-Protein Peptide to Dr2 Isotypes and for its Recognition by Human T-Cell Clones. *J. Exp. Med.* **179**, 279-290 (1994).
306. Warren, K., Catz, I. & Steinman, L. Fine Specificity of the Antibody-Response to Myelin Basic-Protein in the Central-Nervous-System in Multiple-Sclerosis - the Minimal B-Cell Epitope and a Model of its Features. *Proc. Natl. Acad. Sci. U. S. A.* **92**, 11061-11065 (1995).
307. Smith, K., Pyrdol, J., Gauthier, L., Wiley, D. & Wucherpfennig, K. Crystal structure of HLA-DR2 (DRA*0101, DRB1*1501) complexed with a peptide from human myelin basic protein. *J. Exp. Med.* **188**, 1511-1520 (1998).
308. Li, Y., Li, H., Martin, R. & Mariuzza, R. Structural basis for the binding of an immunodominant peptide from myelin basic protein in different registers by two HLA-DR2 proteins. *J. Mol. Biol.* **304**, 177-188 (2000).
309. Li, Y. L. *et al.* Structure of a human autoimmune TCR bound to a myelin basic protein self-peptide and a multiple sclerosis-associated MHC class II molecule. *EMBO J.* **24**, 2968-2979 (2005).
310. Vassall, K. A., Bessonov, K., De Avila, M., Polverini, E. & Harauz, G. The Effects of Threonine Phosphorylation on the Stability and Dynamics of the Central Molecular Switch Region of 18.5-kDa Myelin Basic Protein. *PLoS One* **8**, e68175 (2013).
311. D'Souza, C. A. & Moscarello, M. A. Differences in susceptibility of MBP charge isomers to digestion by stromelysin-1 (MMP-3) and release of an immunodominant epitope. *Neurochem. Res.* **31**, 1045-1054 (2006).
312. D'Souza, C., Wood, D., She, Y. & Moscarello, M. Autocatalytic cleavage of myelin basic protein: An alternative to molecular mimicry. *Biochemistry* **44**, 12905-12913 (2005).
313. Tselios, T. *et al.* Design and synthesis of a potent cyclic analogue of the myelin basic protein epitope MBP72-85: Importance of the Ala(81) carboxyl group and of its cyclic conformation for induction of experimental allergic encephalomyelitis. *J. Med. Chem.* **42**, 1170-1177 (1999).
314. Tselios, T. *et al.* Antagonistic effects of human cyclic MBP87-99 altered peptide ligands in experimental allergic encephalomyelitis and human T-cell proliferation. *J. Med. Chem.* **45**, 275-283 (2002).
315. Mantzourani, E. D. *et al.* A putative bioactive conformation for the altered peptide ligand of myelin basic protein and inhibitor of experimental autoimmune encephalomyelitis [Arg(91), Ala(96)] MBP87-99. *J. Mol. Graph.* **25**, 17-29 (2006).
316. Katsara, M. *et al.* Design and Synthesis of a Cyclic Double Mutant Peptide (cyclo(87-99)[A(91),A(96)]MBP87-99) Induces Altered Responses in Mice after Conjugation to Mannan: Implications in the Immunotherapy of Multiple Sclerosis. *J. Med. Chem.* **52**, 214-218 (2009).

-
317. Deraos, G. *et al.* Properties of myelin altered peptide ligand cyclo(87-99)(Ala91,Ala96) MBP87-99 render it a promising drug lead for immunotherapy of multiple sclerosis. *Eur. J. Med. Chem.* **101**, 13-23 (2015).
 318. Apostolopoulos, V. *et al.* Cyclic citrullinated MBP87-99 peptide stimulates T cell responses: Implications in triggering disease. *Bioorg. Med. Chem.* **25**, 528-538 (2017).
 319. Emmanouil, M. *et al.* A Cyclic Altered Peptide Analogue Based on Myelin Basic Protein 87-99 Provides Lasting Prophylactic and Therapeutic Protection Against Acute Experimental Autoimmune Encephalomyelitis. *Molecules* **23**, 304 (2018).
 320. Wucherpfennig, K. & Strominger, J. Molecular Mimicry in T-Cell-Mediated Autoimmunity - Viral Peptides Activate Human T-Cell Clones Specific for Myelin Basic-Protein. *Cell* **80**, 695-705 (1995).
 321. Tejada-Simon, M., Zang, Y., Hong, J., Rivera, V. & Zhang, J. Cross-reactivity with myelin basic protein and human herpesvirus-6 in multiple sclerosis. *Ann. Neurol.* **53**, 189-197 (2003).
 322. Mao, Y., Lu, C., Wang, X. & Xiao, B. Induction of experimental autoimmune encephalomyelitis in Lewis rats by a viral peptide with limited homology to myelin basic protein. *Exp. Neurol.* **206**, 231-239 (2007).
 323. Namaka, M. *et al.* Molecular mimicry and multiple sclerosis. *Neural Regen. Res.* **6**, 1322-1333 (2011).
 324. Tuusa, J., Raasakka, A., Ruskamo, S. & Kursula, P. Myelin-derived and putative molecular mimic peptides share structural properties in aqueous and membrane-like environments. *Mult. Scler. Demyelinating Disord.* **2**, 4 (2017).
 325. Silva, A., Camara, V. & QuiricoSantos, T. Intrathecal reactivity for myelin components precedes development of neurological symptoms in AIDS patients. *Arch. Med. Res.* **28**, 391-396 (1997).
 326. Ramchandren, S. Charcot-Marie-Tooth Disease and Other Genetic Polyneuropathies. *Continuum (Minneap Minn)* **23**, 1360-1377 (2017).
 327. Casasnovas, C., Cano, L. M., Albertí, A., Céspedes, M. & Rigo, G. Charcot-Marie-tooth disease. *Foot Ankle Spec.* **1**, 350-354 (2008).
 328. Niemann, A., Berger, P. & Suter, U. Pathomechanisms of mutant proteins in Charcot-Marie-Tooth disease. *Neuromol. Med.* **8**, 217-241 (2006).
 329. Pareyson, D., Saveri, P., Sagnelli, A. & Piscoquito, G. Mitochondrial dynamics and inherited peripheral nerve diseases. *Neurosci. Lett.* **596**, 66-77 (2015).
 330. Amptoulach, S. & Tsavaris, N. Neurotoxicity Caused by the Treatment with Platinum Analogues. *Chemother. Res. Pract.* **2011**, 843019 (2011).
 331. Yang, Z. *et al.* Cisplatin preferentially binds mitochondrial DNA and voltage-dependent anion channel protein in the mitochondrial membrane of head and

- neck squamous cell carcinoma: Possible role in apoptosis. *Clin. Cancer Res.* **12**, 5817-5825 (2006).
332. Shy, M. *et al.* Phenotypic clustering in MPZ mutations. *Brain* **127**, 371-384 (2004).
333. Mandich, P. *et al.* Clinical features and molecular modelling of novel MPZ mutations in demyelinating and axonal neuropathies. *Eur. J. Hum. Genet.* **17**, 1129-1134 (2009).
334. Schneider-Gold, C., Koetting, J., Epplen, J. T., Gold, R. & Gerding, W. M. Unusual Charcot-Marie-Tooth Phenotype due to a Mutation within the Intracellular Domain of Myelin Protein Zero. *Muscle Nerve* **41**, 550-554 (2010).
335. Su, Y. *et al.* Myelin Protein Zero Gene Mutated in Charcot-Marie-Tooth Type-1b Patients. *Proc. Natl. Acad. Sci. U. S. A.* **90**, 10856-10860 (1993).
336. Fabrizi, G. *et al.* Gene dosage sensitivity of a novel mutation in the intracellular domain of P0 associated with Charcot-Marie-Tooth disease type 1B. *Neuromusc. Disord.* **16**, 183-187 (2006).
337. Street, V. *et al.* Charcot-Marie-Tooth neuropathy: clinical phenotypes of four novel mutations in the MPZ and Cx32 genes. *Neuromusc. Disord.* **12**, 643-650 (2002).
338. Choi, B. *et al.* Mutational analysis of PMP22, MPZ, GJB1, EGR2 and NEFL in Korean Charcot-Marie-Tooth neuropathy patients. *Hum. Mutat.* **24**, 185-186 (2004).
339. Plante-Bordeneuve, V. *et al.* The range of chronic demyelinating neuropathy of infancy: a clinico-pathological and genetic study of 15 unrelated cases. *J. Neurol.* **248**, 795-803 (2001).
340. Bai, Y. *et al.* Myelin protein zero mutations and the unfolded protein response in Charcot Marie Tooth disease type 1B. *Ann. Clin. Transl. Neurol.* **5**, 445-455 (2018).
341. Prada, V. *et al.* Gain of Glycosylation: A New Pathomechanism of Myelin Protein Zero Mutations. *Ann. Neurol.* **71**, 427-431 (2012).
342. Harauz, G., Ladizhansky, V. & Boggs, J. M. Structural Polymorphism and Multifunctionality of Myelin Basic Protein. *Biochemistry (N. Y.)* **48**, 8094-8104 (2009).
343. Hammarström, M., Woestenenk, E., Hellgren, N., Härd, T. & Berglund, H. Effect of N-terminal solubility enhancing fusion proteins on yield of purified target protein. *J. Struct. Funct. Genomics* **7**, 1-14 (2006).
344. Busso, D., Delagoutte-Busso, B. & Moras, D. Construction of a set Gateway-based destination vectors for high-throughput cloning and expression screening in *Escherichia coli*. *Anal. Biochem.* **343**, 313-321 (2005).
345. Bates, I. *et al.* Characterization of a recombinant murine 18.5-kDa myelin basic protein. *Protein Expr. Purif.* **20**, 285-299 (2000).

-
346. van den Berg, S., Löfdahl, P., Härd, T. & Berglund, H. Improved solubility of TEV protease by directed evolution. *J. Biotechnol.* **121**, 291-298 (2006).
347. Chukhlieb, M., Raasakka, A., Ruskamo, S. & Kursula, P. The N-terminal cytoplasmic domain of neuregulin 1 type III is intrinsically disordered. *Amino Acids* **47**, 1567-1577 (2015).
348. Nagle, J. & Tristram-Nagle, S. Structure of lipid bilayers. *Biochim. Biophys. Acta-Rev. Biomembr.* **1469**, 159-195 (2000).
349. Kucerka, N., Nieh, M. & Katsaras, J. Fluid phase lipid areas and bilayer thicknesses of commonly used phosphatidylcholines as a function of temperature. *Biochim. Biophys. Acta-Biomembr.* **1808**, 2761-2771 (2011).
350. Korade, Z. & Kenworthy, A. K. Lipid rafts, cholesterol, and the brain. *Neuropharmacology* **55**, 1265-1273 (2008).
351. Harayama, T. & Riezman, H. Understanding the diversity of membrane lipid composition. *Nat. Rev. Mol. Cell Biol.* **19**, 281-296 (2018).
352. Silvius, J. R. in *Lipid-Protein Interactions* (eds Jost, P. C. & Griffith, O. H.) 239-281 (John Wiley & Sons, Inc, New York, 1982).
353. Laouini, A. *et al.* Preparation, Characterization and Applications of Liposomes: State of the Art. *J. Colloid Sci. Biotechnol.* **1**, 147-168 (2012).
354. Veatch, S. L. Electro-formation and fluorescence microscopy of giant vesicles with coexisting liquid phases. *Methods Mol. Biol.* **398**, 59-72 (2007).
355. Lasch, J., Weissig, V. & Brandi, M. Preparation of liposomes. *Liposomes: A practical approach. 2nd Edition*, 3-29 (2003).
356. Lapinski, M. M., Castro-Forero, A., Greiner, A. J., Ofoli, R. Y. & Blanchard, G. J. Comparison of liposomes formed by sonication and extrusion: Rotational and translational diffusion of an embedded chromophore. *Langmuir* **23**, 11677-11683 (2007).
357. Bürck, J., Wadhvani, P., Fanghaenel, S. & Ulrich, A. S. Oriented Circular Dichroism: A Method to Characterize Membrane Active Peptides in Oriented Lipid Bilayers. *Acc. Chem. Res.* **49**, 184-192 (2016).
358. Belegriou, S. *et al.* Biomimetic supported membranes from amphiphilic block copolymers. *Soft Matter* **6**, 179-186 (2010).
359. Clifton, L. A. *et al.* An Accurate In Vitro Model of the E. coli Envelope. *Angew. Chem. -Int. Edit.* **54**, 11952-11955 (2015).
360. Junghans, A. *et al.* Analysis of biosurfaces by neutron reflectometry: From simple to complex interfaces. *Biointerphases* **10**, 019014 (2015).
361. Hamley, I. W. in *Introduction to Soft Matter: Synthetic and Biological Self-Assembling Materials* (ed Hamley, I. W.) 161-220 (John Wiley & Sons, Ltd, 2007).

362. Laemmli, U. K. Cleavage of Structural Proteins during the Assembly of the Head of Bacteriophage T4. *Nature* **227**, 680-685 (1970).
363. Perkins, D. N., Pappin, D. J., Creasy, D. M. & Cottrell, J. S. Probability-based protein identification by searching sequence databases using mass spectrometry data. *Electrophoresis* **20**, 3551-3567 (1999).
364. *Gel Filtration: Principles and Methods* 120 (Amersham Biosciences, 2002).
365. Gillis, R. B., Rowe, A. J., Adams, G. G. & Harding, S. E. A review of modern approaches to the hydrodynamic characterisation of polydisperse macromolecular systems in biotechnology. *Biotechnol. Genet. Eng. Rev.* **30**, 142-157 (2014).
366. Slotboom, D. J., Durkens, R. H., Olieman, K. & Erkens, G. B. Static light scattering to characterize membrane proteins in detergent solution. *Methods* **46**, 73-82 (2008).
367. Stetefeld, J., McKenna, S. A. & Patel, T. R. Dynamic light scattering: a practical guide and applications in biomedical sciences. *Biophys. Rev.* **8**, 409-427 (2016).
368. Brewer, A. K. & Striegel, A. M. Characterizing the size, shape, and compactness of a polydisperse prolate ellipsoidal particle via quadruple-detector hydrodynamic chromatography. *Analyst* **136**, 515-519 (2011).
369. Kikhney, A. G. & Svergun, D. I. A practical guide to small angle X-ray scattering (SAXS) of flexible and intrinsically disordered proteins. *FEBS Lett.* **589**, 2570-2577 (2015).
370. Trehwella, J. *Biological Small-Angle Scattering: Theory and Practice*. By Eaton E. Lattman, Thomas D. Grant and Edward H. Snell. Oxford University Press, 2018. Pp. 288. Price GBP 65.00, hardback, ISBN 9780199670871. *Acta Cryst.* **D75**, 109-110 (2019).
371. Grant, T. D. *et al.* Small Angle X-ray Scattering as a Complementary Tool for High-Throughput Structural Studies. *Biopolymers* **95**, 517-530 (2011).
372. Jimenez, A. *et al.* Validation of Electron Microscopy Initial Models via Small Angle X-Ray Scattering Curves. *Bioinformatics* (2018).
373. Afonine, P. V. *et al.* Towards automated crystallographic structure refinement with phenix.refine. *Acta Cryst.* **D68**, 352-367 (2012).
374. Rambo, R. P. & Tainer, J. A. Characterizing Flexible and Intrinsically Unstructured Biological Macromolecules by SAS Using the Porod-Debye Law. *Biopolymers* **95**, 559-571 (2011).
375. Svergun, D. I. Determination of the regularization parameter in indirect-transform methods using perceptual criteria. *J. Appl. Crystallogr* **25**, 495-503 (1992).
376. Svergun, D. Restoring low resolution structure of biological macromolecules from solution scattering using simulated annealing. *Biophys. J.* **76**, 2879-2886 (1999).

-
377. Franke, D. & Svergun, D. I. DAMMIF, a program for rapid ab-initio shape determination in small-angle scattering. *J. Appl. Crystallogr.* **42**, 342-346 (2009).
378. Ruskamo, S. *et al.* Juxtanodin is an intrinsically disordered F-actin-binding protein. *Sci. Rep.* **2**, 899 (2012).
379. Tria, G., Mertens, H. D. T., Kachala, M. & Svergun, D. I. Advanced ensemble modelling of flexible macromolecules using X-ray solution scattering. *IUCrJ* **2**, 207-217 (2015).
380. Svergun, D., Petoukhov, M. & Koch, M. Determination of domain structure of proteins from X-ray solution scattering. *Biophys. J.* **80**, 2946-2953 (2001).
381. Lees, J. G., Miles, A. J., Wien, F. & Wallace, B. A. A reference database for circular dichroism spectroscopy covering fold and secondary structure space. *Bioinformatics* **22**, 1955-1962 (2006).
382. Wallace, B. A. & Janes, R. W. Synchrotron radiation circular dichroism (SRCD) spectroscopy: an enhanced method for examining protein conformations and protein interactions. *Biochem. Soc. Trans.* **38**, 861-873 (2010).
383. Matsuo, K. & Gekko, K. Circular-dichroism and synchrotron-radiation circular-dichroism spectroscopy as tools to monitor protein structure in a lipid environment. *Methods Mol. Biol.* **974**, 151-176 (2013).
384. Greenfield, N. J. Using circular dichroism spectra to estimate protein secondary structure. *Nat. Protoc.* **1**, 2876-2890 (2006).
385. Chiriac, A. P. *et al.* Investigation of a Self-Assembled Nanogel Structure Bearing Spiroacetal Moieties and Cholesterol as Low Molecular Mass Gelator. *Rev. Roum. Chim.* **63**, 673-684 (2018).
386. Lees, J., Smith, B., Wien, F., Miles, A. & Wallace, B. CDtool - an integrated software package for circular dichroism spectroscopic data processing, analysis, and archiving. *Anal. Biochem.* **332**, 285-289 (2004).
387. Wallace, B. A. & Miles, A. J. CDtoolX, a Downloadable Software Package for Processing and Analyses of Circular Dichroism Spectroscopic Data. *Protein Sci.* **27**, 1717-1722 (2018).
388. Miles, A. J. & Wallace, B. A. Circular dichroism spectroscopy of membrane proteins. *Chem. Soc. Rev.* **45**, 4859-4872 (2016).
389. Wallace, B. A. & Janes, R. W. in *Modern Techniques for Circular Dichroism and Synchrotron Radiation* (eds Wallace, B. A. & Janes, R. W.) 13 (IOS Press, The Netherlands, 2009).
390. Zeng, S., Baillargeat, D., Ho, H. & Yong, K. Nanomaterials enhanced surface plasmon resonance for biological and chemical sensing applications. *Chem. Soc. Rev.* **43**, 3426-3452 (2014).

391. Hodnik, V. & Anderluh, G. Surface plasmon resonance for measuring interactions of proteins with lipid membranes. *Methods Mol. Biol.* **974**, 23-36 (2013).
392. Mabrey, S. & Sturtevant, J. M. Investigation of phase-transitions of lipids and lipid mixtures by high sensitivity differential scanning calorimetry. *Proc. Natl. Acad. Sci. U. S. A.* **73**, 3862-3866 (1976).
393. Linari, M. *et al.* Force generation by skeletal muscle is controlled by mechanosensing in myosin filaments. *Nature* **528**, 276-279 (2015).
394. Herrmann, J. *et al.* Environmental Calcium Controls Alternate Physical States of the Caulobacter Surface Layer. *Biophys. J.* **112**, 1841-1851 (2017).
395. Morandat, S., Azouzi, S., Beauvais, E., Mastouri, A. & El Kirat, K. Atomic force microscopy of model lipid membranes. *Anal. Bioanal. Chem.* **405**, 1445-1461 (2013).
396. Krueger, J. K. & Wignall, G. D. in *Neutron Scattering in Biology: Techniques and Applications* (eds Fitter, J. G., T. & Katsaras, J.) 127-160 (Springer Science & Business Media, 2006).
397. Nickels, J. D. *et al.* Mechanical Properties of Nanoscopic Lipid Domains. *J. Am. Chem. Soc.* **137**, 15772-15780 (2015).
398. Mahieu, E. & Gabel, F. Biological small-angle neutron scattering: recent results and development. *Acta Cryst.* **D74**, 715-726 (2018).
399. Majewski, J., Kuhl, T. L., Wong, J. Y. & Smith, G. S. X-ray and neutron surface scattering for studying lipid/polymer assemblies at the air-liquid and solid-liquid interfaces. *J. Biotechnol.* **74**, 207-231 (2000).
400. Scarff, C. A., Fuller, M. J. G., Thompson, R. F. & Iadaza, M. G. Variations on Negative Stain Electron Microscopy Methods: Tools for Tackling Challenging Systems. *J. Vis. Exp.*, e57199 (2018).
401. Franken, L. E., Boekema, E. J. & Stuart, M. C. A. Transmission Electron Microscopy as a Tool for the Characterization of Soft Materials: Application and Interpretation. *Adv. Sci.* **4**, 1600476 (2017).
402. Bai, X., McMullan, G. & Scheres, S. H. W. How cryo-EM is revolutionizing structural biology. *Trends Biochem. Sci.* **40**, 49-57 (2015).
403. Breyton, C. *et al.* Small angle neutron scattering for the study of solubilised membrane proteins. *Eur. Phys. J. E* **36**, 71 (2013).
404. Friess, M. *et al.* Intracellular ion signaling influences myelin basic protein synthesis in oligodendrocyte precursor cells. *Cell Calcium* **60**, 322-330 (2016).
405. Baraban, M., Koudelka, S. & Lyons, D. A. Ca²⁺ activity signatures of myelin sheath formation and growth in vivo. *Nat. Neurosci.* **21**, 19-23 (2018).

-
406. Krasnow, A. M., Ford, M. C., Valdivia, L. E., Wilson, S. W. & Attwell, D. Regulation of developing myelin sheath elongation by oligodendrocyte calcium transients in vivo. *Nat. Neurosci.* **21**, 24-28 (2018).
 407. Harauz, G. & Musse, A. A. A tale of two citrullines - Structural and functional aspects of myelin basic protein deimination in health and disease. *Neurochem. Res.* **32**, 137-158 (2007).
 408. Harauz, G. & Libich, D. S. The Classic Basic Protein of Myelin - Conserved Structural Motifs and the Dynamic Molecular Barcode Involved in Membrane Adhesion and Protein-Protein Interactions. *Curr. Protein Peptide Sci.* **10**, 196-215 (2009).
 409. Sela, B. & Bach, D. Calorimetric Studies on the Interaction of Gangliosides with Phospholipids and Myelin Basic-Protein. *Biochim. Biophys. Acta* **771**, 177-182 (1984).
 410. Bach, D. & Sela, B. Interaction of Myelin Basic-Protein with Gangliosides and Ganglioside-Phospholipid Mixtures. *Biochim. Biophys. Acta* **819**, 225-230 (1985).
 411. Reinl, H. & Bayerl, T. Interaction of Myelin Basic-Protein with Single Bilayers on a Solid Support - an NMR, DSC and Polarized Infrared ATR Study. *Biochim. Biophys. Acta* **1151**, 127-136 (1993).
 412. Haas, H. *et al.* Lamellar order within Langmuir-Blodgett multilayers from phospholipid and myelin basic protein: A neutron reflectivity study. *Langmuir* **23**, 8491-8496 (2007).
 413. Raffaele, R. How the protein concentration affects unfolding curves of oligomers. *Biopolymers* **53**, 221-225 (2000).
 414. Kuznetsova, I. M., Turoverov, K. K. & Uversky, V. N. What Macromolecular Crowding Can Do to a Protein. *Int. J. Mol. Sci.* **15**, 23090-23140 (2014).
 415. Joshi, V., Shivach, T., Yadav, N. & Rathore, A. S. Circular Dichroism Spectroscopy as a Tool for Monitoring Aggregation in Monoclonal Antibody Therapeutics. *Anal. Chem.* **86**, 11606-11613 (2014).
 416. Natali, F. *et al.* Protein-membrane interaction: effect of myelin basic protein on the dynamics of oriented lipids. *Chem. Phys.* **292**, 455-464 (2003).
 417. Knoll, W. *et al.* Dynamic properties of a reconstituted myelin sheath. *Spectroscopy* **24**, 585-592 (2010).
 418. Müller, C., Bauer, N. M., Schaefer, I. & White, R. Making myelin basic protein - from mRNA transport to localized translation. *Front. Cell. Neurosci.* **7**, 169 (2013).
 419. Dyer, C. & Benjamins, J. Organization of oligodendroglial membrane sheet. I: Association of myelin basic protein and 2',3'-cyclic nucleotide 3'-phosphohydrolase with cytoskeleton. *J. Neurosci. Res.* **24**, 201-211 (1989).

420. Bamm, V. V., Ahmed, M. A. M. & Harauz, G. Interaction of myelin basic protein with actin in the presence of dodecylphosphocholine micelles. *Biochemistry* **49**, 6903-6915 (2010).
421. Medveczky, P. *et al.* Myelin basic protein, an autoantigen in multiple sclerosis, is selectively processed by human trypsin 4. *FEBS Lett.* **580**, 545-552 (2006).
422. Fasano, A. *et al.* The different forms of PNS myelin P0 protein within and outside lipid rafts. *J. Neurochem.* **107**, 291-301 (2008).
423. Hasse, B., Bosse, F. & Müller, H. W. Proteins of Peripheral Myelin Are Associated With Glycosphingolipid/Cholesterol Enriched Membranes. *J. Neurosci. Res.* **69**, 227-232 (2002).
424. Ishiyama, N. *et al.* The effects of deimination of myelin basic protein on structures formed by its interaction with phosphoinositide-containing lipid monolayers. *J. Struct. Biol.* **136**, 30-45 (2001).
425. Bates, I., Feix, J., Boggs, J. & Harauz, G. An immunodominant epitope of myelin basic protein is an amphipathic alpha-helix. *J. Biol. Chem.* **279**, 5757-5764 (2004).
426. Baran, C., Smith, G. S. T., Bamm, V. V., Harauz, G. & Lee, J. S. Divalent cations induce a compaction of intrinsically disordered myelin basic protein. *Biochem. Biophys. Res. Commun.* **391**, 224-229 (2010).
427. Myllykoski, M., Raasakka, A., Han, H. & Kursula, P. Myelin 2',3'-Cyclic Nucleotide 3'-Phosphodiesterase: Active-Site Ligand Binding and Molecular Conformation. *PLoS One* **7**, e32336 (2012).
428. Myllykoski, M. *et al.* Crystallographic Analysis of the Reaction Cycle of 2',3'-Cyclic Nucleotide 3'-Phosphodiesterase, a Unique Member of the 2H Phosphoesterase Family. *J. Mol. Biol.* **425**, 4307-4322 (2013).
429. Lee, Y. *et al.* Cellular characterization of MPZ mutations presenting with diverse clinical phenotypes. *J. Neurol.* **257**, 1661-1668 (2010).
430. Trapp, B. *et al.* Polarization of Myelinating Schwann-Cell Surface-Membranes - Role of Microtubules and the Trans-Golgi Network. *J. Neurosci.* **15**, 1797-1807 (1995).
431. Zambrano, F., Fleischer, S. & Fleischer, B. Lipid-Composition of Golgi Apparatus of Rat-Kidney and Liver in Comparison with Other Subcellular Organelles. *Biochim. Biophys. Acta* **380**, 357-369 (1975).
432. Fledrich, R., Stassart, R. M. & Sereda, M. W. Murine therapeutic models for Charcot-Marie-Tooth (CMT) disease. *Br. Med. Bull.* **102**, 89-113 (2012).
433. Wydro, P., Flasiński, M. & Broniatowski, M. Does cholesterol preferentially pack in lipid domains with saturated sphingomyelin over phosphatidylcholine? A comprehensive monolayer study combined with grazing incidence X-ray diffraction and Brewster angle microscopy experiments. *J. Colloid Interface Sci.* **397**, 122-130 (2013).

-
434. Sebastiani, F., Campbell, R. A. & Pfrang, C. Complementarity of neutron reflectometry and ellipsometry for the study of atmospheric reactions at the air-water interface. *RSC Adv.* **5**, 107105-107111 (2015).
435. Nielsen, S. B. & Otzen, D. E. Quartz crystal microbalances as tools for probing protein-membrane interactions. *Methods Mol. Biol.* **974**, 1-21 (2013).
436. Hexemer, A. & Mueller-Buschbaum, P. Advanced grazing-incidence techniques for modern soft-matter materials analysis. *IUCrJ* **2**, 106-125 (2015).
437. Strobl, M. *et al.* BioRef – a time-of-flight neutron reflectometer combined with in-situ infrared spectroscopy at the Helmholtz Centre Berlin. *J. Phys. Conf. Ser.* **251**, 012059 (2010).
438. Tatulian, S. A. Structural characterization of membrane proteins and peptides by FTIR and ATR-FTIR spectroscopy. *Methods Mol. Biol.* **974**, 177-218 (2013).
439. Opella, S. Solid-state NMR of membrane proteins. *Abstr. Pap. Am. Chem. Soc.* **254** (2017).
440. Vadas, O., Jenkins, M. L., Dornan, G. L. & Burke, J. E. Using Hydrogen-Deuterium Exchange Mass Spectrometry to Examine Protein-Membrane Interactions. *Methods Enzymol.* **583**, 143-172 (2017).
441. Stevens, A. J. *et al.* A promiscuous split intein with expanded protein engineering applications. *Proc. Natl. Acad. Sci. U. S. A.* **114**, 8538-8543 (2017).
442. Strandberg, E. & Ulrich, A. NMR methods for studying membrane-active antimicrobial peptides. *Concepts Magn. Reson. Part A* **23A**, 89-120 (2004).
443. Didenko, T., Liu, J. J., Horst, R., Stevens, R. C. & Wuethrich, K. Fluorine-19 NMR of integral membrane proteins illustrated with studies of GPCRs. *Curr. Opin. Struct. Biol.* **23**, 740-747 (2013).
444. Liu, H., Oteiza, P., Gershwin, M., Golub, M. & Keen, C. Effects of Maternal Marginal Zinc-Deficiency on Myelin Protein Profiles in the Suckling Rat and Infant Rhesus-Monkey. *Biol. Trace Elem. Res.* **34**, 55-66 (1992).
445. Bredholt, M. & Frederiksen, J. L. Zinc in Multiple Sclerosis: A Systematic Review and Meta-Analysis. *ASN Neuro* **8**, 1759091416651511 (2016).
446. Earl, C., Chantry, A., Mohammad, N. & Glynn, P. Zinc Ions Stabilize the Association of Basic-Protein with Brain Myelin Membranes. *J. Neurochem.* **51**, 718-724 (1988).
447. Cavatorta, P. *et al.* Myelin Basic-Protein Interaction with Zinc and Phosphate - Fluorescence Studies on the Water-Soluble Form of the Protein. *Biophys. J.* **66**, 1174-1179 (1994).
448. Riccio, P. *et al.* Specificity of zinc binding to myelin basic protein. *Neurochem. Res.* **20**, 1107-1113 (1995).

449. Majava, V. *et al.* Structural analysis of the complex between calmodulin and full-length myelin basic protein, an intrinsically disordered molecule. *Amino Acids* **39**, 59-71 (2010).
450. Smith, G. S. T., Chen, L., Bamm, V. V., Dutcher, J. R. & Harauz, G. The interaction of zinc with membrane-associated 18.5 kDa myelin basic protein: an attenuated total reflectance-Fourier transform infrared spectroscopic study. *Amino Acids* **39**, 739-750 (2010).
451. Binder, H., Arnold, K., Ulrich, A. & Zschornig, O. Interaction of Zn²⁺ with phospholipid membranes. *Biophys. Chem.* **90**, 57-74 (2001).
452. Liu, Y. & Liu, J. Zn²⁺ Induced Irreversible Aggregation, Stacking, and Leakage of Choline Phosphate Liposomes. *Langmuir* **33**, 14472-14479 (2017).
453. Min, Y. *et al.* Critical and Off-Critical Miscibility Transitions in Model Extracellular and Cytoplasmic Myelin Lipid Monolayers. *Biophys. J.* **100**, 1490-1498 (2011).
454. Pritzker, L., Joshi, S., Gowan, J., Harauz, G. & Moscarello, M. Deimination of myelin basic protein. 1. Effect of deimination of arginyl residues of myelin basic protein on its structure and susceptibility to digestion by cathepsin D. *Biochemistry* **39**, 5374-5381 (2000).
455. Pritzker, L., Joshi, S., Harauz, G. & Moscarello, M. Deimination of myelin basic protein. 2. Effect of methylation of MBP on its deimination by peptidylarginine deiminase. *Biochemistry* **39**, 5382-5388 (2000).
456. Ulmer, J. & Braun, P. In vivo Phosphorylation of Myelin Basic-Proteins in Developing Mouse-Brain - Evidence that Phosphorylation is an Early Event in Myelin Formation. *Dev. Neurosci.* **6**, 345-355 (1984).
457. Gillooly, D., Simonsen, A. & Stenmark, H. Cellular functions of phosphatidylinositol 3-phosphate and FYVE domain proteins. *Biochem. J.* **355**, 249-258 (2001).
458. D'Urso, D. & Müller, H. W. Ins and outs of peripheral myelin protein-22: Mapping transmembrane topology and intracellular sorting. *J. Neurosci. Res.* **49**, 551-562 (1997).
459. Greer, J. & Lees, M. Myelin proteolipid protein - the first 50 years. *Int. J. Biochem. Cell Biol.* **34**, 211-215 (2002).

ARTICLE I

The Membrane Association Landscape of Myelin Basic Protein Portrays Formation of the Myelin Major Dense Line at the Molecular Level.

Raasakka A., Ruskamo S., Kowal J., Barker R., Baumann A., Martel A., Tuusa J., Myllykoski M., Bürck J., Ulrich A.S., Stahlberg H. & Kursula P.

Scientific Reports 7(1):4974. DOI: 10.1038/s41598-017-05364-3. (2017)

Abstract

Compact myelin comprises most of the dry weight of myelin, and its insulative nature is the basis for saltatory conduction of nerve impulses. The major dense line (MDL) is a 3-nm compartment between two cytoplasmic leaflets of stacked myelin membranes, mostly occupied by a myelin basic protein (MBP) phase. MBP is an abundant myelin protein involved in demyelinating diseases, such as multiple sclerosis. The association of MBP with lipid membranes has been studied for decades, but the MBP-driven formation of the MDL remains elusive at the biomolecular level. We employed complementary biophysical methods, including atomic force microscopy, cryo-electron microscopy, and neutron scattering, to investigate the formation of membrane stacks all the way from MBP binding onto a single membrane leaflet to the organisation of a stable MDL. Our results support the formation of an amorphous protein phase of MBP between two membrane bilayers and provide a molecular model for MDL formation during myelination, which is of importance when understanding myelin assembly and demyelinating conditions.

SCIENTIFIC REPORTS

OPEN

Membrane Association Landscape of Myelin Basic Protein Portrays Formation of the Myelin Major Dense Line

Arne Raasakka^{1,2}, Salla Ruskamo², Julia Kowal³, Robert Barker^{4,5}, Anne Baumann^{1,6}, Anne Martel⁵, Jussi Tuusa², Matti Myllykoski², Jochen Bürck⁷, Anne S. Ulrich^{7,8}, Henning Stahlberg³ & Petri Kursula^{1,2}

Compact myelin comprises most of the dry weight of myelin, and its insulative nature is the basis for saltatory conduction of nerve impulses. The major dense line (MDL) is a 3-nm compartment between two cytoplasmic leaflets of stacked myelin membranes, mostly occupied by a myelin basic protein (MBP) phase. MBP is an abundant myelin protein involved in demyelinating diseases, such as multiple sclerosis. The association of MBP with lipid membranes has been studied for decades, but the MBP-driven formation of the MDL remains elusive at the biomolecular level. We employed complementary biophysical methods, including atomic force microscopy, cryo-electron microscopy, and neutron scattering, to investigate the formation of membrane stacks all the way from MBP binding onto a single membrane leaflet to the organisation of a stable MDL. Our results support the formation of an amorphous protein phase of MBP between two membrane bilayers and provide a molecular model for MDL formation during myelination, which is of importance when understanding myelin assembly and demyelinating conditions.

Compact myelin (CM) is the most important and abundant structure of the vertebrate myelin sheath in both the central and peripheral nervous systems (CNS and PNS, respectively). The foundation of myelin-accelerated saltatory conduction lies in the insulative nature of CM, which can be disturbed by damage caused by de- or dysmyelination, as well as in the myelin-guided distribution of ion channels on the axonal plasma membrane. Myelin damage often results in chronic neurological conditions, such as multiple sclerosis (MS), Charcot-Marie-Tooth disease, or Dejerine-Sottas syndrome, all of which display a broad spectrum of symptoms, have at least a partial genetic background, and remain difficult to treat, even at an early onset^{1,2}.

Myelin basic protein (MBP) is one of the crucial factors in CM membrane stacking in the CNS, its 18.5-kDa isoform being most abundant³. The presence of many MBP isoforms is further complicated through post-translational modifications, including deimination, which produces a pool of citrullinated variants with decreased net charge⁴. The high positive net charge of MBP is related to the intrinsically disordered conformation of MBP in solution; on the other hand, it allows MBP to interact with the phospholipid-rich cytoplasmic face of myelin membranes. This close interaction results in charge neutralisation, folding, and partial membrane insertion⁵. MBP promotes myelin membrane stacking and the formation of the major dense line (MDL), which is disturbed in demyelinating conditions, including MS and demyelinating neuropathies^{6,7}.

MBP is known for its autoantigenic properties in MS, and the major immunodominant epitope of MBP bound to a T-cell receptor complex has been structurally characterised^{5,8}. The autoantigenic character may arise from the susceptibility of MBP to proteolysis in a lipid composition-dependent manner^{5,9}. Additionally, deimination alters

¹Department of Biomedicine, University of Bergen, Bergen, Norway. ²Faculty of Biochemistry and Molecular Medicine & Biocenter Oulu, University of Oulu, Oulu, Finland. ³Center for Cellular Imaging and NanoAnalytics (C-CINA), Biozentrum, University of Basel, Basel, Switzerland. ⁴School of Physical Sciences, University of Kent, Canterbury, Kent, United Kingdom. ⁵Institut Laue-Langevin (ILL), Grenoble, France. ⁶Division of Psychiatry, Haukeland University Hospital, Bergen, Norway. ⁷Institute of Biological Interfaces (IBG-2), Karlsruhe Institute of Technology, Karlsruhe, Germany. ⁸Institute of Organic Chemistry, Karlsruhe Institute of Technology, Karlsruhe, Germany. Correspondence and requests for materials should be addressed to P.K. (email: petri.kursula@uib.no)

the structure and function of MBP, promoting lowered CM stability and increased protease susceptibility^{10, 11}. Hence, the membrane association mode, structure, and stability of MBP must be considered when investigating the molecular mechanisms of MBP-related diseases.

MBP has been suggested to form an ordered, self-assembled protein meshwork of either anti-parallel or stacked MBP molecules with confined degrees of freedom between myelin cytoplasmic leaflets^{9, 12, 13}. This protein meshwork stabilises CM, while other factors, such as the myelin protein P2, may be involved in the process^{14, 15}. The surface adsorption behaviour of MBP has been intensively studied, and it was proposed that MBP associates with the membrane surface prior to folding to its adhesive conformation¹⁶. This model, based on hard model surfaces, is in corroboration with earlier studies on lipid bilayers¹⁷, and a mostly disordered intermediate MBP folding state has been proposed based on titration experiments and modelling under conditions with decreasing dielectric constant¹⁸.

To elucidate the membrane association mechanisms of MBP, we performed a comprehensive characterisation of recombinant tag-free MBP (rMBP) binding to model membranes. Our combined approach using electron microscopy (EM), atomic force microscopy (AFM), and neutron reflectometry (NR) provides evidence for the formation of a dense protein phase on a single membrane leaflet, suggesting the existence of a protein meshwork¹³ that forms above a critical MBP concentration. Our results illustrate a step-wise formation of the MDL at the biomolecular scale.

Results

Although much is known about the molecular properties of MBP and its interaction with membranes, a comprehensive picture of different steps in the process of myelin membrane compaction has been lacking. We set out to investigate the fine details of MBP-membrane interactions using a panel of biophysical methods to follow membrane binding, protein embedding, and bilayer stacking.

Characterisation of untagged rMBP. A notable amount of past MBP research has been performed using C-terminally His₆-tagged recombinant MBP (MBP-His)^{12, 14, 15, 19, 20} or MBP purified from nerve tissue^{4, 9, 10, 16, 17, 21}. To overcome problems arising from construct design or contaminants and heterogeneity in tissue extracts, we used untagged recombinant murine MBP (rMBP) corresponding to the major 18.5-kDa isoform, similarly to other recent studies^{18, 22–24}. rMBP appeared as a single band in denaturing gel electrophoresis (SDS-PAGE) and monomeric and monodisperse in size-exclusion chromatography (SEC) and dynamic light scattering (DLS), with a hydrodynamic radius (R_h) of 3.5 nm (Supplementary Fig. S1). The identity of rMBP was confirmed using tryptic peptide mass analysis, and the molecular weight of pure rMBP was as expected (18544 Da).

In the absence of additives, rMBP was always disordered in aqueous solution according to synchrotron radiation circular dichroism (SRCD) spectroscopy, which further revealed moderate helical folding in 2,2,2-trifluoroethanol (TFE) as well as with negatively charged sodium dodecyl sulphate (SDS) and several neutral detergent micelles (Supplementary Fig. S1). Using synchrotron small-angle X-ray scattering (SAXS), we found that rMBP was monomeric and highly elongated in solution (Fig. 1a, Supplementary Fig. S1, Supplementary Table S1). This explains the obtained radius of gyration (R_g ; 3.7–4.0 nm, depending on method) being higher than the measured R_h ; this is typical for particles deviating significantly from globularity²⁵. The *ab initio* model (Fig. 1b) is elongated and similar to previously described models^{20, 21}. Ensemble optimisation analysis (EOM) revealed distinct subpopulations of both R_g and maximum particle dimension (D_{max}), suggesting the presence of different rMBP conformational species in solution (Fig. 1c). rMBP mostly adopts a reasonably compact conformation, close to that expected for a random polymer, instead of being fully extended (Fig. 1c, Supplementary Table S1). To study this further, we collected small-angle neutron scattering (SANS) data of rMBP in the absence and presence of *n*-dodecylphosphocholine (DPC) micelles (Fig. 1d, Supplementary Fig. S2, Supplementary Table S1). Size comparison of a computationally modelled DPC micelle²⁶ and a single rMBP conformer suggests that each micelle can most likely only embed a single rMBP molecule (Fig. 1e), as suggested earlier¹⁹. It is noteworthy that the number of detergent molecules can vary within DPC micelles, with effects on micellar size and surface curvature²⁶. Micellar scattering was masked using the contrast match-point of DPC, which allowed us to focus on the scattering of rMBP alone: EOM analysis of the SANS data revealed that DPC-bound rMBP shifted quantitatively to the more compact population, with a sharpened R_g distribution of 2.6–3.8 nm and a D_{max} distribution of 8–12 nm (Fig. 1f, Supplementary Table S1). Whilst being still relatively elongated, the data fit to a scenario where part of rMBP is embedded within a DPC micelle and partially folded, which is also supported by SRCD experiments (Supplementary Fig. S1) as well as SANS data analysis (Supplementary Fig. S2) using the Porod–Debye law²⁷.

Membrane interaction and folding of rMBP. We next investigated the membrane association of rMBP. For rapid screening of interactions, we used solution-state SRCD, as MBP gains secondary structure upon lipid binding²⁰. rMBP reproducibly presented a clear increase in α -helical content with negatively charged small unilamellar vesicles (SUVs), with a slightly higher increase in the presence of saturated (dimyristoylphosphatidylcholine (DMPC): dimyristoylphosphatidylglycerol (DMPG)) than unsaturated lipids (dioleoylphosphatidylcholine (DOPC): dioleoylphosphatidylserine (DOPS)) (Fig. 2a). The importance of membrane surface charge is very clear, as rMBP does not undergo conformational changes with net neutral phosphatidylcholine lipids, indicating abolished, or at least altered or weakened, binding, as described previously²⁸. To assess the effect of the abundant myelin lipids cholesterol, sphingomyelin, and phosphatidylethanolamine (DMPE) on folding, we included 10% (w/w) of each lipid separately in a standard DMPC:DMPG (1:1) mixture (Fig. 2b). None of these additives significantly affected the rMBP helical content, indicating that the surface net charge of the membrane dominates over lipid fluidity or hydrocarbon tails in initiating MBP folding.

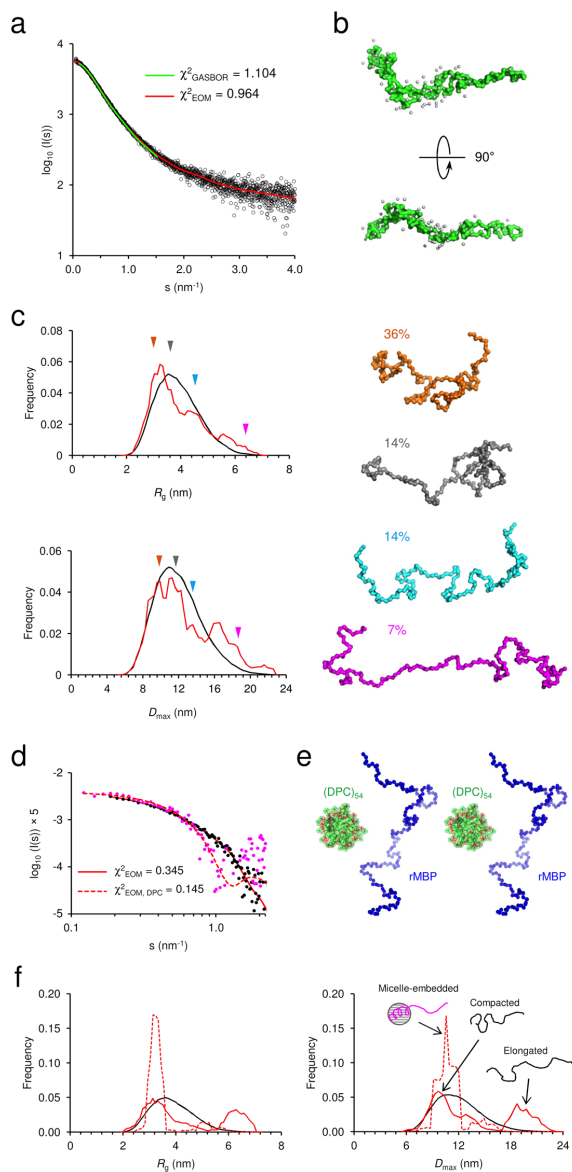


Figure 1. rMBP conformation in solution. **(a)** rMBP is significantly elongated based on SAXS data. GASBOR and EOM fits have been plotted over the raw data with their respective χ^2 values indicated. **(b)** The GASBOR *ab initio* model is elongated, with a maximum dimension around 12 nm. **(c)** EOM analysis of rMBP reveals wide R_g and D_{max} populations in an ensemble that represents the measured SAXS data. Selected models from EOM analysis (right) with their mass fractions within the total population are indicated. The coloured arrows denote the R_g and D_{max} of each model within the distributions. **(d)** SANS curves of rMBP in the absence and presence of DPC micelles (black and magenta, respectively). The EOM fits have been plotted over the data. **(e)** Stereoscopic image illustrating the size of an rMBP conformer and a DPC micelle of 54 detergent molecules²⁶. **(f)** SANS EOM distributions of rMBP in the absence and presence of DPC micelles (solid and dashed lines, respectively). In the presence of DPC micelles (grey sphere), a distinct compacted population dominates (magenta cartoon) over the mixed elongated and compacted populations (black cartoons).

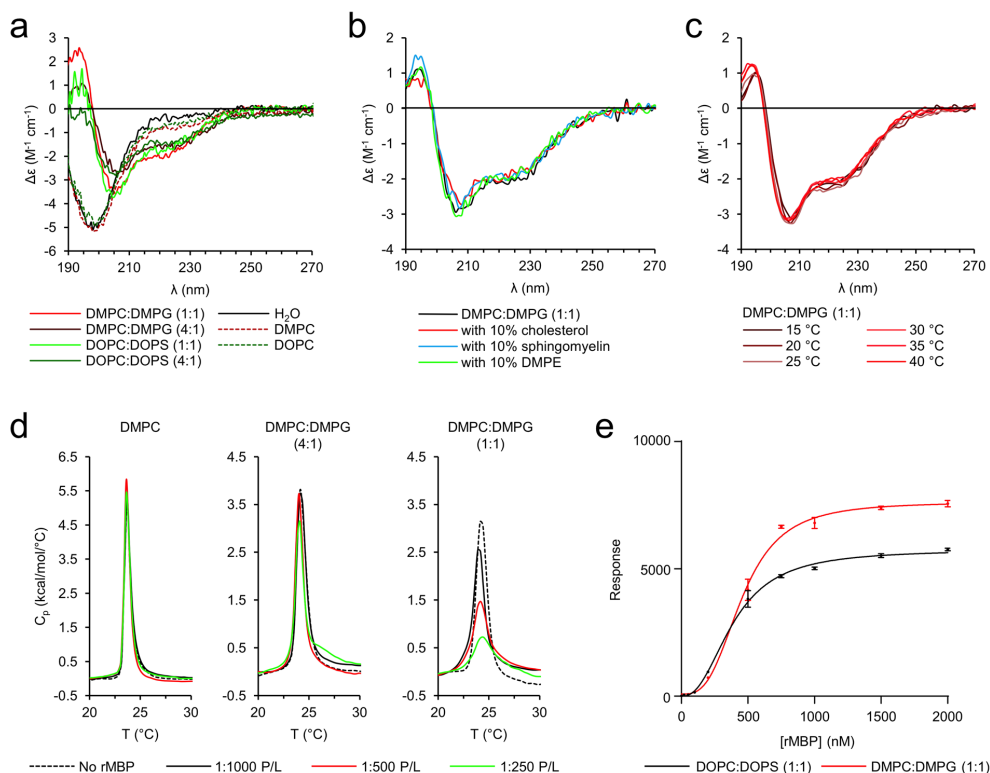


Figure 2. Lipid interactions of rMBP. (a) rMBP gains secondary structure in the presence of liposomes with increasing net negative surface charge, whereas it remains unfolded with net neutral lipids. (b) Cholesterol, sphingomyelin, or DMPE do not alter the secondary structure content of rMBP in net negatively charged DMPC:DMPG (1:1) vesicles. (c) Scanning around the lipid tail phase transition temperature does not affect the folding of MBP (right). (d) rMBP changes the lipid tail endothermic phase transition behaviour only when the MLV surface charge is net negative. (e) The association of rMBP with immobilised lipid vesicles probed using SPR. Error bars represent standard deviations.

The SRCD experiments provided evidence for membrane binding being mostly affected by electrostatics. Since the effect was practically the same with different lipid tails, we employed other strategies to observe possible membrane insertion. Differential scanning calorimetry (DSC) allows the determination of lipid phase transition temperatures, which reflect the conformational freedom of the lipid hydrocarbon tails. As a function of increasing temperature, dimyristoyl lipids present a small endothermic pre-transition (T_p) from the planar gel phase (L_3') to the rippled gel phase (P_3'), which is shortly followed by a major endothermic transition (T_m) from P_3' to the liquid crystalline phase (L_α) typically at $+23$ – $+24$ °C²⁹. We screened several protein-to-lipid (P/L) ratios of rMBP against DMPC:DMPG multilamellar vesicles (MLVs) with varying net negative surface charges using DSC, monitoring any rMBP-induced effects on the observed lipid T_m (Fig. 2d). Upon increasing the concentrations of rMBP, the endothermic main phase transition signal of negatively charged lipid membranes was broadened. Net neutral DMPC showed no difference in phase transition behaviour in the presence of rMBP. The data suggest MBP membrane insertion after charge neutralisation, supporting the conclusions from SRCD data.

DSC suggested lipid tail interactions with rMBP, even though the observed changes in rMBP conformation in SRCD with different lipid tails were minor. Next, we followed the conformation of rMBP in DMPC:DMPG (1:1) vesicles as a function of temperature (Fig. 2c). Scanning around the apparent T_m of dimyristoyl tails did not alter the conformation of rMBP, suggesting that lipid tail phase behaviour does not notably affect folding after rMBP has bound, but the dielectric environment inside the membrane is a maintaining factor for folding. To shed light on factors affecting binding affinity, we performed binding experiments of rMBP to immobilised DOPC:DOPS (1:1) and DMPC:DMPG (1:1) large unilamellar vesicles (LUVs) using surface plasmon resonance (SPR) (Fig. 2e). In a previous study²⁰, we used SPR to address MBP-His binding to PC membranes in the presence of phosphoinositides, and we observed more binding with increased negative membrane charge, as well as a sigmoidal dependence of binding on MBP concentration. The association of rMBP with lipid vesicles was irreversible, as reported before for

| | R_{hi} | R_{lo} | A_1 | A_2 | R^2 |
|-----------------|------------------|--------------------|-------------------|--------------------|--------|
| DOPC:DOPS (1:1) | 5751 ± 79.84 | -3.647 ± 48.78 | 389.5 ± 10.77 | 2.374 ± 0.1117 | 0.9978 |
| DMPC:DMPG (1:1) | 7624 ± 118.1 | 85.57 ± 73.49 | 455.5 ± 12.36 | 3.061 ± 0.2189 | 0.9968 |

Table 1. Surface plasmon resonance fitting parameters.

MBP-His³⁰, since we observed essentially no rMBP dissociation from the lipids (data not shown). This suggests that the conformational change from disordered to helical structure occurs after initial electrostatic binding and anchors rMBP tightly onto the lipid surface. We performed saturation experiments by rMBP titration, which allowed the acquisition of key parameters of membrane binding (Fig. 2e, Table 1). While dimyristoyl-based lipids generally had higher responses (R_{hi}) upon rMBP injection, the obtained saturation midpoint concentrations (A_1), which can be considered apparent dissociation constants (K_d), were similar for both DOPC:DOPS (1:1) and DMPC:DMPG (1:1), sharing the same surface net charge (Table 1). We performed a kinetic analysis by fitting the association phases of rMBP binding into a one-phase exponential association model (Supplementary Fig. S3). While the calculated k_{on} values are similar for both lipid compositions (Supplementary Table S2), the one-phase association model does not fit our data well enough to draw solid conclusions regarding association kinetics, and therefore, we conclude that MBP binding to a membrane surface is a complex binding event. It is clear that the initial association of rMBP onto a membrane surface is mostly governed by surface electrostatics, but the lipid tails do influence the amount of rMBP that can be integrated into liposomal bilayers, with a minimal effect on binding affinity or folding. Our results thus far clearly indicate rMBP membrane insertion and folding upon membrane binding.

Effect of membrane fluidity and rMBP concentration on membrane stacking. We have earlier shown spontaneous bilayer stacking by MBP and myelin protein P2 using AFM¹⁴. To observe this process in more detail, we prepared oriented DOPC:DOPS (1:1) bilayers with and without 10% (w/w) cholesterol on mica, and different concentrations of rMBP were added. After removal of unbound rMBP, the samples were imaged. rMBP bound onto the membrane surface and reproducibly induced membrane stacking, but the presence of cholesterol was not essential. However, the inclusion of cholesterol did cause the stacked membrane patches to appear larger and more uniform (Fig. 3a), suggesting that membrane fluidity plays a major role in stack formation, as demonstrated earlier using vesicle experiments³⁰. We tested several concentrations of rMBP and found that a critical amount of rMBP has to accumulate onto the membranes before stacks emerge spontaneously: at 0.9 μ M rMBP, membrane stacks were not typically observed, but at 1.8 μ M, multilayers were always visible (Fig. 3a). Cholesterol did not affect this trend. In our earlier study, 1.8 μ M MBP-His caused only minimal stacking of brain lipids, while extensive stacking was present at higher concentrations¹⁴. It is noteworthy that the observed critical concentration for membrane stacking in AFM corresponds to the rMBP concentration after reaching plateau for membrane surface binding in SPR. Thus, membrane stacking apparently requires surface saturation with MBP.

We next assessed the effect of lipid tail saturation and cholesterol on vesicle aggregation, similarly to our earlier experiments on P2³¹. The aggregation behaviour was the same for both DMPC:DMPG (1:1) and DOPC:DOPG (1:1), both with and without 10% (w/w) cholesterol (Fig. 3b), implying that the association of protein-decorated membranes is not dependent on cholesterol or lipid tail saturation. The differences in membrane fluidity resulting from cholesterol are most likely the reason to the observed stacking behaviour differences in AFM, as the presence of 10% (w/w) cholesterol did not notably affect the folding of rMBP either. Finally, we investigated whether rMBP produces vesicle aggregates with a distinct repeat distance. A Bragg peak corresponding to a mean repeat distance of 80 Å was present in our small-angle X-ray diffraction (SAXD) data from rMBP bound to DMPC:DMPG (1:1) vesicles (Fig. 3c). Bragg diffraction has been observed before from model vesicles and membranes as well as myelinated tissue^{9,15,31,32}. The result confirms the induction of ordered membrane stacks by rMBP, which were further used in imaging experiments.

A membrane stack is uniformly occupied by a gel-like rMBP phase. To gain more detailed information about the assembly of MBP within membrane stacks, we studied MBP-aggregated vesicle samples using EM. As shown by nanogold labelling, in vesicle aggregates, MBP-His expectedly resided mostly between vesicle surfaces (Fig. 4a), as demonstrated earlier^{33,34}.

We investigated rMBP assembly between membranes using cryo-EM. We imaged rMBP-adhered vesicle membrane stacks and picked images of MBP between membranes for single particle analysis (Fig. 4b,c). rMBP settled tightly between the membranes and formed stacks with a total thickness of 11–13 nm (two 5-nm bilayers with a 1–3-nm protein phase between them). Particle analysis revealed that, as opposed to the membranes without rMBP that presented a loose space with a varying distance between apposing membranes, the intermembrane space in the presence of rMBP was occupied by a narrow uniform protein phase with no distinct globular particles. The space between lipid membranes was ~1 nm, with protein present both between and inside the membranes. Distances of ~2.5 nm between MBP molecules can be estimated, but the distances vary and the proteins are not clearly visible. This resembles the cohesive MBP meshwork proposed earlier¹⁵. Thus, further particle averaging and higher-resolution structure determination were not carried out. Despite the lipid bilayers in these experiments being symmetric, unlike in myelin, it is noteworthy that in cryo-EM, we only observed protein-containing stacks of two apposing lipid bilayers (Fig. 4b,c). This suggests that once MBP inserts into the membrane, it changes the membrane properties and can prevent further MBP insertion from the opposite side, unless a great excess of MBP is present. As shown by neutron scattering, the molecular dynamics of a lipid bilayer are affected by MBP^{15,35,36}. MBP can thus alter the overall structural and dynamical properties of an entire lipid bilayer, driving it towards asymmetric behaviour even when the lipid composition is symmetric. The molecular details of this asymmetry are currently unknown.

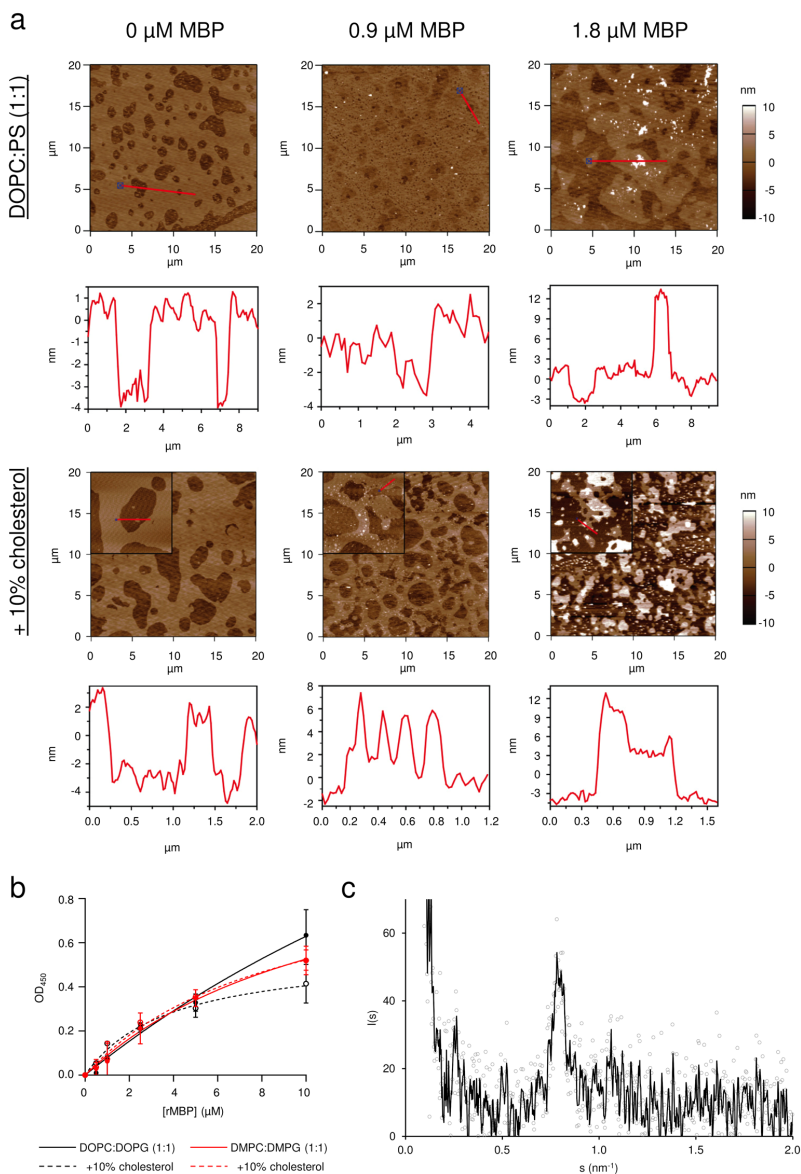


Figure 3. Membrane-stacking properties of rMBP. **(a)** In AFM, rMBP binds to supported DOPC:DOPS (1:1) lipid bilayers and spontaneously produces bilayer stacks after reaching sufficient protein concentration. The quality and area of the observed membrane stacks are influenced by the presence of cholesterol, without a significant effect on the measured stack thickness. Red lines denote the walk sections in the images, for which height diagrams have been plotted below. The walks from the cholesterol images have been extracted from 5- μm image insets for better quality. A single bilayer and stack are ~ 4 and 12 nm in height, respectively. **(b)** Turbidity measurements show that the tendency of rMBP to aggregate vesicles remains mostly unaffected by the lipid tail saturation degree or the presence of cholesterol. Error bars represent standard deviations. **(c)** rMBP mixed with DMPC:DMPG (1:1) SUVs displays a Bragg peak in SAXD that corresponds to a mean repeat distance of 80 Å at 1:100 molar P/L. A running average (black line) has been added for clarity over the raw measurement data (grey circles).

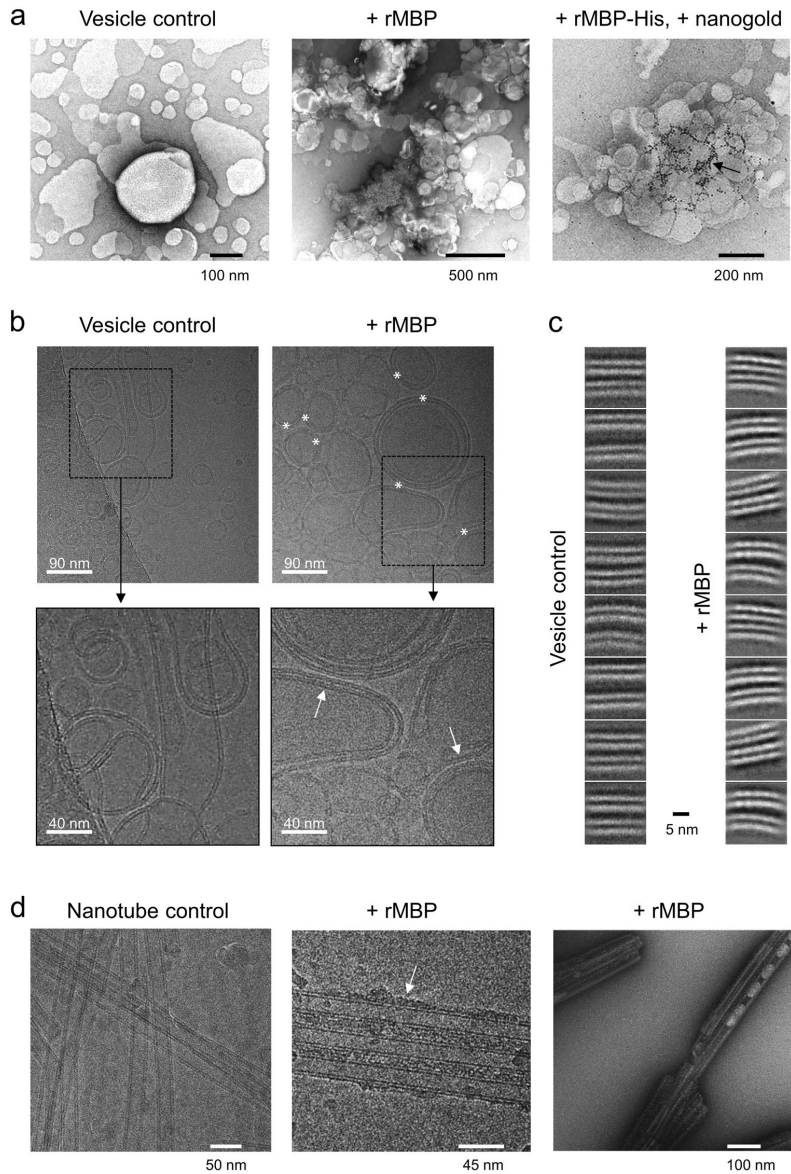


Figure 4. Architecture of rMBP in membrane stacks. **(a)** MBP aggregates vesicles and settles between membranes. rMBP-His was labelled with nanogold particles to localise the protein between vesicles (black arrow). **(b)** In cryo-EM, membrane stacking by MBP is evident when mixed with lipid vesicles (white asterisks). MBP also slightly flattens the membrane curvature of vesicles when more than one stack builds up (white arrows). **(c)** Particle analysis of cryo-EM imaged vesicles unveils an intermembrane compartment occupied by a uniform rMBP phase devoid of clear single particle boundaries, which brings the two opposing membranes into close vicinity to each other. The space between adjacent vesicle bilayers in the absence of rMBP is notably wider. **(d)** MBP coats GalCer-DOGS-NTA-Ni²⁺ nanotubes, displaying an extended conformation (white arrow). MBP also aggregates nanotubes, as evident from negatively stained samples (right).

For observing concentration dependence of MBP-induced membrane stacking, we imaged vesicles with varying amounts of rMBP (Supplementary Fig. S4). While membrane multilayers were present in vesicle mixtures at high rMBP concentrations, stacking was lost as rMBP concentration decreased. Despite a different sample setup (freely tumbling vesicles) compared to AFM experiments (supported lipid bilayers), these observations do again suggest a critical MBP concentration for inducing membrane stacking.

We also imaged rMBP binding to lipidic nanotubes (Fig. 4d). rMBP bound nanotubes together, which was visible both with negatively stained samples as well as in cryo-EM. Compared to vesicles, nanotubes have different membrane fluidity, composition, and curvature. Importantly, we also observed the accumulation of rMBP onto nanotube exposed surfaces without stacking, corresponding to the accumulation of MBP onto a single membrane surface. As opposed to the more compact confinement within membrane stacks formed from vesicles, MBP appeared elongated when bound to nanotubes, similarly to DPC-bound rMBP in SANS.

The formation of a protein phase on a single bilayer prior to stacking. The EM experiments raised a question regarding the conformation of rMBP on lipid bilayers prior to stacking. This is likely a physiologically relevant state during myelination; AFM demonstrated concentration dependence upon stack induction, and MBP can insert into membranes. Does MBP insert into a single membrane before a stack forms, and will MBP fold into a compact conformation before stacking? To answer these questions, we carried out NR experiments on uniform proteinous lipid bilayer samples.

The Langmuir-Blodgett/Schaefer approach to depositing lipid bilayers on solid substrates involves the sequential transfer of lipids from a Langmuir monolayer, with controlled area per molecule, by first slowly pulling the substrate out through the monolayer, with the interface perpendicular to the water surface (Langmuir-Blodgett) and then rotating the substrate by 90°, so that the interface is parallel to the water surface, and slowly pushing the substrate through the monolayer to deposit the outer leaflet of the bilayer (Langmuir-Schaefer). This approach allows precise control of the composition and coverage of both leaflets of the lipid bilayer independently, ensuring a high-coverage bilayer across the entirety of the large substrate surfaces necessary for NR measurements. NR is an excellent tool for studying *in-situ* the structure, perpendicular to the surface, of buried, hydrated thin films of biological and soft-matter molecules at the solid-liquid interface. The large penetrability of neutrons, combined with their high sensitivity to hydrogenated and deuterated materials, makes NR an ideal probe of interactions between proteins and biomembranes, simultaneously providing information on the interaction both at the surface and buried within the membrane.

Using the Langmuir-Blodgett/Schaefer technique, we prepared uniform lipid bilayers of hydrogenated and perdeuterated DMPC:DMPG (1:1) on Si-crystal substrates with water as a subphase solvent. A flow cell setup allowed us to exchange the bulk solvent to buffers and to characterize the membranes with different solvent contrasts, as well as to inject rMBP inside the cell and follow its association as a function of time (Fig. 5a,b). Based on SPR and AFM, we chose to add rMBP onto the membrane at 0.5 μM , which retained the integrity of the membrane and did not induce spontaneous stacking (Fig. 5a). Initially, we observed that after injecting the protein, there was a time window that presented a rearrangement within the sample (Fig. 5b). After stabilisation of the sample and washing out unbound protein, the resulting reflectivity curve was best fitted to a model with a uniform protein layer, having a defined thickness and low roughness, on top of the existing DMPC:DMPG (1:1) bilayer, with full insertion of the protein into the outer leaflet of the bilayer, potentially displacing both lipid and water molecules from this leaflet (Fig. 5a, Table 2). Similar behaviour was observed with both hydrogenated and perdeuterated lipids (Fig. 5a, Supplementary Fig. S5), but not with DMPC alone (Supplementary Fig. S5), again demonstrating the importance of membrane surface charge. The parameters used to describe the best fit to each set of data clearly show that the protein layer covered ~25% of the membrane surface and was 7.5–8.5 nm thick. An additional ~3 nm of the protein was inserted within the outer leaflet of the bilayer, displacing ~40% of the lipids in this leaflet and leading to a rearrangement of the membrane to support this. The analysis suggests compaction compared to the most elongated conformers suggested by SAXS, fitting well to the narrowed EOM population observed by SANS for DPC-bound rMBP. The protein layer, however, does not represent a completely collapsed MBP, thought to reside within the mature bilayer stack⁵, but a previously undetected pre-stack MBP conformation: a brush-like layer of mostly disordered protein, anchored onto the membrane most likely *via* one or more helical segments. The introduction of another membrane leaflet could result in a second insertion event, followed by protein folding and compaction, a single MBP molecule potentially penetrating both bilayer surfaces. The protein meshwork has been suggested to be composed of laterally self-assembled¹² or dimeric MBP¹². Taking into account our observations and earlier data, it is obvious that MBP forms a protein phase onto a membrane surface, and this process involves also self-association. However, we find it unlikely that MBP would, even when bound to membranes within compact myelin, fold into structurally highly ordered assemblies with a well-defined oligomeric state.

To further study the protein-membrane association, we added 0.5 μM rMBP to a membrane in a time-resolved NR experiment (Fig. 5b, Supplementary Table S3). While this concentration is not high enough to provide information about stacking, we could observe the entire association process of rMBP. It should be noted that this experiment was carried out with a single contrast, increasing the uncertainty in the fitted parameters. However, clear trends were still seen, as the association took place on a reasonably long time scale, during which three distinct phases could be resolved: initially a 7-nm thick, diffuse protein layer formed on the membrane, with a very high roughness, indicating high heterogeneity and no insertion into the membrane. Next, this layer collapsed into a denser, more homogeneous layer with some insertion into the headgroup region of the bilayer outer leaflet. Only after this, one can observe full membrane insertion, displacing lipids from the outer leaflet of the bilayer, which suggests that rMBP has to accumulate and fold onto the membrane prior to embedding. The coverage of the protein was very high during these time-resolved measurements, up to 50%, as opposed to the buffer-exchanged sample (~25%; Table 2), with less displacement of lipid from the outer leaflet, indicating that

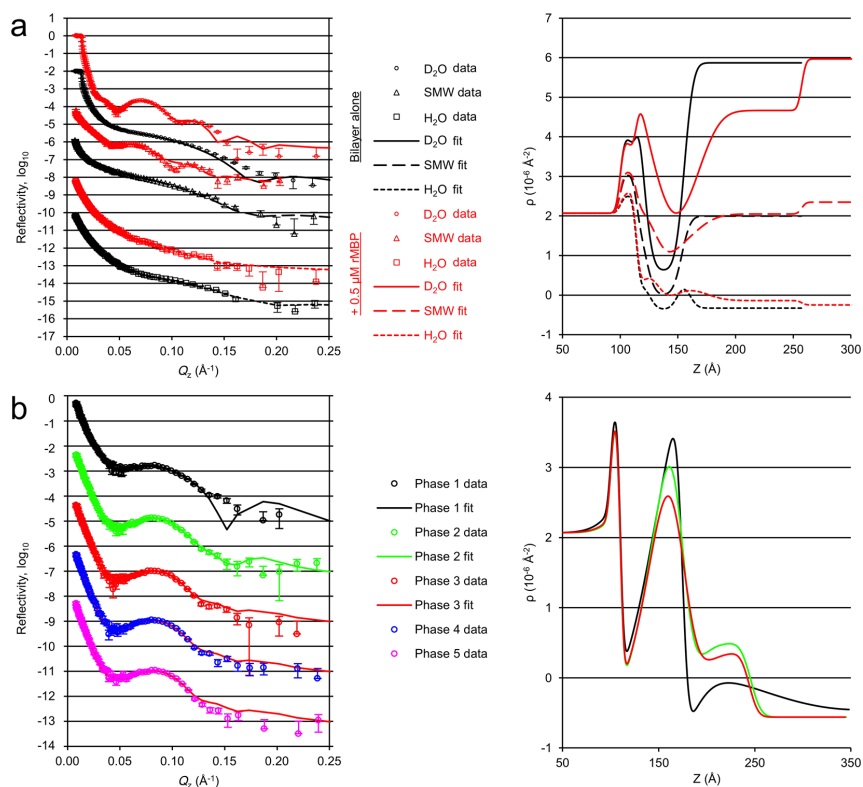


Figure 5. Accumulation of rMBP onto lipid bilayers. Data and fits are plotted on the left and scattering length density (ρ) profiles on the right. All reflectivity curves have been offset for clarity. **(a)** Steady-state NR experiment of DMPC:DMPG lipid bilayers with and without rMBP at different solvent contrasts. **(b)** Time-resolved NR experiment. The phases represent 15-min time-slices of rMBP associating with a d_{54} -DMPC: d_{54} -DMPG bilayer in an H_2O contrast. The fitting curve for phase 3 has also been overlaid with phases 4 and 5, demonstrating steady state. The error bars represent standard deviations.

the rinsing of the membrane may remove some additional lipid molecules along with excess protein. The third phase in our time-resolved measurement was essentially the steady state, and the system remained stable beyond this time point (phases 4 & 5 in Fig. 5b).

Discussion

Using a recombinant form of MBP accurately mimicking the major 18.5-kDa isoform, we have provided a full physicochemical picture of MBP-induced stacking of lipid bilayers. MBP is an intrinsically disordered protein in solution, which after lipid membrane binding gains secondary structure and embeds deep into the bilayer. On top of the membrane, an amorphous protein brush is formed, which is likely to be of high importance, when an apposing membrane is bound. A fully compacted MBP conformation is only present between two bilayers. Our results provide a comprehensive molecular framework for membrane binding and stacking by MBP, which is a peripheral membrane protein with unique molecular properties.

Our extensive characterisation of tag-free rMBP shows that MBP is disordered in solution and binds lipid membranes through electrostatic interactions. While the lipid composition of myelin is more complex than that used in the current study, we decided here to focus on simple lipid mixtures that generally behave well in various biophysical techniques and can be used to screen for basic membrane properties, including surface charge, lipid headgroup, level of saturation, and fluidity. While the lipid hydrocarbon tails do not affect the binding affinity, kinetics, or folding of MBP substantially, the dynamic freedom and spatial occupation of the tails define how much MBP can bind to saturate the membrane surface. MBP also affects the biophysical properties of the entire lipid bilayer, as for example highlighted by the observation of MBP-induced stacks of only two, but not more, bilayers in cryo-EM, as well as previous studies with cultured oligodendrocytes^{37,38}. The importance of both the lipid and protein components in affecting the dynamics and function of each other has been highlighted earlier for both MBP^{17,35,36,39} and myelin protein P2^{40,41}.

| Parameters | | DMPC:DMPG (1:1) | | d ₅₁ -DMPC:d ₅₁ -DMPG (1:1) | |
|------------|--|-----------------|-----------|---|-----------|
| | | Bilayer alone | With rMBP | Bilayer alone | With rMBP |
| Substrate | Oxide thickness (Å) | 14 ± 1 | | 10 ± 1 | |
| | Oxide coverage (%) | 75 ± 1 | | 90 ± 4 | |
| | Oxide roughness (Å) | 3 ± 1 | | 3 ± 2 | |
| | Hydration layer between oxide and bilayer (Å) | 5 ± 1 | 5 ± 2 | 20 ± 5 | 25 ± 6 |
| Bilayer | Bilayer area-per-molecule (Å ² /molecule) | 60 ± 4 | 45 ± 3 | 63 ± 8 | 52 ± 10 |
| | Water molecules per lipid head | 3 ± 1 | 10 ± 2 | 3 ± 1 | 10 ± 1 |
| | Water molecules per lipid tail | 4 ± 2 | 17 ± 3 | 6 ± 2 | 17 ± 2 |
| | Global bilayer roughness (Å) | 5 ± 1 | 8 ± 1 | 18 ± 6 | 22 ± 3 |
| | Local bilayer inner roughness (Å) | 3 ± 1 | 4 ± 2 | 3 ± 2 | 5 ± 1 |
| | Local bilayer outer roughness (Å) | | 11 ± 2 | | 0 ± 3 |
| rMBP | MBP in outer leaflet (%) | 39 ± 7 | | 44 ± 9 | |
| | MBP layer thickness (Å) | 84 ± 2 | | 75 ± 4 | |
| | MBP layer coverage (%) | 26 ± 1 | | 23 ± 3 | |
| | MBP layer roughness (Å) | 3 ± 2 | | 10 ± 4 | |

Table 2. Neutron reflectometry parameters.

Our results demonstrate that charge neutralisation is a key event before MBP folding and membrane insertion can take place. Once charge neutralisation and membrane saturation with MBP occur, a string of downstream events is triggered, ultimately leading to stable myelin-like membrane stacks. Based on our observations, and considering earlier literature, we now propose a molecular mechanism for the stepwise, MBP-driven formation of the MDL (Fig. 6).

In the initial step, the highly positively charged, disordered MBP is attracted to a negatively charged membrane surface by electrostatic interactions, which starts the association cascade. When encountering the membrane surface, MBP binds through electrostatics, and opposite charges are neutralised – this allows other factors, such as hydrogen bonding and the hydrophobic effect, to take over and causes MBP to fold and subsequently insert deeper into the inner membrane leaflet, and even partially into the outer, as proposed already decades ago³⁰. The process occurs in a fairly small volume: only partial protein insertion and folding occurs, while most of MBP remains elongated outside the membrane, maintaining a positive net charge. This is plausible, as several distinct segments of MBP have been shown to have propensity to fold independently upon interacting with lipids/detergents^{42–46}. This initial association, however, may already be essentially irreversible^{12,20,42}, although it is likely that there are folded species in the system that present weak affinity and are removable, possibly due to electrostatic repulsion.

Next, given the fairly confined electrostatic field of the lipid bilayer, which gets neutralised by the embedded protein, more MBP continues to bind and integrate within the single membrane leaflet. A fairly thick amorphous peripheral protein phase emerges, which translates into a strong accumulation of positive charge covering the membrane surface. This protein layer is likely to represent the distinct MBP protein phase described earlier¹³. Brush-like phases consisting of disordered proteins and peptides have been recently reported^{47,48}. Our SANS data in the presence of detergent micelles provide evidence for a brush-like property for membrane-bound MBP, although the detailed organisation of this protein phase currently remains unknown. This phase was also visualised by cryo-EM on the surface of lipid nanotubes, providing a starting point for further studies into its molecular details.

Finally, when a critical surface-bound MBP concentration has been reached, the soft protein brush adheres to a second membrane leaflet, resulting in full charge neutralisation. MBP undergoes a second compaction event to fit into the confined space between the two bilayers, forming a meshwork of extraordinary stability between the two cytoplasmic membrane leaflets. It is likely that this phase transition is governed by specific aromatic residues in MBP¹³. The meshwork may involve lateral MBP assembly^{9,12}, and the 3-nm MDL can easily be spanned by a single MBP monomer, as suggested earlier^{5,16,17,49}. During myelination, both membrane bilayers involved in stack formation are likely to accumulate MBP continuously. Since the membranes are in close proximity to each other, the stacking could proceed *via* a zipper-like mechanism, whereby only the leading part of accumulated MBP reaches the critical concentration at a given time and effectively transitions into a molecular adhesive. Interactions of MBP with cytosolic proteins, such as calmodulin^{20,50} or the cytoskeleton^{19,51}, may regulate this process.

The above string of events is a feasible molecular model for myelin membrane stacking, assuming enough MBP is available locally. During CNS myelination, MBP is translated in the vicinity of the growing membrane from transported mRNA⁵². The local synthesis of MBP is likely to be a key triggering factor for myelin membrane compaction. In myelin formation and maintenance, cytoskeletal networks and other proteins, such as 2',3'-cyclic nucleotide 3'-phosphodiesterase (CNPase), play central roles⁵³. An interplay between MBP and membrane-bound CNPase may be important, as both CNPase and MBP bind microtubules and actin^{19,51}. Recent data also suggest that myelin formation is driven by cytoskeletal disassembly⁵⁴, in addition to proteo-lipid protein-driven myelin formation^{55–57}. CNPase overexpression inhibits MBP-based myelin compaction and causes aberrations in the periaxonal membrane⁵⁸. A model outlining the interplay between CNPase and MBP

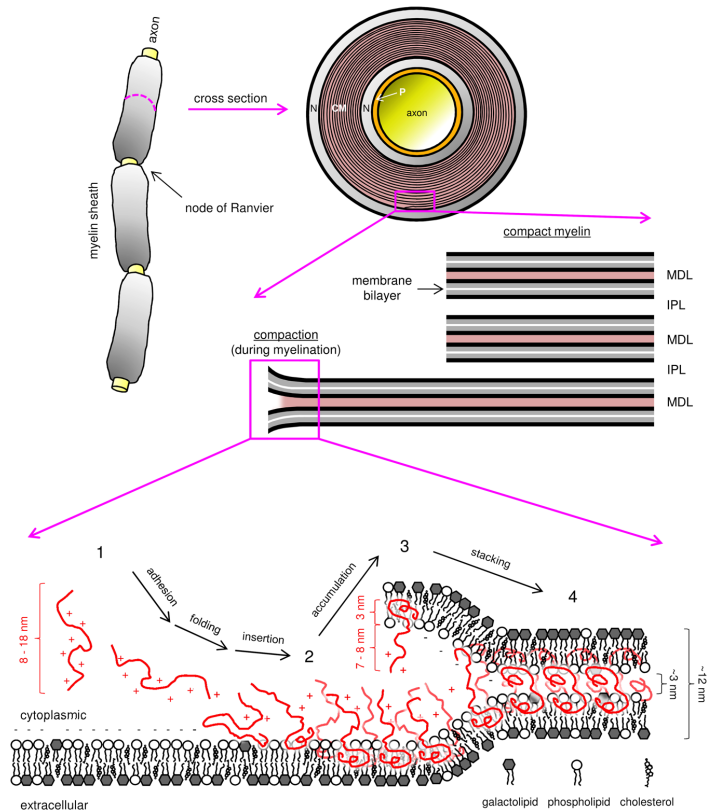


Figure 6. The association landscape of MBP with myelin membranes leads to the formation of MDL. MBP (red) in solution is disordered and approaches the cytoplasmic membrane surface through electrostatic interactions (1), which eventually leads to charge neutralisation, subsequent folding, and membrane insertion (2). Membrane-adhered MBP accumulates on the surface, which increases the binding propensity of a second membrane leaflet (3). Once a critical surface occupancy is reached, another insertion and possible folding event occurs, resulting in a dense protein phase that forms the 3-nm MDL within the 12-nm membrane stack (4). CM, compact myelin; N, non-compact myelin; P, periaxonal space; MDL, major dense line; IPL, intraperiod line.

in maintaining the interface and balance between CM and cytosolic channels was recently proposed, showing antagonistic effects of CNPase and MBP on channel formation⁵⁹.

Changes in the expression patterns of key proteins (e.g. CNPase) during myelination and in mature myelin could switch the formation and stability of the MDL to a point where MBP is re-exposed to the cytosol, making it susceptible to proteolysis. While we do not yet know enough about the reversibility of myelination at the molecular level, MBP accumulated on a single membrane surface is a more suitable substrate for proteases and other modifying enzymes than a folded, membrane-embedded MBP. This could further decrease the stability of the MDL through disruption of the MBP meshwork, setting out a rolling wheel that may eventually result in a neurological condition, possibly by exposing autoimmune epitopes of MBP and other myelin proteins. Autoantigenic MBP peptides, as well as molecular mimics thereof, have been discovered and characterised⁶⁰. These could be disease-triggering or even preventive factors when modified correctly^{61, 62}, the underlying mechanisms currently being unclear. Picturing the above molecular steps of MDL formation should allow to better understand the myelination process as well as demyelinating disorders.

Stability of the proteolipid membrane multilayer is a key factor for keeping myelin healthy. Initial interactions between MBP and lipid membranes are mostly electrostatic, and deiminated charge variants of MBP have been linked to MS⁴. Decreased positive charge on MBP leads to weaker membrane interactions^{20, 42, 63}. Modified variants could affect myelin stability through slight structural, functional, and compositional differences, as well as susceptibility to proteolysis^{10, 11, 20}. The concentration of divalent ions, most importantly Ca²⁺ and Zn²⁺, is likely to influence the formation and stability of compact myelin⁶⁴. An obvious factor to consider is the membrane lipid

composition; the negatively charged cytoplasmic leaflet and the high cholesterol content of myelin are most probably in a delicate balance with the rest of the different lipid species, as shown by experimental disease models^{3, 49, 65}. The high abundance of cholesterol has a major impact on membrane fluidity as well as myelin development^{30, 66, 67}, likely being a key requirement together with various phosphoinositides^{68–70} to provide a suitable physiological medium for membrane-embedded proteins, including MBP. The stability of the MDL, the condition of MBP within it, and the post-natal myelinating machinery should be taken into account when it comes to understanding and possibly treating demyelinating diseases.

To conclude, through the use of multidisciplinary methodologies, the structural importance of MBP as a multifunctional compact myelin protein is unfolding. An MBP-driven scheme outlining the formation and stability of the myelin MDL unravels, while the MDL remains a poorly understood compartment of developmental, functional, and medical importance. The molecular steps of formation of the myelin MDL rely on an equilibrium between electrostatic and hydrophobic interactions, protein concentration, membrane association, and charge accumulation to form the final product: a stable, dense protein phase that occupies the MDL and binds lipid bilayers tightly together. The elucidation of the molecular foundation of MBP-mediated membrane stacking allows us to better understand this intriguing biological system, and it could act as a key to unlock the discovery of remedies to conditions that present aberrant myelination and disturbed myelin ultrastructure. To further refine the model, more complex molecular systems should be studied, such as multiprotein systems including integral membrane proteins of myelin. Other myelin proteins, e.g. the cytoplasmic extension of myelin protein zero⁷¹ and P2^{14, 15, 31}, function similarly to MBP, likely leading to functional synergies and possibly competition. Once the underlying detailed kinetics and the effects of other molecular components of myelin, including proteins and ionic species, on proteolipid membrane association and stacking are deciphered, we can truly understand the complexity of myelination in a logical, structured manner.

Methods

Cloning, expression, and purification. A synthetic gene encoding the 18.5-kDa isoform of mouse MBP (DNA2.0) was subcloned into the Gateway donor vector pDONR221 (Life Technologies). A Tobacco Etch Virus (TEV) protease digestion site (ENLYFQG) was added before the gene, and *attB1* and *attB2* recombination sites before and after the gene, respectively. This entry clone was used to generate an expression clone in the pTH27 vector⁷², which codes for an N-terminally His₆-tagged protein (His-rMBP).

The expression of His-rMBP was performed in the *E. coli* BL21(DE3)pLysS RARE strain in LB medium at +37 °C using a 2-h induction with 1 mM isopropyl β-D-1-thiogalactopyranoside, after an initial culture OD₆₀₀ of 0.3 had been reached. After harvesting, cell pellets were re-suspended into 50 mM HEPES (pH 7.5), 500 mM NaCl, 6 M urea, 20 mM imidazole, 1 mM phenylmethylsulphonyl fluoride, with added EDTA-free protease inhibitors (Roche) and lysed by ultrasonication. His-rMBP was purified using Ni-NTA chromatography. Elution was done using 40 mM HEPES (pH 7.5), 400 mM NaCl, 4.8 M urea, 500 mM imidazole, and the elution fraction was dialysed sequentially against several dialysis reservoirs, lowering the urea content in a stepwise manner from 4.8 to 2 M. After this, recombinant TEV protease was added to digest the N-terminal His₆-tag of His-rMBP, resulting in a near-native 18.5-kDa rMBP with one extra N-terminal Gly residue from the TEV digestion site. Cleavage was carried out overnight at +4 °C, while dialyzing against 40 mM HEPES (pH 7.5), 400 mM NaCl, 1 M urea. The digested protein was dialysed back into 50 mM HEPES (pH 7.5), 500 mM NaCl, 6 M urea, 20 mM imidazole, and another Ni-NTA purification was performed. The unbound and wash fractions were combined and dialysed against 40 mM HEPES (pH 7.5), 400 mM NaCl overnight. After the final dialysis step, protein was concentrated and subjected SEC on a Superdex 75 pg column (GE Healthcare). Either HBS (10 mM HEPES, 150 mM NaCl, pH 7.5) or 20 mM HEPES (pH 7.5), 300 mM NaCl, 1% (w/v) glycerol was used as the running buffer, depending on downstream experiments. The purity of the protein was checked using SDS-PAGE and DLS using a Malvern Zetasizer Nano ZS instrument. The SEC fractions containing pure rMBP were snap-frozen using liquid N₂ and stored at –80 °C. The protein fractions were thawed, pooled, and concentrated immediately before downstream experiments.

C-terminally His-tagged MBP (MBP-His²⁰) was expressed and purified similarly to rMBP, omitting TEV digestion and the second Ni-NTA step. After the first Ni-NTA step and stepwise dialysis, the protein was immediately subjected to SEC, and the fractions containing pure MBP-His were snap-frozen.

Mass spectrometry. The accurate molecular mass of rMBP was determined using liquid chromatography-coupled electrospray ionisation time-of-flight mass spectrometry in positive ion mode, using a Waters Acquity UPLC-coupled Synapt G2 mass analyser with a Z-Spray ESI source. The identity of rMBP was further verified using peptide fingerprinting by in-gel trypsin proteolysis and matrix-assisted laser desorption/ionisation time-of-flight mass spectrometry with a Bruker Ultra flexXtreme mass analyser. The peptide fingerprints were compared directly against theoretical peptides from the protein sequence.

Small-angle scattering. SAXS data for rMBP were collected from samples at 1–4 mg ml^{–1} on the EMBL P12 beamline, DESY (Hamburg, Germany). The buffer contained 20 mM HEPES (pH 7.5), 300 mM NaCl, and 1% (w/v) glycerol. Monomeric bovine serum albumin was used as a molecular weight standard. See Supplementary Table S1 for further details.

SANS data for 2.3 mg ml^{–1} (124 μM) MBP in the absence and presence of 0.25% (7.1 mM) DPC micelles were collected on the D22 beamline, ILL (Grenoble, France) using a 1-mm pathlength Hellma 100-QS quartz cuvette at +10 °C with a 1-h exposure time. The used buffer was 20 mM Tris-HCl (pH 7.5), 150 mM NaCl. The measurements were carried out at 4-m collimation and sample-detector distances, using a monochromatic neutron wavelength of 6 Å ± 10%. Data were corrected for the transmission, the pathlength, the empty cell, and the blocked beam, and scaled to absolute intensity using the measurement of beam flux at the sample position. Neutron

scattering data for 5 mg ml⁻¹ DPC micelles in 100, 80, 60, 40, 20, and 0% D₂O were collected, and a contrast match point of DPC was determined to be 9% D₂O, as previously described⁷³. The used D₂O solvent contrasts were 9% and 98% for MBP with and without DPC, respectively. Initial data processing was done using GRASP (www.ill.eu/instruments-support/instruments-groups/groups/lss/grasp/home/) and CNR SANS reduction macros for Igor⁷⁴.

Data were processed and analysed using the ATSAS package⁷⁵. GNOM was used to calculate distance distribution functions⁷⁶, and *ab initio* modelling was performed using GASBOR⁷⁷. Ensemble optimisation analysis was performed using EOM⁷⁸.

Liposome preparation. Cholesterol, DMPC, DMPE, DMPG, dioleoylphosphatidylglycerol (DOPG), DOPC, and sphingomyelin were from Larodan Fine Chemicals AB (Malmö, Sweden). DOPS and the deuterated d₅₄-DMPC and d₅₄-DMPG were from Avanti Polar Lipids (Alabaster, Alabama, USA).

Lipid stocks were prepared by dissolving dry lipids in chloroform or chloroform:methanol (1:1 v/v) at 5–10 mg ml⁻¹. Mixtures were prepared from the stocks at desired ratios, followed by solvent evaporation under a gentle stream of N₂ and freeze-drying for at least 4 h at -52 °C under vacuum. The dried lipids were either stored air-tight at -20 °C or used directly to prepare liposomes.

Liposomes were prepared by adding either deionised water or HBS to the dried lipids to reach a final concentration of 2–10 mg ml⁻¹, followed by vigorous mixing and gentle sonication for 15 min in a water bath sonicator at ambient temperature, to ensure that no unsuspended lipids remained in the vessel. MLVs were prepared by seven cycles of freeze-thawing using liquid N₂ and a warm water bath, with vigorous vortexing after each cycle. LUVs were prepared by extruding MLVs 11 times through a 0.1-µm membrane on a +40 °C heat block and used immediately in experiments. SUVs were prepared using sonication of MLVs. Either probe tip sonicators (a Branson Model 450 and a Sonics & Materials Inc. Vibra-Cell VC-130) or a strong water bath sonicator with temperature control (UTR200, Hielscher, Germany) were used to clarify the liposome suspensions, while avoiding overheating. The SUVs were immediately used in experiments.

Synchrotron radiation circular dichroism spectroscopy. SRCD data were collected from 0.3–0.5 mg ml⁻¹ protein samples in water on the UV-CD12 beamline at ANKA (KIT, Karlsruhe, Germany)⁷⁹ and the AU-CD beamline at ASTRID2 (ISA, Aarhus, Denmark). Samples with lipids were prepared on-site by mixing rMBP and freshly sonicated SUVs, followed by 5–10 min of degassing using a water bath sonicator at ambient temperature. 100-µm pathlength closed circular cells (Suprasil, Hellma Analytics) were used. SRCD spectra were measured from 170 to 280 nm at +30 °C, and the raw CD units were converted to Δε (M⁻¹ cm⁻¹), using rMBP concentration determined from absorbance at 280 nm. SDS and TFE were purchased from Sigma-Aldrich and the detergents LDAO, OG, and DPC from Affymetrix. The unfolded nature of rMBP, as well as its tendency to fold in DMPC:DMPG (1:1) and DOPC:DOPS (1:1), were reproducible between beamtime sessions.

Differential scanning calorimetry. Various concentrations of rMBP were mixed with MLVs in HBS containing 160 µM of either DMPC, DMPC:DMPG (4:1), or DMPC:DMPG (1:1), in a final volume of 700 µl. Lipid samples without added rMBP were prepared as controls. The P/L ratio was 1:250–1:1000. The samples were incubated at +37 °C for 10 min to ensure thorough protein association with the vesicles, and degassed in a vacuum with stirring at +10 °C prior to measurements. All samples were prepared and measured in duplicate, the observed trends being reproducible.

DSC was performed using a MicroCal VP-DSC with a cell volume of 500 µl. A HBS reference was used for all samples. Each calorimetric cycle (one per sample) was performed from +10 to +50 to +10 °C with 1 °C min⁻¹ increments. Baselines were corrected and zeroed at +20 °C to make cross-comparison straightforward.

Surface plasmon resonance. SPR was performed on a Biacore T200 system (GE Healthcare). According to the manufacturer's protocol, 100-nm LUVs of 1 mM DMPC:DMPG (1:1) and 1 mM DOPC:DOPS (1:1) were immobilised on separate channels on an L1 sensor chip (GE Healthcare) in 20 mM HEPES (pH 7.5), 150 mM NaCl, followed by the injection of rMBP. Chip regeneration was done with a 2:3 (v:v) mixture of 2-propanol and 50 mM NaOH. rMBP was at 20–2000 nM in the running buffer, and a single concentration per each lipid capture was studied; all samples were performed in duplicate, with one sample in each series measured twice to rule out instrumental artifacts or deviations. The binding response as a function of protein concentration was plotted and fitted to the 4-parameter model

$$R = R_{hi} - \frac{R_{hi} - R_{lo}}{1 + \left(\frac{[MBP]}{A_1}\right)^{A_2}}, \quad (1)$$

to gain information about association affinity. For kinetic analyses, all association phases (180 s after injection of rMBP) were individually fitted to a one-phase exponential association model using GraphPad Prism 7. The obtained *k*_{obs} values were plotted against rMBP concentration and fitted using linear regression to determine *k*_{on} (slope of the curve) and *k*_{off} (Y-intercept of the curve). The latter values were extracted from two individually fitted datasets: one containing all data (Fitting set 1) as well as one omitting data points below 500 nM rMBP (Fitting set 2).

Vesicle aggregation and small-angle X-ray diffraction. SUVs of 0.5 mM DOPC:DOPG (1:1) and DMPC:DMPG (1:1), both with and without supplemented 10% (w/w) cholesterol, were mixed with 0.5–10 µM

rMBP in duplicate. Turbidity was recorded at 450 nm for 10 min at +25 °C using a Tecan M1000Pro plate reader. The results were analysed after turbidity was stable.

SAXD was performed to find the mean repeat distance of rMBP-stacked multilayers in aggregated lipid vesicle samples. 2–20 μM MBP was mixed with SUVs of 1–3 mM DMPC:DMPG (1:1) in HBS at ambient temperature and analysed at +25 °C on the EMBL P12 BioSAXS beamline, DESY (Hamburg, Germany). Buffer references were subtracted from the data. Lipid samples without added rMBP were used to verify the absence of Bragg peaks. The peak positions of momentum transfer, s , in rMBP-lipid samples were used to calculate the mean repeat distance, d , in a proteolipid multilayer, using the equation

$$d = \frac{2\pi}{s}, \text{ where } s = \frac{4\pi \sin\theta}{\lambda}. \quad (2)$$

Atomic force microscopy. Fresh DOPC:DOPS (1:1) and DOPC:DOPS (1:1), 10% (w/w) cholesterol SUVs were unrolled on freshly cleaved mica (\varnothing 1.2 cm) in HBS-Ca (10 mM HEPES, 150 mM NaCl, 2 mM CaCl₂, pH 7.5), by covering the mica entirely with 0.2 mg ml⁻¹ SUVs, incubating for 20 min at +30 °C, and washing twice with HBS-Ca.

Freshly prepared samples were imaged in HBS at ambient temperature using an Asylum Research MFP-3D Bio instrument and TR800PSA cantilevers (Olympus; spring constant (k) range 0.59–0.68 N m⁻¹, resonance frequency 77 kHz) in alternative current (AC) mode. Square 256 × 256 pixel scans were acquired from areas of 5–20 μm, with a 90° scanning angle and a scan speed of 0.6–0.8 Hz. The resulting scan images were processed with Igor Pro 6.37.

After confirming the presence of lipid bilayers, 0.5–3.6 μM MBP was added onto the bilayer samples in HBS. The samples were incubated for 15 min at ambient temperature, washed twice with HBS, and scanned as above. For every protein concentration, 2–6 samples were prepared and scanned with excellent reproducibility. Scans from at least 3 different areas for each sample were acquired to rule out artifacts originating from sample heterogeneity.

Electron microscopy. *Protein reconstitution into lipid vesicles.* The lipid mixture contained polar brain lipid extract (Avanti), palmitoylcholinephosphatidylcholine (POPC, Avanti), and cholesterol (Anatrace) in the ratio 3:1:1. Vesicles were prepared as above, except that organic solvent was evaporated under argon and the sample vacuum-dried at room temperature, prior to resuspending in aqueous solvents. For EM experiments, 0.4 mg ml⁻¹ of rMBP was mixed with 0.4 mg ml⁻¹ polar brain lipid:POPC:cholesterol vesicles in a buffer containing 20 mM Tris pH 7.5, 200 mM NaCl, 1% glycerol, and the sample was incubated for 24 h at room temperature. For negatively stained EM imaging of lipid vesicles, samples containing 730 μM DMPC:DMPG (1:1) SUVs were prepared with 0–7.3 μM rMBP, to achieve different P/L ratios. The samples were incubated for 1 h at room temperature before grid preparation.

Negative stain EM. For negatively stained EM, the sample was applied to glow-discharged, thin carbon film-coated copper EM grids and incubated for 1 min. The grid was then blotted with paper, washed with 4 drops of H₂O, and negatively stained with 2 drops of 2% uranyl acetate. Grids were imaged on Philips CM200 TEM operated at 200 keV or a Tecnai G2 Spirit 120 kV instrument equipped with a Quamesa CCD camera (Olympus Soft Imaging Solutions).

MBP-His reconstituted into lipid vesicles (brain lipids:POPC:cholesterol) was labelled with 5 nm Ni-NTA-Nanogold particles (Nanoprobe). The sample was immobilised on a glow-discharged, carbon-coated electron microscopy grid prior to labelling. The grid was incubated 30 min upside-down on a droplet of 0.02 × Nanogold label solution on parafilm. The grid was washed twice with a buffer containing 20 mM Tris pH 7.5, 200 mM NaCl, 1% glycerol, and 100 mM imidazole, and negatively stained with 2% uranyl acetate.

Nanotube preparation. GalCer-DOGS-NTA-Ni nanotubes were generated as previously described⁸⁰. MBP-His and rMBP (0.4 mg ml⁻¹) were incubated for 1 h with 0.2 nmol ml⁻¹ nanotubes. Samples were imaged with negative stain or cryoEM.

Cryo EM grid preparation, imaging, and processing. Approximately 3 μl of the samples (~0.4 mg ml⁻¹) were applied to glow-discharged Quantifoil holey carbon grids (R 1.2/1.3, R 2/2, or R3.5/1, Cu 400 mesh, Quantifoil Micro Tools GmbH, Germany). After 2-s blotting, grids were flash frozen in liquid ethane, using an FEI Vitrobot IV (Vitrobot, Maastricht Instruments) with the environmental chamber set at 90% humidity and a temperature of 20 °C. Samples were imaged with FEI Titan Krios TEM operated at 300 keV, and images were recorded using a Gatan K2-Summit direct electron detector. Images were collected manually in electron-counting mode at a nominal magnification of ×22,500 and a calibrated pixel size of 1.3 Å. Each image was dose-fractionated to 40 frames (8 s in total, 0.2-s frames, dose rate 6–7 e⁻/pixel/s). Movie frames were aligned with MotionCorr⁸¹ and preprocessed on the fly with 2dx_automator⁸². Particles were boxed using e2boxer.py in EMAN2⁸³ and further processed by SPRING⁸⁴. In total, from 20 aligned images, 9000 overlapping, CTF-corrected segments with a size of 190 Å × 190 Å were used to calculate 2D class averages.

Neutron reflectometry. Supported lipid bilayers were prepared onto flat 80 mm × 50 mm × 15 mm Si-crystal blocks (polished by Sil'tronix Silicon Technologies, Archamps, France to a 5 Å RMS roughness

tolerance). Three samples were prepared from chloroform-methanol stocks of 1 mg ml⁻¹:DMPC, DMPC:DMPG (1:1), and d₅₄-DMPC:d₅₄-DMPG (1:1). The two leaflets of the bilayer were deposited sequentially using the Langmuir-Blodgett and Langmuir-Schaefer techniques. Deposition was carried out at a surface pressure held constant at 30 mN m⁻¹, following the procedure described previously for mixed, charged lipid systems^{85,86}. The blocks were assembled into low-volume measurement flow cells, to enable the *in situ* exchange of solvent and injection of protein samples⁸⁷, and transferred directly to the neutron reflectometer for measurement.

Each data point was collected at incident angles of 0.8° and 3.2°, on the D17 neutron reflectometer at the ILL (Grenoble, France)⁸⁸. A slit geometry was used such that full use could be made of the coherent summing method for processing the data⁸⁹, maximizing both intensity and resolution during time-resolved measurements. The sample temperature was kept at a constant +30°C throughout. HBS buffer was used for all measurements, prepared at a final concentration of 95% (v/v) deuterium oxide (D₂O, Sigma-Aldrich) and in H₂O. The bilayers were characterised, before and after the introduction of rMBP, at three different solvent contrasts, varying the D₂O-H₂O volume fraction introduced into the sample cell: (1) 95% D₂O, (2) water contrast-matched to Si (SMW; 38-to-62 volume ratio of D₂O/H₂O), and (3) 100% H₂O. During the injection of rMBP, in H₂O, time-resolved measurements were carried out, cycling between the two angles to give a time resolution of ~15 minutes. rMBP was allowed to interact with the membrane for 3 h, until no further changes were seen in the reflectivity. Any excess rMBP was then washed out from the bulk solution by pumping solvent slowly through the sample cell, until the cell volume had been exchanged 20 times.

Data analysis was carried out using custom procedures with the RasCAL software package (<https://sourceforge.net/p/rscl/wiki/Home/>). A complete description of the theory and procedures involved in neutron reflectivity analysis for biomembrane systems involving small molecule interactions is discussed elsewhere⁸⁵. Briefly, all equilibrium measurements for one sample, before and after addition of rMBP, were fitted simultaneously with the parameters used to describe the silicon oxide thickness, coverage, and interfacial roughness held constant between all the contrasts. The lipid bilayers were analysed using just five parameters, using scattering length densities and a custom-built model, as described previously in detail⁸⁶. The parameters used were: area per lipid molecule (APM), the number of water molecules associated with the headgroups (H₂O_{head}) and the tails (H₂O_{tail}) of each lipid molecule, and the roughness of the system (both local and global). To account for the interaction of rMBP with the bilayer after injection, four different models were used to try and fit the data: (1) A layer of MBP on top of the membrane but with no penetration in to the bilayer; (2) A layer of MBP on top of the membrane and penetrating into the lipid ‘headgroups’ in the outer leaflet of the bilayer, displacing water molecules; (3) A layer of MBP on top of the membrane and full insertion in to the outer leaflet of the bilayer, potentially displacing both lipid and water molecules from this leaflet; (4) A layer of MBP on top of the membrane and full insertion into both leaflets of the bilayer, potentially displacing water and lipid molecules from both. These displacement/insertion models were set up as quantified and described in earlier work⁹⁰; in all cases, a new ‘local outer leaflet’ roughness was introduced to describe the interface between the lipid heads and the MBP layer. The uncertainty on the value of each parameter used to fit the data was calculated by ‘bootstrapping’, a Monte Carlo error analysis approach built in to RasCAL, taking into account the error and instrumental resolution per data point⁹¹. This error estimation provides an indication of the uniqueness of the applied model within the error bars of the data.

Data availability. The datasets generated and analysed during the current study are available from the corresponding author on reasonable request.

References

- Kawachi, I. & Lassmann, H. Neurodegeneration in multiple sclerosis and neuromyelitis optica. *J. Neurol. Neurosurg. Psychiatry* **88**, 137–145 (2017).
- Mathis, S., Magy, L. & Vallat, J. Therapeutic options in Charcot-Marie-Tooth diseases. *Expert. Rev. Neurother* **15**, 355–366 (2015).
- Han, H., Myllykoski, M., Ruskamo, S., Wang, C. & Kursula, P. Myelin-specific proteins: A structurally diverse group of membrane-interacting molecules. *Biofactors* **39**, 233–241 (2013).
- Beniac, D. R. *et al.* Marburg’s variant of multiple sclerosis correlates with a less compact structure of myelin basic protein. *Mol. Cell. Biol. Res. Commun* **1**, 48–51 (1999).
- Vassall, K. A., Bamm, V. V. & Harauz, G. MyelStones: the executive roles of myelin basic protein in myelin assembly and destabilization in multiple sclerosis. *Biochem. J.* **472**, 17–32 (2015).
- Dupouey, P. *et al.* Immunohistochemical studies of myelin basic protein in shiverer mouse devoid of major dense line of myelin. *Neurosci. Lett.* **12**, 113–118 (1979).
- Privat, A., Jacque, C., Bourre, J., Dupouey, P. & Baumann, N. Absence of the major dense line in myelin of the mutant mouse shiverer. *Neurosci. Lett.* **12**, 107–112 (1979).
- Li, Y. *et al.* Structure of a human autoimmune TCR bound to a myelin basic protein self-peptide and a multiple sclerosis-associated MHC class II molecule. *EMBO J.* **24**, 2968–2979 (2005).
- Shaharabani, R. *et al.* Structural transition in myelin membrane as initiator of multiple sclerosis. *J. Am. Chem. Soc.* **138**, 12159–12165 (2016).
- Pritzker, L., Joshi, S., Gowan, J., Harauz, G. & Moscarello, M. Deimination of myelin basic protein. 1. Effect of deimination of arginyl residues of myelin basic protein on its structure and susceptibility to digestion by cathepsin D. *Biochemistry* **39**, 5374–5381 (2000).
- D’Souza, C. A. & Moscarello, M. A. Differences in susceptibility of MBP charge isomers to digestion by stromelysin-1 (MMP-3) and release of an immunodominant epitope. *Neurochem. Res.* **31**, 1045–1054 (2006).
- Kattinig, D. R., Bund, T., Boggs, J. M., Harauz, G. & Hinderberger, D. Lateral self-assembly of 18.5-kDa myelin basic protein (MBP) charge component-C1 on membranes. *Biochim. Biophys. Acta.* **1818**, 2636–2647 (2012).
- Aggarwal, S. *et al.* Myelin membrane assembly is driven by a phase transition of myelin basic proteins into a cohesive protein meshwork. *PLoS Biol.* **11**, e1001577 (2013).
- Suresh, S., Wang, C., Nanekar, R., Kursula, P. & Edwardson, J. M. Myelin basic protein and myelin protein 2 act synergistically to cause stacking of lipid bilayers. *Biochemistry* **49**, 3456–3463 (2010).
- Knoll, W. *et al.* Structural and dynamical properties of reconstituted myelin sheaths in the presence of myelin proteins MBP and P2 studied by neutron scattering. *Soft Matter* **10**, 519–529 (2014).

16. Lee, D. W. *et al.* Adsorption mechanism of myelin basic protein on model substrates and its bridging interaction between the two surfaces. *Langmuir* **31**, 3159–3166 (2015).
17. Lee, D. W. *et al.* Lipid domains control myelin basic protein adsorption and membrane interactions between model myelin lipid bilayers. *Proc. Natl. Acad. Sci. USA* **111**, E768–E775 (2014).
18. Vassall, K. A., Jenkins, A. D., Bamm, V. V. & Harauz, G. Thermodynamic analysis of the disorder-to- α -helical transition of 18.5-kDa myelin basic protein reveals an equilibrium intermediate representing the most compact conformation. *J. Mol. Biol.* **427**, 1977–1992 (2015).
19. Bamm, V. V., Ahmed, M. A. M. & Harauz, G. Interaction of myelin basic protein with actin in the presence of dodecylphosphocholine micelles. *Biochemistry* **49**, 6903–6915 (2010).
20. Wang, C. *et al.* Charge isomers of myelin basic protein: Structure and interactions with membranes, nucleotide analogues, and calmodulin. *PLoS One* **6**, e19915 (2011).
21. Stadler, A. M. *et al.* Internal nanosecond dynamics in the intrinsically disordered myelin basic protein. *J. Am. Chem. Soc.* **136**, 6987–6994 (2014).
22. Smith, G. S. T., Chen, L., Bamm, V. V., Dutcher, J. R. & Harauz, G. The interaction of zinc with membrane-associated 18.5 kDa myelin basic protein: an attenuated total reflectance-Fourier transform infrared spectroscopic study. *Amino Acids* **39**, 739–750 (2010).
23. Baran, C., Smith, G. S. T., Bamm, V. V., Harauz, G. & Lee, J. S. Divalent cations induce a compaction of intrinsically disordered myelin basic protein. *Biochem. Biophys. Res. Commun.* **391**, 224–229 (2010).
24. Vassall, K. A. *et al.* Substitutions mimicking deimination and phosphorylation of 18.5-kDa myelin basic protein exert local structural effects that subtly influence its global folding. *Biochim. Biophys. Acta-Biomembr* **1858**, 1262–1277 (2016).
25. Brewer, A. K. & Striegel, A. M. Characterizing the size, shape, and compactness of a polydisperse prolate ellipsoidal particle via quadrupole-detector hydrodynamic chromatography. *Analyst* **136**, 515–519 (2011).
26. Tieleman, D., van der Spoel, D. & Berendsen, H. Molecular dynamics simulations of dodecylphosphocholine micelles at three different aggregate sizes: Micellar structure and chain relaxation. *J. Phys. Chem. B* **104**, 6380–6388 (2000).
27. Rambo, R. P. & Tainer, J. A. Characterizing Flexible and Intrinsically Unstructured Biological Macromolecules by SAS Using the Porod-Debye Law. *Biopolymers* **95**, 559–571 (2011).
28. Menon, N., Williams, R., Kampf, K. & Campagnoni, A. An Analysis of the Regions of the Myelin Basic-Protein that Bind to Phosphatidylcholine. *Neurochem. Res.* **15**, 777–783 (1990).
29. Mabrey, S. & Sturtevant, J. M. Investigation of phase-transitions of lipids and lipid mixtures by high sensitivity differential scanning calorimetry. *Proc. Natl. Acad. Sci. USA* **73**, 3862–3866 (1976).
30. Jo, E. & Boggs, J. Aggregation of Acidic Lipid Vesicles by Myelin Basic-Protein - Dependence on Potassium Concentration. *Biochemistry (N. Y.)* **34**, 13705–13716 (1995).
31. Ruskamo, S. *et al.* Atomic resolution view into the structure-function relationships of the human myelin peripheral membrane protein P2. *Acta Cryst. D* **70**, 165–176 (2014).
32. Schmitt, F. O., Bear, R. S. & Palmer, K. J. X-ray diffraction studies on the structure of the nerve myelin sheath. *J. Cell. Physiol.* **18**, 31–42 (1941).
33. Sedzik, J., Blarock, A. & Hochli, M. Lipid Myelin Basic-Protein Multilayers - A Model for the Cytoplasmic Space in Central Nervous-System Myelin. *J. Mol. Biol.* **174**, 385–409 (1984).
34. Riccio, P., Fasano, A., Borenshtein, N., Blevé-Zacheo, T. & Kirschner, D. Multilamellar packing of myelin modeled by lipid-bound MBP. *J. Neurosci. Res.* **59**, 513–521 (2000).
35. Natali, F. *et al.* Protein-membrane interaction: effect of myelin basic protein on the dynamics of oriented lipids. *Chem. Phys.* **292**, 455–464 (2003).
36. Natali, F. *et al.* The influence of the lipid-protein interaction on the membrane dynamics. *Physica B* **350**, E623–E626 (2004).
37. Fitzner, D. *et al.* Myelin basic protein-dependent plasma membrane reorganization in the formation of myelin. *EMBO J.* **25**, 5037–5048 (2006).
38. Steshenko, O. *et al.* Reorganization of Lipid Diffusion by Myelin Basic Protein as Revealed by STED Nanoscopy. *Biophys. J.* **110**, 2441–2450 (2016).
39. Hu, Y. *et al.* Synergistic interactions of lipids and myelin basic protein. *Proc. Natl. Acad. Sci. USA* **101**, 13466–13471 (2004).
40. Knoll, W. *et al.* Dynamic properties of a reconstituted myelin sheath. *Spectroscopy* **24**, 585–592 (2010).
41. Laulumaa, S. *et al.* Dynamics of the peripheral membrane protein P2 from human myelin measured by neutron scattering—A comparison between wild-type protein and a hinge mutant. *PLoS One* **10**, e0128954 (2015).
42. Bates, I., Boggs, J., Feix, J. & Harauz, G. Membrane-anchoring and charge effects in the interaction of myelin basic protein with lipid bilayers studied by site-directed spin labeling. *J. Biol. Chem.* **278**, 29041–29047 (2003).
43. Bates, I., Feix, J., Boggs, J. & Harauz, G. An immunodominant epitope of myelin basic protein is an amphipathic α -helix. *J. Biol. Chem.* **279**, 5757–5764 (2004).
44. Zhong, L., Bamm, V. V., Ahmed, M. A. M., Harauz, G. & Ladizhansky, V. Solid-state NMR spectroscopy of 18.5 kDa myelin basic protein reconstituted with lipid vesicles: Spectroscopic characterisation and spectral assignments of solvent-exposed protein fragments. *Biochim. Biophys. Acta-Biomembr* **1768**, 3193–3205 (2007).
45. Libich, D. S. & Harauz, G. Backbone dynamics of the 18.5 kDa isoform of myelin basic protein reveals transient α -helices and a calmodulin-binding site. *Biophys. J.* **94**, 4847–4866 (2008).
46. Libich, D. S. *et al.* Fuzzy complexes of myelin basic protein: NMR spectroscopic investigations of a polymorphic organizational linker of the central nervous system. *Biochem. Cell. Biol.* **88**, 143–155 (2010).
47. Srinivasan, N., Bhagawati, M., Ananthanarayanan, B. & Kumar, S. Stimuli-sensitive intrinsically disordered protein brushes. *Nat. Commun.* **5**, 5145 (2014).
48. Bhagawati, M. *et al.* Site-specific modulation of charge controls the structure and stimulus responsiveness of intrinsically disordered peptide brushes. *Langmuir* **32**, 5990–5996 (2016).
49. Min, Y. *et al.* Interaction forces and adhesion of supported myelin lipid bilayers modulated by myelin basic protein. *Proc. Natl. Acad. Sci. USA* **106**, 3154–3159 (2009).
50. Majava, V. *et al.* Structural analysis of the complex between calmodulin and full-length myelin basic protein, an intrinsically disordered molecule. *Amino Acids* **39**, 59–71 (2010).
51. Smith, G. S. T., Homchaudhuri, L., Boggs, J. M. & Harauz, G. Classic 18.5- and 21.5-kDa myelin basic protein isoforms associate with cytoskeletal and SH3-domain proteins in the immortalized N19-oligodendroglial cell line stimulated by phorbol ester and IGF-1. *Neurochem. Res.* **37**, 1277–1295 (2012).
52. Müller, C., Bauer, N. M., Schaefer, I. & White, R. Making myelin basic protein - from mRNA transport to localized translation. *Front. Cell. Neurosci.* **7**, 169 (2013).
53. Dyer, C. & Benjamins, J. Organization of oligodendroglial membrane sheet. I: Association of myelin basic protein and 2',3'-cyclic nucleotide 3'-phosphohydrolase with cytoskeleton. *J. Neurosci. Res.* **24**, 201–211 (1989).
54. Zuchero, J. B. *et al.* CNS myelin wrapping is driven by actin disassembly. *Dev. Cell* **34**, 152–167 (2015).
55. Baron, W. & Hoekstra, D. On the biogenesis of myelin membranes: Sorting, trafficking and cell polarity. *FEBS Lett* **584**, 1760–1770 (2010).

56. Bakhti, M. *et al.* Loss of electrostatic cell-surface repulsion mediates myelin membrane adhesion and compaction in the central nervous system. *Proc. Natl. Acad. Sci. USA* **110**, 3143–3148 (2013).
57. Ozgen, H., Baron, W., Hoekstra, D. & Kahya, N. Oligodendroglial membrane dynamics in relation to myelin biogenesis. *Cell. Mol. Life. Sci.* **73**, 3291–3310 (2016).
58. Yin, X., Peterson, J., Gravel, M., Braun, P. & Trapp, B. CNP overexpression induces aberrant oligodendrocyte membranes and inhibits MBP accumulation and myelin compaction. *J. Neurosci. Res.* **50**, 238–247 (1997).
59. Snaidero, N. *et al.* Antagonistic functions of MBP and CNP establish cytosolic channels in CNS myelin. *Cell Rep* **18**, 314–323 (2017).
60. Albert, L. & Inman, R. Mechanisms of disease: Molecular mimicry and autoimmunity. *N. Engl. J. Med.* **341**, 2068–2074 (1999).
61. Deraos, G. *et al.* Properties of myelin altered peptide ligand cyclo(87–99)(Ala91,Ala96) MBP87–99 render it a promising drug lead for immunotherapy of multiple sclerosis. *Eur. J. Med. Chem.* **101**, 13–23 (2015).
62. Perera, C. J. *et al.* Effects of active immunisation with myelin basic protein and myelin-derived altered peptide ligand on pain hypersensitivity and neuroinflammation. *J. Neuroimmunol.* **286**, 59–70 (2015).
63. Boggs, J. *et al.* Effect of arginine loss in myelin basic protein, as occurs in its deiminated charge isoform, on mediation of actin polymerization and actin binding to a lipid membrane *in vitro*. *Biochemistry* **44**, 3524–3534 (2005).
64. Friess, M. *et al.* Intracellular ion signaling influences myelin basic protein synthesis in oligodendrocyte precursor cells. *Cell Calcium* **60**, 322–330 (2016).
65. Zenker, J. *et al.* A role of peripheral myelin protein 2 in lipid homeostasis of myelinating Schwann cells. *Glia* **62**, 1502–1512 (2014).
66. Min, Y. *et al.* Critical and Off-Critical Miscibility Transitions in Model Extracellular and Cytoplasmic Myelin Lipid Monolayers. *Biophys. J.* **100**, 1490–1498 (2011).
67. Saher, G., Quintes, S. & Nave, K. Cholesterol: a novel regulatory role in myelin formation. *Neuroscientist* **17**, 79–93 (2011).
68. Musse, A., Gao, W., Homchaudhuri, L., Boggs, J. & Harauz, G. Myelin basic protein as a “PI(4,5)P2-modulin”: a new biological function for a major central nervous system protein. *Biochemistry* **47**, 10372–10382 (2008).
69. Nawaz, S. *et al.* Phosphatidylinositol 4,5-Bisphosphate-Dependent Interaction of Myelin Basic Protein with the Plasma Membrane in Oligodendroglial Cells and Its Rapid Perturbation by Elevated Calcium. *J. Neurosci.* **29**, 4794–4807 (2009).
70. Snaidero, N. *et al.* Myelin Membrane Wrapping of CNS Axons by PI(3,4,5)P3-Dependent Polarized Growth at the Inner Tongue. *Cell* **156**, 277–290 (2014).
71. Luo, X. *et al.* Cytoplasmic domain of human myelin protein zero likely folded as beta-Structure in compact myelin. *Biophys. J.* **92**, 1585–1597 (2007).
72. Hammarström, M., Woestenenk, E., Hellgren, N., Hård, T. & Berglund, H. Effect of N-terminal solubility enhancing fusion proteins on yield of purified target protein. *J. Struct. Funct. Genomics* **7**, 1–14 (2006).
73. Compton, E. L. R., Karinou, E., Naismith, J. H., Gabel, F. & Javelle, A. Low resolution structure of a bacterial SLC26 transporter reveals dimeric stoichiometry and mobile intracellular domains. *J. Biol. Chem.* **286**, 27058–27067 (2011).
74. Kline, S. R. Reduction and analysis of SANS and USANS data using IGOR Pro. *J. Appl. Crystallogr.* **39**, 895–900 (2006).
75. Konarev, P., Petoukhov, M., Volkov, V. & Svergun, D. ATSAS 2.1, a program package for small-angle scattering data analysis. *J. Appl. Crystallogr.* **39**, 277–286 (2006).
76. Svergun, D. I. Determination of the regularization parameter in indirect-transform methods using perceptual criteria. *J. Appl. Crystallogr.* **25**, 495–503 (1992).
77. Svergun, D., Petoukhov, M. & Koch, M. Determination of domain structure of proteins from X-ray solution scattering. *Biophys. J.* **80**, 2946–2953 (2001).
78. Tria, G., Mertens, H. D. T., Kachala, M. & Svergun, D. I. Advanced ensemble modelling of flexible macromolecules using X-ray solution scattering. *Iucrj* **2**, 207–217 (2015).
79. Buerck, J. *et al.* UV-CD12: synchrotron radiation circular dichroism beamline at ANKA. *J. Synchrotron Radiat.* **22**, 844–852 (2015).
80. Wilson-Kubalek, E., Brown, R., Celia, H. & Milligan, R. Lipid nanotubes as substrates for helical crystallization of macromolecules. *Proc. Natl. Acad. Sci. USA* **95**, 8040–8045 (1998).
81. Li, X. *et al.* Electron counting and beam-induced motion correction enable near-atomic-resolution single-particle cryo-EM. *Nat. Methods* **10**, 584–590 (2013).
82. Scherer, S. *et al.* 2dx_automator: Implementation of a semiautomatic high-throughput high-resolution cryo-electron crystallography pipeline. *J. Struct. Biol.* **186**, 302–307 (2014).
83. Tang, G. *et al.* EMAN2: An extensible image processing suite for electron microscopy. *J. Struct. Biol.* **157**, 38–46 (2007).
84. Desfosses, A., Ciuffa, R., Gutsche, I. & Sachse, C. SPRING - An image processing package for single-particle based helical reconstruction from electron cryomicrographs. *J. Struct. Biol.* **185**, 15–26 (2014).
85. Barker, R. D., McKinley, L. E. & Tittmuss, S. Neutron Reflectivity as a Tool for Physics-Based Studies of Model Bacterial Membranes. *Adv. Exp. Med. Biol.* **915**, 261–282 (2016).
86. Hubbard, A. T. M. *et al.* The mechanism of action of a membrane-active quinoline-based antimicrobial on natural and model bacterial membranes. *Biochemistry* **56**, 1163–1174 (2017).
87. Junghans, A. *et al.* Analysis of biosurfaces by neutron reflectometry: From simple to complex interfaces. *Biointerphases* **10**, 019014 (2015).
88. Cubitt, R. & Fragneto, G. D17: the new reflectometer at the ILL. *Appl. Phys. A* **74**, S329–S331 (2002).
89. Cubitt, R., Saerbeck, T., Campbell, R. A., Barker, R. & Gutfreund, P. An improved algorithm for reducing reflectometry data involving divergent beams or non-flat samples. *J. Appl. Crystallogr.* **48**, 2006–2011 (2015).
90. Bello, G. *et al.* The influence of rough lipopolysaccharide structure on molecular interactions with mammalian antimicrobial peptides. *Biochim. Biophys. Acta.* **1858**, 197–209 (2016).
91. Efron, B. & Tibshirani, R. J. In *An introduction to the bootstrap* (Chapman & Hall, New York, London, 1993).

Acknowledgements

This work was financially supported by the Academy of Finland (Finland), the Sigrid Jusélius Foundation (Finland), the Emil Aaltonen Foundation (Finland), the University of Oulu Graduate School (Finland), the Norwegian Research Council (SYNKNØYT program), the General Medical Research Fund (University of Bergen, Norway), and Western Norway Regional Health Authority (Norway). We thank Dr. Marte Inneset Flydal for practical guidance in using DSC. We gratefully acknowledge the synchrotron radiation facilities and the beamline support at ANKA, ASTRID2, and EMBL/DESY, as well as the Partnership for Soft Condensed Matter facilities and neutron beamtimes at ILL (Proposal Nos 8-02-745 and 8-03-865). We also express our gratitude towards the Biocenter Oulu Proteomics and Protein Analysis Core Facility for providing access to mass spectrometric instrumentation.

Author Contributions

Study design: A.R., J.K., S.R., R.B., H.S., P.K.; Prepared samples and performed experiments: A.R., J.K., S.R., R.B., A.B., A.M., J.T., M.M., J.B.; Processed and analysed data: A.R., J.K., S.R., R.B., A.B., A.M., P.K.; Original text and figures: A.R., P.K.; Review & editing: A.R., R.B., A.M., J.B., A.S.U., H.S., P.K.; Supervision: A.S.U., H.S., P.K.

Additional Information

Supplementary information accompanies this paper at doi:[10.1038/s41598-017-05364-3](https://doi.org/10.1038/s41598-017-05364-3)

Competing Interests: The authors declare that they have no competing interests.

Publisher's note: Springer Nature remains neutral with regard to jurisdictional claims in published maps and institutional affiliations.



Open Access This article is licensed under a Creative Commons Attribution 4.0 International License, which permits use, sharing, adaptation, distribution and reproduction in any medium or format, as long as you give appropriate credit to the original author(s) and the source, provide a link to the Creative Commons license, and indicate if changes were made. The images or other third party material in this article are included in the article's Creative Commons license, unless indicated otherwise in a credit line to the material. If material is not included in the article's Creative Commons license and your intended use is not permitted by statutory regulation or exceeds the permitted use, you will need to obtain permission directly from the copyright holder. To view a copy of this license, visit <http://creativecommons.org/licenses/by/4.0/>.

© The Author(s) 2017

Membrane Association Landscape of Myelin Basic Protein Portrays Formation of the Myelin Major Dense Line

Arne Raasakka^{1,2}, Salla Ruskamo², Julia Kowal³, Robert Barker^{4,5}, Anne Baumann^{1,6}, Anne Martel⁵,
Jussi Tuusa², Matti Myllykoski², Jochen Bürck⁷, Anne S. Ulrich^{7,8}, Henning Stahlberg³ & Petri
Kursula^{1,2}

¹Department of Biomedicine, University of Bergen, Bergen, Norway

²Faculty of Biochemistry and Molecular Medicine & Biocenter Oulu, University of Oulu, Oulu, Finland

³Center for Cellular Imaging and NanoAnalytics (C-CINA), Biozentrum, University of Basel, Basel, Switzerland

⁴School of Physical Sciences, University of Kent, Canterbury, Kent, United Kingdom

⁵Institut Laue-Langevin (ILL), Grenoble, France

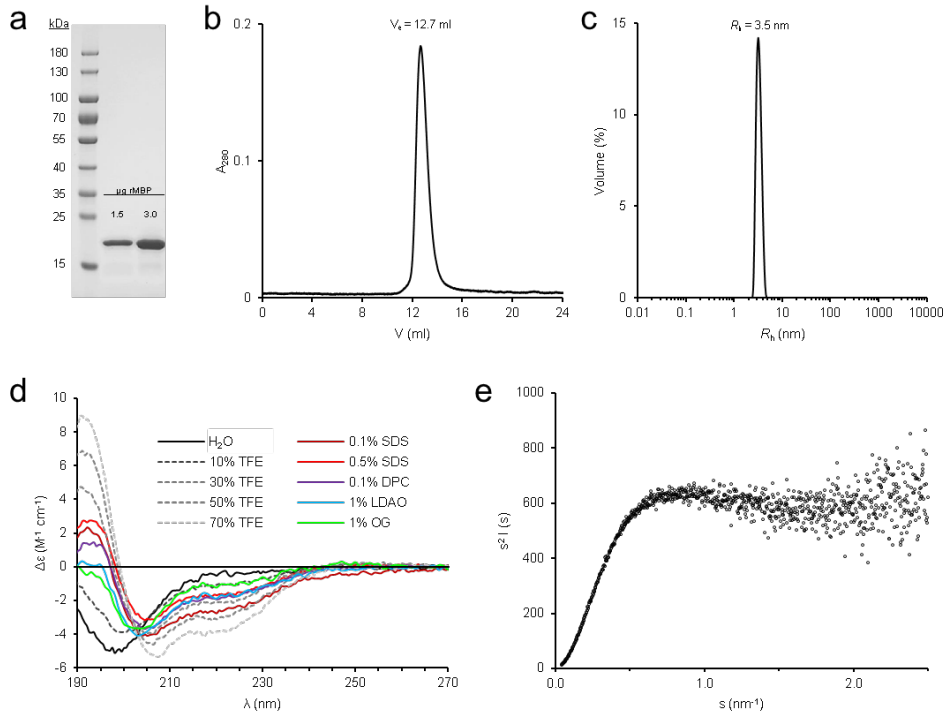
⁶Division of Psychiatry, Haukeland University Hospital, Bergen, Norway

⁷Institute of Biological Interfaces (IBG-2), Karlsruhe Institute of Technology, Karlsruhe, Germany

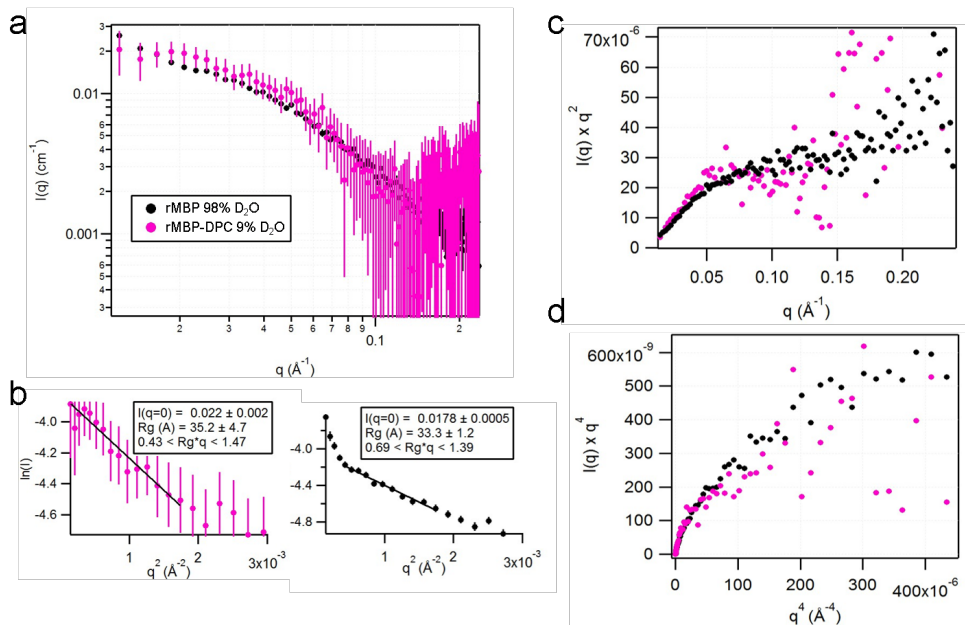
⁸Institute of Organic Chemistry, Karlsruhe Institute of Technology, Karlsruhe, Germany

Corresponding author: petri.kursula@uib.no

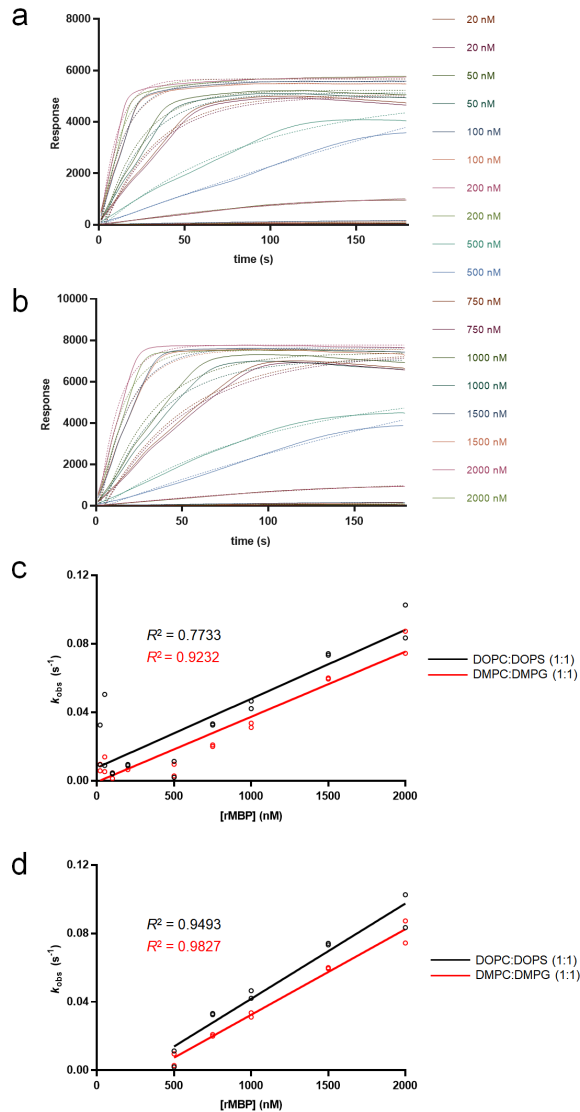
Supplementary information



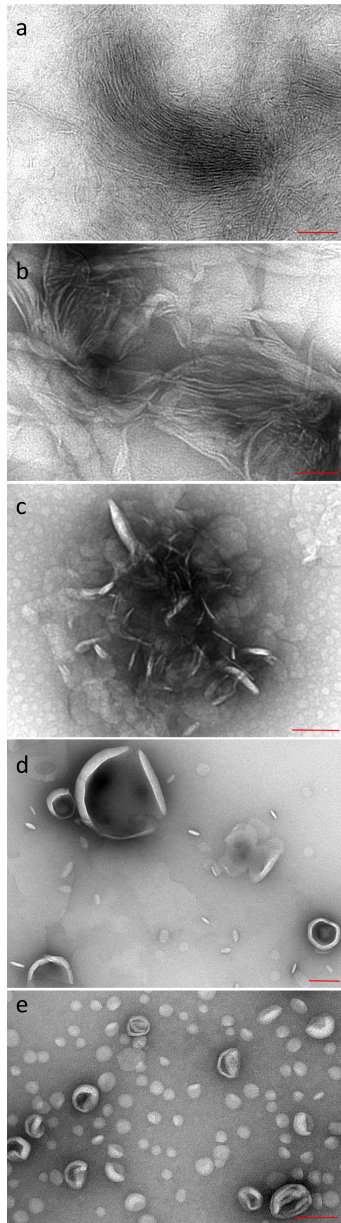
Supplementary Fig. 1. The purity, monodispersity, and folding of rMBP. (a) The purity of rMBP as determined by SDS-PAGE. (b) Size-exclusion chromatogram of rMBP when analysed using a Superdex 75 pg 10/300GL column. (c) Size distribution of rMBP in DLS. (d) The conformational changes of rMBP in TFE and various detergents were followed by CD spectroscopy. (e) rMBP appears mostly elongated based on SAXS data, when plotted in a Kratky plot.



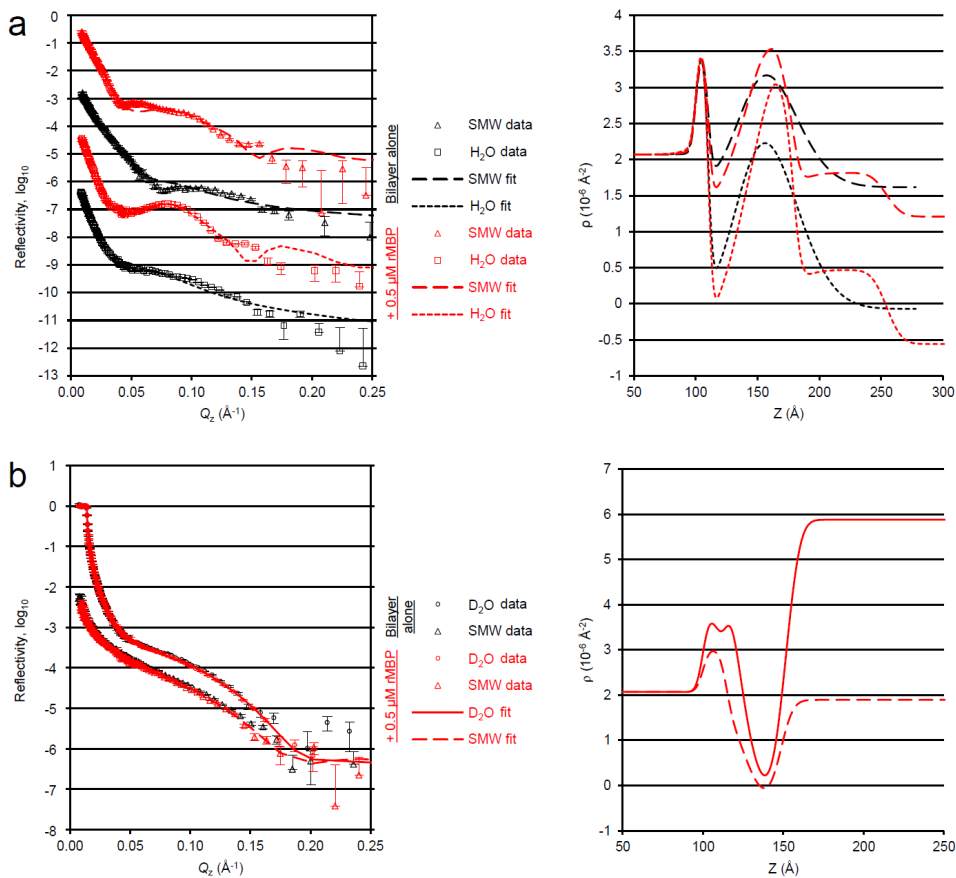
Supplementary Fig. 2. SANS data analysis. (a) Neutron scattering data of rMBP and DPC-bound rMBP. (b) Guinier analysis. (c) Kratky plot. (d) Porod-Debye plot. Comparison of the two datasets suggests that in the presence of DPC, rMBP forms a partially folded structure that represents a micelle-embedded segment, while still remaining mostly extended.



Supplementary Fig. 3. Kinetic analysis of SPR data. The association data (solid lines) of rMBP binding to DOPC:DOPS (a) and DMPC:DMPG (b) vesicles were fitted individually to an exponential one-phase association binding model (dashed lines). The derived k_{obs} values were plotted against rMBP concentration, and the apparent k_{on} and k_{off} values were extracted (see Supplementary Table 2) for DOPC:DOPS and DMPC:DMPG by fitting linear functions to the entire data (c) as well as omitting all datapoints prior to the critical binding concentration of rMBP (d), which results in a better linear function.



Supplementary Fig. 4. Concentration dependence of membrane stacking induced by rMBP studied by EM. Vesicle aggregation and membrane stacking is very pronounced when rMBP is abundant and gradually decreases together with the concentration of rMBP, as demonstrated by the P/L ratios 1:100 (a), 1:200 (b), 1:500 (c), and 1:1000 (d). Empty vesicles are devoid of aggregation (e). Scale bar: 100 nm.



Supplementary Fig. 5. NR control binding experiments. (a) rMBP binds perdeuterated d₅₄-DMPC:d₅₄-DMPG membranes similarly to the hydrogenated membranes. (b) The addition of rMBP to DMPC membranes displays reflectograms that are nearly identical to the naked bilayer, indicating that rMBP is not binding. Data and fits are plotted on the left. All reflectivity curves have been offset for clarity. Scattering length density (ρ) profiles are plotted on the right. The error bars correspond to standard deviation.

Supplementary Table 1. Small-angle scattering data collection and analysis.

| Data collection parameters | | | |
|--|---------------------|------------------|-----------------------|
| Method; dataset | SAXS; MBP | SANS; MBP | SANS; MBP + 0.25% DPC |
| Instrument | P12, PETRAIII, DESY | D22, ILL | D22, ILL |
| Wavelength (nm) | 0.124 | 0.6 | 0.6 |
| Angular range (nm ⁻¹) | 0.027 - 4.801 | 0.12 - 2.364 | 0.12 - 2.364 |
| Exposure time (s) | 0.045 | 3600 | 3600 |
| Concentration range (mg ml ⁻¹) | 1.1 - 4.4 | 2.3 | 2.3 |
| Temperature (°C) | 20 | 10 | 10 |
| D ₂ O contrast (% v/v) | 0 | 98 | 9 |
| Structural parameters | | | |
| <i>I</i> ₀ (relative) [from p(r)] | 5687 | | |
| <i>R</i> _g (nm) [from p(r)] | 4.02 | | |
| <i>I</i> ₀ (relative) [from Guinier] | 5582.53 | 0.0178 | 0.022 |
| <i>R</i> _g (nm) [from Guinier] | 3.68 | 3.3 | 3.5 |
| <i>R</i> _g (nm) [from EOM ensemble] | 3.96 | 4.4 | 3.5 |
| <i>D</i> _{max} (nm) [from GNOM] | 17.82 | 12.0 | 10.0 |
| <i>D</i> _{max} (nm) [from EOM ensemble] | 12.92 | 13.8 | 11.2 |
| Molecular mass determination | | | |
| Molecular mass <i>M</i> , (kDa) [from <i>I</i> ₀ using p(r)] | 25.8 | | |
| Molecular mass <i>M</i> , (kDa) [from <i>I</i> ₀ using Guinier] | 25.4 | | |
| Theoretical <i>M</i> , from sequence (kDa) | 18.5 | 18.5 | 18.5 |
| Software | | | |
| Primary data reduction | PRIMUS | GRASP, NCMR SANS | GRASP, NCMR SANS |
| Data processing | PRIMUS | PRIMUS | PRIMUS |
| <i>Ab initio</i> analysis | GASBOR | | |
| Conformational ensemble analysis | EOM | EOM | EOM |
| Validation and averaging | PRIMUS | PRIMUS | PRIMUS |
| Three-dimensional graphics representation | PyMOL | | |
| EOM model parameters | | | |
| <i>Conformer #1</i> | | | |
| <i>R</i> _g (nm) | 5.72 | 3.38 | 3.14 |
| <i>D</i> _{max} (nm) | 17.81 | 10.87 | 9.91 |
| Mass fraction | 0.07 | 0.273 | 0.647 |
| <i>Conformer #2</i> | | | |
| <i>R</i> _g (nm) | 4.51 | 4.75 | 5.09 |
| <i>D</i> _{max} (nm) | 13.31 | 13.25 | 14.37 |
| Mass fraction | 0.14 | 0.091 | 0.182 |
| <i>Conformer #3</i> | | | |
| <i>R</i> _g (nm) | 4.45 | 6.42 | 3.39 |
| <i>D</i> _{max} (nm) | 14.20 | 19.47 | 11.43 |
| Mass fraction | 0.07 | 0.364 | 0.182 |
| <i>Conformer #4</i> | | | |
| <i>R</i> _g (nm) | 3.14 | 3.57 | |
| <i>D</i> _{max} (nm) | 9.34 | 12.30 | |
| Mass fraction | 0.07 | 0.091 | |
| <i>Conformer #5</i> | | | |
| <i>R</i> _g (nm) | 3.14 | 2.92 | |
| <i>D</i> _{max} (nm) | 9.47 | 9.47 | |
| Mass fraction | 0.36 | 0.182 | |
| <i>Conformer #6</i> | | | |
| <i>R</i> _g (nm) | 3.51 | | |
| <i>D</i> _{max} (nm) | 11.82 | | |
| Mass fraction | 0.14 | | |
| <i>Conformer #7</i> | | | |
| <i>R</i> _g (nm) | 4.26 | | |
| <i>D</i> _{max} (nm) | 12.83 | | |
| Mass fraction | 0.07 | | |
| <i>Conformer #8</i> | | | |
| <i>R</i> _g (nm) | 6.41 | | |
| <i>D</i> _{max} (nm) | 18.65 | | |
| Mass fraction | 0.07 | | |
| Total mass fraction of main conformers | 0.99 | 1.00 | 1.00 |

Supplementary Table 2. Kinetic parameters derived from rMBP association phase with vesicles.

| Vesicle composition | Fitting set 1 ^a | | | Fitting set 2 ^a | | |
|---------------------|--|--|-------|--|--|-------|
| | k_{on} ($\text{nM}^{-1} \text{s}^{-1}$) ($\times 10^5$) ^b | k_{off} (s^{-1}) ($\times 10^2$) ^c | R^2 | k_{on} ($\text{nM}^{-1} \text{s}^{-1}$) ($\times 10^5$) ^b | k_{off} (s^{-1}) ($\times 10^2$) ^c | R^2 |
| DOPC:DOPS (1:1) | 4.0 \pm 0.54 | 0.76 \pm 0.52 | 0.77 | 5.6 \pm 0.45 | -1.4 \pm 0.58 | 0.95 |
| DMPC:DMPG (1:1) | 3.8 \pm 0.27 | -0.066 \pm 0.26 | 0.92 | 5.0 \pm 0.23 | -1.8 \pm 0.30 | 0.98 |

^a Fitting set 1 contains all data points from the linear fit, whereas data points below 500 nM were omitted from Fitting set 2.

^b Slope of the linear fit function to $k_{obs(on)}$ vs. [rMBP].

^c Y-axis intercept of the linear fit function to $k_{obs(on)}$ vs. [rMBP]

Supplementary Table 3. Time-resolved neutron reflectometry parameters.

| Parameters | | d ₅₄ -DMPC:d ₅₄ -DMPG (1:1) | | |
|------------|--|---|-------------|-------------|
| | | Phase 1 | Phase 2 | Phase 3 |
| Substrate | Oxide thickness (\AA) | 10 \pm 1 | | |
| | Oxide coverage (%) | 90 \pm 4 | | |
| | Oxide roughness (\AA) | 3 \pm 1 | | |
| | Hydration layer between oxide and bilayer (\AA) | 25 \pm 6 | | |
| Bilayer | Bilayer area per molecule ($\text{\AA}^2/\text{molecule}$) | 59 \pm 7 | 58 \pm 6 | 53 \pm 2 |
| | Water per lipid head | 10 \pm 2 | 10 \pm 5 | 10 \pm 2 |
| | Water per lipid tail | 6 \pm 3 | 7 \pm 1 | 8 \pm 2 |
| | Global bilayer roughness (\AA) | 20 \pm 5 | 24 \pm 2 | 24 \pm 2 |
| | Local bilayer inner roughness (\AA) | 5 \pm 3 | 8 \pm 1 | 12 \pm 1 |
| | Local bilayer outer roughness (\AA) | 1 \pm 2 | 6 \pm 2 | 1 \pm 1 |
| rMBP | rMBP in outer heads (%) | 0 | 28 \pm 10 | 48 \pm 12 |
| | rMBP in outer tails (%) | 0 | 0 | 20 \pm 5 |
| | rMBP layer thickness (\AA) | 70 \pm 20 | 56 \pm 3 | 52 \pm 3 |
| | rMBP layer coverage (%) | 25 \pm 7 | 47 \pm 10 | 37 \pm 6 |
| | rMBP layer roughness (\AA) | 58 \pm 20 | 8 \pm 3 | 7 \pm 5 |

II

ARTICLE II

Molecular structure and function of myelin protein P0 in membrane stacking.

Raasakka A., Ruskamo S., Kowal J., Han H., Baumann A., Myllykoski M., Fasano A., Rossano R., Riccio P., Bürck J., Ulrich A.S., Stahlberg H. & Kursula P.

Scientific Reports **9**(1):642. DOI: 10.1038/s41598-018-37009-4. (2019)

Abstract

Compact myelin forms the basis of nerve insulation essential for higher vertebrates. Dozens of myelin membrane bilayers undergo tight stacking, and in the peripheral nervous system, this is partially enabled by myelin protein zero (P0). Consisting of an immunoglobulin (Ig)-like extracellular domain, a single transmembrane helix, and a cytoplasmic extension (P0ct), P0 harbours an important task in ensuring the integrity of compact myelin in the extracellular compartment, referred to as the intraperiod line. Several disease mutations resulting in peripheral neuropathies have been identified for P0, reflecting its physiological importance, but the arrangement of P0 within the myelin ultrastructure remains obscure. We performed a biophysical characterization of recombinant P0ct. P0ct contributes to the binding affinity between apposed cytoplasmic myelin membrane leaflets, which not only results in changes of the bilayer properties, but also potentially involves the arrangement of the Ig-like domains in a manner that stabilizes the intraperiod line. Transmission electron cryomicroscopy of native full-length P0 showed that P0 stacks lipid membranes by forming antiparallel dimers between the extracellular Ig-like domains. The zipper-like arrangement of the P0 extracellular domains between two membranes explains the double structure of the myelin intraperiod line. Our results contribute to the understanding of PNS myelin, the role of P0 therein, and the underlying molecular foundation of compact myelin stability in health and disease.

SCIENTIFIC REPORTS

OPEN

Molecular structure and function of myelin protein P0 in membrane stacking

Arne Raasakka^{1,2}, Salla Ruskamo^{1,2}, Julia Kowal^{3,4}, Huijong Han², Anne Baumann^{1,5}, Matti Myllykoski², Anna Fasano⁶, Rocco Rossano⁷, Paolo Riccio⁷, Jochen Bürck⁸, Anne S. Ulrich^{8,9}, Henning Stahlberg^{1,3} & Petri Kursula^{1,2}

Compact myelin forms the basis of nerve insulation essential for higher vertebrates. Dozens of myelin membrane bilayers undergo tight stacking, and in the peripheral nervous system, this is partially enabled by myelin protein zero (P0). Consisting of an immunoglobulin (Ig)-like extracellular domain, a single transmembrane helix, and a cytoplasmic extension (P0ct), P0 harbours an important task in ensuring the integrity of compact myelin in the extracellular compartment, referred to as the intraperiod line. Several disease mutations resulting in peripheral neuropathies have been identified for P0, reflecting its physiological importance, but the arrangement of P0 within the myelin ultrastructure remains obscure. We performed a biophysical characterization of recombinant P0ct. P0ct contributes to the binding affinity between apposed cytoplasmic myelin membrane leaflets, which not only results in changes of the bilayer properties, but also potentially involves the arrangement of the Ig-like domains in a manner that stabilizes the intraperiod line. Transmission electron cryomicroscopy of native full-length P0 showed that P0 stacks lipid membranes by forming antiparallel dimers between the extracellular Ig-like domains. The zipper-like arrangement of the P0 extracellular domains between two membranes explains the double structure of the myelin intraperiod line. Our results contribute to the understanding of PNS myelin, the role of P0 therein, and the underlying molecular foundation of compact myelin stability in health and disease.

Myelin enwraps axonal segments in the vertebrate nervous system, accelerating nerve impulse propagation as well as providing trophic and mechanical support to fragile neuronal processes¹. The insulative nature of myelin arises from its water-deficient structure, compact myelin, where layers of the plasma membrane are stacked upon each other and adhered together by specific proteins². This array of proteins partially differs between the central and peripheral nervous systems (CNS and PNS, respectively), and the disruption of PNS compact myelin has a severe effect on action potential velocity³. This manifests as a set of medical conditions, including the peripheral neuropathies Charcot-Marie-Tooth disease (CMT) and Dejerine-Sottas syndrome (DSS). Such diseases are incurable and difficult to treat, and they show significant genetic background, resulting from mutations in proteins that affect the formation or stability of myelin, either directly or indirectly⁴⁻⁷. The development of eventual CMT/DSS-targeting remedies is hindered by the lack of basic molecular structural knowledge on the formation and eventual disruption of PNS myelin⁸.

Myelin protein zero (P0; also known as MPZ) is the most abundant protein in PNS myelin⁹. It resides in compact myelin and spans the myelin membrane *via* a single transmembrane helix with an N-terminal immunoglobulin (Ig)-like domain on the extracellular side of the membrane. A short cytoplasmic tail (P0ct) follows the transmembrane domain³. Point mutations in P0 account for 10–12% of all dominant demyelinating CMT type 1 cases¹⁰.

¹Department of Biomedicine, University of Bergen, Bergen, Norway. ²Faculty of Biochemistry and Molecular Medicine & Biocenter Oulu, University of Oulu, Oulu, Finland. ³Center for Cellular Imaging and NanoAnalytics (C-CINA), Biozentrum, University of Basel, Basel, Switzerland. ⁴Institute of Molecular Biology and Biophysics, Department of Biology, ETH Zurich, Switzerland. ⁵Division of Psychiatry, Haukeland University Hospital, Bergen, Norway. ⁶Department of Biosciences, Biotechnologies and Biopharmaceutics, University of Bari, Bari, Italy. ⁷Department of Sciences, University of Basilicata, Potenza, Italy. ⁸Institute of Biological Interfaces (IBG-2), Karlsruhe Institute of Technology, Karlsruhe, Germany. ⁹Institute of Organic Chemistry, Karlsruhe Institute of Technology, Karlsruhe, Germany. Correspondence and requests for materials should be addressed to P.K. (email: petri.kursula@uib.no)

Received: 22 August 2018

Accepted: 30 November 2018

Published online: 24 January 2019

The extracellular Ig-like domain of P0 is a major contributor to the formation of the myelin intraperiod line¹¹. Crystal structures of this domain have provided clues about details of membrane adhesion, and one theory involves oligomerization of Ig-like domains from two apposing membranes^{12,13}. This would explain the roughly 5-nm spacing of the intraperiod line in compact myelin, compared to the 3-nm cytoplasmic compartment, or the major dense line, between two cytoplasmic membrane leaflets^{14–16}. Dozens of CMT- and DSS-linked mutations have been reported for the Ig-like domain, signifying its importance in myelination¹⁷.

At physiological pH, P0ct is a positively charged segment of 69 amino acids, predicted to be disordered in solution³. The central part of P0ct (amino acids 180–199 of mature human P0 isoform 1) contains an immunodominant, neurotogenic segment, which can be used to generate animal models with experimental autoimmune neuritis (EAN)¹⁸. It is noteworthy that most CMT-linked point mutations in P0ct are localized in this region^{17,19–22}. P0ct interacts with lipid membranes, and it gains a significant amount of secondary structure upon binding^{23–25}. P0ct aggregates negatively charged lipid vesicles²³, suggesting that P0ct might harbour a similar membrane-stacking function as myelin basic protein (MBP)¹⁶ and peripheral myelin protein 2 (P2)²⁶. However, the tertiary conformation of P0ct and details of its lipid binding are not fully understood, and the potential function of P0ct in membrane stacking remains to be further elucidated.

We characterized human P0ct using several complementary methods, to gain a structural insight into its membrane binding, insertion, and contribution to myelin membrane stacking. Using electron cryomicroscopy (cryo-EM), we observed a zipper-like assembly of bovine full-length P0 in reconstituted membranes. Additionally, we investigated a synthetic P0ct-derived peptide (P0ct_{pept}), corresponding to the neurotogenic sequence, under membrane-mimicking conditions using synchrotron radiation circular dichroism spectroscopy (SRCD) and computational predictions. Our results show that P0ct is likely to be involved in maintaining the stability of compact PNS myelin together with other cytosolic PNS myelin proteins. A combined approach of EM, small-angle X-ray diffraction (SAXD), atomic force microscopy (AFM), and differential scanning calorimetric (DSC) suggests that P0ct may have a role in regulating the lateral structure within the membrane, together with the ultrastructure formed by the Ig-like domains in the extracellular compartment.

Results

To study the putative function of P0ct as a classical membrane stacking protein, we performed a biophysical characterization, as well as binding experiments with lipids, similarly to our earlier study on MBP¹⁶. Additionally, we investigated the stacking behaviour of full-length P0 using cryo-EM, and the folding and orientation of P0ct_{pept} in membranes with SRCD.

Characterization of P0ct. We purified P0ct to homogeneity using a two-step purification process. P0ct appeared as a single band on SDS-PAGE, presenting a monodisperse profile in size exclusion chromatography (SEC) with a monomeric mass in solution, as shown with SEC-coupled multi-angle light scattering (SEC-MALS), despite its unusual migration in SDS-PAGE (Supplementary Fig. S1a). The obtained mass (7.5 kDa) was very close to the one determined using mass spectrometry (7991 Da), matching the expected mass based on the primary structure (7990.25 Da).

The folding of P0ct was studied in the presence of different additives using SRCD. The results were as expected based on earlier investigations²⁴. P0ct was mostly disordered in solution and gained significant secondary structure content, when introduced to increasing concentrations of 2,2,2-trifluoroethanol (TFE), as well as *n*-dodecylphosphocholine (DPC) or sodium dodecyl sulphate (SDS) micelles, but not with *n*-octylglucoside (OG) or lauryldimethylamine *N*-oxide (LDAO) (Supplementary Fig. S1b).

To investigate the solution behaviour of P0ct, we used small-angle X-ray scattering (SAXS) to reveal that P0ct is monomeric and extended (Fig. 1a,b, Supplementary Fig. S1c, Supplementary Table S1), which was best explained by a dynamic ensemble of elongated conformers, as observed for MBP (Fig. 1c)¹⁶. Similarly to MBP, P0ct appeared to favour a slightly compacted conformation over a completely extended one.

P0ct binds irreversibly to lipid structures and influences their properties. A gain in helical structure of P0ct was observed earlier in membrane-mimicking conditions, including neutral and charged detergent micelles, TFE, and different lipids²⁴. This could represent a physiologically relevant state of folding, which prompted us to investigate the lipid interaction propensity of P0ct in the presence of various lipid compositions by SRCD (Fig. 2a–c). Magnitude differences in the CD signals were detected between different samples, which most likely arose from lipid batch heterogeneity and the resulting differences in protein-lipid turbidity, causing light scattering and lowered signal intensity. This did not compromise data interpretation, as the relevant data for each comparison were acquired at the same time. Therefore, the SRCD traces in Fig. 2a–c should be compared only within panels. We observed a high degree of P0ct folding in the presence of negatively charged small unilamellar vesicles (SUVs), whereas neutral SUVs displayed no gain in secondary structure content compared to P0ct in water (Fig. 2a). A 1:1 molar mixture of the fully saturated lipids dimyristoylphosphatidylcholine (DMPC) and dimyristoylphosphatidylglycerol (DMPG), enhanced the folding notably compared to a 1:1 mixture of dioleoylphosphatidylcholine (DOPC) and dioleoylphosphatidylserine (DOPS), indicating a specific effect by the lipid tails, and/or a difference between the negatively charged PG and PS headgroups. The dimyristoyl lipids were compared to dioleoyl lipids due to the fact that the bilayer thickness in these cases is nearly identical. Importantly, SPR experiments (see below) indicated similar affinities towards both lipid mixtures. To check whether other lipid species could influence the folding, we included 10% (w/w) cholesterol, dimyristoylphosphatidylethanolamine (DMPE), or sphingomyelin (SM) in DMPC:DMPG (1:1) (Fig. 2b). Cholesterol and SM appeared to slightly favour folding, suggesting that P0ct is sensitive to fluidity differences within the membrane, as reported earlier²⁴. Additionally, these interactions seem specific from a molecular point of view, as changing between the gel and liquid disordered phases of DMPC:DMPG (1:1) *via* temperature scanning did not influence P0ct folding (Fig. 2c).

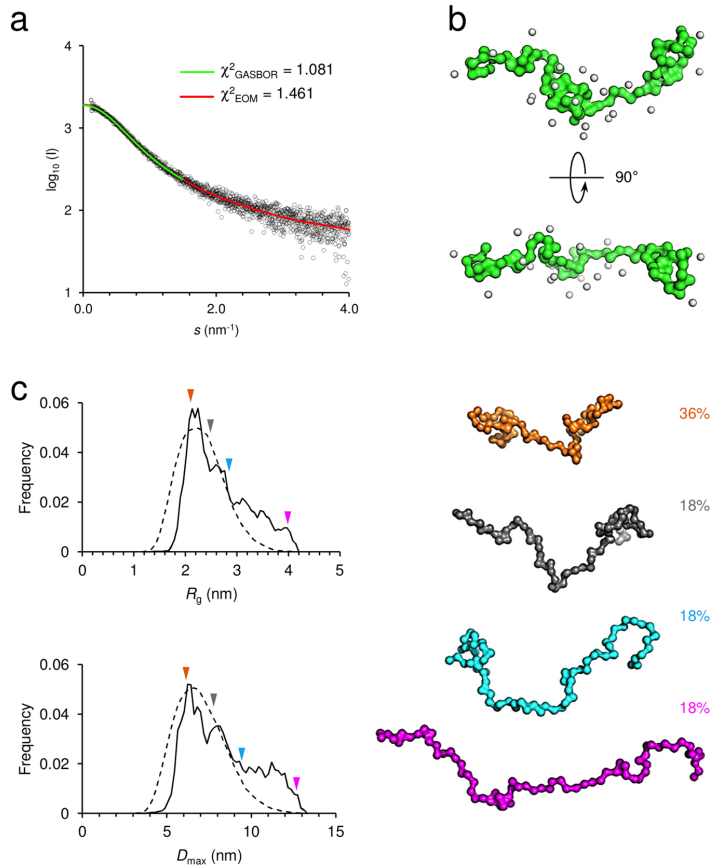


Figure 1. SAXS analysis of P0ct. **(a)** SAXS data reveals the elongated nature of P0ct. GASBOR and EOM fits are plotted over the entire measurement data with their respective χ^2 values indicated. **(b)** The GASBOR *ab initio* model is clearly elongated, measuring up to 8 nm in length. **(c)** An ensemble of dynamic conformers in solution, presenting wide R_g and D_{max} populations (left), satisfy the SAXS data well. Most abundant conformers by mass are presented as models (right; colored arrows denote the R_g and D_{max} values within the analyzed distributions from EOM).

SM and cholesterol are known to interact²⁷, and together, they contribute to the formation of lipid rafts, in which major PNS myelin proteins localize²⁸. These include P0, as well as its known interaction partner peripheral myelin protein 22 (PMP22)^{29,30}, for which the presence of SM is absolutely required for reconstitution into functional model systems³¹.

In our model lipid compositions, we did not observe structures rich in β -sheets, and to study more physiologically relevant conditions, we measured SRCD spectra of P0ct in the presence of a native myelin-like cytoplasmic leaflet composition, DMPC:dimyristoylphosphatidylserine (DMPS):DMPE:SM:cholesterol (25.9:7.29:6.2:31.6), as well as an experimental autoimmune encephalomyelitis (EAE)-like composition, DMPC:DMPS:DMPE:SM:cholesterol (20.1:7.4:32.9:2.2:37.4) (Fig. 2b)³². P0ct gained a high amount of secondary structure in the presence of native myelin-like lipids, but did not display enriched amounts of β -structure. The mixed secondary structure content had a high proportion of α -helix, as evident from the observed double minima at 208 and 222 nm. Predominantly β -sheet-rich structures would form a single minimum at 215 nm³³. The folding was clearly diminished in EAE-like lipids, and a key influencing factor might be the different phase behaviour of the two lipid compositions; the EAE lipid composition, which mimics a pathogenic myelin composition, has been demonstrated to co-exist as mixed lamellar and hexagonal phases *in vitro*, as opposed to the native myelin-like composition, which forms a completely lamellar lipid phase³⁴. Considering the composition, the largest relative difference is the much lower fraction of SM in the EAE-like lipids. Judging from the intensity of the observed double minima at 209 and 222 nm, the helical folding of P0ct in our model lipids matches the native-like lipid composition better than the EAE composition, validating our simplified model system for further studies.

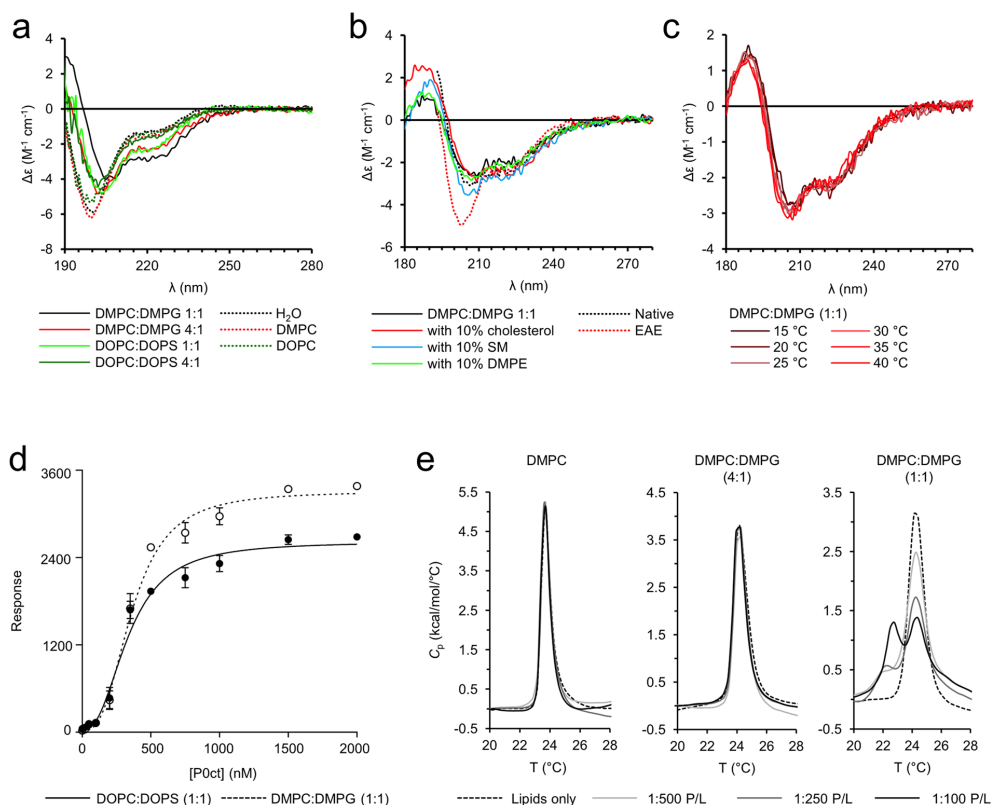


Figure 2. Folding and lipid binding properties of P0ct. **(a)** While P0ct remains disordered in the presence of neutral lipid bodies, a large gain in regular secondary structure content is evident especially in the presence of DMPC:DMPG (1:1). **(b)** P0ct appears to fold slightly differently in the presence of vesicles containing cholesterol or SM when mixed with a DMPC:DMPG (1:1) composition. Native and EAE-like lipid compositions (compositions based on previously published data³²) present a different degree of folding. **(c)** P0ct retains its folding in SRCD around the typical DMPC:DMPG (1:1) lipid phase transition temperature. **(d)** P0ct binds immobilized lipid vesicles in SPR. Error bars represent standard deviation. **(e)** The lipid tails of LMVs with a strong negative surface net charge exhibit a second endothermic transition at 22.5 °C upon the addition of P0ct.

| Lipid composition | R_{hl} | R_{lo} | A_1 | A_2 | R^2 |
|-------------------|-------------|-------------|--------------|-------------|--------|
| DOPC:DOPS (1:1) | 2617 ± 80.9 | 29.1 ± 64.7 | 337.2 ± 20.7 | 2.44 ± 0.31 | 0.9800 |
| DMPC:DMPG (1:1) | 3309 ± 71.4 | 19.8 ± 58.4 | 363.0 ± 15.0 | 2.76 ± 0.26 | 0.9893 |

Table 1. SPR fitting parameters.

The folding of P0ct in the presence of lipid vesicles is a strong indicator of binding, which prompted us to study the binding kinetics and affinity using surface plasmon resonance (SPR; Fig. 2d). P0ct irreversibly associated with immobilized large unilamellar lipid vesicles (LUVs), and comparison of saturated and unsaturated lipid tails only revealed differences in maximum response, reflecting the amount of bound P0ct, while the affinity (K_d) remained similar (Table 1). These results suggest that the saturated lipids DMPC:DMPG can incorporate more P0ct than DOPC:DOPS; furthermore, P0ct gained more secondary structure in the presence of DMPC:DMPG (Fig. 2a). We were interested in the underlying kinetics of association; similarly to MBP, we observed a complex association pattern¹⁶, which could not be analyzed confidently using simple binding models. Data are provided here for comparison with earlier data from MBP (Supplementary Fig. S2, Supplementary Table S2). Additional studies will be required to shed light on the details of membrane association kinetics of both P0ct, MBP, and other myelin proteins.

Having observed a similar lipid-dependent binding behaviour for P0ct as for MBP, we employed differential scanning calorimetry (DSC) to check for any thermodynamic changes in lipid tail behaviour of large

multilamellar vesicles (LMVs) in the presence of P0ct (Fig. 2e). While the phase behaviour of neutral lipids remained unaffected by the presence of P0ct, displaying only the $\sim 24^\circ\text{C}$ peak typical for dimyristoyl compounds³⁵, the inclusion of the negatively charged DMPG allowed us to observe an additional endothermic phase transition peak around 22.5°C . The lipid phase transition at 22.5°C increased in intensity with the addition of more P0ct, indicating direct binding to vesicles and concentration dependency. Note that P0ct did not display folding differences at temperatures around the observed phase transitions (Fig. 2c), suggesting that P0ct does not exist in several temperature-dependent conformational states. P0ct seems to directly interact with lipid tails, being capable of affecting the lipid phase behaviour by lowering the phase transition temperature.

P0ct induces the formation of an ordered proteolipid membrane. Since we confirmed the binding of P0ct to lipid structures, the next step was to investigate its putative membrane stacking function, as the biological function of many myelin proteins relates to multilayer formation. We used turbidimetry to indirectly quantify vesicle aggregation by P0ct (Fig. 3a). P0ct induced turbidity in the presence of several lipid mixtures with net negative surface charge.

The turbidimetric experiments strongly indicated that P0ct induced vesicle aggregation. To further elucidate the level of order within the system, we subjected protein-lipid samples to small-angle X-ray diffraction (SAXD) (Fig. 3b,c). While vesicles alone did not show Bragg peaks in the X-ray scattering profile (not shown), P0ct induced two intensive Bragg peaks, which changed their position in momentum transfer (s) in a nearly linear fashion as a function of protein-to-lipid (P/L) ratio, indicating concentration dependency in the formation of order and membrane spacing.

While the vesicle-based experiments provided indirect evidence of membrane stacking, we used atomic force microscopy (AFM) to determine whether P0ct can spontaneously stack membranes, similarly to MBP and P2²⁶ (Fig. 3d). However, under the experimental conditions we employed, P0ct did not form detectable stacked systems even at relatively high concentrations, rather appearing to accumulate on membranes, increasing their thickness and changing their mechanical properties. The morphology of the membranes changed in the presence of P0ct. The smooth, round edges of lipid bilayers appeared much less regular when P0ct accumulated on the membrane (Fig. 3c). P0ct seemed to concentrate at the edges of membranes (Fig. 3d), leaving some central parts of the SLBs less abundant in P0ct, as suggested by the thickness and rigidity of these regions being similar to SLBs not treated with P0ct.

We further exploited EM to check, whether aggregated vesicles form in the presence of P0ct (Fig. 4a–d). Surprisingly, the EM data revealed an absence of both vesicle aggregation and well-defined membrane stacks; the difference to control lipid samples was the formation of large vesicular bodies in the presence of P0ct, possibly formed through P0ct-mediated fusion, at most tested P/L ratios. At high protein concentrations, we observed 10–20-nm thick filament/tubule-like assemblies, seemingly formed of tightly adhered membranes. This is an indication of ordered protein-membrane structures, although such filamentous structures are not present in endogenous myelin. It appears that high enough P0ct concentrations may affect membrane bilayer curvature, which could be relevant for myelination. It should be noted that in these experiments, the required P/L ratio for P0ct to form any kind of visibly stacked systems was roughly an order of magnitude higher compared to MBP¹⁶. In PNS myelin, full-length P0 can be estimated to comprise up to $\sim 10\%$ of the membrane dry weight. This would correspond to a P/L ratio of $\sim 1:300$. The concentration of P0 in PNS compact myelin is several-fold higher than that of MBP, and P0ct could be functional in membrane stacking *in vivo*. The large vesicular structures suggest an unexpected mechanism, which does explain the observed turbidity at moderate P/L ratios; at the same time, the Bragg peaks in SAXD indicate the presence of well-defined repeat distances, possibly originating from local patches of adhered membranes. It is noteworthy that at P/L ratios of 1:50 and 1:100, the Bragg peaks are most intensive, and the repeat distance plateaus at 75.0 \AA , suggesting that the most condensed structure has been reached. A repeat distance of 75 \AA is in good corroboration with the thickness of cytoplasmic membrane stacks in myelin¹⁵; this distance is shorter than that observed with MBP and P2 earlier. These results indicate that P0ct can function as a membrane-stacking molecule. Taking all of our results together, the contribution of P0ct in membrane stacking *per se* is most likely low; however, in myelin, P0ct is not free but anchored to the cytoplasmic face of the membrane, which could affect its biophysical properties *in vivo*.

The folding and orientation of P0ct_{pept} in membranes. The P0ct_{pept} peptide has been used to induce EAN in animal models¹⁸. To shed light on its membrane association and conformation, we studied P0ct_{pept} using SRCD and oriented SRCD (OCD). P0ct_{pept} was disordered in solution and gained secondary structure in the presence of TFE or negatively charged detergent micelles, and somewhat less in negatively charged lipids (Fig. 5a,b). P0ct_{pept} did not fold with neutral lipids, and relatively weakly with negatively charged lipids, except with DMPC:DMPG (1:1). In the latter composition, the gain in secondary structure was notable, and the CD spectrum does not directly resemble classical α -helical or β -sheet lineshape: the observed maximum and minimum at 188 nm and 205 nm, respectively, are close to typical $\pi \rightarrow \pi^*$ transitions observed in peptides and proteins with mostly α -helical structures. However, the $n \rightarrow \pi^*$ band, normally observed as a minimum at 222 nm in α -helices, is poorly resolved. While P0ct_{pept} did not gain significant structure in DPC, the negatively charged detergent SDS induced higher secondary structure gain than 70% TFE, in contrast to P0ct and several other proteins^{16,36,37}, suggesting a role for electrostatic neutralization in the folding of P0ct_{pept}.

To shed light on the orientation of P0ct_{pept} in membranes, we prepared stacked membranes with P0ct_{pept} on planar quartz glass substrates at high relative humidity ($>97\%$). The samples were oriented perpendicular to the incident synchrotron radiation beam, and we collected OCD spectra of P0ct_{pept} in DMPC and DMPC:DMPG (1:1) membranes (Fig. 5c), which allows the investigation of helix orientation within oriented membranes^{38,39}. Comparison of the OCD spectra with isotropic spectra revealed folding in both cases. The OCD spectrum in DMPC is weak, but presents helical content, with both minima typical for in-plane helices in bilayers present;

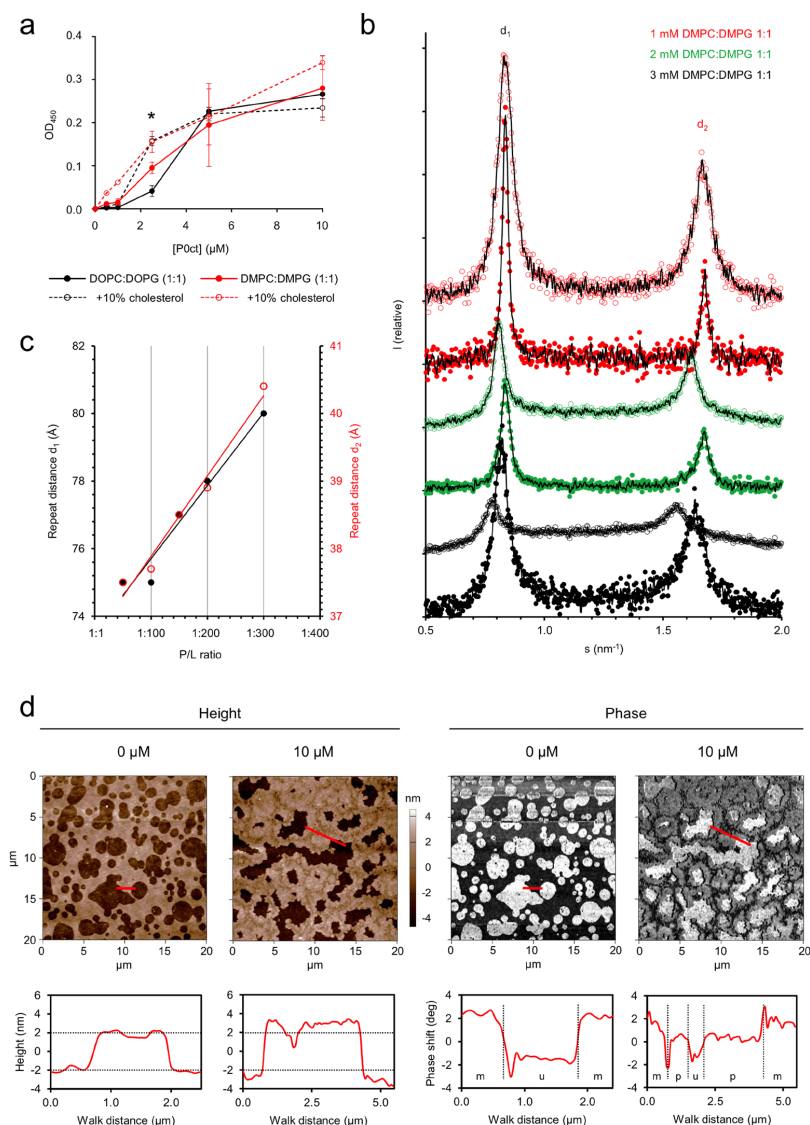


Figure 3. P0ct modulates the properties of lipid structures. **(a)** The turbidity caused by the presence of P0ct in SUVs somewhat changes depending on the lipid tail saturation degree or the presence of cholesterol. Error bars represent standard deviation. Asterisk: P/L ratio of 1:200. **(b)** Mixing P0ct with DMPC:DMPG (1:1) SUVs result in X-ray diffraction patterns that display two major Bragg peaks per dataset within the measured s -range. Added P0ct concentrations of 10 and 20 μM are shown as open and filled markers, respectively. A moving average (black line) has been plotted over each dataset, all of which have been offset for clarity. None of the data has been scaled in respect to one another. **(c)** The mean repeat distances, calculated from the s -values corresponding to the intensity summit of each Bragg peak, plotted as a function of P/L ratio. Linear fits are shown as solid lines for both d_1 and d_2 distributions. **(d)** In AFM, P0ct accumulates into supported DOPC:DOPS (1:1) bilayers without spontaneous induction of myelin-like membrane stacking, but increases the local thickness of the membrane by as much as 2 nm. This is evident especially at the edges of the membranes, where the membrane morphology is also changed. The phase difference of the membrane indicates that the mechanical properties of the membrane change in these areas, with a larger change at the edges of the membrane, where P0ct is supposedly most abundant. Height and phase difference graphs are plotted below the images, with the walk path indicated in red. Annotations in phase image walk graphs: m, mica; u, lipid bilayer; p, P0ct-embedded bilayer. Dashed horizontal and vertical dividers have been added to aid comparison.

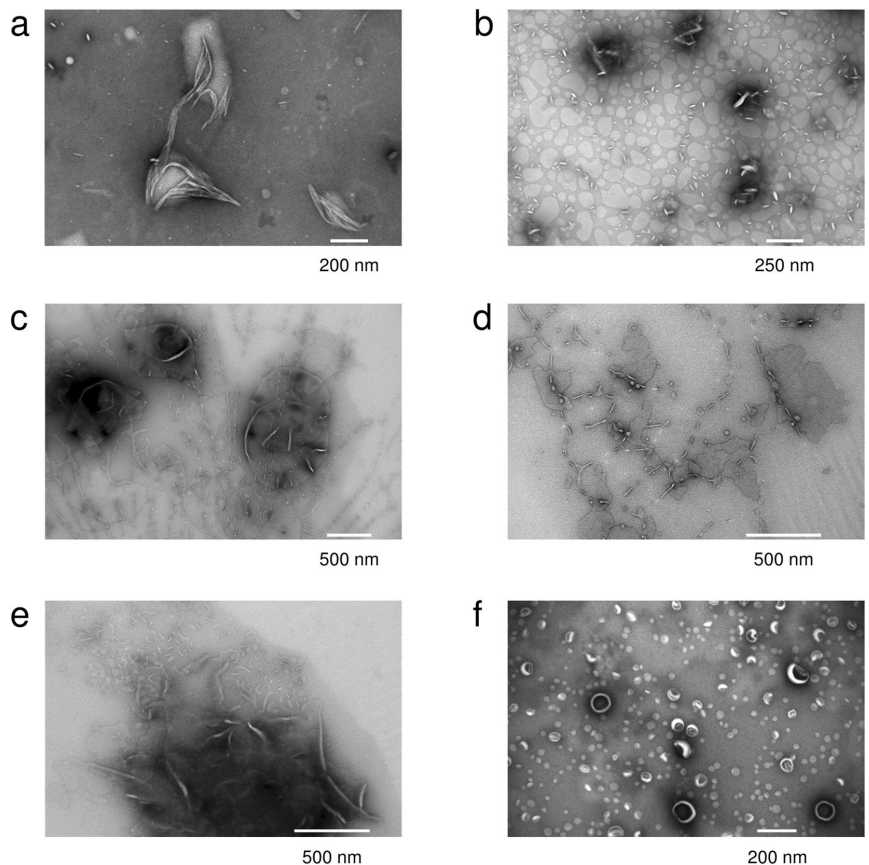


Figure 4. Vesicle fusion and membrane insertion of P0ct. EM concentration series of (a) 1:25, (b) 1:50, (c) 1:100, (d) 1:250 and (e) 1:500 P/L P0ct in the presence of DMPC:DMPG (1:1) vesicles shows the absence of membrane stacks, oppositely to the case of MBP¹⁶. The effect resembles vesicle fusion and the formation of large lipid bodies. (f) Vesicle control in the absence of P0ct.

compared to the isotropic spectrum, this reflects the fact that in OCD, there is much less free water phase and the peptide is forced to bind to DMPC. In DMPC:DMPG (1:1), the spectral intensity is higher, and the minimum typically observed at 208 nm is weakened, indicating that the helical segment of P0ct_{pept} is in a tilted orientation with respect to the lipid surface, although the shift is not strong enough to represent a completely perpendicular helix.

We generated models of P0ct_{pept} to learn more about its potential conformation. The N-terminal, basic half of P0ct_{pept} is likely flexible, whereas the more hydrophobic segment, corresponding to residues 189–199, folds into a well-defined helix (Fig. 5d,e). Linking the models to the observed OCD spectra, the peptide most likely adopts mixed orientations in DMPC, whereas in the presence of negatively charged headgroups, the N-terminal half of P0ct_{pept} can form ionic interactions. This could result in charge neutralization and induce folding into a second helical segment, which would adopt a more perpendicular orientation, explaining the measured OCD spectrum. The central Pro residue breaks the helix and could allow the two halves to adopt different orientations with respect to one another and the membrane. It is possible that at least the central helical segment of P0ct is ‘anchored’ at the level of the charged headgroups, and as such, is likely to give P0ct a specific orientation in the cytoplasmic leaflet of the myelin membrane.

P0 forms an intermembrane zipper composed of Ig-like domains. To complement the characterization of P0ct, we investigated membrane stacking by full-length P0, purified from the raft fraction of bovine peripheral myelin⁴⁰. During purification, the protein was embedded in SDS micelles, and after exchange into n-decyl-β-D-maltopyranoside (DM), the protein was monodisperse based on negative stain EM (Fig. 6a). SRCD investigations of P0 in detergents or net negatively charged lipids showed high structural content (Fig. 6b), and monodispersity was further analyzed using SEC-MALS (Fig. 6c, Supplementary Fig. S3). The oligomeric status

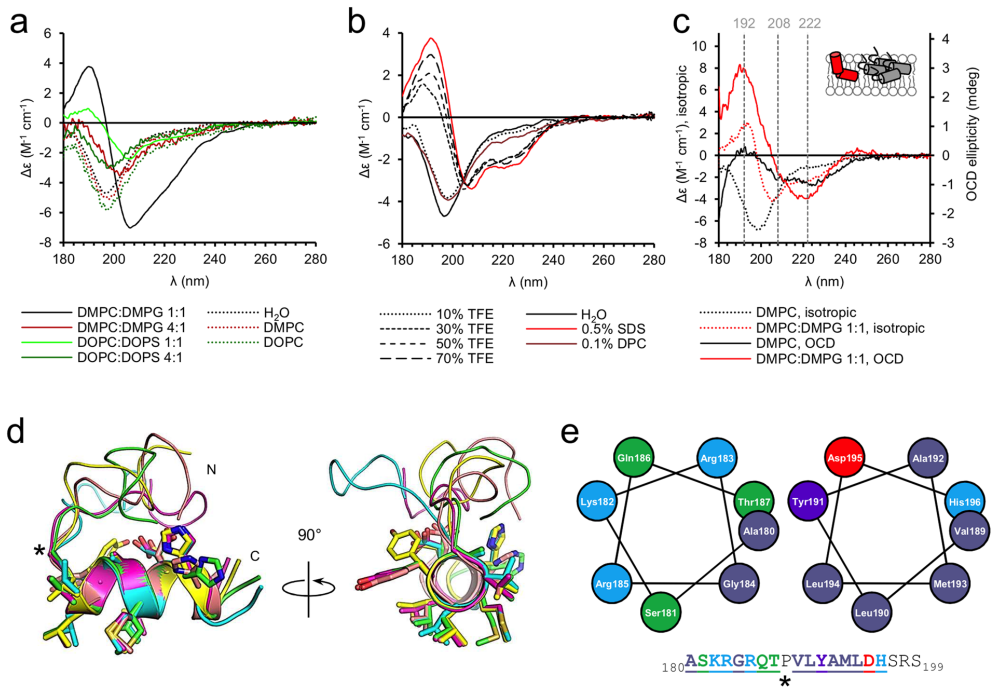


Figure 5. Folding of P0ct_{pept}. **(a)** SRCD data show that P0ct_{pept} only displays folding with negatively charged SUVs. The most notable spectrum is the DMPC:DMPG (1:1) spectrum, which does not resemble classical helical content, nor β -sheets. **(b)** The effect of TFE and detergents on the conformation of P0ct_{pept}. While P0ct_{pept} only displays marginal folding with DPC, SDS induces an even higher secondary structure gain than 70% TFE, indicating the major importance of electrostatics in the folding of P0ct_{pept}. **(c)** OCD data of P0ct_{pept} in DMPC and DMPC:DMPG (1:1). Isotropic spectra are shown for reference. The DMPC OCD data is weak, typical for an aggregated sample, while also showing traces of helical content. The DMPC:DMPG (1:1) data displays clear folding and a more perpendicular orientation within the membrane. A simple cartoon has been drawn for clarity for both OCD datasets. Colors match the shown data. **(d)** Superposition of five predicted structures of P0ct_{pept} reveal the N-terminus likely to be disordered, followed by a kinking Pro (black asterisk), and a helical C-terminal segment. **(e)** Helical wheel projections of the basic N-terminal half (left) and the hydrophobic half (right) of P0ct_{pept}. The residues are colored based on chemical properties with matched indications in the peptide sequence (down). The underlined segments are shown in the projections. The potentially helix-breaking Pro has been indicated with an asterisk.

of full-length P0 depended on detergent, and in accordance with earlier studies^{41,42}, both tetrameric and dimeric species were observed. The main species in DPC was tetrameric, while LDAO showed the presence of dimeric full-length P0. It is noteworthy that the folding of P0ct was different in these two detergents (Supplementary Fig. S1b), suggesting a possible involvement of P0ct in the oligomerization of P0.

We reconstituted P0 into SUVs prepared from both DOPC and *E. coli* polar lipids and imaged the samples using cryo-EM. We observed similar membrane stacking in both lipid compositions, suggesting that, under these conditions, the lipid composition plays a minor role in membrane stacking by full-length P0 (Fig. 6d–f).

The extracellular domain of P0 was organized between the two apposing lipid bilayers, forming a tightly packed zipper consisting of monomers from both apposed membranes (Fig. 6d–f). The thickness of the zipper determined the spatial width, measuring 50 ± 10 Å, between the membrane leaflets – a physiologically relevant value present in natural myelin, as shown by X-ray diffraction of myelin extracts^{14,15}. Each bilayer measured a typical 45-Å thickness. The distance between the apposing P0 monomers was 10–15 Å, if not in direct contact, whereas the spacing between lateral P0 monomers was 25–30 Å. It is realistic to assume that similar distances are present in native myelin, P0 constituting up to 50% of total protein in myelin. The tightly packed, uniform, zipper-like arrangement suggests that even though the underlying intermolecular interactions might be relatively weak at the level of single molecules, the large surface interaction area formed by a P0-enriched membrane can generate a strong force for keeping apposed membranes tightly together, both on the extracellular and cytosolic sides.

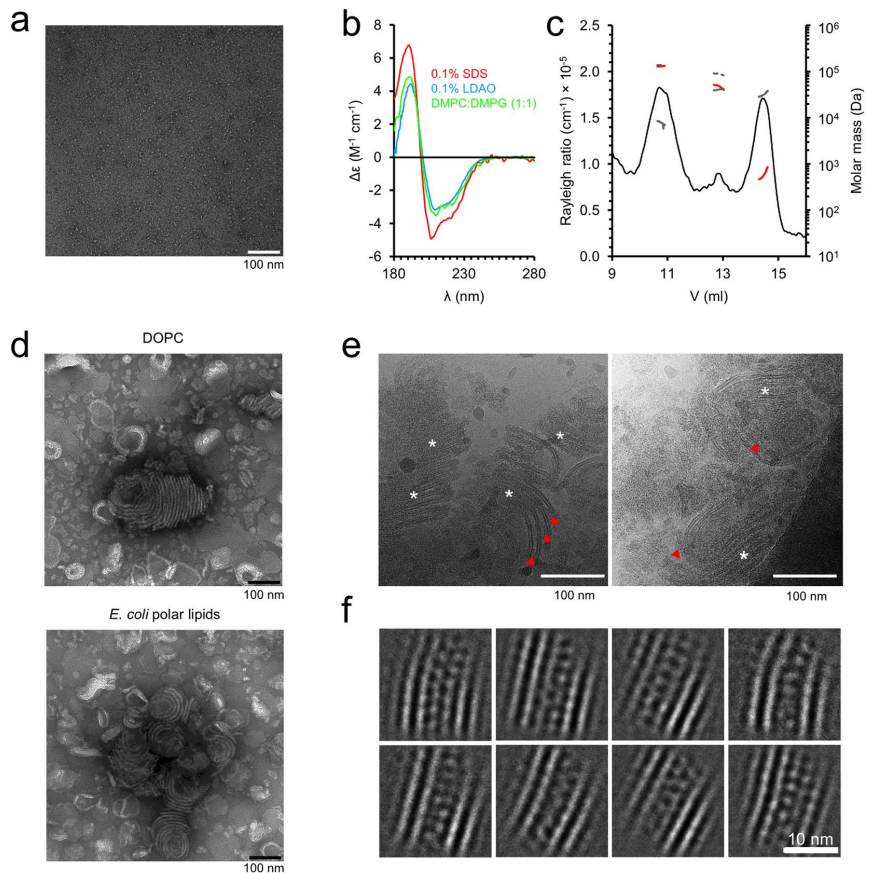


Figure 6. Full-length P0 in a membrane environment. (a) Cryo-EM of full length P0 displays good monodispersity in 0.4% DM. (b) SRCD spectra of full length P0 in detergents and lipids. (c) Analysis of full-length P0 monodispersity and oligomeric state using SEC-MALS. Shown are data measured in DPC. The Rayleigh ratio is shown (black) together with the total mass (gray dash), protein mass (red) and detergent mass for each peak (gray solid). (d) P0 reconstituted into DOPC and *E. coli* polar lipid extract vesicles result in membrane stacks that resemble myelin. (e) Cryo-EM micrographs of *E. coli* polar lipid extract with reconstituted P0. Both curved loosened and planar tight bilayer adhesions are present. In the latter, a significantly higher protein density between the membranes is evident. The loose and tight areas are marked with red arrows and white asterisks, respectively. (f) 2D class averages generated from the tight adhesions of P0 in *E. coli* polar lipids sample cryo-EM micrographs display a zipper of apposing Ig-like domains that interact with each other and settle between the two lipid bilayers.

Discussion

The cytoplasmic domain of P0 is disordered in solution, and once it irreversibly interacts with negatively charged lipids, it folds and becomes embedded, influencing the physical behaviour of the lipids within the membrane, but also potentially inducing larger-scale structural membrane reorganization. P0ct gains helical secondary structure with lipids, rather than the β -sheet-rich structures suggested earlier²⁴. This was notable also in a lipid composition that resembles the cytoplasmic leaflet of myelin, and the degree of folding was diminished in an EAE-like lipid composition.

Similarly to MBP¹⁶, the initial association of P0ct with lipids is governed by electrostatics, suggesting that P0ct possesses similar physicochemical properties as MBP within the myelin environment. However, due to the folding differences observed in SRCD with different lipid tails, correlated with amount of protein bound in SPR, one can speculate that the membrane-bound concentration of P0ct may influence its overall folding population. Already early studies in the 1930s and 1940s have shown that native myelin is an ordered structure diffracting X-rays^{43,44}. P0ct stacks membranes at such a level of order that X-ray diffraction bands are observed, and a repeat distance of 75 Å can be deduced in the multilayers. Lipid-bound MBP, having a high content of PE and low

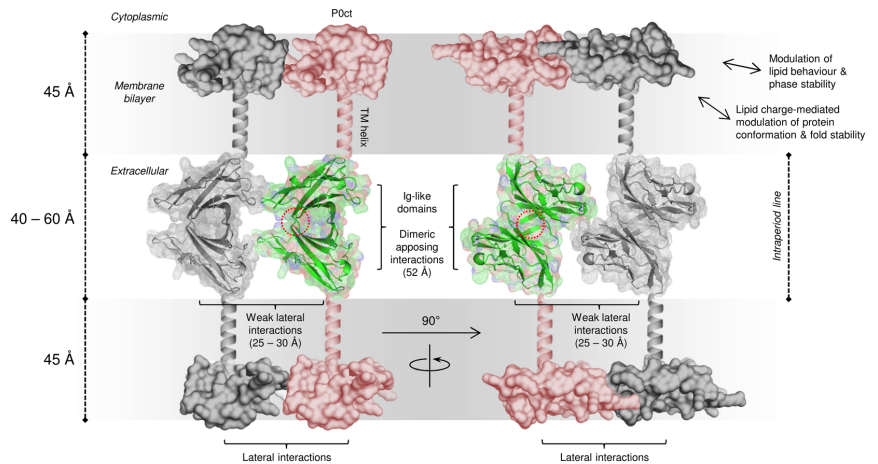


Figure 7. Model for the ultrastructure of the intraperiod line. Potential arrangement of P0 in the intraperiod line and lipid bilayers. Antiparallel apposing Ig-like domains interact weakly with each other through a β -strand stretch (red dotted circle; based on crystal contacts in PDB ID 1neu¹²) and form the basis of membrane stacking in the extracellular space. This arrangement results in the C-terminal end of the crystal structure to face the membrane, which logically would continue into the subsequent transmembrane helix. Additionally, the size of the antiparallel dimer is similar to the width of the intraperiod line. While the lateral Ig-like domain monomers are not necessarily in close contact with one another, P0ct anchors onto the cytoplasmic phospholipid headgroups through electrostatic interactions, gaining folding and potentially forming a stable, ordered protein lattice within the membrane, which forces P0 molecules to adjacency, including the extracellular domains. Additionally, P0ct changes the phase transition properties of the lipid bilayer, potentially influencing the stiffness and stability of PNS compact myelin, given that P0ct is capable of changing the mechanical properties of membranes in its bilayer-bound state. The given lengths in brackets match the measured dimensions from the crystal structure, cryo-EM micrographs, and SAXD.

content of bound cholesterol and SM, was shown to similarly generate stacked multilayers with repeat distances between 70–85 Å⁴⁵. Our study provides evidence that P0ct may not harbour a similar role in the formation of the major dense line as MBP, although it is definitely able to bridge charged membranes together at high protein concentrations *in vitro*. In this respect, it is important to remember that *in vivo*, P0ct is an extension of the transmembrane domain of P0, and solidly anchored to the membrane surface, possibly allowing stronger effects on membrane stacking than observed with the P0ct in isolation.

Our cryo-EM experiments on full-length P0 reconstituted into bilayers answer an important question regarding the arrangement of the intraperiod line: the Ig-like domains of P0 organize into apposed dimers, forming a zipper between the two membranes. This is apparently independent of lipid composition, and the interaction is mediated directly through the Ig-like domains. The data clearly indicate that the Ig-like domain of P0 from one membrane does not bind directly to the apposing membrane, but two rows of Ig-like domains are present in the extracellular compartment. This arrangement explains the double structure observed at the intraperiod line in high-resolution electron micrographs⁴⁶. Full-length P0 from the raft fraction, purified with the protocol used in our experiments, contains lipids typical of raft microdomains, including cholesterol and sphingomyelin, as well as N-linked glycan structures belonging to hybrid types⁴⁰. The glycan moieties present in P0 were in an earlier study suggested to play a role in the assembly of complex structures and different populations of P0 partitioning in and outside the raft microdomains of PNS myelin⁴⁰. The latter suggestion stems from the varying glycan content of P0 extracted from different myelin membrane subdomains.

From our data, it is not yet possible to observe atomic resolution details of dimerization. To understand P0 assembly in myelin, the crystal structure of the P0 extracellular domain can be used. As discussed in the original publication¹², the packing of the P0 Ig-like domain in the crystal state provides a potential dimerization scheme with one N-terminal β -strand of each apposing dimer forming an antiparallel β sheet (Fig. 7). In this assembly, the C terminus of each Ig domain monomer, near the start of the transmembrane helix, would directly face a membrane surface. The single 26-residue transmembrane helix of P0 is predicted to be roughly 4.5 nm long, spanning a single lipid bilayer.

While P0 dimerizes through apposing Ig-like domain monomers, the adjacent dimers in the lateral dimension are separated from one another, forming a uniformly spaced, lattice-like structure. Therefore, the lateral architecture is likely to be achieved by other factors than the Ig-like domains alone, perhaps through contributions by P0ct on the cytoplasmic face. Our diffraction studies suggest that P0ct is capable of forming higher order structures with membranes, indicating stable molecular interactions (Fig. 7). One can speculate that the function of P0ct is twofold: Firstly, P0ct may affect the lateral organization of P0 molecules in a manner that spaces the Ig

domains on the extracellular side in a manner productive for membrane stacking. The formation of organized P0-rich areas could provide a strong enough interaction surface to keep the apposing bilayers together. This apposition would be primarily mediated by the orientation and even spacing of the Ig-like domains to allow the subsequent 'zipper structure'; this arrangement of P0 could be affected by attractive and/or repulsive interactions between P0ct moieties on the cytoplasmic leaflet. The details of such interactions remain to be determined. Secondly, P0ct influences the phase behaviour of the membrane itself by destabilizing the gel phase by lowering the T_m , potentially by directly associating with certain lipid species, including saturated lipid tails, cholesterol, and SM, which influence lipid behaviour that favours productive stacking and the stability of myelin. This could also contribute to the lateral organization of P0 and its interaction partners, such as PMP22^{29,30}. Similarly to P0, mutations in PMP22, many of which are located in transmembrane helices, are hallmark features of CMT and DSS⁴⁷. Changes in the properties and conformation of proteins inside the myelin membrane can have a significant impact on myelin morphology and disease etiology.

Our studies involving the folding of P0ct and P0ct_{pept} suggest a strong influence of lipid electrostatics. While both display folding in the presence of negatively charged lipids, P0ct_{pept} appears to gain a tilted orientation in the membrane upon charge neutralization. This neurotogenic segment of P0ct can directly interact with lipid headgroups and fold into a rigid segment, and as the cytoplasmic side of the lipid bilayer is negatively charged, P0ct could adopt a defined orientation within the membrane. Other positively charged regions of P0ct might function in a similar manner. The adoption of a specific orientation in a membrane would aid in the formation of higher-order structures, which in turn could alter the behaviour, morphology, and rigidity of the membrane *per se*—as exemplified by our EM results at high protein concentrations. In general, membrane curving has been linked to phenomena highly relevant to P0 behaviour observed here at the molecular level; these include the asymmetric insertion of proteins to membrane leaflets, as well as the oligomerization of protein monomers into structures stabilizing a curved membrane shape⁴⁸.

The current study sheds light on the role of P0 at both the major dense line and the intraperiod line. If P0ct stabilizes the arrangement of P0 within a membrane, its importance for the integrity of myelin becomes obvious, and hints of potential molecular disease mechanisms arising from mutations within P0ct, many of which are specifically located within the neurotogenic helical sequence. The impact of these mutations has not yet been studied at the molecular level. Once the molecular basis of the disease mutations in P0ct has been solved, more functional aspects of P0ct will unravel, contributing to a better understanding of PNS compact myelin and its relation to CMT disease etiology.

Experimental Procedures

Cloning, protein expression, and Purification. A synthetic gene encoding for the 69 C-terminal residues (amino acids 151–219) of mature human myelin protein zero isoform 1 (UniProt ID: P25189) was transferred into the Gateway donor vector pDONR221 (Life Technologies). A tobacco etch virus (TEV) protease digestion site (ENLYFQG) was added before the gene, and the required *attB1* and *attB2* recombination sites before and after the gene, respectively. This entry clone was used to generate an expression clone in the pHMWGA vector⁴⁹, which encodes for an N-terminal His₆-tag, followed by a segment encoding for maltose-binding protein (MaBP), and finally followed by the inserted P0ct gene itself (His-MaBP-P0ct). A Cys153Leu mutation was included in the construct for two reasons: this cysteine is known to be palmitoylated *in vivo*, and free cysteines in small, disordered proteins are reactive and can easily result in unwanted intermolecular disulfides³⁷. While the introduced Leu residue is not comparable to native palmitoylation, it does manifest as a bulky hydrophobic residue, whilst keeping the protein in a soluble state.

His-MaBP-P0ct was expressed in *Escherichia coli* BL21(DE3) using 0.4 mM IPTG induction for 3 hours in LB medium, at 37 °C. After expression, the cells were collected using centrifugation, broken by ultrasonication in Ni-NTA washing buffer (40 mM HEPES, 400 mM NaCl, 20 mM imidazole, pH 7.5) supplemented with an EDTA-free protease inhibitor cocktail (Roche). Purification was performed using Ni-NTA affinity chromatography using standard procedures. Elution was performed using 32 mM HEPES, 320 mM NaCl, 500 mM imidazole, pH 7.5. The eluted protein was pre-dialyzed at 4 °C with constant stirring against 40 mM Tris-HCl, 400 mM NaCl, 1 mM DTT, pH 8.5, before addition of recombinant TEV protease for His-MaBP tag removal⁵⁰. Quantitative proteolysis was achieved by overnight dialysis, which resulted in cleaved P0ct with an additional N-terminal Gly residue. After this, sequential SEC using a HiLoad Superdex 75 pg 16/60 column (GE Healthcare) was used to separate the cleaved protein from any contaminants, TEV protease, and the cleaved tag, resulting in pure, monodisperse P0ct. Depending on downstream application, either 20 mM HEPES, 300 mM NaCl, 1% (w/v) glycerol, pH 7.5 (SEC buffer) or 20 mM HEPES, 150 mM NaCl, pH 7.5 (HBS) was used as size-exclusion buffer.

Full length P0 was obtained from the raft fraction of bovine nerves as described⁴⁰. The SDS extract was lyophilized until use. The protein was redissolved in water to regain the original buffer conditions and reconstituted into lipid membranes or other detergents through extensive dialysis. For EM imaging, control samples were taken from redissolved, non-reconstituted samples to control for the presence of putative membranes and multilayers from the original tissue source.

Mass spectrometry. The identity and accurate molecular weight of P0ct were verified by mass spectrometry. In short, the undigested mass of P0ct was determined using ultra-performance liquid chromatography (UPLC) coupled electrospray ionization (ESI) time-of-flight mass spectrometry in positive ion mode using a Waters Acquity UPLC-coupled Synapt G2 mass analyzer with a Z-Spray ESI source. The identity of P0ct was determined using peptide fingerprinting as described earlier for MBP¹⁶.

Multi-angle light scattering. SEC-MALS was used to determine the monodispersity and molecular weight of P0ct in solution. Chromatography was performed using an Äkta Purifier (GE Healthcare) and a Superdex 75 pg 10/300GL (GE Healthcare) column with 20 mM HEPES, 300 mM NaCl, pH 7.5 as mobile phase. A 250- μ g P0ct sample was injected into the column at an isocratic flow of 0.4 ml/min, and light scattering recorded using a Wyatt miniDAWN TREOS instrument. The UV signal recorded at 280 nm was used as concentration source using the extinction coefficient of P0ct (Abs 0.1% = 1.061) calculated using ProtParam⁵¹. Data were analyzed using the ASTRA software (Wyatt).

Full length P0 was similarly run on SEC-MALS in the presence of different detergent micelles. The running buffer contained 250 mM sodium phosphate (pH 8.0), 1 mM EDTA, and 0.1% of either DPC or LDAO. A Superdex 200 column was used in the experiment. The protein conjugate analysis routine in the ASTRA software was used to obtain the molecular weight of P0 and the detergent in the separated peaks.

Small-angle X-ray scattering. SAXS data for P0ct were collected from samples at 1.1–4.2 mg ml⁻¹ in SEC buffer on the EMBL P12 beamline, DESY (Hamburg, Germany). Monomeric bovine serum albumin was used as a molecular weight standard. See Supplementary Table 1 for further details. Data were processed and analyzed using the ATSAS package⁵². GNOM was used to calculate distance distribution functions⁵³, and *ab initio* modeling was performed using GASBOR⁵⁴. Ensemble optimization analysis was performed using EOM⁵⁵.

Vesicle preparation. Cholesterol, DMPC, DMPG, DMPS, DOPC, DOPG and SM were purchased from Larodan Fine Chemicals AB (Malmö, Sweden). DMPE, DOPS and the deuterated d₅₄-DMPC and d₅₄-DMPG were purchased from Avanti Polar Lipids (Alabaster, Alabama, USA).

Lipid stocks were prepared by dissolving the dry lipids in chloroform or chloroform:methanol (1:1 v/v) at 10 mg ml⁻¹. All mixtures were prepared from the stocks at desired molar or mass ratios, followed by solvent evaporation under an N₂ stream and freeze-drying for at least 4 h at -52 °C under vacuum. The dried lipids were either stored air-tight at -20 °C or used directly to prepare liposomes.

Liposomes were prepared by agitating dried lipids with either water or HBS at a concentration of 2–10 mg ml⁻¹, followed by inverting at ambient temperature, to ensure that no unsuspended lipids remained in the vessel. MLVs were subjected to freeze-thawing using liquid N₂ and a warm water bath, with vigorous vortexing afterwards. Such a cycle was performed 7 times. LUVs were prepared by passing fresh MLVs through a 0.1- μ m membrane 11 times on a 40 °C heat block. SUVs were prepared by sonicating fresh MLVs. Either probe tip sonicators (a Branson Model 450 and a Sonics & Materials Inc. Vibra-Cell VC-130) or a water bath sonicator with temperature control (UTR200, Hielscher, Germany) were used to clarify the liposome suspensions, while avoiding overheating. All lipid preparations were immediately used for the designated experiments.

Synchrotron radiation circular dichroism spectroscopy. The synthetic P0ct_{pept} peptide (NH₂-ASKRGRQTPVLYAML DHSRS-COOH) was ordered from GenScript as 5 mg lyophilized aliquots, which were dissolved directly in water. Folding predictions of P0ct_{pept} were generated using PEP-FOLD⁵⁶.

Full-length P0 was studied with SDS, LDAO, and DOPC:DOPS. For preparing P0 in detergents, the sample from purification was dialyzed against 10 mM sodium phosphate buffer (pH 8.0) containing either 0.1% SDS or 0.1% LDAO. For reconstitution into lipids, DOPC:DOPS (1:1) were added to 1 mg/ml, and dialysis was carried out against 10 mM sodium phosphate buffer (pH 8.0).

Isotropic SRCD data were collected from 0.2–0.5 mg ml⁻¹ protein and peptide samples in water on the UV-CD12 beamline at KARA (KIT, Karlsruhe, Germany)³⁹ and the AU-CD beamline at ASTRID2 (ISA, Aarhus, Denmark). We used unbuffered conditions to exclude any unwanted effects, like the electrostatic binding of inorganic phosphate to P0ct, which could interfere with protein binding to detergents and phospholipids. Samples containing lipids were prepared right before measurement by mixing P0ct (P/L ratio 1:200) or P0ct_{pept} (P/L ratio 1:25) with freshly sonicated SUVs, followed by degassing in a water bath sonicator at ambient temperature for 5–10 min. 100- μ m pathlength closed cylindrical cells (Suprasil, Hellma Analytics) were used for the measurements. Spectra were recorded from 170 to 280 nm at 30 °C and truncated based on detector voltage levels as well as noise. After baseline subtraction, CD units were converted to $\Delta\epsilon$ (M⁻¹ cm⁻¹), using P0 and P0ct concentration determined from absorbance at 280 nm, or by calculating from the stock concentration of the peptide. SDS and TFE were purchased from Sigma-Aldrich and the detergents LDAO, OG, DM, and DPC from Affymetrix. P0ct and P0ct_{pept} were measured several times in the absence of additives, as well as with DOPC:DOPS (1:1) and DMPC:DMPG (1:1) and the observed spectra were deemed reproducible – the observed trends were always the same and the spectral maxima and minima were accurately present at their typically observed wavelengths.

OCD spectra were measured at the UV-CD12 beamline at KARA (KIT, Karlsruhe, Germany)³⁹. 10 μ g of P0ct was mixed with 200 μ g DMPC or DMPC:DMPG (1:1) SUVs to yield 1:50 P/L samples in water, which were carefully dispensed on quartz glass plates (Suprasil QS, Hellma Optik GmbH, Jena, Germany) within a circular (\varnothing 1.2 cm) area and allowed to dry at ambient temperature. A background sample without peptide was also prepared. The samples were assembled into humidifier chambers containing a saturated K₂SO₄ solution, and allowed to swell for 16 hours at 30 °C and over 97% relative humidity. After the swelling-induced formation of oriented lipid bilayers, the sample chambers were mounted on the beamline (swelled sample perpendicular to the incident beam) and allowed to equilibrate to the original 30 °C temperature and >97% relative humidity. Single-scan spectra were recorded from 170 to 280 nm in 0.5 nm steps at sample rotation angles 0, 45, 90, 135, 180, 225, 270, 315°. The eight spectra were averaged and the lipid background spectrum was subtracted from the sample spectrum.

Differential scanning calorimetry. P0ct was mixed with MLVs in HBS at several protein-to-lipid ratios (1:250–1:1000), always containing 160 μ M of either DMPC, DMPC:DMPG (4:1), or DMPC:DMPG (1:1), in final volumes of 700 μ l. Lipid samples without P0ct were prepared as controls. The samples were incubated at 37 °C for

10 min to ensure thorough protein association with the vesicles, and degassed for 10 min in vacuum with stirring at 10 °C before measurements.

DSC was performed using a MicroCal VP-DSC calorimeter with a cell volume of 527.4 µl. The reference cell was filled with HBS. Each sample was scanned from 10 to 50 °C and again back to 10 °C in 1 °C min⁻¹ increments. Baselines were subtracted from sample curves and zeroed between 15 and 20 °C to enable easier cross-comparison. All samples were prepared and measured twice, with the underlying trends being reproducible.

Surface plasmon resonance. SPR was performed on a Biacore T200 system (GE Healthcare). According to the manufacturer's instructions, 100-nm LUVs of 1 mM DMPC:DMPG (1:1) and 1 mM DOPC:DOPS (1:1) were immobilized on separate channels on an L1 sensor chip (GE Healthcare) in HBS, followed by the injection of P0ct. Chip regeneration was performed using a 2:3 (v:v) mixture of 2-propanol and 50 mM NaOH. The used P0ct concentrations were 20–2000 nM in HBS, and a single concentration per each lipid capture was studied; all samples were prepared and measured in duplicate. In each run, a single sample was measured twice to rule out instrumental deviation. The binding response as a function of protein concentration was plotted and fitted to the 4-parameter model,

$$R = R_{hi} - \frac{R_{hi} - R_{lo}}{1 + \left(\frac{[P0ct]}{A_1}\right)^{A_2}},$$

to gain information about association affinity. For kinetic analyses, all association phases (180 s after injection of P0ct) were individually fitted to a one-phase exponential association model using GraphPad Prism 7. The determined k_{obs} values were plotted against P0ct concentration and fitted using linear regression to determine k_{on} (slope of the curve) and k_{off} (Y-intercept of the curve). The values were extracted from two individually fitted data-sets: one containing all data (Fitting set 1) as well as one omitting all data points below 350 nM P0ct (Fitting set 2).

Vesicle turbidimetry and X-ray diffraction. For turbidimetric measurements, SUVs of 0.5 mM DOPC:DOPG (1:1) and DMPC:DMPG (1:1), both with and without supplemented 10% (w/w) cholesterol, were mixed with 0.5–10 µM P0ct in duplicate. Light scattering was recorded at 450 nm for 10 min at 25 °C using a Tecan M1000Pro plate reader. The results were analyzed after the observed optical density per time had stabilized.

SAXD experiments were performed to investigate any repetitive structures in turbid samples. 10 and 20 µM P0ct was mixed with SUVs of 1–3 mM DMPC:DMPG (1:1) in HBS at ambient temperature and exposed at 25 °C on the EMBL P12 BioSAXS beamline, DESY (Hamburg, Germany). A HBS buffer reference was subtracted from the data. Lipid samples without added P0ct were devoid of Bragg peaks. The peak positions of momentum transfer, s , in P0ct-lipid samples were used to calculate mean real-space repeat distances, d , in proteolipid structures, using the equation

$$d = \frac{2\pi}{s}, \text{ where } s = \frac{4\pi \sin \theta}{\lambda}.$$

Atomic force microscopy. Fresh DOPC:DOPS (1:1) SUVs were unrolled on freshly cleaved mica (Ø 1.2 cm) in HBS-Ca (10 mM HEPES, 150 mM NaCl, 2 mM CaCl₂, pH 7.5), by covering the mica entirely with 0.2 mg ml⁻¹ SUVs, followed by a 20-min incubation at 30 °C, and washing twice with HBS-Ca.

The samples were imaged immediately in HBS at ambient temperature using an Asylum Research MFP-3D Bio instrument. TR800PSA cantilevers (Olympus; spring constant (k) range 0.59–0.68 N m⁻¹, resonance frequency 77 kHz) were used in alternative current (AC) mode. Square 256 × 256 pixel scans were acquired from areas between 5–20 µm, using a 90° scanning angle and a 0.6–0.8 Hz scan speed. The resulting scan images were processed in Igor Pro 6.37.

After confirming the presence of lipid bilayers, 1.8–10 µM P0ct was added onto the bilayer samples in HBS. After a 15-min incubation period at ambient temperature, the bilayers were washed twice with HBS, and imaged as above. For each protein concentration, 2 samples were prepared and scanned with identical results. At least 3 different parts per sample were scanned to gain an insight into any sample heterogeneity.

Electron microscopy. For negative stain EM, 740 µM DMPC:DMPG (1:1) SUVs were mixed with P0ct using protein-to-lipid ratios of 1:25, 1:50, 1:100, 1:200 and 1:500 and incubated at 22 °C for 1 h. EM grids with P0ct or full-length P0 samples were then prepared, stained, and imaged as described^{7,16}.

For cryo-EM, full-length P0 (0.9 mg/ml) was reconstituted into lipid membranes, after dissolving the lyophilized protein extract in 10 mM sodium phosphate (pH 8.0), 0.4% DM. P0 was mixed with *E. coli* polar lipids or DOPC (both at 5 mg/ml in 2% DM) at lipid-to-protein ratio of 0.5 (w/w) and dialyzed against 10 mM sodium phosphate (pH 8.0) for 5 days at 37 °C. The total ternary mixture volume was 65 µl.

Approximately 3 µl of the P0 reconstituted into *E. coli* polar lipids (~0.65 mg ml⁻¹) were applied onto glow-discharged Quantifoil holey carbon grids (R 1.2/1.3, R 2/2, or R3.5/1, Cu 400 mesh, Quantifoil Micro Tools GmbH, Germany). After 2-s blotting, grids were flash frozen in liquid ethane, using an FEI Vitrobot IV (Vitrobot, Maastricht Instruments) with the environmental chamber set at 90% humidity and a temperature of 20 °C. Samples were imaged with FEI Titan Krios TEM operated at 300 keV, and images were recorded using a Gatan K2-Summit direct electron detector. Images were collected manually in electron-counting mode at a nominal magnification of ×22,500 and a calibrated pixel size of 1.3 Å. Each image was dose-fractionated to 40 frames (8 s in total, 0.2-s frames, dose rate 6–7 e⁻/pixel/s). Movie frames were aligned with MotionCorr⁵⁷ and pre-processed on the fly with 2dx_automator⁵⁸. For image processing were used 20 drift-corrected cryo-EM images.

Particles were boxed and segmented using e2boxer.py in EMAN2⁵⁹. From all images more than 9000 overlapping, CTF-corrected, segments with size of 160 × 160 pixels (208 Å × 208 Å) were selected. 2D class averages of P0 between lipid bilayers were calculated with SPRING software⁶⁰.

Data Availability

The datasets generated and analyzed during the current study are available from the corresponding author on reasonable request.

References

- Nave, K. Myelination and the trophic support of long axons. *Nat. Rev. Neurosci.* **11**, 275–283 (2010).
- Hartline, D. K. What is myelin? *Neuron Glia Biol* **4**, 153–163 (2008).
- Han, H., Myllykoski, M., Ruskamo, S., Wang, C. & Kursula, P. Myelin-specific proteins: A structurally diverse group of membrane-interacting molecules. *Biofactors* **39**, 233–241 (2013).
- Berger, P., Niemann, A. & Suter, U. Schwann cells and the pathogenesis of inherited motor and sensory neuropathies (Charcot-Marie-Tooth disease). *Glia* **54**, 243–257 (2006).
- Cartoni, R. & Martinou, J. Role of mitofusin 2 mutations in the physiopathology of Charcot-Marie-Tooth disease type 2A. *Exp. Neurol.* **218**, 268–273 (2009).
- Brennan, K. M. *et al.* Absence of Dystrophin Related Protein-2 disrupts Cajal bands in a patient with Charcot-Marie-Tooth disease. *Neuromusc. Disord.* **25**, 786–793 (2015).
- Ruskamo, S. *et al.* Molecular mechanisms of Charcot-Marie-Tooth neuropathy linked to mutations in human myelin protein P2. *Sci Rep* **7**, 6510 (2017).
- Mathis, S., Magy, L. & Vallat, J. Therapeutic options in Charcot-Marie-Tooth diseases. *Expert. Rev. Neurother.* **15**, 355–366 (2015).
- Greenfield, S., Brostoff, S., Eylar, E. H. & Morell, P. Protein composition of myelin of the peripheral nervous system. *J Neurochem* **20**, 1207–1216 (1973).
- Saporta, A. S. D. *et al.* Charcot-Marie-Tooth Disease Subtypes and Genetic Testing Strategies. *Ann. Neurol.* **69**, 22–33 (2011).
- Eichberg, J. Myelin P-0: New knowledge and new roles. *Neurochem. Res.* **27**, 1331–1340 (2002).
- Shapiro, L., Doyle, J., Hensley, P., Colman, D. & Hendrickson, W. Crystal structure of the extracellular domain from P-0, the major structural protein of peripheral nerve myelin. *Neuron* **17**, 435–449 (1996).
- Liu, Z. *et al.* Crystal structure of the extracellular domain of human myelin protein zero. *Proteins* **80**, 307–313 (2012).
- Kirschner, D. A., Inouye, H., Ganser, A. L. & Mann, V. Myelin Membrane-Structure and Composition Correlated - a Phylogenetic Study. *J. Neurochem.* **53**, 1599–1609 (1989).
- Campi, G. *et al.* Intrinsic dynamical fluctuations of PNS myelin. *arXiv:1705.09730* (2017).
- Raasakka, A. *et al.* Membrane Association Landscape of Myelin Basic Protein Portrays Formation of the Myelin Major Dense Line. *Sci Rep* **7**, 4974 (2017).
- Shy, M. *et al.* Phenotypic clustering in MPZ mutations. *Brain* **127**, 371–384 (2004).
- de Seze, J. *et al.* Chronic inflammatory demyelinating polyradiculoneuropathy: A new animal model for new therapeutic targets. *Rev. Neurol.* **172**, 767–769 (2016).
- Plante-Bordeneuve, V. *et al.* The range of chronic demyelinating neuropathy of infancy: a clinico-pathological and genetic study of 15 unrelated cases. *J. Neurol.* **248**, 795–803 (2001).
- Street, V. *et al.* Charcot-Marie-Tooth neuropathy: clinical phenotypes of four novel mutations in the MPZ and Cx 32 genes. *Neuromusc. Disord.* **12**, 643–650 (2002).
- Choi, B. *et al.* Mutational analysis of PMP22, MPZ, GJB1, EGR2 and NEFL in Korean Charcot-Marie-Tooth neuropathy patients. *Hum. Mutat.* **24**, 185–186 (2004).
- Fabrizi, G. *et al.* Gene dosage sensitivity of a novel mutation in the intracellular domain of P0 associated with Charcot-Marie-Tooth disease type 1B. *Neuromusc. Disord.* **16**, 183–187 (2006).
- Ding, Y. & Brunden, K. The Cytoplasmic Domain of Myelin Glycoprotein P0 Interacts with Negatively Charged Phospholipid-Bilayers. *J. Biol. Chem.* **269**, 10764–10770 (1994).
- Luo, X. *et al.* Cytoplasmic domain of human myelin protein zero likely folded as beta-structure in compact myelin. *Biophys. J.* **92**, 1585–1597 (2007).
- Myllykoski, M., Baumgartel, P. & Kursula, P. Conformations of peptides derived from myelin-specific proteins in membrane-mimetic conditions probed by synchrotron radiation CD spectroscopy. *Amino Acids* **42**, 1467–1474 (2012).
- Suresh, S., Wang, C., Nanekar, R., Kursula, P. & Edwardson, J. M. Myelin basic protein and myelin protein 2 act synergistically to cause stacking of lipid bilayers. *Biochemistry* **49**, 3456–3463 (2010).
- García-Arribas, A. B., Alonso, A. & Goñi, F. M. Cholesterol interactions with ceramide and sphingomyelin. *Chem Phys Lipids* **199**, 26–34 (2016).
- Hasse, B., Bosse, F. & Müller, H. W. Proteins of Peripheral Myelin Are Associated With Glycosphingolipid/Cholesterol Enriched Membranes. *J Neurosci Res* **69**, 227–232 (2002).
- D'Urso, D., Ehrhardt, P. & Müller, H. W. Peripheral myelin protein 22 and protein zero: a novel association in peripheral nervous system myelin. *J Neurosci* **19**, 3396–3403 (1999).
- Hasse, B., Bosse, F., Hanenberg, H. & Müller, H. W. Peripheral myelin protein 22 kDa and protein zero: domain specific trans-interactions. *Mol Cell Neurosci* **27**, 370–378 (2004).
- Mittendorf, K. F. *et al.* Peripheral myelin protein 22 alters membrane architecture. *Sci Adv* **3**, e1700220 (2017).
- Min, Y. *et al.* Interaction forces and adhesion of supported myelin lipid bilayers modulated by myelin basic protein. *Proc. Natl. Acad. Sci. USA* **106**, 3154–3159 (2009).
- Greenfield, N. J. Using circular dichroism spectra to estimate protein secondary structure. *Nature Protocols* **1**, 2876–2890 (2006).
- Shaharabani, R. *et al.* Structural transition in myelin membrane as initiator of multiple sclerosis. *J. Am. Chem. Soc.* **138**, 12159–12165 (2016).
- Mabrey, S. & Sturtevant, J. M. Investigation of phase-transitions of lipids and lipid mixtures by high sensitivity differential scanning calorimetry. *Proc. Natl. Acad. Sci. USA* **73**, 3862–3866 (1976).
- Ruskamo, S. *et al.* Juxtanodin is an intrinsically disordered F-actin-binding protein. *Sci Rep* **2**, 899 (2012).
- Chukhlieb, M., Raasakka, A., Ruskamo, S. & Kursula, P. The N-terminal cytoplasmic domain of neuropilin 1 type III is intrinsically disordered. *Amino Acids* **47**, 1567–1577 (2015).
- Muruganandam, G., Buerck, J., Ulrich, A. S., Kursula, I. & Kursula, P. Lipid Membrane Association of Myelin Proteins and Peptide Segments Studied by Oriented and Synchrotron Radiation Circular Dichroism Spectroscopy. *J Phys Chem B* **117**, 14983–14993 (2013).
- Buerck, J. *et al.* UV-CD12: synchrotron radiation circular dichroism beamline at ANKA. *J. Synchrotron Radiat.* **22**, 844–852 (2015).
- Fasano, A. *et al.* The different forms of PNS myelin P0 protein within and outside lipid rafts. *J. Neurochem.* **107**, 291–301 (2008).
- Inouye, H., Tsuruta, H., Sedzik, J., Uyemura, K. & Kirschner, D. A. Tetrameric Assembly of Full-Sequence Protein Zero Myelin Glycoprotein by Synchrotron X-Ray Scattering. *Biophys J* **76**, 423–437 (1999).

42. Thompson, A. J., Cronin, M. S. & Kirschner, D. A. Myelin protein zero exists as dimers and tetramers in native membranes of *Xenopus laevis* peripheral nerve. *J Neurosci Res* **67**, 766–771 (2002).
43. Schmitt, F. O., Bear, R. S. & Clark, G. L. The Role of Lipoids in the X-Ray Diffraction Patterns of Nerve. *Science* **82**(2115), 44–45 (1935).
44. Schmitt, F. O., Bear, R. S. & Palmer, K. J. X-ray diffraction studies on the structure of the nerve myelin sheath. *J. Cell. Physiol.* **18**, 31–42 (1941).
45. Riccio, P., Fasano, A., Borenshtein, N., Blevé-Zacheo, T. & Kirschner, D. Multilamellar packing of myelin modeled by lipid-bound MBP. *J. Neurosci. Res.* **59**, 513–521 (2000).
46. Raine, C. S. In *Myelin* (ed. Morell, P.) 1–50 (Springer, Boston, MA, 1984).
47. Li, J., Parker, B., Martyn, C., Natarajan, C. & Guo, J. The PMP22 Gene and Its Related Diseases. *Mol. Neurobiol.* **47**, 673–698 (2013).
48. Jarsch, I. K. & Daste, F. & Gallop, J. L. Membrane curvature in cell biology: An integration of molecular mechanisms. *J. Cell Biol.* **214**, 375–387 (2016).
49. Hammarström, M., Woestenenk, E., Hellgren, N., Härd, T. & Berglund, H. Effect of N-terminal solubility enhancing fusion proteins on yield of purified target protein. *J. Struct. Funct. Genomics* **7**, 1–14 (2006).
50. van den Berg, S., Löfdahl, P., Härd, T. & Berglund, H. Improved solubility of TEV protease by directed evolution. *J Biotechnol* **121**, 291–298 (2006).
51. Gasteiger, E. et al. In *The Proteomics Protocols Handbook* (ed. Walker, J.) 571–607 (Humana Press, New Jersey, USA, 2005).
52. Konarev, P., Petoukhov, M., Volkov, V. & Svergun, D. ATASAS 2.1, a program package for small-angle scattering data analysis. *J. Appl. Crystallogr.* **39**, 277–286 (2006).
53. Svergun, D. I. Determination of the regularization parameter in indirect-transform methods using perceptual criteria. *J. Appl. Crystallogr.* **25**, 495–503 (1992).
54. Svergun, D., Petoukhov, M. & Koch, M. Determination of domain structure of proteins from X-ray solution scattering. *Biophys. J.* **80**, 2946–2953 (2001).
55. Tria, G., Mertens, H. D. T., Kachala, M. & Svergun, D. I. Advanced ensemble modelling of flexible macromolecules using X-ray solution scattering. *Iucrj* **2**, 207–217 (2015).
56. Shen, Y., Maupetit, J., Derreumaux, P. & Tuffery, P. Improved PEP-FOLD Approach for Peptide and Miniprotein Structure Prediction. *J. Chem. Theory Comput.* **10**, 4745–4758 (2014).
57. Li, X. et al. Electron counting and beam-induced motion correction enable near-atomic-resolution single-particle cryo-EM. *Nat. Methods* **10**, 584–590 (2013).
58. Scherer, S. et al. 2dx_automator: Implementation of a semiautomatic high-throughput high-resolution cryo-electron crystallography pipeline. *J. Struct. Biol.* **186**, 302–307 (2014).
59. Tang, G. et al. EMAN2: An extensible image processing suite for electron microscopy. *J. Struct. Biol.* **157**, 38–46 (2007).
60. Desfosses, A., Ciuffa, R., Gutsche, I. & Sachse, C. SPRING - An image processing package for single-particle based helical reconstruction from electron cryomicrographs. *J. Struct. Biol.* **185**, 15–26 (2014).

Acknowledgements

This work was financially supported by the Academy of Finland (Finland), the Sigrid Jusélius Foundation (Finland), the Emil Aaltonen Foundation (Finland), the University of Oulu Graduate School (Finland), the Norwegian Research Council (SYNKNØYT program), and Western Norway Regional Health Authority (Norway). We thank Dr. Marte Innsset Flydal for practical guidance in using DSC. We gratefully acknowledge the synchrotron radiation facilities and the beamline support at ASTRID2, and EMBL/DESY. We acknowledge the KIT light source for provision of instruments at the beamline UV-CD12 of the Institute of Biological Interfaces (IBG2), and we would like to thank the Institute for Beam Physics and Technology (IBPT) for the operation of the storage ring, the Karlsruhe Research Accelerator (KARA). We also express our gratitude towards the Biocenter Oulu Proteomics and Protein Analysis Core Facility for providing access to mass spectrometric instrumentation and the BISS facility (Department of Biomedicine, University of Bergen) for the availability of biophysical instrumentation.

Author Contributions


Study design: A.R., S.R., J.K., H.H., P.R., H.S., P.K. Prepared samples and performed experiments: A.R., S.R., J.K., H.H., A.B., M.M., A.F., R.R., J.B. Processed and analyzed data: A.R., J.K., S.R., H.H., A.B., P.K. Original text and figures: A.R., P.K. Review & editing: A.R., S.R., P.R., J.B., A.S.U., H.S., P.K. Supervision: P.R., A.S.U., H.S., P.K.

Additional Information

Supplementary information accompanies this paper at <https://doi.org/10.1038/s41598-018-37009-4>.

Competing Interests: The authors declare no competing interests.

Publisher's note: Springer Nature remains neutral with regard to jurisdictional claims in published maps and institutional affiliations.

 **Open Access** This article is licensed under a Creative Commons Attribution 4.0 International License, which permits use, sharing, adaptation, distribution and reproduction in any medium or format, as long as you give appropriate credit to the original author(s) and the source, provide a link to the Creative Commons license, and indicate if changes were made. The images or other third party material in this article are included in the article's Creative Commons license, unless indicated otherwise in a credit line to the material. If material is not included in the article's Creative Commons license and your intended use is not permitted by statutory regulation or exceeds the permitted use, you will need to obtain permission directly from the copyright holder. To view a copy of this license, visit <http://creativecommons.org/licenses/by/4.0/>.

© The Author(s) 2019

Supplementary information

Molecular structure and function of myelin protein P0 in membrane stacking

Arne Raasakka^{1,2}, Salla Ruskamo², Julia Kowal^{3,4}, Huijong Han², Anne Baumann^{1,5}, Matti Myllykoski², Anna Fasano⁶, Rocco Rossano⁷, Paolo Riccio⁷, Jochen Bürck⁸, Anne S. Ulrich^{8,9}
Henning Stahlberg³ & Petri Kursula^{1,2,†}

¹Department of Biomedicine, University of Bergen, Bergen, Norway

²Faculty of Biochemistry and Molecular Medicine & Biocenter Oulu, University of Oulu, Oulu, Finland

³Center for Cellular Imaging and NanoAnalytics (C-CINA), Biozentrum, University of Basel, Basel, Switzerland

⁴Institute of Molecular Biology and Biophysics, Department of Biology, ETH Zurich, Switzerland

⁵Division of Psychiatry, Haukeland University Hospital, Bergen, Norway

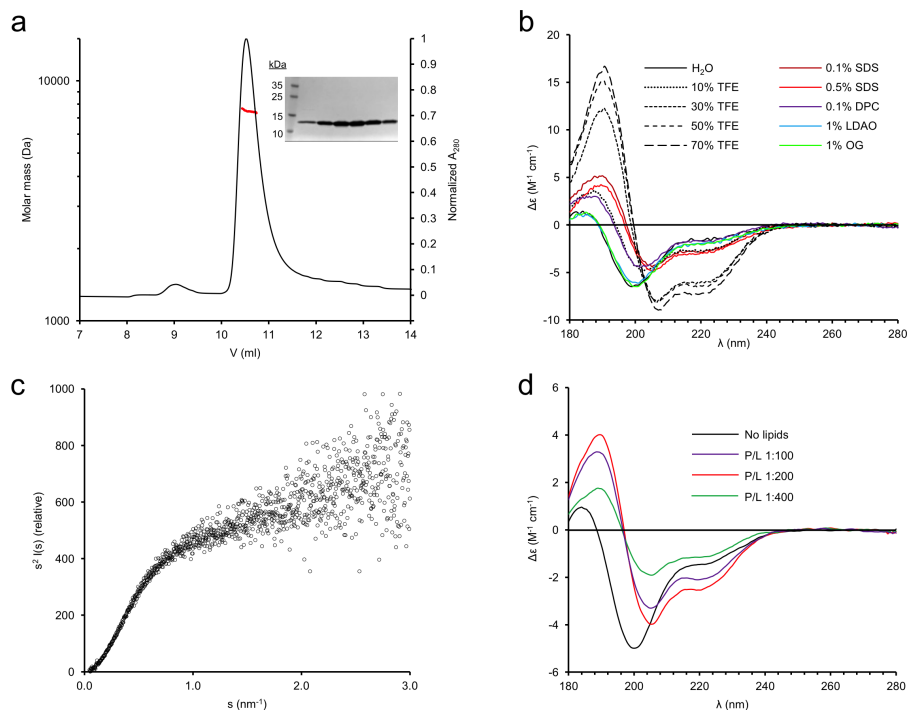
⁶Department of Biosciences, Biotechnologies and Biopharmaceutics, University of Bari, Bari, Italy

⁷Department of Sciences, University of Basilicata, Potenza, Italy

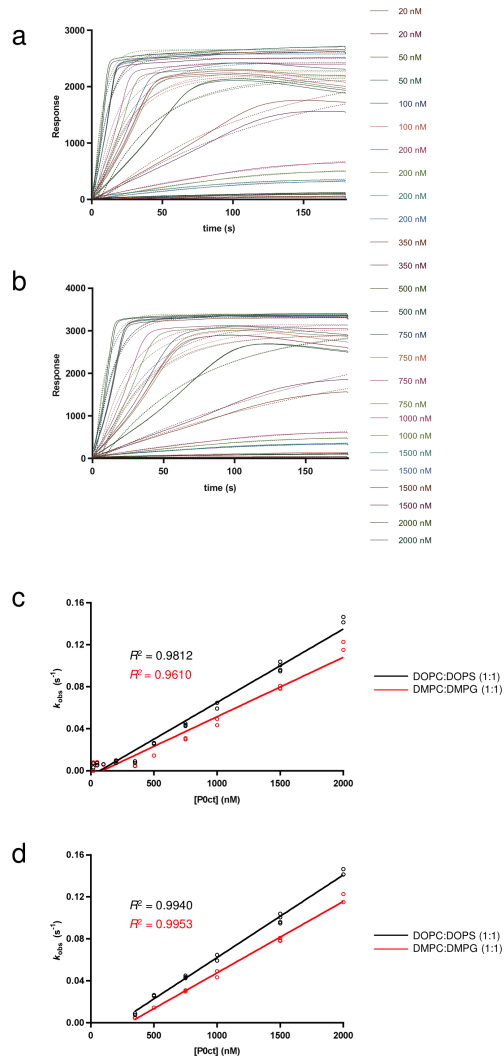
⁸Institute of Biological Interfaces (IBG-2), Karlsruhe Institute of Technology, Karlsruhe, Germany

⁹Institute of Organic Chemistry, Karlsruhe Institute of Technology, Karlsruhe, Germany

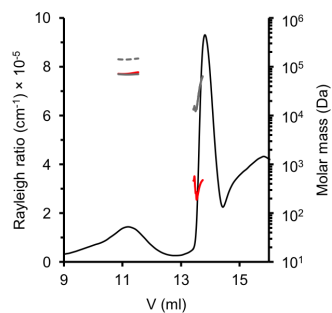
[†]Corresponding author. E-mail: petri.kursula@uib.no



Supplementary Fig. S1. The purity, monodispersity, and folding of P0ct. (a) SEC-MALS profile of P0ct displays a mostly monodisperse preparation, with a single major peak corresponding to P0ct when eluting from a Superdex 75 10/300GL column. The calculated mass (7.5 kDa) matches that of a P0ct monomer. SDS-PAGE analysis of the purity of P0ct fractionated with a Superdex 75 16/60 HiLoad SEC column is shown as inset. (b) P0ct gains significant secondary structure content in TFE, DPC and SDS, but not in LDAO or OG, as shown using CD spectroscopy. (c) The Kratky plot displays the highly elongated nature of P0ct. (d) The SRCD spectra of P0ct in DMPC:DMPG (1:1) display different degrees of folding at different P/L ratios, 1:200 producing the strongest signal.



Supplementary Fig. S2. Kinetic analysis of SPR association data. The data (solid lines) of irreversible P0ct association with DOPC:DOPS (1:1) and DMPC:DMPG (1:1) (shown as panels a and b, respectively) vesicles fitted individually to an exponential one-phase binding model (dashed lines). (c) The derived k_{obs} values plotted against P0ct concentration, with the DOPC:DOPS (1:1) and DMPC:DMPG (1:1) data fitted to linear functions (see Supplementary Table 2 for the extracted k_{on} and k_{off} values). (d) Same data but all data points below the critical binding concentration have been omitted, resulting in a better linear fit.



Supplementary Fig. S3. SEC-MALS of P0 in LDAO. Analysis of full-length P0 monodispersity and oligomeric state using SEC-MALS in LDAO. The Rayleigh ratio is shown (black) together with the total mass (gray dash), protein mass (red) and detergent mass for each peak (gray solid).

Supplementary Table S1. SAXS parameters.

| Data collection parameters | |
|---|---------------------|
| Instrument | P12, PETRAIII, DESY |
| Wavelength (nm) | 0.124 |
| Angular range (nm ⁻¹) | 0.027 - 4.801 |
| Exposure time (s) | 0.045 |
| Concentration range (mg ml ⁻¹) | 1.1 - 4.2 |
| Temperature (°C) | 20 |
| Structural parameters | |
| I_0 (relative) [from p(r)] | 1882 |
| R_g (nm) [from p(r)] | 2.67 |
| I_0 (relative) [from Guinier] | 1892 |
| R_g (nm) [from Guinier] | 2.46 |
| R_z (nm) [from EOM ensemble] | 2.69 |
| D_{max} (nm) [from GNOM] | 11.06 |
| D_{max} (nm) [from EOM ensemble] | 8.03 |
| Molecular mass determination | |
| Molecular mass M_r (kDa) [from I_0 using p(r)] | 8.4 |
| Molecular mass M_r (kDa) [from I_0 using Guinier] | 8.4 |
| Theoretical M_r from sequence (kDa) | 7.99 |
| Software | |
| Primary data reduction | PRIMUS |
| Data processing | PRIMUS |
| <i>Ab initio</i> analysis | GASBOR |
| Conformational ensemble analysis | EOM |
| Validation and averaging | PRIMUS |
| Three-dimensional graphics representation | PyMOL |
| EOM model parameters | |
| <i>Conformer #1</i> | |
| R_z (nm) | 2.488 |
| D_{max} (nm) | 7.904 |
| Mass fraction | 0.182 |
| <i>Conformer #2</i> | |
| R_z (nm) | 2.867 |
| D_{max} (nm) | 8.264 |
| Mass fraction | 0.182 |
| <i>Conformer #3</i> | |
| R_z (nm) | 3.946 |
| D_{max} (nm) | 12.73 |
| Mass fraction | 0.182 |
| <i>Conformer #4</i> | |
| R_z (nm) | 2.068 |
| D_{max} (nm) | 6.14 |
| Mass fraction | 0.364 |
| <i>Conformer #5</i> | |
| R_z (nm) | 2.954 |
| D_{max} (nm) | 9.862 |
| Mass fraction | 0.090 |
| Total mass fraction of main conformers | 1.000 |

Supplementary Table S2. Kinetic parameters derived from P0ct association phase with vesicles.

| Vesicle composition | Fitting set 1 ^a | | | Fitting set 2 ^a | | |
|---------------------|---|---|--------|---|---|--------|
| | k_{on} ($\text{nM}^{-1} \text{s}^{-1}$) ^b $\times 10^5$ | k_{off} (s^{-1}) ^c $\times 10^2$ | R^2 | k_{on} ($\text{nM}^{-1} \text{s}^{-1}$) ^b $\times 10^5$ | k_{off} (s^{-1}) ^c $\times 10^2$ | R^2 |
| DOPC:DOPS (1:1) | 6.994 \pm 0.1978 | -0.4874 \pm 0.1827 | 0.9812 | 7.873 \pm 0.1629 | -1.655 \pm 0.1629 | 0.9940 |
| DMPC:DMPG (1:1) | 5.657 \pm 0.2326 | -0.5059 \pm 0.2148 | 0.9610 | 6.804 \pm 0.1252 | -2.042 \pm 0.1468 | 0.9953 |

^a Fitting set 1 contains all data points from the linear fit, whereas all data points below 350 nM were omitted from Fitting set 2.

^b Slope of the linear fit function to $k_{\text{obs(on)}}$ vs. [P0ct].

^c Y-axis intercept of the linear fit function to $k_{\text{obs(on)}}$ vs. [P0ct]

III

ARTICLE III

Ionic strength and calcium regulate the membrane interactions of myelin basic protein and the cytoplasmic domain of myelin protein zero.

Raasakka A., Jones N.C., Hoffmann S.V. & Kursula P.

bioRxiv 529586. DOI: 10.1101/529586. Preprint. (2019)

Abstract

The formation of a mature myelin sheath in the vertebrate nervous system requires specific protein membrane interactions. Several myelin-specific proteins are involved in the stacking of lipid membranes into multilayered structures around neuronal axons, and misregulation of these processes may contribute to chronic demyelinating diseases. Two key proteins functioning in myelin membrane binding and stacking are the myelin basic protein (MBP) and protein zero (P0). Other factors, including Ca^{2+} , are important for the regulation of myelination. Here, we studied the effects of ionic strength and Ca^{2+} on the direct molecular membrane interactions of MBP and the cytoplasmic domain of P0 (P0ct). While both MBP and P0ct bound and aggregated negatively charged lipid vesicles, while simultaneously folding, both ionic strength and calcium had systematic effects on these interactions. Especially when decreasing membrane net negative charge, the level and kinetics of vesicle aggregation, which is a functional assay for myelin membrane stacking proteins, were affected by both salt and Ca^{2+} . The results indicate that the effects on lipid membrane surfaces by ions can directly affect myelin protein-membrane interactions at the molecular level, in addition to signalling effects in myelinating glia.

1 **Ionic strength and calcium regulate the membrane interactions of myelin basic protein and**
2 **the cytoplasmic domain of myelin protein zero**

3

4 *Arne Raasakka¹, Nykola C. Jones², Søren Vrønning Hoffmann² & Petri Kursula^{1,3,†}*

5

6

7 ¹ Department of Biomedicine, University of Bergen, Bergen, Norway

8 ² ISA, Department of Physics and Astronomy, Aarhus University, Ny Munkegade 120, 8000 Aarhus C, Denmark

9 ³ Faculty of Biochemistry and Molecular Medicine, University of Oulu, Oulu, Finland

10

11 [†] Corresponding author. E-mail: petri.kursula@uib.no

12

1 **Abstract**

2 The formation of a mature myelin sheath in the vertebrate nervous system requires specific protein-
3 membrane interactions. Several myelin-specific proteins are involved in the stacking of lipid membranes into
4 multilayered structures around neuronal axons, and misregulation of these processes may contribute to
5 chronic demyelinating diseases. Two key proteins functioning in myelin membrane binding and stacking are
6 the myelin basic protein (MBP) and protein zero (P0). Other factors, including Ca^{2+} , are important for the
7 regulation of myelination. Here, we studied the effects of ionic strength and Ca^{2+} on the direct molecular
8 membrane interactions of MBP and the cytoplasmic domain of P0 (P0ct). While both MBP and P0ct bound
9 and aggregated negatively charged lipid vesicles, while simultaneously folding, both ionic strength and
10 calcium had systematic effects on these interactions. Especially when decreasing membrane net negative
11 charge, the level and kinetics of vesicle aggregation, which is a functional assay for myelin membrane-
12 stacking proteins, were affected by both salt and Ca^{2+} . The results indicate that the effects on lipid membrane
13 surfaces by ions can directly affect myelin protein-membrane interactions at the molecular level, in addition
14 to signalling effects in myelinating glia.

15

16 **Keywords**

17 Myelin basic protein; myelin protein zero; intrinsically disordered protein; protein folding; lipid binding;
18 calcium; ionic strength

19

20

1 Introduction

2 Myelin contributes greatly to the efficiency of both the central and peripheral nervous system (CNS and PNS
3 respectively) *via* axonal insulation and trophic support (1,2). Comprised of tightly stacked lipid membranes,
4 held together by a specific assortment of proteins, compact myelin (CM) – a water-deficient structure –
5 insulates selected axonal segments and enables fast saltatory nerve impulse conduction. While neuronal
6 axons undergo frequent membrane depolarization, and $[K^+]$ and $[Na^+]$ vary upon action potential firing, the
7 ionic conditions in myelinating glia remain fairly constant, with higher $[K^+]$ and $[Na^+]$ compared to neurons
8 in general (3).

9 In myelinating cells, $[Ca^{2+}]$ and $[Zn^{2+}]$ (1 mM and 50 μ M, respectively) are relatively high compared to
10 many other cell types (3,4). This signifies the importance of the underlying Ca^{2+} signalling (5–7); due to the
11 narrow bilayer spacing and low water content in CM, intracellular divalent cations must be subjects of
12 attractive and repulsive interactions. These involve negatively charged and zwitterionic phospholipid
13 headgroups, as well as myelin proteins, which are often highly positively charged and directly participate in
14 interactions with other proteins and lipids. Both Ca^{2+} and Zn^{2+} have been studied with respect to
15 autoimmune diseases and pathogenesis (5,8–10), and intracellular Ca^{2+} levels and changes therein have
16 been directly linked to the correct development of myelin (11–14).

17 Myelin basic protein (MBP) plays a fundamental role in forming and maintaining stable myelin membrane
18 stacks, defining the boundaries between CM and non-compact myelin (15–18). MBP is involved in multiple
19 sclerosis (MS) (19–21), being an intrinsically disordered protein (IDP) that folds upon lipid binding-induced
20 charge neutralization (16,22,23). MBP is highly positively charged and manifests as a pool of post-
21 translationally citrullinated variants with differing net charges (24). MBP requires negatively charged lipids
22 for membrane adhesion, but correct myelin morphology is also dependent on the presence of other lipids and
23 a controlled ionic content (14,16,25). MBP interacts with divalent cations (26–30), with the underlying
24 mechanisms being very specific; one would expect electrostatic repulsion due to its unusually high positive
25 net charge. MBP binds to calmodulin in a Ca^{2+} -dependent manner (27,31–33), and the pool of different MBP
26 isoforms has been shown to regulate oligodendroglial Ca^{2+} influx (34,35). Concentration-dependent binding
27 of divalent cations to different MBP variants could, together with altered membrane compositions, influence
28 their *in vivo* functions, having implications in MS etiology and the stability of CM (6,14,27,36).

29 Myelin protein zero (P0) is a transmembrane protein in PNS myelin, with relevance in human peripheral
30 neuropathies and animal models (37–39). It consists of an extracellular domain with an immunoglobulin-like
31 fold (40), a single transmembrane helix, and a short cytoplasmic segment (P0ct) involved in the regulation of
32 membrane fluidity (41). Similarly to MBP, P0ct is highly positively charged and directly interacts with
33 phospholipids through electrostatics, gaining secondary structure in the process (41,42), which might make it
34 susceptible to effects caused by cationic species.

1 In this study, the effects of ionic strength and Ca^{2+} on the structural and functional properties of recombinant
2 MBP and P0ct binding to lipid membranes were studied using different biophysical techniques. The results
3 shed new light on the interplay between ions and proteins in CM and support the proposed role of Ca^{2+} as a
4 regulator of the bilayer-MBP interaction (14,36,43).

5

6

1 **Experimental procedures**

2 Protein expression and purification

3 Mouse MBP and human P0ct were expressed and purified as described (16,41). The final size-exclusion
4 chromatography after affinity purification and tag removal was performed using Superdex75 16/60 HiLoad
5 and Superdex75 increase 10/300GL columns (GE Healthcare) with 20 mM HEPES, 150 mM NaCl, pH 7.5
6 (HBS) as mobile phase. When required, the buffer was exchanged to water by sequential dialysis. The
7 purified proteins were either used fresh or snap-frozen in liquid N₂ and stored at -80 °C for later use.

8 Vesicle preparation

9 1,2-dimyristoyl-*sn*-glycero-3-phosphocholine (DMPC), 1,2-dimyristoyl-*sn*-glycero-3-phospho-(1'-rac-
10 glycerol) (Na-salt) (DMPG), and the deuterated d₅₄-DMPC, d₅₄-DMPG, and d₇-cholesterol were from Avanti
11 Polar Lipids (Alabaster, Alabama, USA). The detergent *n*-dodecylphosphocholine (DPC) was from
12 Affymetrix.

13 Lipid stocks were prepared by dissolving the dry lipids in chloroform or chloroform:methanol (9:1 v/v) at 10
14 – 30 mM. All mixtures were prepared from the stocks at desired molar ratios, followed by solvent
15 evaporation under an N₂ stream and freeze-drying overnight at -52 °C under vacuum. The dried lipids were
16 either stored air-tight at -20 °C or used fresh for liposome preparation.

17 Liposomes were prepared by agitating dried lipids with either water or HBS at a concentration 10 – 15 mM,
18 followed by gentle mixing at ambient temperature, to ensure that no unsuspended lipids remained in the
19 vessel. MLVs were prepared by freeze-thawing using liquid N₂ and a warm water bath, with vigorous
20 vortexing afterwards. Such a cycle was performed 7 times. SUVs were prepared by sonicating fresh MLVs
21 using a probe tip sonicator (Materials Inc. Vibra-Cell VC-130) until clear, while avoiding overheating. All
22 lipid preparations were immediately used for experiments.

23 Vesicle turbidimetry

24 For turbidimetric measurements, samples containing 0.5 mM DMPC:DMPG (1:1) SUVs were prepared with
25 2.5 μM P0ct or MBP in duplicate at 150 μl final volume on a Greiner 655161 96-well plate. Optical density
26 at 450 nm was recorded immediately after thorough mixing at 25 °C using a Tecan Spark 20M plate reader.

27 Synchrotron radiation circular dichroism spectroscopy

28 SRCD data were collected from 0.1–0.4 mg ml⁻¹ protein samples in water or 0.5% SDS on the AU-CD
29 beamline at ASTRID2 (ISA, Aarhus, Denmark). Samples containing lipids were prepared immediately
30 before measurement by mixing P0ct (P/L ratio 1:200) or MBP (P/L ratio 1:300) with freshly sonicated
31 SUVs. 100-μm and 1-mm pathlength closed circular cells (Suprasil, Hellma Analytics) were used for the

1 measurements, and SRCD spectra were recorded from 170 to 280 nm at 30 °C and truncated based on
2 detector voltage levels as well as noise. Baseline spectra were subtracted from sample spectra, and CD units
3 were converted to $\Delta\epsilon$ ($M^{-1} \text{ cm}^{-1}$) using CDtoolX (44).

4 Stopped-flow SRCD

5 Rapid kinetic SRCD data were collected using an SX-20 stopped-flow instrument (Applied Photophysics)
6 mounted on the AU-AMO beamline at ASTRID2 (ISA, Aarhus, Denmark) at 30 °C. Acquisition of kinetic
7 data comprised of 6–10 shots (160- μ l total volume per shot) per sample. The two 1-ml syringes were loaded
8 as follows: syringe 1 contained 0.1 mg/ml protein and syringe 2 a lipid solution (final molar P/L ratios of
9 1:200 and 1:300 for P0ct and MBP, respectively). The contents per each shot were rapidly mixed (2 ms dead
10 time) before injection into the measurement cell (2-mm pathlength). Change in CD signal (mdeg) was
11 monitored at 195 nm for 5 s per shot. The successful overlaying shots were averaged into a single curve for
12 each sample. All sample sets were prepared and measured in duplicate. Water baselines were subtracted from
13 sample curves, and data were analyzed in GraphPad Prism 7 using single- and two-phase exponential decay
14 functions to obtain rate constants.

15

1 **Results**

2 In the current project, the folding and lipid membrane aggregation of MBP and P0ct were studied. Optical
3 density measurements were used to observe the aggregation of lipid vesicles in the presence of proteins and
4 different ionic species. The studies were expanded to different ratios of DMPC:DMPG, which affects the
5 surface net charge of the SUVs. Using SRCD spectroscopy, the folding of the two proteins was probed, and
6 time-resolved experiments provided data on membrane aggregation kinetics.

7 The effect of ionic content on myelin protein-induced vesicle turbidity

8 As a functional assay for MBP and P0ct, turbidimetric experiments on SUVs were carried out. In our earlier
9 studies, we concluded that in the presence of MBP, net negatively charged lipid vesicles aggregate and
10 subsequently form myelin-like bilayer stacks, resulting in sample turbidity (16). P0ct, on the other hand, can
11 cause SUVs to undergo fusion events to produce large aggregated lipid bodies (41), which may cause
12 additional sample turbidity.

13 The turbidity induced by the proteins for 1:1, 4:1, and 9:1 DMPC:DMPG SUVs, at a 1:200 protein-to-lipid
14 (P/L) ratio, was determined. The experiments were carried out at various concentrations of NaCl, NaF, and
15 CaCl₂. Since ionic species, especially multivalent cations, are known to induce lipid aggregation in the
16 absence of proteins (45), control samples without proteins were included (Fig. 1). Protein-free sample
17 turbidity was observed mostly in the presence of CaCl₂, with more CaCl₂ needed for induction, when the net
18 charge of the lipids became more negative. The effect of monovalent ions as inducers of turbidity *per se* in
19 protein-free samples was low.

20 NaCl and NaF boosted the measured turbidity levels in all lipid mixtures at least to some extent. The
21 turbidity induced by MBP was higher than that of P0ct, with the exception of DMPC:DMPG (9:1), in which
22 P0ct was surprisingly more efficient than MBP. In the presence of either protein, the induced turbidity
23 systematically increased with salt concentration DMPC:DMPG (1:1) (Fig. 1A). In DMPC:DMPG (4:1) and
24 (9:1) the turbidity decreased above a certain ionic strength (Fig. 1B,C), indicating that the balance between
25 ionic strength and the net charge of the lipids plays a role in protein-induced membrane aggregation. The
26 turbidification of DMPC:DMPG (9:1) was completely abolished at ionic concentrations of 150 mM or
27 above. In all three lipid mixtures, both proteins in the presence of NaCl and NaF produced roughly the same
28 levels of turbidity, or at least the observed concentration-dependent trends were identical. This indicates that
29 the choice of monovalent anion matters little in the level of induced turbidity.

30 In order to follow the physiological concentration regime in myelinating glia, CaCl₂ was included at much
31 lower concentration than NaCl and NaF, but the increased turbidity was still observed. CaCl₂ alone was able
32 to induce lipid turbidity in the absence of protein; the levels varied as a function of concentration. Calcium-
33 induced turbidity showed differences between the three DMPC:DMPG ratios: the turbidification of

1 DMPC:DMPG (1:1) vesicles was more resistant to increased CaCl_2 concentration than 4:1 and 9:1 mixtures
2 (Fig. 1).

3 CaCl_2 changed the turbidity induced by MBP and P0ct, depending on the membrane composition. In
4 DMPC:DMPG (1:1), turbidity was higher than in the other two lipid mixtures, being at a similar level to that
5 induced by the presence of salt (Fig. 1A). DMPC:DMPG (9:1) showed the least turbidity, and high calcium
6 concentrations brought OD to the baseline level (Fig. 1C). Interestingly, in DMPC:DMPG (4:1), the presence
7 of 0.5 mM and 1 mM CaCl_2 showed a great difference in turbidity in the absence of proteins, but when
8 proteins were included the turbidity levels were almost identical, indicating that the proteins could override
9 the aggregating effect of CaCl_2 at moderate concentrations (Fig. 1B). Increasing CaCl_2 to 1.5 mM diminished
10 the turbidity induced by MBP or P0ct in all membrane compositions. Taking all these results together, it is
11 evident that while salt can influence the interactions between proteins and lipids, and protein-decorated
12 vesicles with each other, the effect of Ca^{2+} with phospholipid headgroups is rather specific. Even small
13 changes in divalent cation levels, in the range 0.5-1.5 mM, can alter the protein-lipid interactions required for
14 vesicle aggregation and fusion, given that negatively charged lipid species do not dominate in abundance
15 over neutral/zwitterionic lipids.

16 Folding of lipid-bound MBP and P0ct

17 We observed lipid-induced increase in secondary structure content for both MBP and P0ct in our earlier
18 studies, in the absence of salt (16,41). To investigate the effect of ionic strength and divalent cations on
19 protein folding, SRCD was carried out with 150 mM NaF and 1 mM CaCl_2 . NaF was used due to the high
20 UV absorbance of Cl^- . NaF had a very similar concentration-dependent behavior to NaCl in turbidimetric
21 studies (Fig. 1).

22 NaF and CaCl_2 had no effect on MBP or P0ct overall folding in water and 0.5% SDS (Supplementary Fig.
23 S1). The SRCD spectra acquired for proteins in the presence lipids often suffer from turbidity-induced light
24 scattering, here, especially at 1:1 and 4:1 DMPC:DMPG ratios in the presence of CaCl_2 (Fig. 2A,B). Under
25 such conditions, the positions of the spectral peaks can be used to detect the presence of secondary structure.
26 The observed changes in conformation correspond well to the turbidimetry assays under the same conditions,
27 whereby the negative peak in SRCD at 200 nm is indicative of unfolded structure and possibly lack of
28 membrane binding.

29 Without additives, MBP reached a similar secondary structure content in all lipid compositions (Fig. 2). In
30 DMPC:DMPG (9:1), the presence of NaF or CaCl_2 decreased MBP helical content, potentially indicating
31 less binding to lipids (Fig. 2C). Also P0ct obtained secondary structure in lipid mixtures, and the decrease of
32 membrane negative charge (DMPG) correlated with the loss of P0ct helical structure - as seen through the
33 movement of the main spectral minimum towards 200 nm (Fig. 2). NaF had a small unfolding effect on the
34 P0ct secondary structure with all lipid mixtures.

1 The kinetics of initial vesicle nucleation

2 To visualize the underlying kinetics involved in MBP and P0ct binding to lipid vesicles, stopped flow
3 measurements were carried out using an SRCD setup. The original goal was to study the folding kinetics of
4 MBP and P0ct when encountering lipid membranes, but initial measurements and optimization attempts
5 revealed that the proteins gained their folding completely within the dead time of the instrument (~2 ms),
6 which made the underlying kinetics practically impossible to follow.

7 Despite the setback with protein folding kinetics, a strong decay in SRCD signal was observed within a 5-10
8 s measurement window (before the onset of induced photodegradation; data not shown), when proteins were
9 mixed with lipids in the presence of 150 mM NaF or 1 mM CaCl₂ (Fig. 3A). This resembled exponential
10 decay and could be described with two potentially independent rate constants (Supplementary Table 1).
11 Since we observed similar behaviour in the absence of proteins (Supplementary Fig. S2, Supplementary
12 Table 1), the effect does not stem from changes in protein folding. Considering the wavelength of the used
13 monochromatic beam (195 nm), which is in the size range of large vesicular lipid bodies, and the strength of
14 the decay (spanning tens of mdeg), the effect is caused by light scattering from initial vesicle fusion and/or
15 aggregation, especially since the lipid mixtures and ionic conditions correlate with the observed steady states
16 in turbidimetry (Fig. 1).

17 While lipids mixed with CaCl₂ alone produced quite noisy data with individual shots and replicates not
18 overlaying very well, all protein samples had excellent reproducibility both in terms of shot quality and
19 between replicates, which is evident from the small standard deviations. The data could be fitted with
20 confidence, and in most cases, two rate constants were obtained: k_1 , which describes a fast event ($> 2 \text{ s}^{-1}$),
21 and k_2 , for a slower event ($< 1 \text{ s}^{-1}$). The obtained rate constants in the presence of proteins vary between the
22 three different lipid compositions (Fig. 3B). The accuracy of k_2 is rather low, given the limited time window
23 used in the experiments.

24 In the absence of proteins, the turbidity kinetics induced by Ca²⁺ were similar in DMPC:DMPG (4:1) and
25 (9:1), and clearly slower in DMPC:DMPG (1:1) (Supplementary Fig. S2, Supplementary Table 1),
26 suggesting that electrostatic repulsion plays a role in the observed effect. Considering the fact that the two
27 less charged lipid compositions aggregate with roughly the same rate, the latter effect is more likely to occur
28 due to saturation of the surface with Ca²⁺, although more experiments are required to fully understand the
29 mechanism. It should be noted that the concentration of CaCl₂ in these experiments was 1 mM, while the
30 total concentration of negative headgroups in the lipid mixtures was either 0.25, 0.1, or 0.05 mM. It appears
31 that the membranes with less charge are fully neutralized, while the neutralization might be partial for the 1:1
32 mixture.

1 In protein-lipid samples, in the presence of NaF and CaCl₂, DMPC:DMPG (1:1) presents a higher k_1 value
2 than the other two lipid compositions. The effects of the two salts on k_1 on turbidity increase with the molar
3 percentage of DMPG (Fig. 3B, Supplementary Table 1).

4 Interestingly, in DMPC:DMPG (9:1), the aggregation effect was dominated by the 1 mM CaCl₂ over proteins
5 (Supplementary Table 1); this correlates with the steady-state turbidity under the same condition (Fig. 1C).
6 The rate constants are similar regardless of the presence of protein, indicating that the aggregation behaviour
7 under this condition is governed by the cation. On the other hand, 150 mM NaF inhibits aggregation of
8 DMPC:DMPG (9:1) vesicles (Fig. 1C, Supplementary Table 1), and in salt-free conditions, the proteins
9 display aggregation, which was not the case for the other two vesicle compositions (Fig. 3A). Taken
10 together, the kinetics measurements correlate well with the results from turbidimetry, providing further
11 insights into determinants of membrane binding and stacking.

12

13

1 **Discussion**

2 Myelination requires a delicate balance between myelin protein expression, protein-membrane interactions,
3 and additional regulatory factors, such as calcium (6,13). Both MBP and P0ct are IDPs in aqueous solution,
4 but upon binding to lipid membranes, they fold into helical structures, at the same time altering the physical
5 properties of the membrane (16,18,23,33,41). The salt sensitivity of the protein-membrane interactions
6 supports the role of electrostatic interactions in these processes, and the effects of calcium on the molecular
7 interactions are reflective of more specific mechanisms of regulation.

8 Phospholipid vesicle aggregation was followed using optical density methods as well as SRCD to see how
9 salt content and Ca^{2+} influence the activity and folding of MBP and P0ct. Our results show that while vesicle
10 turbidity increases with ionic strength, both in the steady state and in initial kinetics, the effect of salt varies
11 with membrane surface net charge. Considering the combination of ionic strength and membrane charge, it
12 seems clear that high salt concentrations effectively screen the protein-membrane interactions, while lower
13 concentrations, in fact, have an inducing effect. The results are in line with earlier data on extractability of
14 MBP from myelin and myelin swelling under different conditions (46–48).

15 The effects of calcium are likely to be more specific than the electrostatic competition caused by near-
16 physiological ionic strength *per se*. Ca^{2+} alone induces spontaneous vesicle turbidity, showing that it affects
17 the surface properties of the membrane. Calcium influences both the steady-state levels and the kinetics of
18 MBP- and P0ct-mediated vesicle aggregation. The binding of divalent cations by MBP has been observed in
19 earlier studies (26,28,29), and calcium is known to affect both MBP solubility in purified myelin as well as
20 myelin membrane spacing (48,49). It, thus, appears that calcium might be able to affect the surface of both
21 the protein and the membrane in a manner that can regulate the direct molecular interaction.

22 A new SRCD-based time-resolved technique was used to follow the kinetics of vesicle aggregation by MBP
23 and P0ct, as well as by Ca^{2+} alone. While it is at the moment unclear what the rate constants actually
24 represent, some conditions are physiologically relevant, and the observed differences in kinetics may be
25 relevant to myelin membrane stacking. Considering the k_1 values alone, P0ct is faster than MBP at inducing
26 turbidity. The difference could arise from the smaller size of P0ct, which potentially both tumbles in solution
27 faster than MBP and folds/neutralizes more easily upon membrane interaction. Due to its larger size, MBP
28 will experience more steric and repulsive effects from protein molecules already bound to the membrane.
29 The smaller P0ct may possess higher accessibility to the vesicle surface.

30 Several studies have highlighted calcium as a major regulator of proper myelination (5,6,11,12,36,50), and in
31 addition to being crucial for signalling and cellular homeostasis, it has been suggested to directly affect
32 MBP-membrane interactions (14,36,48). Phosphoinositides are important constituents of the myelin
33 membrane, involved in MBP-membrane interactions regulated by Ca^{2+} (36). Various mechanisms have been
34 proposed for the effects of calcium on myelin structure and formation; these include activation of calpains,

1 possibly degrading MBP, the involvement of calmodulin, signalling pathways, cytoskeletal events, as well as
2 effects on protein-lipid interactions (6,11–14,36).

3 It was proposed that a "sweet spot" concentration of calcium exists during myelination, which promotes
4 normal myelin formation (13). Deviations from this range might be relevant for dys/demyelination. In fact,
5 similar effects have been observed in early studies on MBP extraction from nerve tissue (43,48). Here,
6 concentrations around the physiological $[Ca^{2+}]$ were used to follow myelin protein-membrane interactions,
7 and indeed, concentration dependence around 1 mM $[Ca^{2+}]$ is evident. Together with the membrane surface
8 charge, calcium may either promote or inhibit lipid membrane stacking induced by myelin proteins. The
9 obvious next steps would involve studies on the effects of calcium on myelin protein-membrane interactions
10 in more physiological lipid compositions corresponding to the myelin cytoplasmic leaflet; the experiments
11 here using simplified lipid mixtures pave the way for these studies.

12 MBP and P0 are not related by sequence; however, as shown by us and others, the physicochemical
13 properties of MBP and the P0 cytoplasmic domain are very similar (16,18,23,33,41,42). Both bind to
14 membrane surfaces through electrostatic interactions, get embedded and fold, and affect properties of the
15 lipid bilayer. Functional similarity is also true considering the effects of ionic strength and calcium studied
16 here. In addition, other myelin proteins, such as P2 in the PNS and PLP in the CNS (51–54), have likely
17 roles in membrane stacking and will have to work in synergy with MBP and P0 during myelination. Our
18 observations point towards common regulatory mechanisms for the function of different myelin proteins in
19 membrane stacking during myelin maturation and maintenance.

20

1 **Acknowledgements**

2 This work was financially supported by the Norwegian Research Council (SYNKNØYT programme). We
3 acknowledge the ASTRID2 synchrotron facility and the Biophysics, Structural Biology, and Screening
4 (BiSS) facility at the University of Bergen. The research leading to this result has been supported by the
5 project CALIPSOplus under the Grant Agreement 730872 from the EU Framework Programme for Research
6 and Innovation HORIZON 2020.

7

8 **Author contributions**

9 Study design, original text and figures: A.R., P.K.

10 Prepared samples and performed experiments: A.R.

11 Processed and analyzed data: A.R., N.C.J., S.V.H., P.K.

12 Review & editing: A.R., N.C.J., S.V.H., P.K.

13 Supervision: P.K.

14

15 **Competing financial interests**

16 The authors declare no competing financial interests.

17

18 **Data availability**

19 The datasets generated and analyzed during the current study are available from the corresponding author on
20 reasonable request.

21

1 **Figure legends**

2 Fig. 1. Vesicle turbidimetry. MBP (red) and P0ct (blue)-induced turbidity was studied in (A) 1:1, (B) 4:1,
3 and (C) 9:1 DMPC:DMPG vesicles under different salt conditions. Each condition in the absence of protein
4 is shown for reference (gray). Error bars represent standard deviation.

5 Fig. 2. Lipid-induced protein folding in the presence of salt and divalent cations. SRCD experiments reveal
6 differences in the folding of MBP and P0ct in different lipid compositions. Trace explanations: no additive
7 (green); 150 mM NaF (blue); 1 mM CaCl₂ (red). Protein controls without additives or lipids in water (black)
8 are plotted for reference in each panel.

9 Fig. 3. Rapid kinetics of protein-induced lipid turbidity. A. The SRCD signal at 195 nm was monitored for 5
10 s using stopped-flow measurements. Proteins were mixed with lipids in the absence (green) and presence of
11 150 mM NaF (blue) and 1 mM CaCl₂ (red). Error bars represent standard deviation. Fits (dashed black) are
12 shown where data fitting was successful. B. Comparison of kinetic parameters. Evolution of the determined
13 rate constants (k_1 , solid markers; k_2 , open markers) as a function of DMPC:DMPG molar ratio in 150 mM
14 NaF (black) and 1 mM CaCl₂ (red). The values for MBP and P0ct are shown as circles and squares,
15 respectively. Error bars represent standard deviation. See Supplementary Table 1 for all rate constants.

16

17

18

1 References

- 2 1. Hartline DK. What is myelin? *Neuron Glia Biol* (2008) 4, 153-163.
- 3 2. Nave KA. Myelination and the trophic support of long axons. *Nat Rev Neurosci* (2010) 11, 275-283.
- 4 3. Stys PK, Lehning E, Saubermann AJ, LoPachin RM. Intracellular concentrations of major ions in rat myelinated
5 axons and glia: calculations based on electron probe X-ray microanalyses. *J Neurochem* (1997) 68, 1920-1928.
- 6 4. Bourre JM, Cloez I, Galliot M, Buisine A, Dumont O, Piciotti M, *et al.* Occurrence of manganese, copper and
7 zinc in myelin. Alterations in the peripheral nervous system of dysmyelinating trembler mutant are at variance
8 with brain mutants (quaking and shiverer). *Neurochem Int* (1987) 10, 281-286.
- 9 5. Blank WF, Bunge MB, Bunge RP. The sensitivity of the myelin sheath, particularly the Schwann cell-axolemmal
10 junction, to lowered calcium levels in cultured sensory ganglia. *Brain Res* (1974) 67, 503-518.
- 11 6. Friess M, Hammann J, Unichenko P, Luhmann HJ, White R, Kirischuk S. Intracellular ion signaling influences
12 myelin basic protein synthesis in oligodendrocyte precursor cells. *Cell Calcium* (2016) 60, 322-330.
- 13 7. Haak LL, Grimaldi M, Russell JT. Mitochondria in myelinating cells: calcium signaling in oligodendrocyte
14 precursor cells. *Cell Calcium* (2000) 28, 297-306.
- 15 8. Bonaventura P, Benedetti G, Albarède F, Miossec P. Zinc and its role in immunity and inflammation.
16 *Autoimmun Rev* (2015) 14, 277-285.
- 17 9. Choi BY, Jung JW, Suh SW. The Emerging Role of Zinc in the Pathogenesis of Multiple Sclerosis. *Int J Mol Sci*
18 (2017) 18,
- 19 10. Micu I, Jiang Q, Coderre E, Ridsdale A, Zhang L, Woulfe J, *et al.* NMDA receptors mediate calcium
20 accumulation in myelin during chemical ischaemia. *Nature* (2006) 439, 988-992.
- 21 11. Baraban M, Koudelka S, Lyons DA. Ca²⁺ activity signatures of myelin sheath formation and growth in vivo. *Nat*
22 *Neurosci* (2018) 21, 19-23.
- 23 12. Krasnow AM, Ford MC, Valdivia LE, Wilson SW, Attwell D. Regulation of developing myelin sheath
24 elongation by oligodendrocyte calcium transients in vivo. *Nat Neurosci* (2018) 21, 24-28.
- 25 13. Miller RH. Calcium control of myelin sheath growth. *Nat Neurosci* (2018) 21, 2-3.
- 26 14. Weil MT, Möbius W, Winkler A, Ruhwedel T, Wrzos C, Romanelli E, *et al.* Loss of Myelin Basic Protein
27 Function Triggers Myelin Breakdown in Models of Demyelinating Diseases. *Cell Rep* (2016) 16, 314-322.
- 28 15. Aggarwal S, Snaidero N, Pähler G, Frey S, Sánchez P, Zweckstetter M, *et al.* Myelin membrane assembly is
29 driven by a phase transition of myelin basic proteins into a cohesive protein meshwork. *PLoS Biol* (2013) 11,
30 e1001577.
- 31 16. Raasakka A, Ruskamo S, Kowal J, Barker R, Baumann A, Martel A, *et al.* Membrane Association Landscape of
32 Myelin Basic Protein Portrays Formation of the Myelin Major Dense Line. *Sci Rep* (2017) 7, 4974.
- 33 17. Snaidero N, Velte C, Myllykoski M, Raasakka A, Ignatev A, Werner HB, *et al.* Antagonistic Functions of MBP
34 and CNP Establish Cytosolic Channels in CNS Myelin. *Cell Rep* (2017) 18, 314-323.
- 35 18. Vassall KA, Bamm VV, Harauz G. MyelStones: the executive roles of myelin basic protein in myelin assembly
36 and destabilization in multiple sclerosis. *Biochem J* (2015) 472, 17-32.
- 37 19. Li Y, Huang Y, Lue J, Quandt JA, Martin R, Mariuzza RA. Structure of a human autoimmune TCR bound to a
38 myelin basic protein self-peptide and a multiple sclerosis-associated MHC class II molecule. *EMBO J* (2005) 24,
39 2968-2979.
- 40 20. Sospedra M, Martin R. Immunology of Multiple Sclerosis. *Semin Neurol* (2016) 36, 115-127.
- 41 21. Steinman L. Multiple sclerosis: a coordinated immunological attack against myelin in the central nervous system.
42 *Cell* (1996) 85, 299-302.
- 43 22. Mendz GL, Miller DJ, Ralston GB. Interactions of myelin basic protein with palmitoyllysophosphatidylcholine:
44 characterization of the complexes and conformations of the protein. *Eur Biophys J* (1995) 24, 39-53.
- 45 23. Polverini E, Fasano A, Zito F, Riccio P, Cavatorta P. Conformation of bovine myelin basic protein purified with
46 bound lipids. *Eur Biophys J* (1999) 28, 351-355.
- 47 24. Harauz G, Musse AA. A tale of two citrullines--structural and functional aspects of myelin basic protein
48 demination in health and disease. *Neurochem Res* (2007) 32, 137-158.
- 49 25. Widder K, Träger J, Kerth A, Harauz G, Hinderberger D. Interaction of Myelin Basic Protein with Myelin-like
50 Lipid Monolayers at Air-Water Interface. *Langmuir* (2018) 34, 6095-6108.
- 51 26. Baran C, Smith GS, Bamm VV, Harauz G, Lee JS. Divalent cations induce a compaction of intrinsically
52 disordered myelin basic protein. *Biochem Biophys Res Commun* (2010) 391, 224-229.
- 53 27. Majava V, Wang C, Myllykoski M, Kangas SM, Kang SU, Hayashi N, *et al.* Structural analysis of the complex
54 between calmodulin and full-length myelin basic protein, an intrinsically disordered molecule. *Amino Acids*
55 (2010) 39, 59-71.
- 56 28. Riccio P, Giovannelli S, Bobba A, Romito E, Fasano A, Blevè-Zacheo T, *et al.* Specificity of zinc binding to
57 myelin basic protein. *Neurochem Res* (1995) 20, 1107-1113.
- 58 29. Smith GS, Chen L, Bamm VV, Dutcher JR, Harauz G. The interaction of zinc with membrane-associated 18.5
59 kDa myelin basic protein: an attenuated total reflectance-Fourier transform infrared spectroscopic study. *Amino*

- 1 Acids (2010) 39, 739-750.
- 2 30. Tsang D, Tsang YS, Ho WK, Wong RN. Myelin basic protein is a zinc-binding protein in brain: possible role in
3 myelin compaction. *Neurochem Res* (1997) 22, 811-819.
- 4 31. Chan KF, Robb ND, Chen WH. Myelin basic protein: interaction with calmodulin and gangliosides. *J Neurosci*
5 *Res* (1990) 25, 535-544.
- 6 32. Libich DS, Hill CM, Haines JD, Harauz G. Myelin basic protein has multiple calmodulin-binding sites. *Biochem*
7 *Biophys Res Commun* (2003) 308, 313-319.
- 8 33. Wang C, Neugebauer U, Bürck J, Myllykoski M, Baumgärtel P, Popp J, *et al.* Charge isomers of myelin basic
9 protein: structure and interactions with membranes, nucleotide analogues, and calmodulin. *PLoS One* (2011) 6,
10 e19915.
- 11 34. Paez PM, Spreuer V, Handley V, Feng JM, Campagnoni C, Campagnoni AT. Increased expression of golli
12 myelin basic proteins enhances calcium influx into oligodendroglial cells. *J Neurosci* (2007) 27, 12690-12699.
- 13 35. Smith GS, Paez PM, Spreuer V, Campagnoni CW, Boggs JM, Campagnoni AT, *et al.* Classical 18.5- and 21.5-
14 kDa isoforms of myelin basic protein inhibit calcium influx into oligodendroglial cells, in contrast to golli
15 isoforms. *J Neurosci Res* (2011) 89, 467-480.
- 16 36. Nawaz S, Kippert A, Saab AS, Werner HB, Lang T, Nave KA, *et al.* Phosphatidylinositol 4,5-bisphosphate-
17 dependent interaction of myelin basic protein with the plasma membrane in oligodendroglial cells and its rapid
18 perturbation by elevated calcium. *J Neurosci* (2009) 29, 4794-4807.
- 19 37. de Sèze J, Kremer L, Alves do Rego C, Taleb O, Lam D, Beiano W, *et al.* Chronic inflammatory demyelinating
20 polyradiculoneuropathy: A new animal model for new therapeutic targets. *Rev Neurol (Paris)* (2016) 172, 767-
21 769.
- 22 38. Mandich P, Fossa P, Capponi S, Geroldi A, Acquaviva M, Gulli R, *et al.* Clinical features and molecular
23 modelling of novel MPZ mutations in demyelinating and axonal neuropathies. *Eur J Hum Genet* (2009) 17,
24 1129-1134.
- 25 39. Shy ME, Jáni A, Krajewski K, Grandis M, Lewis RA, Li J, *et al.* Phenotypic clustering in MPZ mutations. *Brain*
26 (2004) 127, 371-384.
- 27 40. Shapiro L, Doyle JP, Hensley P, Colman DR, Hendrickson WA. Crystal structure of the extracellular domain
28 from P0, the major structural protein of peripheral nerve myelin. *Neuron* (1996) 17, 435-449.
- 29 41. Raasakka A, Ruskamo S, Kowal J, Han H, Baumann A, Myllykoski M, *et al.* Molecular structure and function of
30 myelin protein P0 in membrane stacking. *Sci Rep* (2019) 9, 642.
- 31 42. Luo X, Sharma D, Inouye H, Lee D, Avila RL, Salmona M, *et al.* Cytoplasmic domain of human myelin protein
32 zero likely folded as beta-structure in compact myelin. *Biophys J* (2007) 92, 1585-1597.
- 33 43. Glynn P, Chantry A, Groome N, Czuzner ML. Basic protein dissociating from myelin membranes at physiological
34 ionic strength and pH is cleaved into three major fragments. *J Neurochem* (1987) 48, 752-759.
- 35 44. Miles AJ, Wallace BA. CDtoolX, a downloadable software package for processing and analyses of circular
36 dichroism spectroscopic data. *Protein Sci* (2018) 27, 1717-1722.
- 37 45. Ohki S, Düzgüneş N, Leonards K. Phospholipid vesicle aggregation: effect of monovalent and divalent ions.
38 *Biochemistry* (1982) 21, 2127-2133.
- 39 46. Caspar DL, Melchior V, Hollingshead CJ, Kirschner DA. Dynamics of myelin membrane contacts. *Soc Gen*
40 *Physiol Ser* (1980) 34, 195-211.
- 41 47. Hollingshead CJ, Caspar DL, Melchior V, Kirschner DA. Compaction and particle segregation in myelin
42 membrane arrays. *J Cell Biol* (1981) 89, 631-644.
- 43 48. Johnson D, Toms R, Weiner H. Studies on myelin breakdown in vitro. In: Kim SU, ed. Myelination and
44 demyelination - Implications for multiple sclerosis. Springer (1989). 219-236.
- 45 49. Padrón R, Mateu L, Kirschner DA. X-ray diffraction study of the kinetics of myelin lattice swelling. Effect of
46 divalent cations. *Biophys J* (1979) 28, 231-239.
- 47 50. Cheli VT, Santiago González DA, Namgyal Lama T, Spreuer V, Handley V, Murphy GG, *et al.* Conditional
48 Deletion of the L-Type Calcium Channel Cav1.2 in Oligodendrocyte Progenitor Cells Affects Postnatal
49 Myelination in Mice. *J Neurosci* (2016) 36, 10853-10869.
- 50 51. Palaniyar N, Semotok JL, Wood DD, Moscarello MA, Harauz G. Human proteolipid protein (PLP) mediates
51 winding and adhesion of phospholipid membranes but prevents their fusion. *Biochim Biophys Acta* (1998) 1415,
52 85-100.
- 53 52. Ruskamo S, Yadav RP, Sharma S, Lehtimäki M, Laulumaa S, Aggarwal S, *et al.* Atomic resolution view into the
54 structure-function relationships of the human myelin peripheral membrane protein P2. *Acta Crystallogr D Biol*
55 *Crystallogr* (2014) 70, 165-176.
- 56 53. Ruskamo S, Nieminen T, Kristiansen CK, Vatne GH, Baumann A, Hallin EI, *et al.* Molecular mechanisms of
57 Charcot-Marie-Tooth neuropathy linked to mutations in human myelin protein P2. *Sci Rep* (2017) 7, 6510.
- 58 54. Sinoway MP, Kitagawa K, Timsit S, Hashim GA, Colman DR. Proteolipid protein interactions in transfectants:
59 implications for myelin assembly. *J Neurosci Res* (1994) 37, 551-562.
- 60

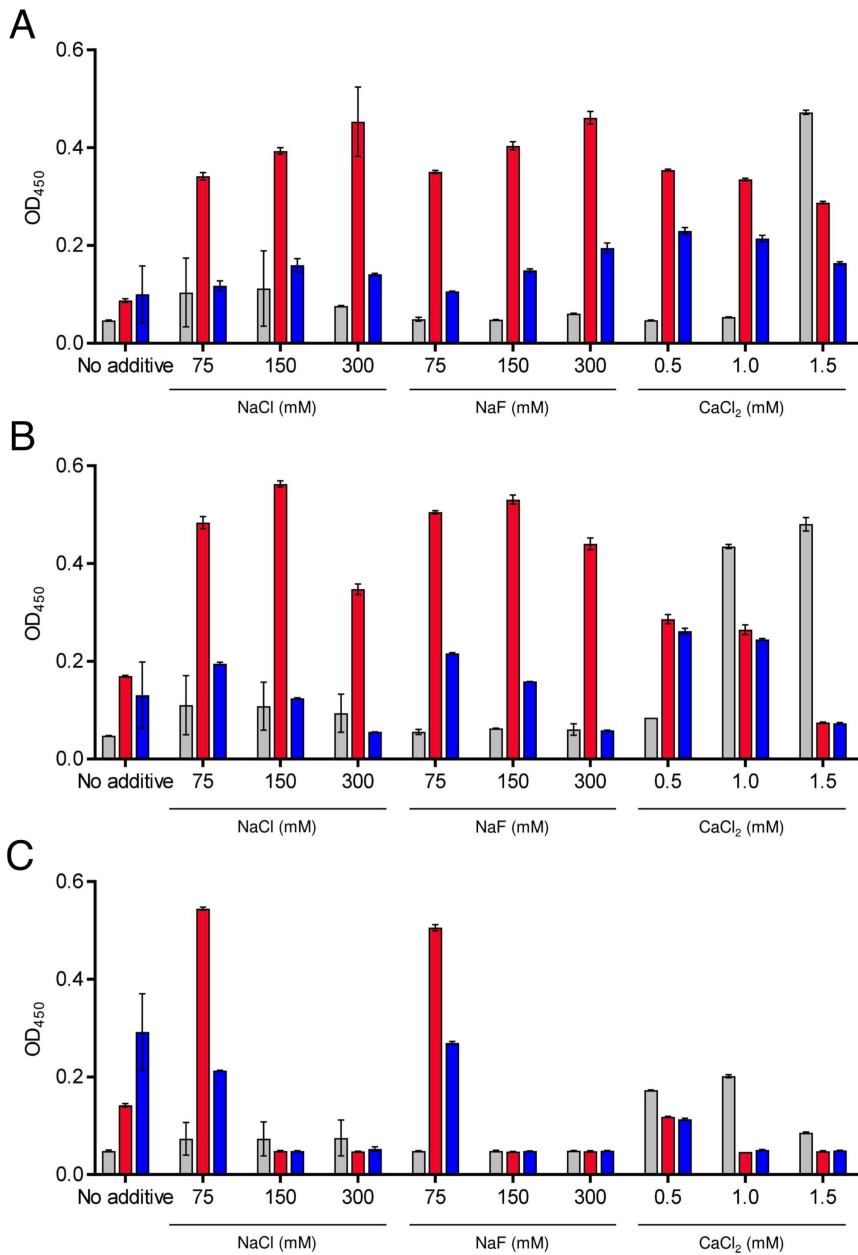


Fig.1

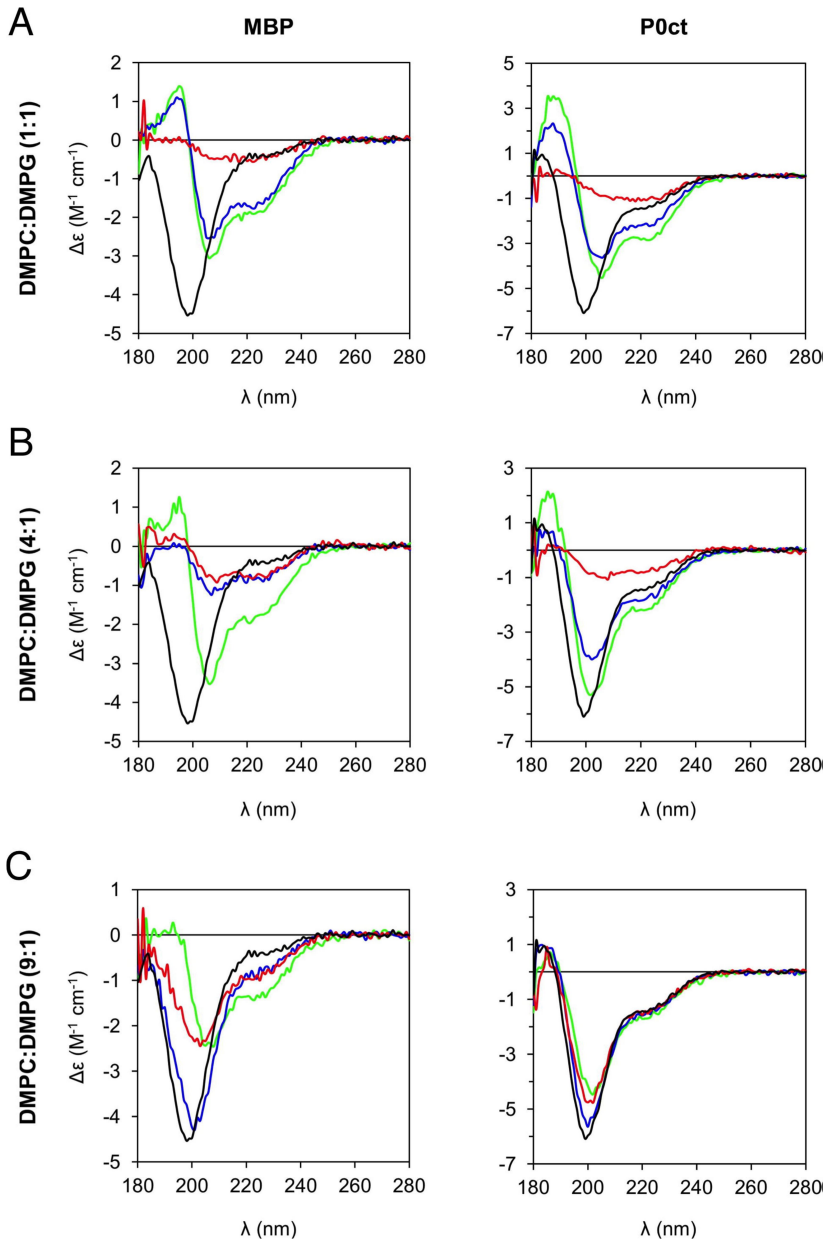


Fig. 2

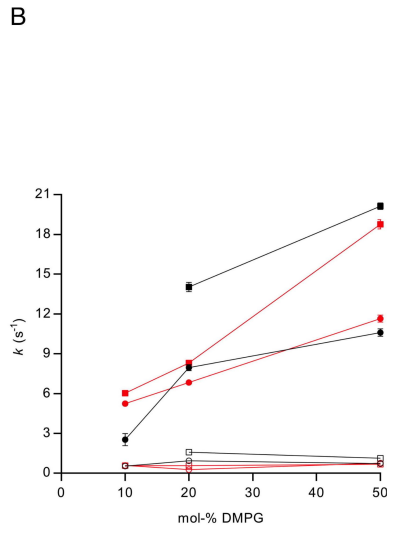
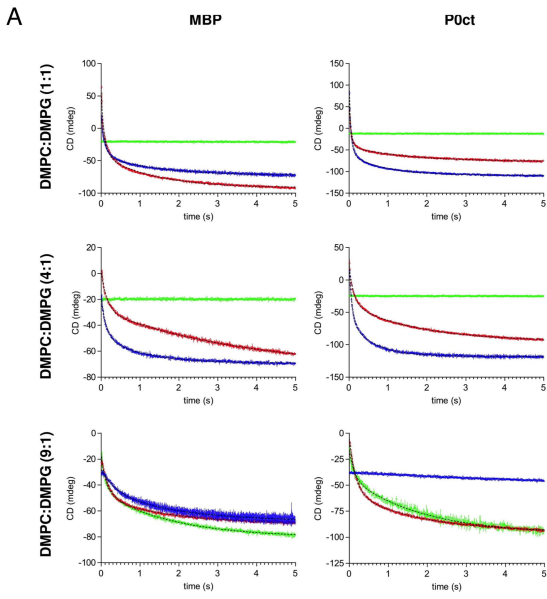
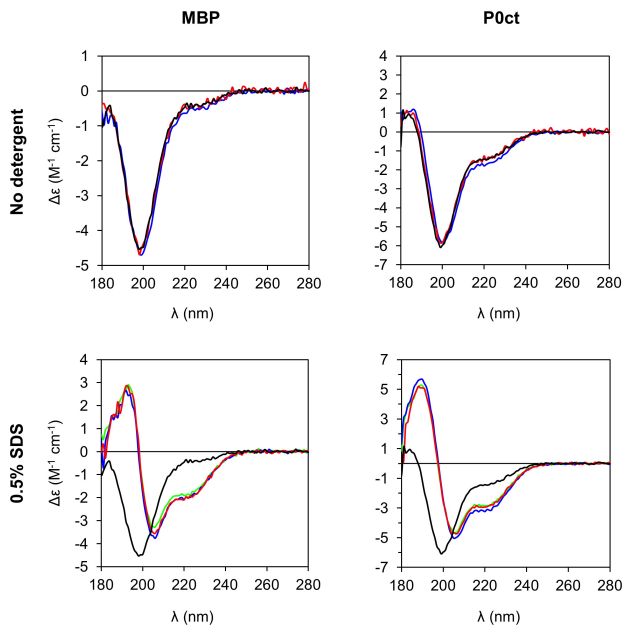
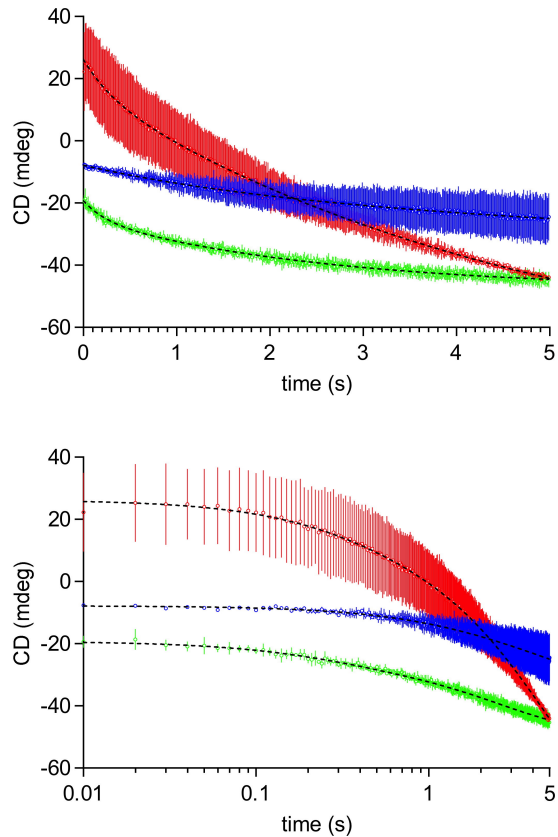


Fig. 3

Supplementary information



Supplementary Fig. S1. SRCD control experiments. The folding of MBP and P0ct in the absence (top) and presence (bottom) of 0.5% SDS as determined by SRCD spectroscopy. No additive (green); 150 mM NaF (blue); 1 mM CaCl_2 (red). Protein controls without additives or detergents in water (black) are plotted for reference in each panel.



Supplementary Fig. S2. Rapid kinetics of Ca^{2+} -induced initial lipid turbidity. Evolution of the SRCD signal at 195 nm was monitored for 5 s using stopped flow measurements. For clarity, linear (top) and logarithmic (bottom) time scales are shown. Ca^{2+} was mixed at a final concentration of 1 mM with 2.5 mM DMPC:DMPG 1:1 (green), 4:1 (blue), and 9:1 (red) molar lipid ratios. Error bars represent standard deviation. Fits (dashed black) are shown; see Supplementary Table 1 for rate constants.

Supplementary Table 1. Two-phase exponential decay rate order parameters from rapid kinetics SRCD experiments. Values marked with a dash could not be fitted, as the CD signal decayed very little, if at all, within the measurement time window. All errors represent standard deviation.

| Protein | DMP C:DM PG ratio | No additive | | | | 150 mM NaF | | | | 1 mM CaCl ₂ | | | |
|------------|----------------------------|--------------------------|--------------------------|--------------|------------|--------------------------|--------------------------|--------------|------------|---------------------------|--------------------------|--------------|-------------------------|
| | | k_1 (s ⁻¹) | k_2 (s ⁻¹) | k_1/k_2 | R^2 | k_1 (s ⁻¹) | k_2 (s ⁻¹) | k_1/k_2 | R^2 | k_1 (s ⁻¹) | k_2 (s ⁻¹) | k_1/k_2 | R^2 |
| No protein | 1:1 | - | - | - | - | - | - | - | - | 0.29 ± 0.04 ^a | - | - | 0.625 0 ^a |
| | 4:1 | - | - | - | - | - | - | - | - | 3.23 ± 1.38 | 0.20 ± 0.03 | 15.89 ± 5.09 | 0.929 1 |
| | 9:1 | - | - | - | - | - | - | - | - | 4.20 ± 0.78 | 0.39 ± 0.03 | 10.89 ± 1.56 | 0.956 4 |
| MBP | 1:1 | - | - | - | - | 10.59 ± 0.29 | 0.73 ± 0.02 | 14.55 ± 0.37 | 0.98 00 | 11.65 ± 0.26 ^b | 0.76 ± 0.01 ^b | 15.23 ± 0.30 | 0.987 8 ^b |
| | 4:1 | - | - | - | - | 7.95 ± 0.24 | 0.93 ± 0.02 | 8.59 ± 0.20 | 0.98 68 | 6.84 ± 0.17 | 0.27 ± 0.01 | 25.34 ± 0.62 | 0.993 4 |
| | 9:1 | 8.52 ± 0.25 | 0.56 ± 0.01 | 15.13 ± 0.36 | 0.99 27 | 2.53 ± 0.46 | 0.54 ± 0.09 | 4.68 ± 0.41 | 0.93 76 | 5.24 ± 0.11 | 0.58 ± 0.02 | 9.04 ± 0.18 | 0.992 4 |
| P0ct | 1:1 | - | - | - | - | 20.14 ± 0.25 | 1.12 ± 0.01 | 17.96 ± 0.22 | 0.99 34 | 18.77 ± 0.36 | 0.67 ± 0.01 | 27.95 ± 0.61 | 0.983 7 |
| | 4:1 | - | - | - | - | 14.03 ± 0.36 | 1.58 ± 0.03 | 8.89 ± 0.18 | 0.98 93 | 8.30 ± 0.16 | 0.57 ± 0.01 | 14.50 ± 0.23 | 0.995 4 |
| | 9:1 | 7.79 ± 0.61 | 0.53 ± 0.01 | 14.59 ± 0.97 | 0.97 85 | - | - | - | - | 6.03 ± 0.09 | 0.57 ± 0.01 | 10.57 ± 0.13 | 0.996 3 |

^a Data fit best into one-phase exponential decay function, but the change in SRCD signal overall is very small.

^b Dataset is visibly more complicated than what can be described with two rate constants.

ARTICLE IV

Neuropathy-related mutations alter the membrane binding properties of the human myelin protein P0 cytoplasmic tail.

Raasakka A., Ruskamo S., Barker R., Krokengen O.C., Vatne G.H., Kristiansen C.K., Hallin E.I., Skoda M.W.A., Bergmann U., Wacklin-Knecht H., Jones N.C., Hoffmann S.V. & Kursula P.

bioRxiv 535013. DOI: 10.1101/535013. (2019)

Abstract

Schwann cells myelinate selected axons in the peripheral nervous system (PNS) and contribute to fast saltatory conduction *via* the formation of compact myelin, in which water is excluded from between tightly adhered lipid bilayers. Peripheral neuropathies, such as Charcot-Marie-Tooth disease (CMT) and Dejerine-Sottas syndrome (DSS), are incurable demyelinating conditions that result in pain, decrease in muscle mass, and functional impairment. Many Schwann cell proteins, which are directly involved in the stability of compact myelin or its development, are subject to mutations linked to these neuropathies. The most abundant PNS myelin protein is protein zero (P0); point mutations in this transmembrane protein cause CMT subtype 1B and DSS. P0 tethers apposing lipid bilayers together through its extracellular immunoglobulin-like domain. Additionally, P0 contains a cytoplasmic tail (P0ct), which is membrane-associated and contributes to the physical properties of the lipid membrane. Six CMT- and DSS-associated missense mutations have been reported in P0ct. We generated recombinant disease mutant variants of P0ct and characterized them using biophysical methods. Compared to wild-type P0ct, some mutants have negligible differences in function and folding, while others highlight functionally important amino acids within P0ct. For example, the D224Y variant of P0ct induced tight membrane multilayer stacking. Our results show a putative molecular basis for the hypermyelinating phenotype observed in patients with this particular mutation and provide overall information on the effects of disease-linked mutations in a flexible, membrane-binding protein segment.

1 ***Neuropathy-related mutations alter the membrane binding properties of the human***
2 ***myelin protein P0 cytoplasmic tail***

3

4 Arne Raasakka¹, Salla Ruskamo^{2,3}, Robert Barker⁴, Oda C. Krokengen¹, Guro H. Vatne¹, Cecilie K.
5 Kristiansen¹, Erik I. Hallin¹, Maximilian W.A. Skoda⁵, Ulrich Bergmann^{2,3}, Hanna Wacklin-
6 Knecht⁶, Nykola C. Jones⁷, Søren Vrønning Hoffmann⁷ & Petri Kursula^{1,2,*}

7

8 ¹*Department of Biomedicine, University of Bergen, Bergen, Norway*

9 ²*Faculty of Biochemistry and Molecular Medicine, University of Oulu, Oulu, Finland*

10 ³*Biocenter Oulu, University of Oulu, Oulu, Finland*

11 ⁴*School of Physical Sciences, University of Kent, Kent, United Kingdom*

12 ⁵*ISIS Neutron and Muon Source, Science & Technology Facilities Council, Rutherford Appleton Laboratory, OX11*
13 *OQX Didcot, United Kingdom*

14 ⁶*Division of Physical Chemistry, Department of Chemistry, Lund University & European Spallation Source ERIC,*
15 *Lund, Sweden*

16 ⁷*ISA, Department of Physics and Astronomy, Aarhus University, Ny Munkegade 120, 8000 Aarhus C, Denmark*

17

18

19

20 *Corresponding author. E-mail: petri.kursula@uib.no

21

22

1 **Abstract**

2 Schwann cells myelinate selected axons in the peripheral nervous system (PNS) and contribute to fast
3 saltatory conduction *via* the formation of compact myelin, in which water is excluded from between tightly
4 adhered lipid bilayers. Peripheral neuropathies, such as Charcot-Marie-Tooth disease (CMT) and Dejerine-
5 Sottas syndrome (DSS), are incurable demyelinating conditions that result in pain, decrease in muscle mass,
6 and functional impairment. Many Schwann cell proteins, which are directly involved in the stability of
7 compact myelin or its development, are subject to mutations linked to these neuropathies. The most abundant
8 PNS myelin protein is protein zero (P0); point mutations in this transmembrane protein cause CMT subtype
9 1B and DSS. P0 tethers apposing lipid bilayers together through its extracellular immunoglobulin-like
10 domain. Additionally, P0 contains a cytoplasmic tail (P0ct), which is membrane-associated and contributes
11 to the physical properties of the lipid membrane. Six CMT- and DSS-associated missense mutations have
12 been reported in P0ct. We generated recombinant disease mutant variants of P0ct and characterized them
13 using biophysical methods. Compared to wild-type P0ct, some mutants have negligible differences in
14 function and folding, while others highlight functionally important amino acids within P0ct. For example, the
15 D224Y variant of P0ct induced tight membrane multilayer stacking. Our results show a putative molecular
16 basis for the hypermyelinating phenotype observed in patients with this particular mutation and provide
17 overall information on the effects of disease-linked mutations in a flexible, membrane-binding protein
18 segment.

19

20 **Keywords**

21 Myelin protein zero; membrane binding; peripheral neuropathy; CMT; DSS; disease mutation; gain of
22 function

23

24

1 Introduction

2 Fast saltatory nerve impulse conduction requires myelin, a structure composed of tightly stacked lipid
3 bilayers that wrap around selected axonal segments in the central and peripheral nervous systems (CNS and
4 PNS, respectively). The insulative nature of myelin enables efficient nerve impulse propagation, and the
5 destruction of myelin, demyelination, underlies a range of chronic diseases. In the PNS, peripheral
6 neuropathies affect Schwann cell compact myelin. These include Charcot-Marie-Tooth disease (CMT) and
7 its more severe, rapidly progressive form known as Dejerine-Sottas syndrome (DSS), which cause incurable
8 chronic disability (Hartline 2008; Stassart *et al.* 2018). CMT and DSS manifest through both dominant and
9 recessive inheritance, and they harbour a strong genetic component, typically caused by mutations in
10 proteins relevant for the formation and stability of PNS myelin, while axonal forms also exist.

11 Myelin protein zero (P0) is a type I transmembrane protein consisting of an extracellular immunoglobulin
12 (Ig)-like domain (Shapiro *et al.* 1996), a single transmembrane helix, and a 69-residue C-terminal
13 cytoplasmic tail (P0ct). P0ct is likely to be involved in the regulation of myelin membrane behaviour,
14 supporting the arrangement of the P0 Ig-like domains in the extracellular space upon the formation of the
15 myelin intraperiod line (Luo *et al.* 2007; Raasakka *et al.* 2019b; Wong and Filbin 1994). P0ct contains a
16 neuritogenic segment, which can be used to induce experimental autoimmune neuritis (EAN) in animal
17 models (de Sèze *et al.* 2016). *In vitro*, P0ct is disordered in aqueous solution, gaining secondary structure
18 upon binding to negatively charged phospholipids (Luo *et al.* 2007; Raasakka *et al.* 2019b). In its lipid-
19 bound state, P0ct affects the phase behaviour of lipids and promotes the fusion of lipid vesicles. High-degree
20 molecular order, most likely from stacked lipid bilayers, can be detected *via* X-ray diffraction of P0ct-bound
21 membranes (Raasakka *et al.* 2019b). This suggests that P0ct harbours a structural role in mature myelin.

22 Dozens of mutations have been identified in P0, most of which affect the Ig-like domain. These mutations
23 affect myelin morphology and integrity, leading to the development of peripheral neuropathies (Mandich *et al.*
24 *et al.* 2009; Shy *et al.* 2004). Six known missense mutations are located within P0ct, of which four cause
25 dominant demyelinating CMT type 1B (CMT1B). These include T216ER (Su *et al.* 1993), D224Y (also
26 referred to as D195Y and D234Y) (Fabrizi *et al.* 2006; Miltenberger-Miltenyi *et al.* 2009; Schneider-Gold *et al.*
27 *et al.* 2010), R227S (Shy *et al.* 2004), and the deletion of Lys236 (K236del) (Street *et al.* 2002). In addition,
28 K236E has been linked to dominant axonal CMT type 2I (CMT2I) (Choi *et al.* 2004), and A221T, which was
29 discovered as a co-mutation together with the deletion of Val42 in the Ig-like domain, was identified in a
30 patient with DSS (Planté-Bordeneuve *et al.* 2001). How these mutations relate to CMT/DSS etiology is not
31 known, although P0 mutations have been linked to the unfolded protein response (UPR) (Bai *et al.* 2013; Bai
32 *et al.* 2018; Wrabetz *et al.* 2006), indicating issues in either translation or folding that induce stress within the
33 endoplasmic reticulum (ER).

34 Considering the small size of P0ct and the nature of the disease mutations in it, many of which change its
35 electrostatic charge, impairment in the function of P0ct as a membrane binding/stabilizing segment is a

1 possible functional mechanism. We used methodologies established earlier for myelin basic protein (MBP)
2 (Raasakka *et al.* 2017) and wild-type P0ct (wt-P0ct) (Raasakka *et al.* 2019a; Raasakka *et al.* 2019b) to
3 characterize structure-function relationships of the CMT- and DSS-related P0ct variants. Our results suggest
4 that D224Y is a hypermyelinating gain-of-function mutation, which is in line with the clinically relevant
5 phenotype of abnormally thickened myelin sheaths (Fabrizi *et al.* 2006).

6

7

1 **Results**

2 We have earlier studied the binding of MBP and P0ct to model lipid membranes (Raasakka *et al.* 2017;
3 Raasakka *et al.* 2019a; Raasakka *et al.* 2019b), using a biophysical workflow that allows the determination of
4 binding affinity, gain in folding, alteration of lipid phase behaviour, quantification and visualization of
5 vesicle aggregation and fusion, and supported lipid bilayer (SLB) stacking. In the current study, we
6 examined whether and how CMT and DSS mutations within P0ct influence its structure and function. For
7 this purpose, we expressed and purified the wild-type protein and six mutant variants, each harbouring one of
8 the following amino acid changes: T216ER, A221T, D224Y, R227S, K236E, and K236del.

9

10 **Characterization of P0ct CMT mutants**

11 wt-P0ct and the six CMT variants were purified to homogeneity. Most mutants were straightforward to
12 purify, showing identical behaviour to wt-P0ct in size-exclusion chromatography (SEC) (Fig. 1b). D224Y,
13 on the other hand, had to be gel filtrated at a higher pH and salt concentration than the others, and while
14 yields were generally lower, minor amounts of degradation were present and the migration in SEC was
15 altered, albeit not in denaturing gel electrophoresis (SDS-PAGE) (Fig. 1b. Supplementary Fig. S1). In
16 dynamic light scattering (DLS), all variants displayed a similar hydrodynamic radius (R_h) and an absence of
17 aggregation (Fig. 1c, Supplementary Table 1). All of the variants showed high apparent molecular weight in
18 SDS-PAGE, which reflects the intrinsically disordered nature of P0ct (Raasakka *et al.* 2019b). The molecular
19 weight and the presence of the mutations were confirmed using mass spectrometry (Table 1). The total yields
20 of the purified mutant proteins were different from wt-P0ct (Supplementary Fig. S1, Table 1), most mutants
21 giving larger yields, with the exception of D224Y. It should be noted that all mutants were expressed as
22 maltose-binding protein fusions. Thus, mutations, which represent small changes in the overall sequence and
23 size of the fusion protein, can affect the expression and purification behaviour.

24 Small-angle X-ray scattering (SAXS) verified that for most variants, both the size and behaviour in solution
25 were nearly identical, with radius of gyration (R_g) and maximum dimension (D_{max}) at 2.4 - 2.7 nm and 9.0 –
26 10.7 nm, respectively, and molecular masses matching monomeric protein based on I_0 values (Fig. 2,
27 Supplementary Table 2). D224Y presented a marginally larger D_{max} (11.6 nm) compared to the other
28 variants, but all variants were flexible and extended in solution, as evident from the Kratky plot (Fig. 2d).

29

30 **The folding and lipid binding properties of P0ct CMT mutants**

31 To compare the conformation of the P0ct variants, we carried out a series of synchrotron radiation circular
32 dichroism (SRCD) spectroscopic experiments in the absence and presence of different lipid compositions,
33 detergents, and 2,2,2-trifluoroethanol (TFE), as previously described for wt-P0ct (Raasakka *et al.* 2019b).
34 P0ct is disordered in solution and gains a significant amount of secondary structure upon binding to small

1 unilamellar vesicles (SUV) with a net negative surface charge (Luo *et al.* 2007; Raasakka *et al.* 2019b). In
2 water, all mutants were disordered as expected, with D224Y having less secondary structure than the others
3 (Fig. 3). This is in agreement with the longer D_{\max} determined using SAXS. All mutants closely resembled
4 wt-P0ct in TFE and the detergents sodium dodecyl sulphate (SDS), *n*-dodecylphosphocholine (DPC),
5 lauryldimethylamine *N*-oxide (LDAO), and *n*-octyl glucoside (OG), while K236del was more α -helical than
6 the other variants in the presence of SDS (Fig. 3, Supplementary Fig. S2).

7 Addition of DMPC retained the proteins in a disordered state, with D224Y deviating slightly (Supplementary
8 Fig. S2). In the presence of net negatively charged SUVs composed of DMPC:DMPG ratios of 1:1, 4:1, and
9 9:1, the variants presented some folding differences (Fig. 3, Supplementary Fig. S2). Overall, most folding
10 was observed in 1:1 DMPC:DMPG, and the degree of folding decreased with decreasing fraction of DMPG,
11 *i.e.* negative charge. In DMPC:DMPG (1:1), a small shift to the right of the maximum at 188 nm was evident
12 for D224Y and K236del, indicating slightly increased folding, although the two minima at 208 and 222 nm,
13 typical for helical content, remained the same for all variants (Fig. 3d). In DMPC:DMPG (4:1), this effect
14 was only observed for D224Y (Fig. 3e). In DMPC:DMPG (9:1), the differences in signal magnitude were
15 large, reflecting different levels of turbidity (Supplementary Fig. S2). It can be assumed that the variants
16 showing high turbidity under this condition are membrane-bound, while the ones giving strong CD signal of
17 an unfolded protein do not bind to 9:1 DMPC:DMPG.

18 The affinity of P0ct variants towards immobilized DMPC:DMPG (1:1) SUVs was investigated using surface
19 plasmon resonance (SPR). All variants bound to lipids with similar kinetic parameters (Fig. 3f, Table 2),
20 including the A_1 value, which corresponds to the apparent K_d , of 0.35-0.4 μ M. This value is in the same range
21 with those obtained earlier for wt-P0ct, MBP, and P2 (Raasakka *et al.* 2017; Raasakka *et al.* 2019b;
22 Ruskamo *et al.* 2014; Wang *et al.* 2011). While the differences in K_d were minor, the behaviour of D224Y
23 was unique: the observed maximal response level was higher compared to the other variants. This suggests
24 that the D224Y variant can either accumulate onto immobilized vesicles in higher amounts, or it induces a
25 change on the surface that affects the measurement, such as the fusion, swelling, or aggregation of lipid
26 vesicles.

27

28 **Effect of CMT mutations on lipid membrane properties**

29 To determine the effect of the mutations on lipid structure, experiments probing changes in the
30 thermodynamic and structural properties of lipid membranes were carried out. As shown before (Raasakka *et al.*
31 *et al.* 2019b), the presence of P0ct changes the melting behaviour of dimyristoyl lipid tails, inducing a
32 population that melts 0.9 °C below the major phase transition temperature of 23.8 °C. The presence of the
33 mutations altered this effect mildly (Fig. 4a), with T216ER and R227S behaving similarly to wt-P0ct. The
34 Lys236 mutations deviated from wt-P0ct, with a decreased temperature for the emerged population; K236E
35 and K236del showed lipid phase transition temperatures of 22.7 and 22.8 °C, respectively. A221T presented

1 slightly higher temperature for phase transition compared to wt-P0ct, with the major peak at 23.0 °C. Based
2 on the shape of the calorimetric landscape, D224Y was clearly different from the rest, as the new population
3 did not appear as a single, symmetric peak, but was rather formed of several overlapping peaks.

4 Similarly to MBP and P2 (Raasakka *et al.* 2017; Ruskamo *et al.* 2014), P0ct is capable of inducing
5 concentration-dependent solution turbidification, when mixed with lipid vesicles of net negative charge
6 (Raasakka *et al.* 2019b). The turbidity can arise from vesicle fusion and/or aggregation, and different
7 processes may be dominant in different samples with respect to the measured signal. To determine the effect
8 of P0ct CMT mutations on this function, turbidity experiments were carried out with the different variants.
9 T216ER and A221T produced turbidity levels similar to wt-P0ct (Fig. 4b, Supplementary Fig. S3a). At 1:100
10 P/L ratio, D224Y, R227S, K236E, and K236del all had decreased turbidity. At a P/L ratio of 1:50, however,
11 only D224Y had a significant inhibitory effect on turbidity. This result highlights that the D224Y mutant
12 protein may function differently from the other variants, when it binds to and aggregates vesicles.

13 To shed further light on the protein-induced changes in membrane structure, small-angle X-ray diffraction
14 (SAXD) experiments were performed on P0ct-membrane mixtures. In our earlier study, wt-P0ct mixed with
15 lipids produced two strong Bragg peaks, and the corresponding repeat distance evolved as a function of the
16 P/L ratio (Raasakka *et al.* 2019b). Here, we observed that in all cases, the repeat distance increased when
17 protein concentration in the sample decreased (Fig. 4c, Supplementary Fig. S3b). Each variant presented a
18 minimum repeat distance, which was reached at and above a P/L ratio of 1:100. The repeat distance for wt-
19 P0ct was ~7.5 nm, while D224Y produced a spacing of <7.0 nm. R224S, K236E, and K236del had looser
20 packing than wt-P0ct. K236E had a minimum repeat distance of ~8.0 nm at the highest protein
21 concentration.

22 To understand the effect of the mutations on the function of P0ct, and the origin of the high molecular order
23 reflected by X-ray diffraction, electron microscopy imaging was performed. Most mutants functioned in a
24 manner similar to wt-P0ct, producing large vesicular structures with a spread-out morphology (Fig. 5), with
25 occasional regions indicative of bilayer stacking. D224Y showed a clear difference to wt-P0ct, producing
26 strongly stacked myelin-like membranes in a manner resembling MBP (Raasakka *et al.* 2017). This gain of
27 function was reproducible over a wide range of P/L ratios (Supplementary Fig. S4) and a unique feature
28 among the six mutant P0ct variants. The results confirm that the Bragg peaks seen in SAXD, indeed,
29 originate from repeat distances in membrane multilayers, identically to two other PNS myelin peripheral
30 membrane proteins, MBP and P2 (Raasakka *et al.* 2017; Ruskamo *et al.* 2014; Sedzik *et al.* 1985). The
31 observed bilayer spacing for the D224Y mutant in EM was narrow and in general better defined than seen
32 for MBP (Raasakka *et al.* 2017), suggesting that P0ct forms a tight structure within and/or between the
33 membranes. Based on SAXD, the intermembrane spacing is ~3 nm, a value in close relation to the
34 dimensions of the major dense line (MDL) in myelin.

1 To gain an insight into the kinetic aspects of P0ct-induced lipid fusion/aggregation, stopped-flow kinetics
2 experiments were performed using SRCD (Fig. 6, Table 3) (Raasakka *et al.* 2019a). All variants followed a
3 similar kinetic pattern as wt-P0ct and could be best fitted to a two-phase exponential decay with two rate
4 constants (k_1 , fast and k_2 , slow). Rather minor differences were present: k_2 values were very similar in all
5 cases, and while D224Y presented 10% higher k_1 and k_1/k_2 compared to wt-P0ct and most other variants,
6 both K236E and K236del displayed k_1 and k_1/k_2 20% lower than for wt-P0ct, indicating slower kinetics (Fig.
7 6b). While all variants produced a similar end-level CD value around -100 mdeg, the starting level of
8 K236del was higher than for any other variant, and remained so until ~0.3 s, before settling on a similar level
9 to other variants. It is currently unclear whether this is due to an increased level of protein folding or less
10 scattered light from fused or aggregated vesicles.

11

12 **The membrane insertion mode of P0ct**

13 To understand the membrane insertion of P0ct, how it compares to MBP (Raasakka *et al.* 2017), and how it
14 might be related to disease mutations, we performed neutron reflectometry (NR) experiments (Fig. 7, Table
15 4). The insertion of P0ct to a DMPC:DMPG SLB was quite different to that of MBP. P0ct inserted
16 completely into the membrane, thickening it by 2 nm and increasing its roughness, most likely due to
17 increased bilayer mobility, as the hydration layer below the membrane became thicker (Fig. 7b,c). P0ct was
18 present in the acyl tail fraction of the membrane, as well as the outer headgroup fraction. The data could not
19 be fitted with only these parameters, but a very rough, narrow layer of protein had to be considered on top of
20 the membrane. Unfortunately, the roughness and high solvation fraction of this layer did not allow for
21 precise thickness determination: the layer was modelled to be between 5 – 15 Å thick within the fit to the
22 data. To investigate the effect of the D224Y mutation on P0ct membrane association, NR data were collected
23 for SLB-bound D224Y, which appeared identical to wt-P0ct (Supplementary Fig. S5).

24

25

1 **Discussion**

2 The formation of compact myelin and the major dense line requires an interplay of myelin molecules, many
3 of which have similar functional properties despite lack of sequence homology. Considering the MDL of
4 PNS compact myelin, the major protein components according to current knowledge are MBP, P2, P0ct, and
5 cytosolic loops of PMP-22. We characterized the potential functional anomalies of P0ct CMT mutants in
6 membrane binding using earlier established biophysical strategies (Raasakka *et al.* 2017; Raasakka *et al.*
7 2019a; Raasakka *et al.* 2019b).

8 The six mutations reported in P0ct are clustered within or near the neuritogenic segment. Most of them
9 reside in the vicinity of putatively phosphorylated Ser residues (Fig. 1a), which have been speculated to be
10 affected by P0ct mutations (Su *et al.* 1993; Xu *et al.* 2001). Many P0 mutations have been suggested to lead
11 to UPR activation (Bai *et al.* 2013; Bai *et al.* 2018; Wrabetz *et al.* 2006), indicating problems with translation
12 rate, folding, and/or membrane insertion. Given the fact that P0ct is known to interact with lipid membrane
13 surfaces (Luo *et al.* 2007; Raasakka *et al.* 2019b; Raasakka *et al.* 2019a), these mutations could also have
14 direct effects on the formation of mature compact myelin at the molecular level.

15 ***Mechanism of P0ct binding to membranes***

16 In order to fully understand the effects of P0ct mutations on its structure and function, detailed knowledge
17 about P0ct binding to lipid membranes, and the effects thereof on multilayered membrane stacks, are
18 required. NR allowed us to gain a picture of P0ct in a lipid bilayer. P0ct inserts deep into a membrane, with
19 only a small fraction remaining solvent-exposed on the membrane surface. This is a clear difference to MBP,
20 which forms a brush-like protein phase on top of the membrane surface, while being partially embedded into
21 the bilayer (Raasakka *et al.* 2017). After undergoing charge neutralization and folding, P0ct seems to
22 collapse into a tight conformation and remain stable. The compact, deep conformation of P0ct suggests that
23 instead of directly embedding into two bilayers, which is the working model for *e.g.* MBP-induced stacking
24 (Raasakka *et al.* 2017; Vassall *et al.* 2015), P0ct may change the surface properties of the membrane in a
25 way that supports apposing bilayer surface adhesion. It could also regulate membrane curvature and the
26 twining of lipid bilayers around the axon.

27 At the level of full-length P0, P0ct is a direct extension of the transmembrane segment, and hence, anchored
28 permanently to a membrane surface at its beginning. Membrane stacking could involve the insertion of P0ct
29 across the MDL into an apposing membrane leaflet, which is only 3 nm away. Considering this scenario, P0
30 is basally expressed in Schwann cells even before myelination occurs (Lee *et al.* 1997). Moreover, P0 is
31 translated and inserted into the ER membrane and trafficked through the trans-Golgi network to the plasma
32 membrane after the Ig-like domain has been post-translationally modified (Eichberg 2002; Lemke and Axel
33 1985). If P0ct were to enter an apposing membrane during the formation of compact myelin, it would have to
34 remain in a disordered state until another membrane is present. On the other hand, if P0ct is embedded in the

1 membrane after translation, it might afterwards be able to dissociate and enter the apposing leaflet within
2 compact myelin. Considering the attractive phospholipid bilayer around the transmembrane helix, and the
3 fact that P0ct binds negatively charged lipids essentially irreversibly *in vitro*⁵, both mechanisms described
4 above are unlikely to exist. Thus, the role of P0ct in membrane adhesion is likely to be based on altered lipid
5 membrane properties, as opposed to MBP and P2, which directly interact with two membrane surfaces.
6 While P2 and MBP were observed to synergistically stack lipid bilayers *in vitro* (Suresh *et al.* 2010), mice
7 lacking both proteins formed apparently normal and functional myelin (Zenker *et al.* 2014). Hence, multiple
8 factors must participate in the correct formation of compact myelin; these include both lipid components of
9 the myelin membrane, different myelin proteins, as well as signalling molecules and inorganic ions. Hence,
10 further experiments in more complex sample environments are required to decipher the details of the
11 molecular interplay between these factors in PNS myelin MDL formation.

12 ***P0ct mutations and membrane interactions***

13 Compared to wt-P0ct, we observed only subtle differences for two mutants: T216ER and A221T. While
14 T216ER behaved very similarly to wt-P0ct, its role in CMT etiology could be of another origin than related
15 to protein-membrane binding. A221T, on the other hand, resides in the YAML-motif, which directs the
16 trafficking of P0 (Kidd *et al.* 2006) and might compromise the function of P0 even without inducing changes
17 in membrane binding, especially when combined with a second mutation in the extracellular domain, such as
18 the deletion of Val42 (Planté-Bordeneuve *et al.* 2001).

19 Functionally the most interesting mutant studied here is D224Y, which now has been described in at least 3
20 studies (Fabrizi *et al.* 2006; Miltenberger-Miltenyi *et al.* 2009; Schneider-Gold *et al.* 2010). It is a gain-of-
21 function mutant, inducing ordered lipid bilayer stacks *in vitro*, which are more tightly packed than those
22 formed by wt-P0ct or the other variants. The results correlate well the hypermyelinating disease phenotype
23 (Fabrizi *et al.* 2006). Neutron reflectometry produced a nearly identical result for D224Y compared to wt-
24 P0ct, which together with the SRCD experiments indicates that the conformation of wt-P0ct and D224Y is
25 similar in the membrane. The change of an acidic to an aromatic residue near the lipid bilayer surface most
26 likely enables a specific interaction between surfaces that results in the observed gain of function.

27 P0 is the most abundant protein in PNS myelin (Greenfield *et al.* 1973; Patzig *et al.* 2011), contributing
28 primarily to the formation of the intraperiod line (Filbin *et al.* 1990), and molecular mechanisms of D224Y-
29 induced tight stacking could be two-fold. Firstly, with its short repeat distance – 1-2 nm smaller compared to
30 MBP and P2 based on SAXD (Raasakka *et al.* 2019b; Ruskamo *et al.* 2014; Sedzik *et al.* 1985) – and active
31 membrane binding, as evident from SPR, the mutant might cause size exclusion of P2 and other factors out
32 of the cytoplasmic stack, leading to defective compact myelin maintenance. In PNS compact myelin, P2 is
33 even more abundant in the cytoplasmic compartment than MBP, can form membrane stacks, and harbours a
34 maintenance role in myelin homeostasis as a lipid carrier (Ruskamo *et al.* 2014; Zenker *et al.* 2014).
35 Secondly, the tendency of D224Y to form such ordered, tight systems might affect the Ig-like domains on the

1 extracellular side. In the hypermyelinating phenotype of D224Y patients, membrane stacking seems
2 condensed and regular, without abnormally loosened myelin (Fabrizi *et al.* 2006). SPR indicates that more
3 D224Y can accumulate on membranes, and full-length P0 D224Y could accumulate and tighten up within
4 the membrane, causing also the intraperiod line to become more crowded and/or structured. The original
5 discovery of the D224Y mutation (Fabrizi *et al.* 2006) suggested that it has a gene dosage effect, since
6 heterozygous carriers presented little to no symptoms. Hence, the presence of wild-type P0 can rescue the
7 effects of the mutation. Correct gene dosage of P0 is important for normal myelination in animal models as
8 well as CMT patients (Fabrizi *et al.* 2006; Maeda *et al.* 2012; Martini *et al.* 1995; Quattrini *et al.* 1999;
9 Speevak and Farrell 2013; Wrabetz *et al.* 2000). The molecular details of the involved mechanisms are
10 currently lacking. Further studies on the D224Y mutation *in vitro* and *in vivo* could help in understanding
11 molecular aspects of both normal and abnormal myelination.

12 Lys236 appears to be a functionally important amino acid in P0ct. In its membrane-bound state, P0ct is likely
13 to have Lys236 close to the lipid headgroups, and altering the charge in this environment might influence
14 folding and the global positioning of P0ct on the membrane. Indeed, a gradual effect in membrane packing
15 was observed in SAXD; the repeat structure loosens, as residue 236 neutralizes (K236del) and turns to
16 negative (K236E). Turbidimetry also indicated a clear effect of charge reversal at residue 236. The Lys236
17 mutants folded to a similar degree as wt-P0ct, which suggests that the role of Lys236 is in packing, rather
18 than folding. This is supported by the slower kinetic parameters for Lys236 mutants in stopped-flow
19 measurements.

20 Similarly to Lys236, Arg227 could harbour a role in membrane packing. In our experiments, R227S is one of
21 the mutants that appeared to induce weaker adhesion than the wild-type protein. The mutation results in a
22 loosened repeat structure without a major impact on protein folding. Arg227 might be involved in
23 electrostatic anchoring of the protein to the lipid headgroups – the R227S mutation likely has low impact on
24 ER stress and UPR, as mutated P0 correctly localizes to the plasma membrane (Lee *et al.* 2010).

25 **Concluding remarks**

26 To a large extent, the P0ct CMT variants studied here perform similarly to wt-P0ct in controlled simple
27 environments. This might differ *in vivo*, where other components are present and P0 is present in its full-
28 length form. Our characterization is focused on protein-lipid interactions and does not take into account
29 possible protein-protein interactions with MBP, P2, or PMP22, which might be relevant for myelination and
30 disease phenotypes. Nevertheless, we have uncovered critical amino acids in P0 that may contribute to the
31 formation of healthy myelin and be involved in disease mechanisms. These include Arg227, Lys236, and
32 Asp224. Our results shed light on the molecular fundamentals of myelination in the PNS, but more
33 comprehensive studies in biological model systems, as well as on molecular structure and dynamics of
34 native-like myelin, are needed for deciphering the mechanisms of the P0ct mutations causing human
35 neuropathy.

1 **Experimental procedures**

2 **Bioinformatics, mutagenesis, protein expression & purification**

3 Secondary structure prediction for P0ct was performed using JPred (Drozdetskiy *et al.* 2015). Mutations
4 were generated in the P0ct pHMGWA expression vector (Busso *et al.* 2005; Raasakka *et al.* 2019b) by PCR
5 using Phusion High-Fidelity DNA polymerase (Thermo Fisher Scientific) with 5'-phosphorylated primers
6 that introduced the desired point mutations. The samples were treated with *DpnI* (New England Biolabs) to
7 digest template DNA and linear vectors circularized using T4 DNA ligase (New England Biolabs), followed
8 by transformation and plasmid isolation. The presence of mutations and integrity of the constructs was
9 verified using DNA sequencing.

10 Protein expression and purification were carried out in *E. coli* BL21(DE3) as described for wt-P0ct
11 (Raasakka *et al.* 2019b), with the exception of an added amylose-resin affinity step between Ni-NTA and
12 size-exclusion chromatography. The step was introduced to remove any contaminating maltose-binding
13 protein tags from the tobacco etch virus protease-digested recombinant proteins. Size exclusion
14 chromatography was carried out using Superdex S75 16/60 HiLoad and Superdex 75 10/300GL columns
15 (GE Healthcare) with 20 mM HEPES, 150 mM NaCl, pH 7.5 (HBS) as mobile phase, with the exception of
16 D224Y, where a 20 mM Tris-HCl, 300 mM NaCl, pH 8.5 (TBS) solution was used. The monodispersity and
17 R_h of all proteins were checked from filtered 1 mg/ml samples using a Malvern Zetasizer ZS DLS
18 instrument. The D224Y mutant was then dialyzed into HBS. Additionally, all proteins were dialyzed into
19 water prior to SRCD experiments.

20

21 **Mass spectrometry**

22 The molecular weight and identity of the purified proteins were verified by mass spectrometry. In short, the
23 proteins were subjected to ultra-performance liquid chromatography (UPLC) coupled electrospray ionization
24 (ESI) time-of-flight mass spectrometry in positive ion mode, using a Waters Acquity UPLC-coupled Synapt
25 G2 mass analyzer with a Z-Spray ESI source. This allowed us to determine the undigested masses of each
26 purified P0ct variant. Protein identity and the presence of the desired mutations were confirmed from
27 peptides extracted after in-gel tryptic proteolysis, using a Bruker Ultra fleXtreme matrix-assisted laser
28 desorption/ionization time-of-flight (MALDI-TOF) mass analyzer.

29

30 **Small-angle X-ray scattering**

31 SAXS data were collected from protein samples at 0.3 – 12.9 mg/ml in HBS and TBS on the EMBL P12
32 beamline, PETRA III (Hamburg, Germany) (Blanchet *et al.* 2015). Monomeric bovine serum albumin ($M_r =$
33 66.7 kDa; $I_0 = 499.0$) was used as a molecular weight standard. Data were processed and analyzed using the

1 ATASAS package (Franke *et al.* 2017), and GNOM was used to calculate distance distribution functions
2 (Svergun 1992). See Supplementary Table 2 for further details.

3

4 **Vesicle preparation**

5 DMPC, DMPG, and DOPC were purchased from Larodan Fine Chemicals AB (Malmö, Sweden). DOPS and
6 the deuterated d_{54} -DMPC and d_{54} -DMPG were purchased from Avanti Polar Lipids (Alabaster, Alabama,
7 USA).

8 Lipid stocks were prepared by dissolving dry lipids in chloroform or chloroform:methanol (9:1 v/v) at 10-30
9 mM. Mixtures were prepared from stocks at the desired molar ratios, followed by solvent evaporation under
10 a stream of nitrogen and lyophilizing overnight at -52 °C. The dried lipids were stored at -20 °C or used
11 directly for liposome preparation.

12 Liposomes were prepared by mixing dried lipids with water or HBS at 10-15 mM, followed by inverting at
13 ambient temperature for at least 3 h. Multilamellar vesicles (MLV) were prepared by freeze-thaw cycles in
14 liquid N₂ and a warm water bath and vortexing. The cycle was performed 7 times in total. Large unilamellar
15 vesicles (LUV) were prepared by passing fresh MLVs through a 0.1- μ m membrane 11 times at 40 °C. SUVs
16 were prepared by ultrasonication of fresh MLVs using a probe tip sonicator (Sonics & Materials Inc. Vibra-
17 Cell VC-130) until clarified. All lipid preparations were immediately used in experiments.

18

19 **Synchrotron radiation circular dichroism spectroscopy**

20 SRCD spectra were collected from 0.1 – 0.5 mg/ml protein samples in water on the AU-CD beamline at
21 ASTRID2 synchrotron (ISA, Aarhus, Denmark). Samples containing lipids were prepared right before
22 measurement by mixing proteins (P/L ratio 1:200) with SUVs. 100- μ m pathlength closed circular cells
23 (Suprasil, Hellma Analytics) were used for the measurements. Spectra were recorded from 170 to 280 nm at
24 30 °C. Baselines were subtracted and CD units converted to $\Delta\epsilon$ (M⁻¹ cm⁻¹) in CDtoolX (Miles and Wallace
25 2018). SDS and TFE were from Sigma-Aldrich and the detergents LDAO, OG, DM, and DPC from
26 Affymetrix.

27 Rapid kinetic SRCD data were collected as described (Raasakka *et al.* 2019a). In short, an SX-20 stopped-
28 flow instrument (Applied Photophysics) mounted on the AU-rSRCD branch line of the AU-AMO beamline
29 at ASTRID2 (ISA, Aarhus, Denmark) at was used for data collection at 10 °C. 1-to-1 mixing of a 0.1 mg/ml
30 protein solution and a DMPC:DMPG (1:1) SUV solution (at P/L ratios 1:200) was achieved using a mixer (2
31 ms dead time) before injection into the measurement cell (160 μ l total volume, 2-mm pathlength) per shot.
32 The CD signal (mdeg) was monitored at a fixed wavelength of 195 nm for 5 s with a total of 5 – 10 repeat
33 shots per sample, which were averaged into a single curve. Each sample was prepared and measured in

1 duplicate. Water baselines were subtracted from sample data. The data were fitted to different exponential
2 functions using GraphPad Prism 7.

3

4 **Surface plasmon resonance**

5 SPR was performed on a Biacore T200 system (GE Healthcare). According to the manufacturer's
6 instructions, 100-nm LUVs of 1 mM DMPC:DMPG (1:1) were immobilized on an L1 sensor chip (GE
7 Healthcare) in HBS, followed by the injection of protein solutions. Chip regeneration was performed using a
8 2:3 (v:v) mixture of 2-propanol and 50 mM NaOH. The protein concentration was 20 – 2000 nM in HBS,
9 and a single concentration per lipid capture was studied; all samples were prepared and measured in
10 duplicate. In each run, one sample was measured twice to rule out instrumental deviation. The binding
11 response as a function of protein concentration was plotted and fitted to the 4-parameter model,

$$12 \quad R = R_{hi} - \frac{R_{hi} - R_{lo}}{1 + \left(\frac{[P_{oct}]}{A_1}\right)^{A_2}},$$

13 to gain information about association affinity.

14

15 **Differential scanning calorimetry**

16 Proteins were mixed with MLVs in HBS at a protein-to-lipid ratio of 1:100 or 1:250, always containing 350
17 μ M of DMPC:DMPG (1:1) in a final volume of 700 μ l. Lipid samples without proteins were prepared as
18 controls. The samples were degassed for 10 min under vacuum with stirring at 10 °C before measurements.

19 DSC was performed using a MicroCal VP-DSC calorimeter with a cell volume of 527.4 μ l. The reference
20 cell was filled with HBS. Each sample was scanned from 10 to 40 °C and back to 10 °C in 1 °C/min
21 increments. Baselines were subtracted from sample curves and zeroed between 15 & 20 °C to enable
22 straightforward comparison between samples. All samples were prepared and measured twice, with the
23 observed trends being reproducible.

24

25 **Vesicle turbidimetry and X-ray diffraction experiments**

26 For turbidimetric measurements, SUVs of DMPC:DMPG (1:1) were mixed with 0.5 – 10 μ M protein in
27 duplicate and mixed thoroughly. Turbidity was recorded at 450 nm at 30 °C using a Tecan Spark 20M plate
28 reader. Turbidity of protein-free SUVs was subtracted from the protein samples, and statistical analysis was
29 performed using GraphPad Prism 7.

30 SAXD experiments were performed to investigate repetitive structures in the turbid samples. 10 and 20 μ M
31 proteins were mixed with SUVs of 1 – 3 mM DMPC:DMPG (1:1) in HBS at ambient temperature and

1 exposed at 25 °C on the EMBL P12 BioSAXS beamline, DESY (Hamburg, Germany). A HBS buffer
2 reference was subtracted from the data. Lipid samples without added protein did not produce Bragg peaks.
3 The peak positions of momentum transfer, s , in all measured samples were used to calculate mean repeat
4 distances, d , in proteolipid structures, using the equation

$$5 \quad d = \frac{2\pi}{s}, \text{ where } s = \frac{4\pi\sin\theta}{\lambda}.$$

6

7 **Electron microscopy**

8 For negatively stained EM, 740 μ M DMPC:DMPG (1:1) SUVs were mixed with proteins using protein-
9 to-lipid ratios of 1:58, 1:100, 1:200, and 1:500 and incubated at 22 °C for 1 h. EM grids were then
10 prepared, stained and imaged as described before (Raasakka *et al.* 2017; Raasakka *et al.* 2019b;
11 Ruskamo *et al.* 2017).

12

13 **Neutron reflectometry**

14 Supported lipid bilayers were prepared onto flat (5 Å RMS roughness tolerance) 80 mm \times 50 mm \times 15 mm
15 Si-crystal blocks (Sil'tronix Silicon Technologies, Archamps, France). Samples were prepared from a
16 chloroform-methanol stock of 1 mg/ml DMPC:DMPG (1:1). Using Langmuir-Blodgett and Langmuir-
17 Schaefer techniques, the two membrane leaflets of the bilayers were deposited sequentially. The surface
18 pressure was kept at a constant 30 mN m⁻¹ during the deposition, as described previously (Barker *et al.* 2016;
19 Hubbard *et al.* 2017; Raasakka *et al.* 2017). All sample blocks were assembled into low-volume
20 measurement flow cells, which were used for *in situ* exchange of solvent and injection of protein samples
21 between reflectometric data collections (Jungmans *et al.* 2015).

22 Neutron reflectometric measurements for wt-P0ct were performed as described (Raasakka *et al.* 2017). In
23 short, the D17 neutron reflectometer at the Institut Laue-Langevin (Grenoble, France) was used for data
24 collection at two incident angles (0.8° and 3.2°) (Cubitt and Fragneto 2002). All samples were kept at 30 °C
25 with HBS buffer as the liquid phase, prepared at a final concentration of 95% (v/v) deuterium oxide (D₂O,
26 Sigma-Aldrich) and in H₂O. The deposited bilayers were characterized, before and after the injection of P0ct,
27 at three different solvent contrasts, varying the volume ratio of D₂O and H₂O in to the sample cell: (1) 95%
28 D₂O, (2) Si-matched water (SMW; 38% (v/v) D₂O, 62% (v/v) H₂O), and (3) 100% H₂O. A 0.5 μ M P0ct
29 solution was allowed to interact with the membrane for 3 h whilst monitoring reflectivity, until no further
30 changes were observed. Any excess P0ct was washed out from the bulk solution by exchanging 20 cell
31 volumes of solvent slowly through the sample cell. Fitting was performed using Motofit in Igor Pro 7
32 (Nelson 2006).

1 The scattering length densities of the phospholipids were calculated from volume fractions of the lipid
2 components obtained from molecular dynamics simulations (Armen *et al.* 1998), and for the proteins, they
3 were calculated from the sequences and amino acid volumes (Zamyatnin 1972). The P0ct scattering length
4 density, assuming 90% labile hydrogen exchange, was 3.227, 2.324, and $1.722 \times 10^{-6} \text{ \AA}^{-2}$ in 95%, 38%, and
5 0% D₂O, respectively. The errors in the structural parameters for each sublayer were derived from the
6 maximum acceptable variation in the fitted thickness and lipid volume fraction that allowed a fit to be
7 maintained, subject to a constant molecular area constraint required to maintain a planar bilayer geometry.

8 Details of the analysis of supported lipid membrane structure (Vacklin *et al.* 2005) and interaction with
9 soluble proteins (Wacklin *et al.* 2016) using time-of-flight neutron reflection have been described previously.
10 The fraction of P0 in the lipid bilayers was determined by a simultaneous fit to all contrasts, taking into
11 account the change in protein scattering length density with solvent contrast due to H/D exchange of protons
12 on polar residues with the solvent.

13 For mutant comparison to wt-P0ct, NR data for wt-P0ct and D224Y were collected on the INTER neutron
14 reflectometer at ISIS Neutron and Muon Source (Didcot, United Kingdom) at two incident angles (0.7° and
15 2.3°) (Webster *et al.* 2006) covering a total q-range from 0.01 to 0.34 \AA^{-1} , with a resolution of $\Delta q/q=0.03$.
16 The samples were prepared and handled as above.

17
18

1 **Figure legends**

2 **Fig. 1. Overview of P0ct mutations.** (a) The primary sequence of the wt-P0ct construct, corresponding to
3 amino acids 180 – 248 of the human P0 precursor, with an extra N-terminal Gly residue (gray) left behind
4 from affinity tag cleavage. The Cys182 palmitoylation site was mutated into a Leu (green) in all constructs.
5 Putative serine phosphorylation sites are indicated with asterisks. Residues affected by disease mutations are
6 in bold. CMT1B, CMT2I, and DSS point mutations are shown in blue, red, and orange, respectively. The
7 sequence highlighted in yellow corresponds to the neuritogenic segment used in EAN models (de Sèze *et al.*
8 2016). Secondary structure prediction is shown below. (b) SEC traces of wt-P0ct and mutants as determined
9 using a Superdex 75 10/300GL column. Note the slightly earlier retention volume of D224Y, for which the
10 chromatography had to be performed with a different running buffer than for the other variants. The
11 degradation products (red asterisk) present with D224Y could be completely removed using SEC. The final
12 purity of each P0ct variant (4 μ g per lane) as determined using SDS-PAGE is shown as inset. (c) DLS data
13 of P0ct variants display good monodispersity with minimal variation in R_h .

14

15 **Fig. 2. SAXS analysis of P0ct in solution.** (a) SAXS data for P0ct variants. The scattering curves have been
16 offset for clarity. (b) Guinier fits based on SAXS data. Data range is shown within each graph. (c) Distance
17 distributions. (d) Kratky plots. P0ct variant data point coloring is consistent throughout the figure. GNOM
18 fits to the data are shown as black lines in panels (a) and (c).

19

20 **Fig. 3. Folding and lipid binding analysis of P0ct variants.** The folding of wt-P0ct and mutants was
21 studied using SRCD spectropolarimetry in (a) water, (b) 30% TFE, (c) 0.5% SDS, (d) DMPC:DMPG (1:1),
22 and (e) DMPC:DMPG (4:1) at 1:200 P/L ratio in each lipid condition. Additional spectra are presented in
23 Supplementary Fig. S2. (f) SPR measurements were used to determine the affinity of each P0ct variant to
24 immobilized DMPC:DMPG (1:1) vesicles. The colour coding legend in panel (a) for each mutant trace also
25 corresponds to all other traces in subsequent panels.

26

27 **Fig. 4. Analysis of protein-induced lipid structure behavior.** (a) DSC analysis of lipid tail transition
28 behaviour. (b) Turbidimetric analysis of 0.5 mM DMPC:DMPG (1:1) at 5 μ M (gray) and 10 μ M protein
29 concentration (dark red). These protein concentrations translate to 1:100 and 1:50 P/L ratios, respectively.
30 Error bars represent standard deviation. Statistical analysis was performed using one-way analysis of
31 variance (ANOVA) followed by Dunnett's multiple comparisons test to wt-P0ct turbidity within the same
32 protein concentration series (* : $P < 0.05$; *** : $P < 0.001$). (c) SAXD analysis reveals that D224Y displays a

1 significantly tighter mean repeat distances compared to wt-P0ct, whereas K236E is most loose. The traces
2 have identical colouring to (a).

3

4 **Fig. 5. EM analysis of P0ct mutants.** Negatively stained samples of DMPC:DMPG (1:1) vesicles (a) alone,
5 and with (b) wt-P0ct, (c) T216ER, (d) A221T, (e) D224Y, (f) R227S, (g) K236E, and (h) K236del
6 imaged at 1:200 P/L ratio. D224Y forms multilayered lipid structures that are absent for wt-P0ct.

7

8 **Fig. 6. SRCD stopped-flow kinetics of protein-induced initial lipid turbidification.** (a) The SRCD signal
9 evolution was monitored using rapid kinetics at 195 nm for 5 sec. wt-P0ct and mutants were mixed with
10 DMPC:DMPG (1:1) lipids at 1:200 P/L ratio in the presence of 150 mM NaF. Fits (dashed lines) are plotted
11 over the measurement points. Error bars represent standard deviation. See Table 4 for fitting results. (b)
12 Graphical comparison of the obtained k_1 values.

13

14 **Fig. 7. NR data and fitting.** (a) NR data of a supported DMPC:DMPG (1:1) bilayer before (open markers)
15 and after incubation with wt-P0ct (closed markers). The used solvent contrasts were 95% D₂O (red), Si-
16 matched water (SMW, 38% D₂O; green) and 100% H₂O (blue). Fits are shown as dashed and solid lines for
17 the bilayer before and after addition of wt-P0ct, respectively. (b) Scattering length density (ρ) profiles
18 obtained from the fitting. The error bars denote standard deviation. (c) Model for the P0ct-bound membrane.
19 The protein-free membrane is shown in light gray on the background.

20

21

1 **Tables**

2

3 **Table 1. Recombinant protein characterization.**

| Variant [*] | Condition | pI ^{**} | Purification | | Molecular weight determination | | | Peptide fingerprinting |
|----------------------|-----------|------------------|----------------------|------------|--------------------------------|---------------------------|------------|------------------------|
| | | | Yield ^{***} | Solubility | Measured | Theoretical ^{**} | Difference | Mutation confirmed |
| wt-P0ct | - | 11.11 | 2.1 ± 0.4 | ++ | 7989.0 | 7990.35 | -1.35 | - |
| T216ER | CMT1 | 11.08 | 4.2 ± 0.4 | +++ | 8173.0 | 8174.54 | -1.54 | yes |
| A221T | DSS | 11.11 | 5.0 ± 0.7 | +++ | 8018.0 | 8020.37 | -2.37 | yes |
| D224Y | CMT1 | 11.12 | 0.8 ± 0.3 | + | 8037.0 | 8038.43 | -1.43 | yes |
| R227S | CMT1 | 10.89 | 6.1 ± 2.0 | +++ | 7919.0 | 7921.24 | -2.24 | yes |
| K236E | CMT2 | 10.85 | 5.1 ± 1.8 | +++ | 7989.0 | 7991.29 | -2.29 | yes |
| K236del | CMT1 | 11.09 | 5.2 ± 1.0 | +++ | 7860.0 | 7862.17 | -2.17 | yes |

4 ^{*}All proteins, including wt-P0ct, contain the C182L mutation.

5 ^{**}Values determined from protein sequences using ProtParam

6 ^{***}Expressed as mg protein obtained on average per liter culture. See Supplementary Fig. 1 for graphical
7 representation.

8

9 **Table 2. SPR fitting parameters.**

| Variant | R _{hi} | R _{lo} | A ₁ | A ₂ | R ² |
|---------|-----------------|-----------------|----------------|----------------|----------------|
| wt-P0ct | 2975 ± 79 | -69.10 ± 61.54 | 363.2 ± 15.1 | 3.237 ± 0.411 | 0.9858 |
| T216ER | 3123 ± 86 | -44.63 ± 64.19 | 375.1 ± 15.6 | 3.173 ± 0.409 | 0.9854 |
| A221T | 3061 ± 82 | -44.81 ± 62.30 | 357.0 ± 15.5 | 2.973 ± 0.363 | 0.9863 |
| D224Y | 3811 ± 81 | 11.30 ± 66.26 | 385.2 ± 11.3 | 4.416 ± 0.540 | 0.9886 |
| R227S | 2798 ± 78 | -39.52 ± 55.20 | 384.9 ± 16.0 | 2.936 ± 0.361 | 0.9864 |
| K236E | 2671 ± 92 | -49.48 ± 60.00 | 380.8 ± 20.0 | 2.526 ± 0.340 | 0.9831 |
| K236del | 2880 ± 79 | -33.85 ± 58.90 | 356.1 ± 16.0 | 2.852 ± 0.347 | 0.9862 |

10

11

12

13 **Table 3. Kinetic constants for protein-induced vesicle turbidity.** The kinetic constants were obtained by
14 fitting the data to a two-phase exponential decay function. All errors represent standard deviation.

15

| Variant | k ₁ (s ⁻¹) | k ₂ (s ⁻¹) | k ₁ /k ₂ | R ² |
|---------|-----------------------------------|-----------------------------------|--------------------------------|----------------|
| wt-P0ct | 20.14 ± 0.25 | 1.12 ± 0.01 | 17.96 ± 0.22 | 0.9934 |
| T216ER | 19.54 ± 0.28 | 1.18 ± 0.02 | 16.63 ± 0.25 | 0.9908 |
| A221T | 19.15 ± 0.21 | 1.14 ± 0.01 | 16.76 ± 0.20 | 0.9943 |
| D224Y | 22.11 ± 0.28 | 1.19 ± 0.02 | 18.53 ± 0.25 | 0.9923 |
| R227S | 19.35 ± 0.27 | 1.08 ± 0.02 | 17.95 ± 0.26 | 0.9916 |
| K236E | 14.98 ± 0.12 | 1.02 ± 0.01 | 14.64 ± 0.13 | 0.9969 |
| K236del | 14.25 ± 0.12 | 1.05 ± 0.01 | 13.54 ± 0.13 | 0.9967 |

1

2

3 **Table 4. NR parameters.**

| | | Bilayer alone | Bilayer with 0.5 μM wt-P0ct |
|------------------|--|----------------------|---|
| Substrate | Oxide thickness (\AA) | 10.6 | 11 |
| | Oxide solvation (%) | 0 | 0 |
| | Oxide roughness (\AA) | 4 | 4 |
| | Hydration layer between oxide and bilayer (\AA) | 4.6 | 12 |
| | Hydration layer roughness (\AA) | 3 | 6 |
| Bilayer | Bilayer area-per-molecule ($\text{\AA}^2/\text{molecule}$) | 60 | 70 |
| | Inner headgroups thickness (\AA) | 8.3 | 8 |
| | Inner headgroups roughness (\AA) | 3.6 | 8.1 |
| | Inner headgroups solvation (%) | 35 | 45 |
| | Acyl tails thickness (\AA) | 28.8 | 32 |
| | Acyl tails roughness (\AA) | 3.8 | 13.3 |
| | Acyl tails hydration (%) | 0 | 17 |
| | Outer headgroups thickness (\AA) | 8.8 | 8 |
| | Outer headgroups roughness (\AA) | 4.9 | 9.5 |
| | Outer headgroups solvation (%) | 35 | 53.5 |
| wt-P0ct | Protein in inner headgroups (%) | | 0 |
| | Protein in acyl tails (%) | | 10 |
| | Protein in outer headgroups (%) | | 20 |
| | Protein layer thickness (\AA) | | 7 |
| | Protein layer roughness (\AA) | | 15 |
| | Protein layer solvation (%) | | 86 |

4

5

6

1 References

- 2 Armen R.S., Uitto O.D. and Feller S.E. (1998) Phospholipid component volumes: determination
3 and application to bilayer structure calculations. *Biophys J* 75, 734-744.
- 4 Bai Y., Patzko A. and Shy M.E. (2013) Unfolded protein response, treatment and CMT1B. *Rare*
5 *Dis* 1, e24049.
- 6 Bai Y., Wu X., Brennan K.M., Wang D.S., D'Antonio M., Moran J., Svaren J. and Shy M.E. (2018)
7 Myelin protein zero mutations and the unfolded protein response in Charcot Marie Tooth
8 disease type 1B. *Ann Clin Transl Neurol* 5, 445-455.
- 9 Barker R.D., McKinley L.E. and Titmuss S. (2016) Neutron Reflectivity as a Tool for Physics-
10 Based Studies of Model Bacterial Membranes. *Adv Exp Med Biol* 915, 261-282.
- 11 Blanchet C.E., Spilotos A., Schwemmer F., Graewert M.A., Kikhney A., Jeffries C.M., Franke D.,
12 Mark D., Zengerle R., Cipriani F., Fiedler S., Roessle M. and Svergun D.I. (2015) Versatile
13 sample environments and automation for biological solution X-ray scattering experiments at
14 the P12 beamline (PETRA III, DESY). *J Appl Crystallogr* 48, 431-443.
- 15 Busso D., Delagoutte-Busso B. and Moras D. (2005) Construction of a set Gateway-based
16 destination vectors for high-throughput cloning and expression screening in *Escherichia coli*.
17 *Anal Biochem* 343, 313-321.
- 18 Choi B.O., Lee M.S., Shin S.H., Hwang J.H., Choi K.G., Kim W.K., Sunwoo I.N., Kim N.K. and
19 Chung K.W. (2004) Mutational analysis of PMP22, MPZ, GJB1, EGR2 and NEFL in Korean
20 Charcot-Marie-Tooth neuropathy patients. *Hum Mutat* 24, 185-186.
- 21 Cubitt R. and Fragneto G. (2002) D17: the new reflectometer at the ILL. *Applied Physics A* 74,
22 s329-s331.
- 23 de Sèze J., Kremer L., Alves do Rego C., Taleb O., Lam D., Beiano W., Mensah-Nyagan G.,
24 Trifilieff E. and Brun S. (2016) Chronic inflammatory demyelinating polyradiculoneuropathy:
25 A new animal model for new therapeutic targets. *Rev Neurol (Paris)* 172, 767-769.
- 26 Drozdetskiy A., Cole C., Procter J. and Barton G.J. (2015) JPred4: a protein secondary structure
27 prediction server. *Nucleic Acids Res* 43, W389-94.
- 28 Eichberg J. (2002) Myelin P0: new knowledge and new roles. *Neurochem Res* 27, 1331-1340.
- 29 Fabrizi G.M., Pellegrini M., Angiari C., Cavallaro T., Morini A., Taioli F., Cabrini I., Orrico D. and
30 Rizzuto N. (2006) Gene dosage sensitivity of a novel mutation in the intracellular domain of
31 P0 associated with Charcot-Marie-Tooth disease type 1B. *Neuromuscul Disord* 16, 183-187.
- 32 Filbin M.T., Walsh F.S., Trapp B.D., Pizzey J.A. and Tennekoon G.I. (1990) Role of myelin P0
33 protein as a homophilic adhesion molecule. *Nature* 344, 871-872.
- 34 Franke D., Petoukhov M.V., Konarev P.V., Panjkovich A., Tuukkanen A., Mertens H.D.T.,
35 Kikhney A.G., Hajizadeh N.R., Franklin J.M., Jeffries C.M. and Svergun D.I. (2017) ATSAS
36 2.8: a comprehensive data analysis suite for small-angle scattering from macromolecular
37 solutions. *J Appl Crystallogr* 50, 1212-1225.
- 38 Greenfield S., Brostoff S., Eylar E.H. and Morell P. (1973) Protein composition of myelin of the
39 peripheral nervous system. *J Neurochem* 20, 1207-1216.
- 40 Hartline D.K. (2008) What is myelin? *Neuron Glia Biol* 4, 153-163.
- 41 Hubbard A.T., Barker R., Rehal R., Vandera K.A., Harvey R.D. and Coates A.R. (2017)
42 Mechanism of Action of a Membrane-Active Quinoline-Based Antimicrobial on Natural and
43 Model Bacterial Membranes. *Biochemistry* 56, 1163-1174.
- 44 Junghans A., Watkins E.B., Barker R.D., Singh S., Waltman M.J., Smith H.L., Pocivavsek L. and
45 Majewski J. (2015) Analysis of biosurfaces by neutron reflectometry: from simple to complex
46 interfaces. *Biointerphases* 10, 019014.
- 47 Kidd G.J., Yadav V.K., Huang P., Brand S.L., Low S.H., Weimbs T. and Trapp B.D. (2006) A dual
48 tyrosine-leucine motif mediates myelin protein P0 targeting in MDCK cells. *Glia* 54, 135-145.
- 49 Lee M., Brennan A., Blanchard A., Zoidl G., Dong Z., Taberner A., Zoidl C., Dent M.A., Jessen

- 1 K.R. and Mirsky R. (1997) P0 is constitutively expressed in the rat neural crest and embryonic
2 nerves and is negatively and positively regulated by axons to generate non-myelin-forming
3 and myelin-forming Schwann cells, respectively. *Mol Cell Neurosci* 8, 336-350.
- 4 Lee Y.C., Lin K.P., Chang M.H., Liao Y.C., Tsai C.P., Liao K.K. and Soong B.W. (2010) Cellular
5 characterization of MPZ mutations presenting with diverse clinical phenotypes. *J Neurol* 257,
6 1661-1668.
- 7 Lemke G. and Axel R. (1985) Isolation and sequence of a cDNA encoding the major structural
8 protein of peripheral myelin. *Cell* 40, 501-508.
- 9 Luo X., Sharma D., Inouye H., Lee D., Avila R.L., Salmons M. and Kirschner D.A. (2007)
10 Cytoplasmic domain of human myelin protein zero likely folded as beta-structure in compact
11 myelin. *Biophys J* 92, 1585-1597.
- 12 Maeda M.H., Mitsui J., Soong B.W., Takahashi Y., Ishiura H., Hayashi S., Shiota Y., Ichikawa Y.,
13 Matsumoto H., Arai M., Okamoto T., Miyama S., Shimizu J., Inazawa J., Goto J. and Tsuji S.
14 (2012) Increased gene dosage of myelin protein zero causes Charcot-Marie-Tooth disease.
15 *Ann Neurol* 71, 84-92.
- 16 Mandich P., Fossa P., Capponi S., Geroldi A., Acquaviva M., Gulli R., Ciotti P., Manganelli F.,
17 Grandis M. and Bellone E. (2009) Clinical features and molecular modelling of novel MPZ
18 mutations in demyelinating and axonal neuropathies. *Eur J Hum Genet* 17, 1129-1134.
- 19 Martini R., Zielasek J., Toyka K.V., Giese K.P. and Schachner M. (1995) Protein zero (P0)-
20 deficient mice show myelin degeneration in peripheral nerves characteristic of inherited
21 human neuropathies. *Nat Genet* 11, 281-286.
- 22 Miles A.J. and Wallace B.A. (2018) CDtoolX, a downloadable software package for processing and
23 analyses of circular dichroism spectroscopic data. *Protein Sci* 27, 1717-1722.
- 24 Miltenberger-Miltenyi G., Schwarzbraun T., Löscher W.N., Wanschitz J., Windpassinger C., Duba
25 H.C., Seidl R., Albrecht G., Weirich-Schwaiger H., Zoller H., Utermann G., Auer-Grumbach
26 M. and Janecke A.R. (2009) Identification and in silico analysis of 14 novel GJB1, MPZ and
27 PMP22 gene mutations. *Eur J Hum Genet* 17, 1154-1159.
- 28 Nelson A. (2006) Co-refinement of multiple-contrast neutron/X-ray reflectivity data using
29 MOTOFIT. *J Appl Crystallogr* 39, 273-276.
- 30 Patzig J., Jahn O., Tenzer S., Wichert S.P., de Monasterio-Schrader P., Rosfa S., Kuharev J., Yan
31 K., Bormuth I., Bremer J., Aguzzi A., Orfaniotou F., Hesse D., Schwab M.H., Möbius W.,
32 Nave K.A. and Werner H.B. (2011) Quantitative and integrative proteome analysis of
33 peripheral nerve myelin identifies novel myelin proteins and candidate neuropathy loci. *J*
34 *Neurosci* 31, 16369-16386.
- 35 Planté-Bordeneuve V., Parman Y., Guiochon-Mantel A., Alj Y., Deymeer F., Serdaroglu P.,
36 Eraksoy M. and Said G. (2001) The range of chronic demyelinating neuropathy of infancy: a
37 clinico-pathological and genetic study of 15 unrelated cases. *J Neurol* 248, 795-803.
- 38 Quattrini A., Feltri M.L., Previtali S., Fasolini M., Messing A. and Wrabetz L. (1999) Peripheral
39 nerve dysmyelination due to P0 glycoprotein overexpression is dose-dependent. *Ann N Y*
40 *Acad Sci* 883, 294-301.
- 41 Raasakka A., Jones N.C., Hoffmann S.V. and Kursula P. (2019a) Ionic strength and calcium
42 regulate the membrane interactions of myelin basic protein and the cytoplasmic domain of
43 myelin protein zero. *bioRxiv* 529586.
- 44 Raasakka A., Ruskamo S., Kowal J., Barker R., Baumann A., Martel A., Tuusa J., Myllykoski M.,
45 Bürck J., Ulrich A.S., Stahlberg H. and Kursula P. (2017) Membrane Association Landscape
46 of Myelin Basic Protein Portrays Formation of the Myelin Major Dense Line. *Sci Rep* 7,
47 4974.
- 48 Raasakka A., Ruskamo S., Kowal J., Han H., Baumann A., Myllykoski M., Fasano A., Rossano R.,
49 Riccio P., Bürck J., Ulrich A.S., Stahlberg H., Kursula P. and (2019b) Molecular structure and
50 function of myelin protein P0 in membrane stacking. *Sci Rep* 9, 642.

- 1 Ruskamo S., Nieminen T., Kristiansen C.K., Vatne G.H., Baumann A., Hallin E.I., Raasakka A.,
2 Joensuu P., Bergmann U., Vattulainen I. and Kursula P. (2017) Molecular mechanisms of
3 Charcot-Marie-Tooth neuropathy linked to mutations in human myelin protein P2. *Sci Rep* 7,
4 6510.
- 5 Ruskamo S., Yadav R.P., Sharma S., Lehtimäki M., Laulumaa S., Aggarwal S., Simons M., Bürck
6 J., Ulrich A.S., Juffer A.H., Kursula I. and Kursula P. (2014) Atomic resolution view into the
7 structure-function relationships of the human myelin peripheral membrane protein P2. *Acta*
8 *Crystallogr D Biol Crystallogr* 70, 165-176.
- 9 Schneider-Gold C., Kötting J., Epplen J.T., Gold R. and Gerding W.M. (2010) Unusual Charcot-
10 Marie-Tooth phenotype due to a mutation within the intracellular domain of myelin protein
11 zero. *Muscle Nerve* 41, 550-554.
- 12 Sedzik J., Blaurock A.E. and Hoechli M. (1985) Reconstituted P2/myelin-lipid multilayers. *J*
13 *Neurochem* 45, 844-852.
- 14 Shapiro L., Doyle J.P., Hensley P., Colman D.R. and Hendrickson W.A. (1996) Crystal structure of
15 the extracellular domain from P0, the major structural protein of peripheral nerve myelin.
16 *Neuron* 17, 435-449.
- 17 Shy M.E., Jäni A., Krajewski K., Grandis M., Lewis R.A., Li J., Shy R.R., Balsamo J., Lilien J.,
18 Garbern J.Y. and Kamholz J. (2004) Phenotypic clustering in MPZ mutations. *Brain* 127, 371-
19 384.
- 20 Speevak M.D. and Farrell S.A. (2013) Charcot-Marie-Tooth 1B caused by expansion of a familial
21 myelin protein zero (MPZ) gene duplication. *Eur J Med Genet* 56, 566-569.
- 22 Stassart R.M., Möbius W., Nave K.A. and Edgar J.M. (2018) The Axon-Myelin Unit in
23 Development and Degenerative Disease. *Front Neurosci* 12, 467.
- 24 Street V.A., Meekins G., Lipe H.P., Seltzer W.K., Carter G.T., Kraft G.H. and Bird T.D. (2002)
25 Charcot-Marie-Tooth neuropathy: clinical phenotypes of four novel mutations in the MPZ and
26 Cx 32 genes. *Neuromuscul Disord* 12, 643-650.
- 27 Su Y., Brooks D.G., Li L., Lepercq J., Trofatter J.A., Ravetch J.V. and Lebo R.V. (1993) Myelin
28 protein zero gene mutated in Charcot-Marie-tooth type 1B patients. *Proc Natl Acad Sci U S A*
29 90, 10856-10860.
- 30 Suresh S., Wang C., Nanekar R., Kursula P. and Edwardson J.M. (2010) Myelin basic protein and
31 myelin protein 2 act synergistically to cause stacking of lipid bilayers. *Biochemistry* 49, 3456-
32 3463.
- 33 Svergun D.I. (1992) Determination of the regularization parameter in indirect-transform methods
34 using perceptual criteria. *J Appl Cryst* 25, 495-503.
- 35 Vacklin H.P., Tiberg F., Fragneto G. and Thomas R.K. (2005) Composition of supported model
36 membranes determined by neutron reflection. *Langmuir* 21, 2827-2837.
- 37 Vassall K.A., Bamm V.V. and Harauz G. (2015) MyelStones: the executive roles of myelin basic
38 protein in myelin assembly and destabilization in multiple sclerosis. *Biochem J* 472, 17-32.
- 39 Wacklin H.P., Bremec B.B., Moulin M., Rojko N., Haertlein M., Forsyth T., Anderlüh G. and
40 Norton R.S. (2016) Neutron reflection study of the interaction of the eukaryotic pore-forming
41 actinoporin equinatoxin II with lipid membranes reveals intermediate states in pore formation.
42 *Biochim Biophys Acta* 1858, 640-652.
- 43 Wang C., Neugebauer U., Bürck J., Myllykoski M., Baumgärtel P., Popp J. and Kursula P. (2011)
44 Charge isomers of myelin basic protein: structure and interactions with membranes,
45 nucleotide analogues, and calmodulin. *PLoS One* 6, e19915.
- 46 Webster J., Holt S. and Dalgliesh R. (2006) INTER the chemical interfaces reflectometer on target
47 station 2 at ISIS. *Physica B: Condensed Matter* 385, 1164-1166.
- 48 Wong M.H. and Filbin M.T. (1994) The cytoplasmic domain of the myelin P0 protein influences
49 the adhesive interactions of its extracellular domain. *J Cell Biol* 126, 1089-1097.
- 50 Wrabetz L., D'Antonio M., Pennuto M., Dati G., Tinelli E., Fratta P., Previtali S., Imperiale D.,

- 1 Zielasek J., Toyka K., Avila R.L., Kirschner D.A., Messing A., Feltri M.L. and Quattrini A.
2 (2006) Different intracellular pathomechanisms produce diverse Myelin Protein Zero
3 neuropathies in transgenic mice. *J Neurosci* 26, 2358-2368.
- 4 Wrabetz L., Feltri M.L., Quattrini A., Imperiale D., Previtali S., D'Antonio M., Martini R., Yin X.,
5 Trapp B.D., Zhou L., Chiu S.Y. and Messing A. (2000) P(0) glycoprotein overexpression
6 causes congenital hypomyelination of peripheral nerves. *J Cell Biol* 148, 1021-1034.
- 7 Xu W., Shy M., Kamholz J., Elferink L., Xu G., Lilien J. and Balsamo J. (2001) Mutations in the
8 cytoplasmic domain of P0 reveal a role for PKC-mediated phosphorylation in adhesion and
9 myelination. *J Cell Biol* 155, 439-446.
- 10 Zamyatnin A.A. (1972) Protein volume in solution. *Prog Biophys Mol Biol* 24, 107-123.
- 11 Zenker J., Stettner M., Ruskamo S., Domènech-Estévez E., Baloui H., Médard J.J., Verheijen M.H.,
12 Brouwers J.F., Kursula P., Kieseier B.C. and Chrast R. (2014) A role of peripheral myelin
13 protein 2 in lipid homeostasis of myelinating Schwann cells. *Glia* 62, 1502-1512.
- 14
- 15

1 **Acknowledgements**

2 This work was financially supported by the Academy of Finland (Finland), the Jane and Aatos Erkko
3 Foundation (Finland), and the Norwegian Research Council (SYNKNØYT program). This work has been
4 supported by iNEXT, grant number 653706, funded by the Horizon 2020 programme of the European
5 Commission. The research leading to this result has been supported by the project CALIPSOplus under the
6 Grant Agreement 730872 from the EU Framework Programme for Research and Innovation HORIZON
7 2020. We gratefully acknowledge the synchrotron radiation facilities and the beamline support at ASTRID2
8 and EMBL/DESY, as well as the ILL (Proposal No. 8-02-745) and STFC/ISIS (Proposal No. 1620422;
9 doi:10.5286/ISIS.E.95673822). We express our gratitude towards the Biocenter Oulu Proteomics and Protein
10 Analysis Core Facility for providing access to mass spectrometric instrumentation, as well as the Biophysics,
11 Structural Biology, and Screening (BiSS) facilities at the University of Bergen. Finally, we thank Anushik
12 Safaryan for practical help with liposome preparation.

13

14 **Author contributions**

15 Original text and figures: A.R., P.K.

16 Prepared mutant constructs: A.R., C.K.K., G.H.V., E.I.H.

17 Protein expression and purification: A.R., O.C.K.

18 Prepared samples and performed experiments: A.R., S.R., R.B., M.W.A.S., U.B.

19 Processed and analyzed data: A.R., R.B., U.B., H.W., N.J., S.V.H., P.K.

20 Study design: A.R., S.R., P.K.

21 Review & editing: A.R., S.R., R.B., H.W., N.J., S.V.H., P.K.

22 Supervision: P.K.

23

24 **Competing financial interests**

25 The authors declare no competing financial interests.

26

27 **Data availability**

28 The datasets generated and analyzed during the current study are available from the corresponding author on
29 reasonable request.

1 **Supplementary information**

2

3 **Supplementary Fig. S1. Protein yield.** The purified protein amount from *E. coli* expression, shown as mg
4 of protein obtained per 1 l of culture.

5

6 **Supplementary Fig. S2. The folding of P0ct variants in TFE, detergents, and poorly binding**
7 **membrane compositions.** The folding of wt-P0ct and mutants was studied using SRCD spectropolarimetry
8 in (a) 10% TFE, (b) 50% TFE, (c) 70% TFE, (d) 0.1% DPC, (e) 1% LDAO, (f) 1% OG, (g) DMPC, and (h)
9 9:1 DMPC:DMPG. The colour coding legend in panel (a) for each mutant trace also corresponds to all other
10 traces in subsequent panels.

11

12 **Supplementary Fig. S3. P0ct variant-induced turbidimetry and diffraction.** (a) Turbidimetric analysis of
13 0.5 mM DMPC:DMPG (1:1) vesicles in the presence of 0 – 10 μ M wt-P0ct and mutants. BSA was included
14 as negative control. Error bars represent standard deviation. (b) Examples of Bragg peaks from the P0ct
15 samples mixed with DMPC:DMPG (1:1) vesicles.

16

17 **Supplementary Fig. S4. EM analysis of P0ct D224Y.** Negatively stained samples of DMPC:DMPG (1:1)
18 vesicles mixed with P0ct D224Y at (a) 1:100, (b) 1:200, and (c) 1:500 P/L ratios all display multilayered
19 lipid structures.

20

21 **Supplementary Fig. S5. NR data of wt-P0ct and D224Y.** NR data for DMPC:DMPG (1:1)-bound wt-P0ct
22 and D224Y. The data have been offset for clarity. Solvent contrasts are indicated for each trace on their right
23 hand side. The D224Y H₂O data is incomplete as reflectivity was collected at only one measurement angle
24 (0.7°). The error bars denote standard deviation.

25

26

1 **Supplementary Table 1. DLS parameters.**

| Protein variant | wt-P0ct | T216ER | A221T | D224Y | R227S | K236E | K236del |
|-----------------|---------|--------|-------|-------|-------|-------|---------|
| Sample buffer* | HBS | HBS | HBS | TBS | HBS | HBS | HBS |
| R_h (nm) | 2.96 | 2.87 | 2.72 | 2.26 | 2.93 | 2.88 | 2.80 |

*HBS, 20 mM HEPES, 150 mM NaCl, pH 7.5; TBS, 20 mM Tris-HCl, 300 mM NaCl, pH 8.5.

3

4 **Supplementary Table 2. SAXS parameters.**

| Data collection parameters | | | | | | | |
|---|---------------------|-----------|-----------|-----------|-----------|------------|-----------|
| Instrument | P12, PETRAIII, DESY | | | | | | |
| Wavelength (nm) | 0.124 | | | | | | |
| Angular range (nm ⁻¹) | 0.0403 - 7.3195 | | | | | | |
| Exposure time (s) | 0.045 | | | | | | |
| Measurement temperature (°C) | 10 | | | | | | |
| Protein variant | wt-P0ct | T216ER | A221T | D224Y | R227S | K236E | K236del |
| Concentration range (mg ml ⁻¹) | 0.3 - 1.2 | 1.0 - 3.8 | 2.0 - 8.0 | 0.5 - 2.1 | 1.7 - 6.8 | 3.5 - 12.9 | 2.3 - 9.3 |
| Sample buffer* | HBS | HBS | HBS | TBS | HBS | HBS | HBS |
| Structural parameters | | | | | | | |
| I_0 (relative) [from p(r)] | 58.90 | 64.72 | 59.06 | 58.27 | 56.14 | 62.73 | 58.17 |
| R_g (nm) [from p(r)] | 2.57 | 2.50 | 2.40 | 2.73 | 2.42 | 2.41 | 2.41 |
| I_0 (relative) [from Guinier] | 58.25 | 63.87 | 58.35 | 57.38 | 55.21 | 61.61 | 57.30 |
| R_g (nm) [from Guinier] | 2.39 | 2.33 | 2.26 | 2.43 | 2.25 | 2.23 | 2.23 |
| D_{max} (nm) [from GNOM] | 9.59 | 9.21 | 9.59 | 11.57 | 8.96 | 10.34 | 10.69 |
| Molecular mass determination | | | | | | | |
| Molecular mass M_r (kDa) [from I_0 using p(r)] | 7.87 | 8.65 | 7.89 | 7.79 | 7.50 | 8.38 | 7.78 |
| Molecular mass M_r (kDa) [from I_0 using Guinier] | 7.79 | 8.54 | 7.80 | 7.67 | 7.38 | 8.24 | 7.66 |
| Theoretical M_r from sequence (kDa) | 7.99 | 8.17 | 8.02 | 8.04 | 7.92 | 7.99 | 7.86 |
| Software | | | | | | | |
| Primary data reduction & processing | PRIMUS | | | | | | |

*HBS, 20 mM HEPES, 150 mM NaCl, pH 7.5; TBS, 20 mM Tris-HCl, 300 mM NaCl, pH 8.5.

6

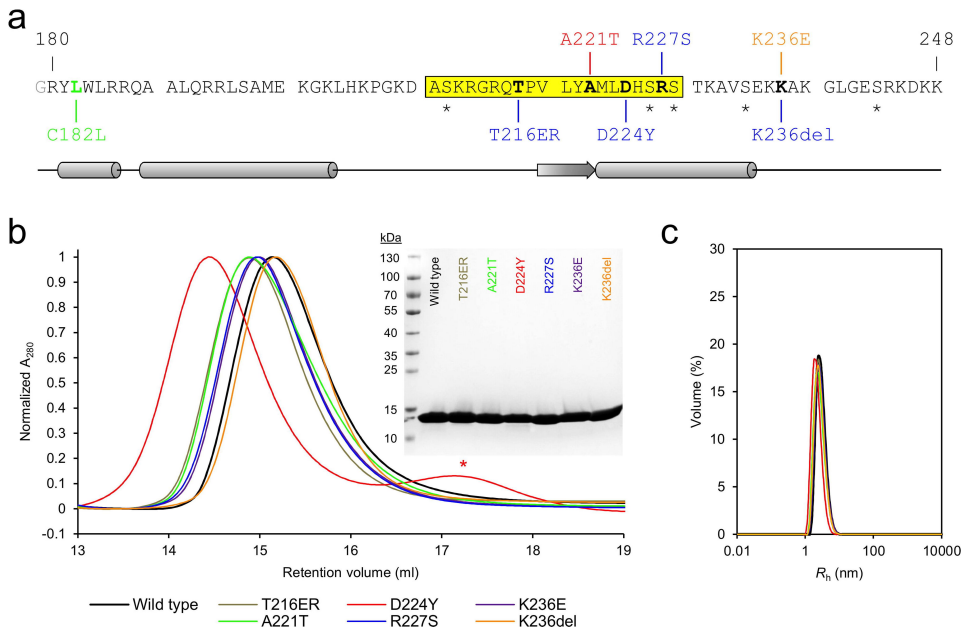


Fig.1

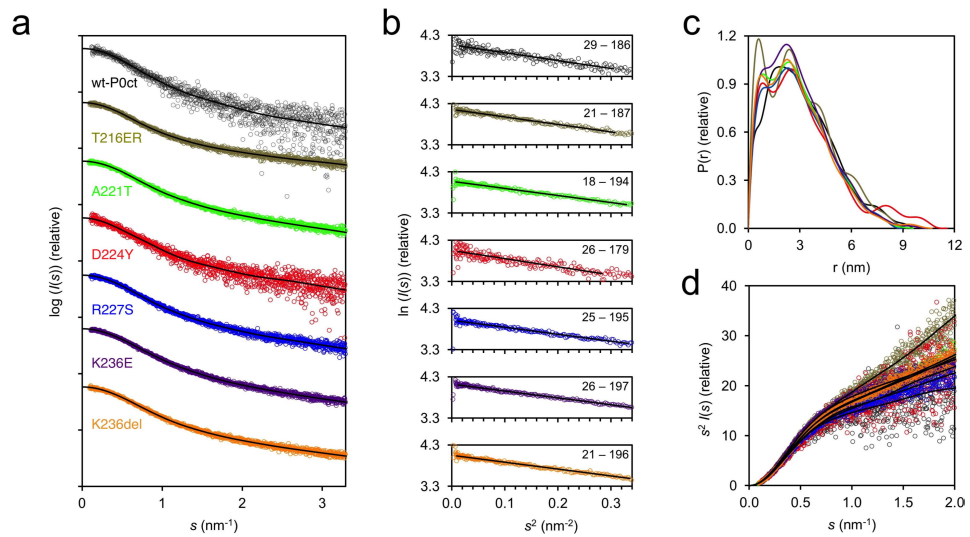


Fig. 2

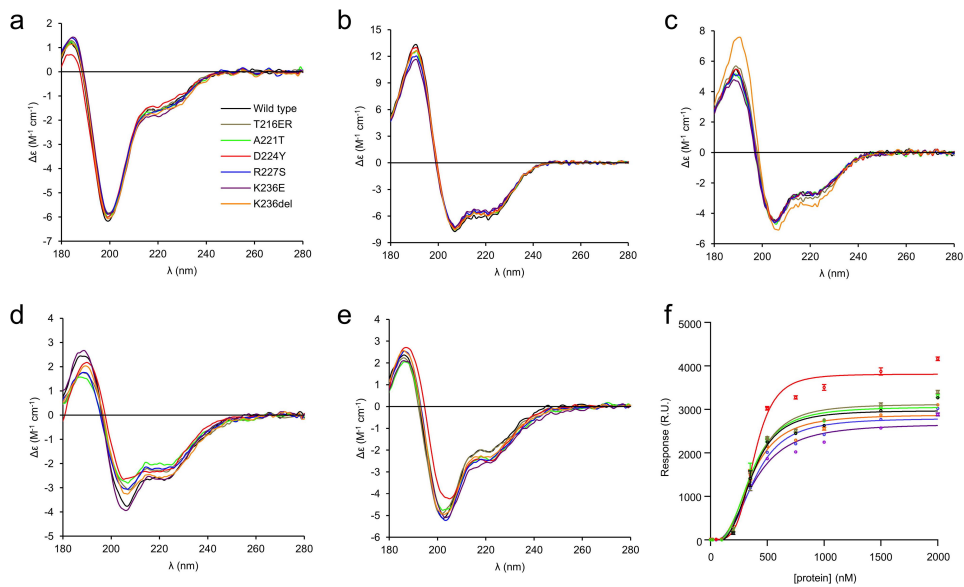


Fig. 3

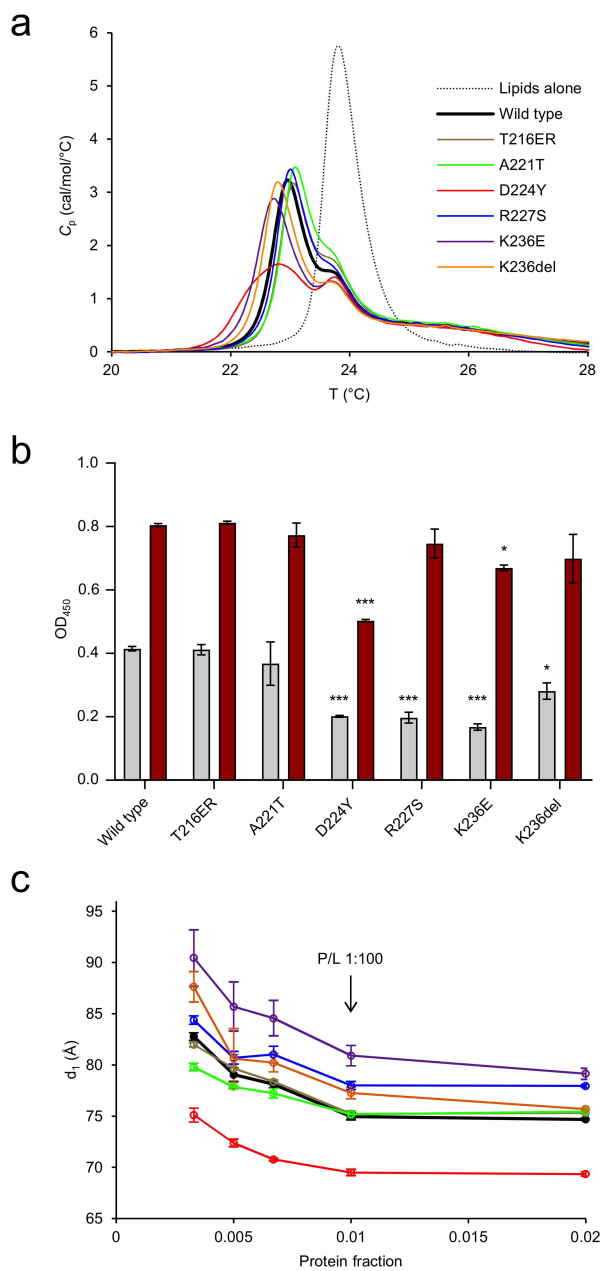


Fig. 4

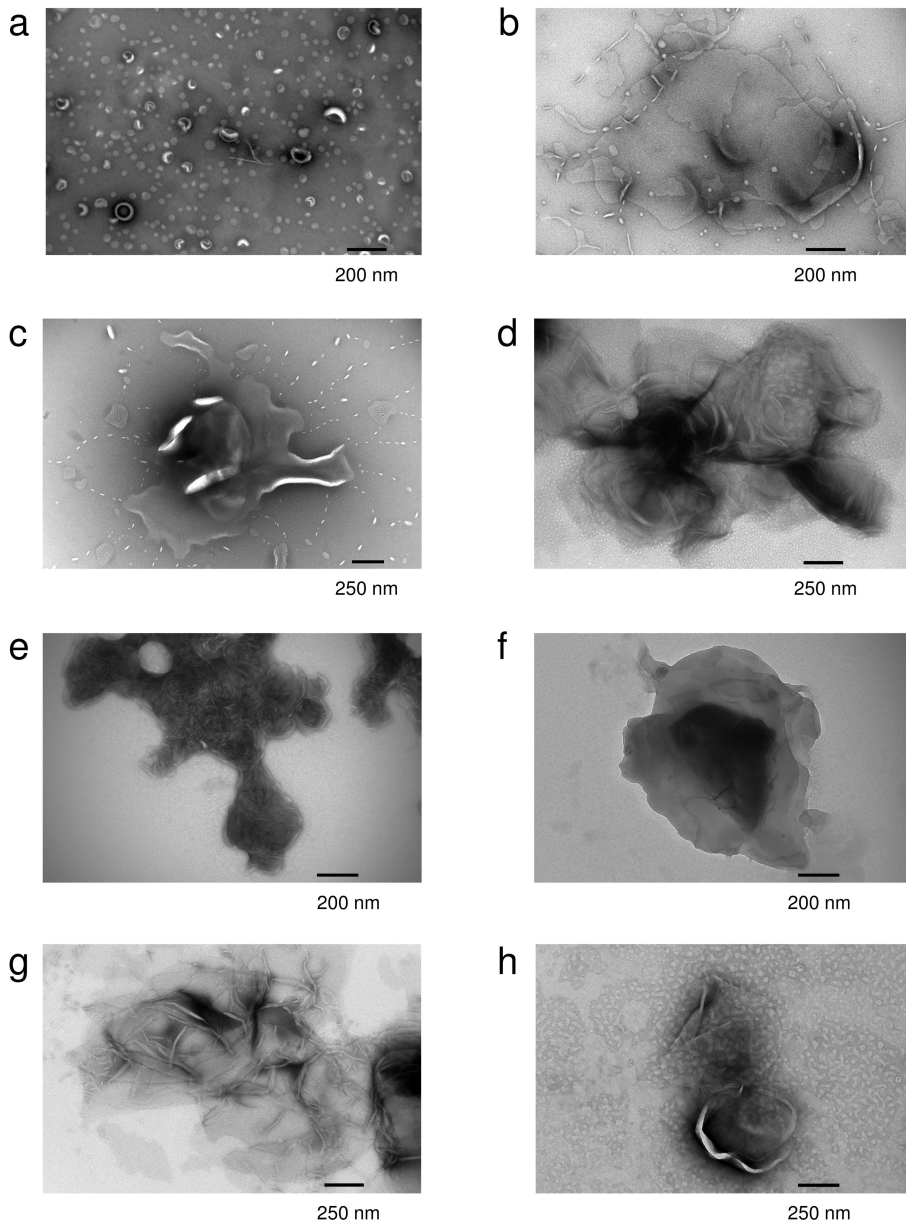


Fig. 5

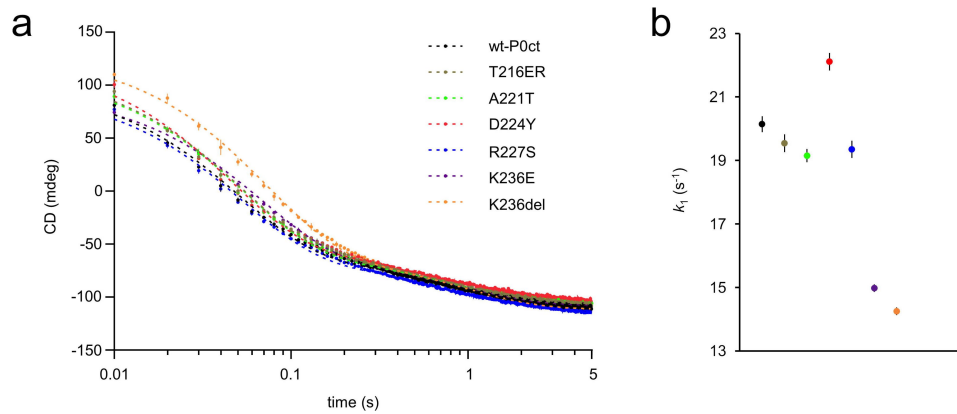


Fig. 6

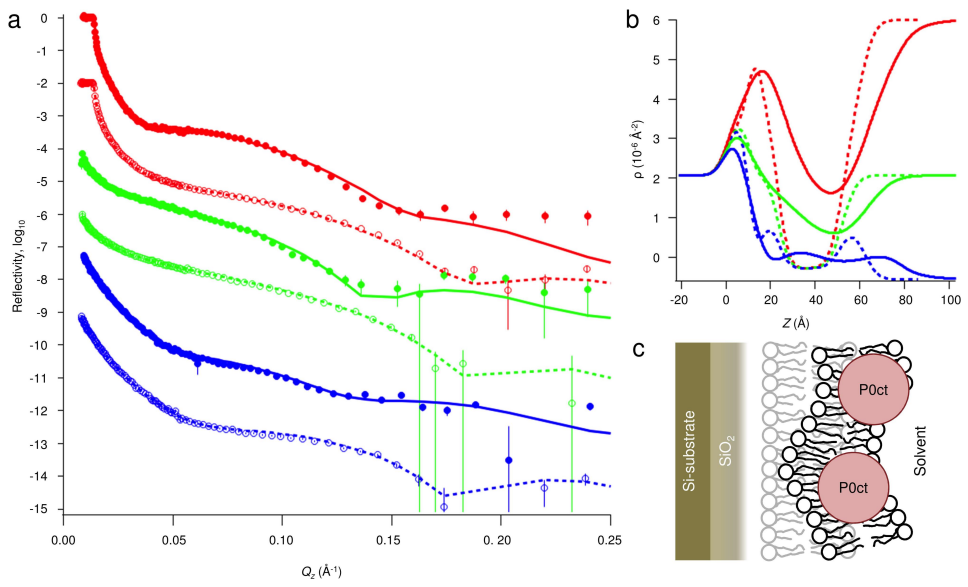
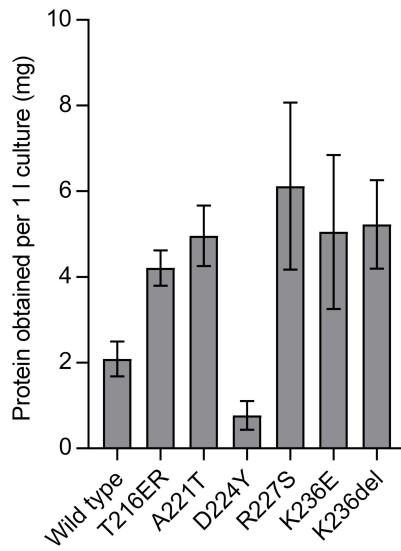
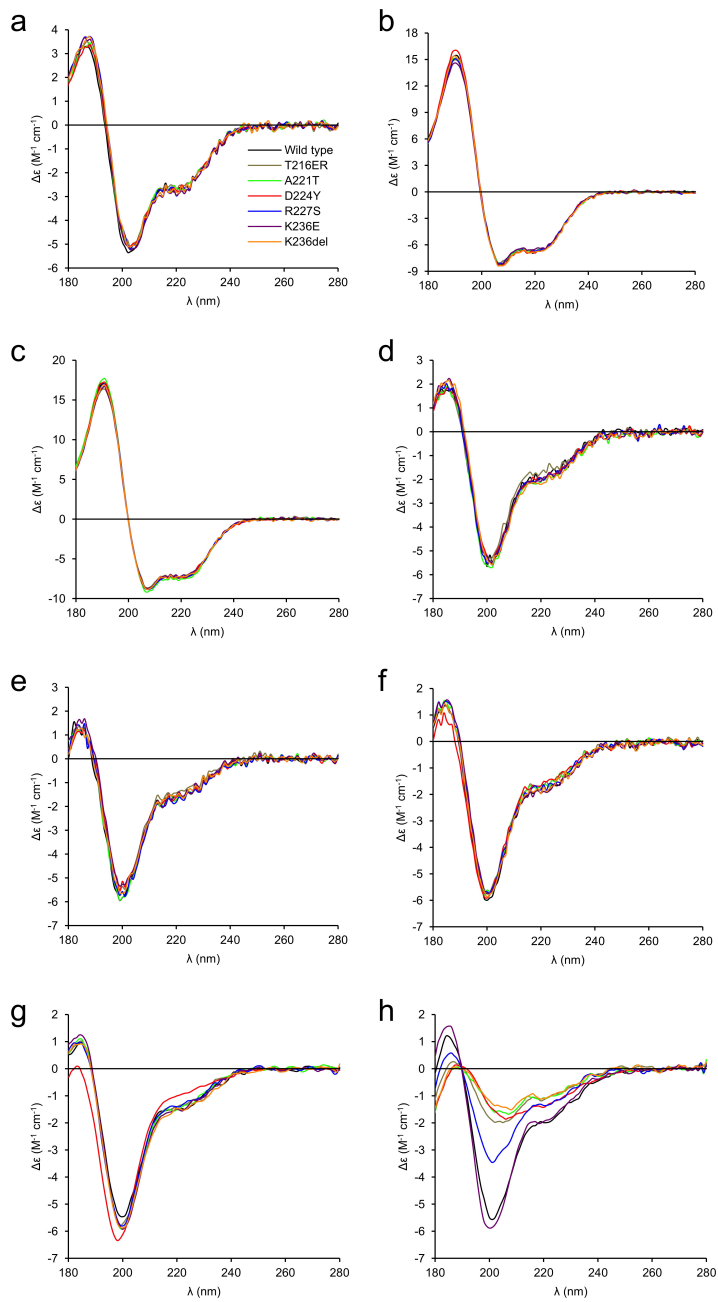


Fig. 7

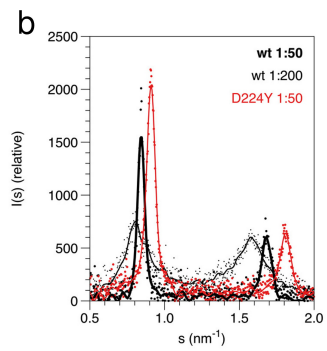
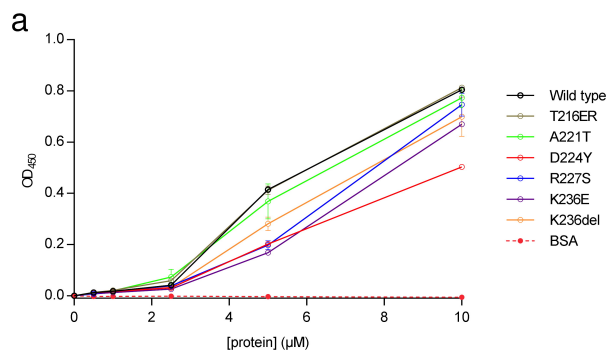
Supplementary information



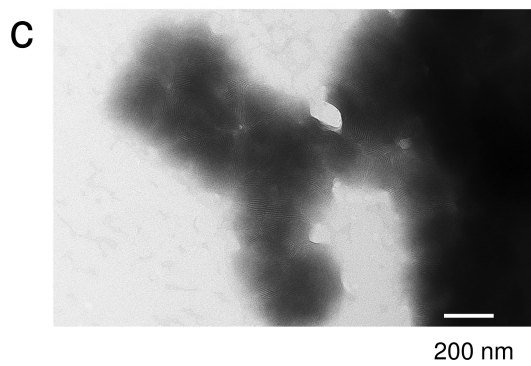
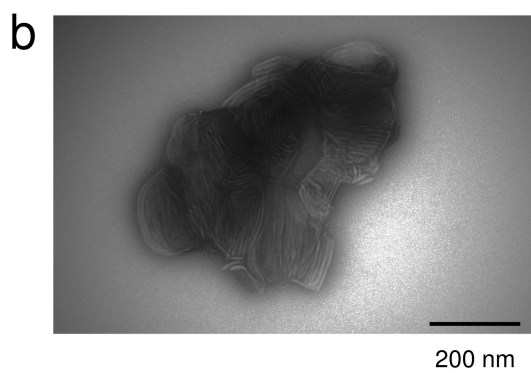
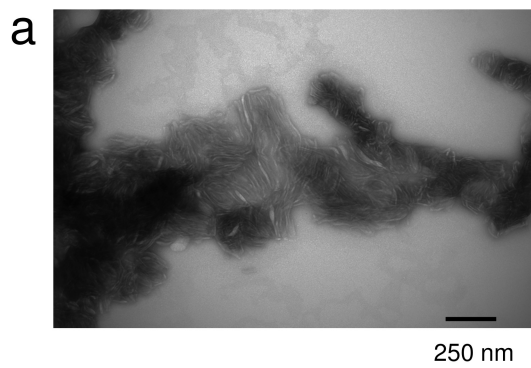
Supplementary Fig. S1



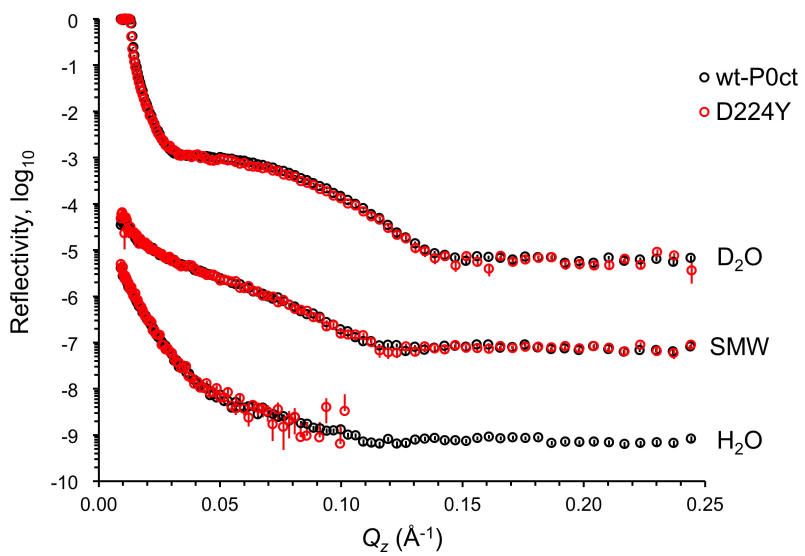
Supplementary Fig. S2



Supplementary Fig. S3



Supplementary Fig. S4



Supplementary Fig. S5



Graphic design: Communication Division, UIB / Print: Skjipes Kommunikasjon AS



uib.no

ISBN: 978-82-308-3520-3